Deformation processes in polycrystalline aggregates of gypsum

Siese de Meer

Deformation processes in polycrystalline

aggregates of gypsum

Siese de Meer

DEFORMATION PROCESSES IN POLYCRYSTALLINE AGGREGATES OF GYPSUM

Vervormingsprocessen in polykristallijne aggregaten van gips
(met een samenvatting in het Nederlands)

PROEFSCHRIFT

TER VERKRIJGING VAN DE GRAAD VAN DOCTOR
AAN DE UNIVERSITEIT TE UTRECHT, OP GEZAG VAN DE
RECTOR MAGNIFICUS, PROF. DR. J.A. VAN GINKEL,
INGEVOLGE HET BESLUIT VAN HET COLLEGE VAN DEKANEN
IN HET OPENBAAR TE VERDEDIGEN OP
MAANDAG 2 OKTOBER 1995 DES NAMIDDAGS TE 16.15 UUR

DOOR

SIESE DE MEER

GEBOREN OP 1 JUNI 1965 TE LEEUWARDEN

PROMOTOR: PROF. DR. C.J. SPIERS

             FACULTEIT AARDWETENSCHAPPEN

             UNIVERSITEIT UTRECHT

SUMMARY

Gypsum-dominated evaporite sequences play an important role in controlling the mechanics of foreland thrust tectonics, as well as forming large-scale halokinetic structures and caprock formations associated with oil and gas accumulations. For this reason, the deformation behaviour of polycrystalline gypsum, and the underlying microphysical processes, form a subject of considerable interest in structural geology, tectonophysics and geomechanics. In addition, the deformation and densification behaviour of polycrystalline gypsum is of fundamental interest for assessing the potential of new gypsum products in load-bearing building applications. This thesis reports an experimental, materials science oriented investigation aimed at providing a better understanding of the ductile flow and densification behaviour of gypsum, under both natural and engineering conditions. Special emphasis is given to fluid assisted (pressure solution) creep and related processes anticipated to be important in solids showing solubility.

In chapter 1, previous experimental work on gypsum is summarized. Aspects of the deformation behaviour of gypsum which remain insufficiently understood are identified and the aims of the present study are defined.

Chapter 2 describes hydrostatic compaction creep experiments performed on granular gypsum aggregates, with grain sizes ranging from 15 to 125 μm, at effective pressures in the range 0.4 to 3.9 MPa and at room temperature. Dry samples showed 10 - 13% instantaneous compaction during application of the load, with no creep thereafter. In contrast, wet samples (i.e. samples flooded with saturated $CaSO_4$ solution) showed relatively rapid creep, at volumetric strain rates ranging from initial values of $\sim 10^{-5}$ s^{-1} to values of $\sim 10^{-9}$ s^{-1} at volumetric strains of $\sim 12\%$. The mechanical data, obtained for the wet experiments, show a 3rd to 4th order power law dependence of compaction rate on effective pressure, and a inverse linear dependence on grain size. Taking into account independent crystal growth data for gypsum, these trends in the mechanical data show good agreement with theoretical models for grain boundary diffusional pressure solution allowing for rate control by precipitation on pore walls. In addition, the wet compacted samples show clear microstructural evidence for the operation of pressure solution creep, such as grain-to-grain indentations, truncations and overgrowths on pore walls. On this basis, it is proposed that the wet samples compacted by grain boundary diffusional pressure solution creep with rate limitation by the precipitation reaction. Discrepancies

between observed and expected creep rates are suggested to be caused by impurities in the natural gypsum starting material (Somerset, England).

In Chapter 3, the uniaxial compaction creep behaviour of wet, granular gypsum (Paris Basin) is investigated under both chemically closed-system (i.e. drained) conditions and open-system (i.e. flow-through) under conditions favouring pressure solution creep. The experiments were performed using applied stresses of 0.5 to 2.5 MPa, grain sizes 32-282 μm, at room temperature and using pore fluids saturated with respect to unstressed sample material. Control experiments done using dry and oil-saturated samples exhibited no creep. In contrast, samples flooded with gypsum solution crept rapidly. In addition, the microstructures developed in all wet tests provide classical evidence for the operation of grain boundary diffusional pressure solution. To justify detailed comparison with theory, it is shown that the water of crystallization present in gypsum influences neither the driving force for pressure solution creep nor the rate limiting steps, so that conventional pressure solution models are applicable. However, the mechanical behaviour observed in the closed-system experiments, though similar to that seen in the hydrostatic tests of Chapter 2, do not fully match existing models for either dissolution, diffusion or precipitation control. Nonetheless, independent crystal growth and dissolution data suggest that precipitation is again most likely to be rate controlling. Additional information on this was provided by the open-system experiments with through-flowing solution. In such experiments, precipitation can no longer control the rate of deformation, so that dissolution or diffusion will take over as the rate limiting process, strongly enhancing the creep rate. Indeed, a 10 to 30 times increase in compaction creep rate was observed, confirming that creep in the closed-system tests probably occurred by precipitation controlled grain boundary diffusional pressure solution.

In Chapter 4, the growth of gypsum using seed crystals and solutions prepared from Paris Basin gypsum was investigated, for comparison with the compaction creep data of Chapter 3. The limited results demonstrate that at low driving forces ($\Delta\mu$ < 1 kJ/mole) precipitation follows second order kinetics, while at larger driving forces the kinetic order is 3 - 4, which agrees well with previous studies. The data also suggest a roughly 1st to 2nd order inverse dependence of growth rate on seed crystal size at low driving forces ($\Delta\mu$ < 1 kJ/mole), and an inverse 2nd to 3rd order dependence at higher driving forces. The growth kinetics obtained are used to predict pressure solution creep rates with rate limitation by precipitation on pore walls. The predicted compaction creep rates are ~10 times faster

than observed in the pressure solution experiments of Chapter 3. However, predicted and experimentally obtained data show an almost identical dependence of creep rate on applied stress and grain size, again supporting the hypothesis that pressure solution in gypsum is precipitation controlled.

Chapter 5 addresses the influence of pore-fluid salinity (i.e. saturated gypsum solutions with NaCl concentrations of 0.01-6.11M) on the uniaxial compaction creep behaviour of granular (Paris Basin) gypsum under drained conditions (chemically closed system). The results show closely similar mechanical behavioural relations and microstructural development to those observed in the tests with NaCl-free pore fluid (Chapter 3). The creep rates however, are systematically faster (by up to 50 times) for compaction with NaCl-bearing pore fluids, in a manner which is closely consistent with the accelerating effect of NaCl on gypsum growth kinetics reported in the literature. This provides further evidence that compaction of wet gypsum under chemically closed conditions occurs by precipitation controlled pressure solution.

Chapter 6 focuses on deformation processes of importance in assessing the possibility of producing new load-bearing building materials by high-speed mechanical densification of gypsum produced in industrial Flue Gas Desulphurization (FGD) processes. It reports uniaxial densification experiments on FGD-gypsum with water contents in the range 0-5wt.%, performed at applied stresses in the range 25-530 MPa, at temperatures ranging from ambient to 150°C, and loading rates in the range 10^4 - 10^7 MPa s^{-1}. At room temperature, dry samples densified to porosities of 8%, in a time-independent manner by grain scale cataclasis accompanied by plastic deformation, and show grain size reduction to ~25 μm. In the wet samples, time-independent compaction involving cataclasis and plastic deformation is also accompanied by fluid-assisted recrystallization and pressure solution processes which reduce grain refinement, enhance instantaneous densification and allow minor densification creep at constant load. At elevated temperatures, both the dry and wet samples show enhanced instantaneous compaction, as well as time-dependent densification creep under constant load, but with no real change in mechanisms. However, at temperatures of (90-110°C), where dehydration begins, fluid-assisted mechanisms are also detected in initially dry samples. At still higher temperatures, all samples show partial or complete dehydrated to hemihydrate and poor densification. The densest samples (~1.5% porosity) were obtained by compaction of wet samples (2.0-2.5wt.% water) at the highest applied stress (530 MPa), at temperatures of 90-100°C, using the highest

loading rates. Such material is highly indurated and warrants further study for possible load-bearing applications in the building industry.

In Chapter 7 general conclusions are drawn based on the findings presented in Chapters 2 to 6. Combining the data obtained for pressure solution creep and growth kinetics, it is concluded that pressure solution in gypsum aggregates, under simple drained conditions, is controlled by a spiral growth precipitation mechanism at stresses below 1-10 MPa (depending on porosity), and by surface nucleation limited growth at higher stresses. The data are coupled with theory to derive constitutive equations for creep by these two pressure solution mechanisms, for both porous and dense gypsum aggregates, taking compositional effects into explicit account. These equations are then used to predict the creep behaviour of gypsum rock under natural conditions, as well as the creep behaviour of dense FGD-gypsum products in structural building applications. Finally, unanswered questions are identified and suggestions are made for further research.

CHAPTER 1

INTRODUCTION: Problem and aims

1.1 BACKGROUND

On the basis of both field and laboratory studies it is well established that polycrystalline gypsum is one of the weakest and most ductile rock materials found in the Earth's crust (e.g. Heard & Rubey, 1966; Murrell & Ismail, 1976; Baumann, 1985; Jordan, 1988; 1991; 1994). The deformation and densification behaviour of polycrystalline gypsum aggregates, and the underlying microphysical processes which control deformation, thus form a subject of considerable interest in a number of areas of structural geology, tectonophysics, geotechnical engineering and geomechanics. In the last 5 years, the mechanical properties of gypsum have also become a point of interest in building materials research.

In the field of structural geology and tectonophysics, gypsum-dominated evaporite sequences have long been recognized to play an important role in controlling the strength of the Earth's upper crust, via their action as weak decollement horizons such as those characterizing the foreland thrust belts of the Pyrenees (Solé-Sugranes, 1978), the Alps (Beach, 1981; Laubscher, 1981; Murrell, 1981; Davis & Engelder, 1985; Mugnier & Vialon, 1986; Jordan, 1988; 1991; 1994; Malavieille & Ritz, 1989; Jordan et al., 1990), the Greek Hellenides (Underhill, 1988) and the Atlas mountains of north Africa (Davis & Engelder, 1985). In addition, gypsum-dominated evaporites frequently develop large scale "halokinetic" structures such as pillows and diapirs (Wall et al., 1961; Gould & De Mille, 1968; Dabbagh et al., 1984; Doglioni, 1984; Laudon, 1984; Davis & Engelder, 1985; Van Berkel et al., 1986; Simón & Suriano, 1986; Underhill, 1988; Kupfer, 1989) which are sometimes associated with, or directly trap, large oil and gas deposits (Balkwill, 1978). Like rocksalt, the characteristically low permeability of gypsum rock and their high hydrocarbon sealing/trapping potential, are of course determined by their low resistance to ductile flow and densification/compaction. For these reasons, interest exists in obtaining a quantitative, mechanism-based understanding of the deformation and densification behaviour of polycrystalline gypsum, suitable as input for numerical modelling studies of both crustal deformation and hydrocarbon migration phenomena.

In geomechanics and geotechnical engineering, information of this kind is also needed for solving a variety of problems associated with gypsum. These include modelling i) the mechanical response of gypsum horizons present in the neighbourhood of evaporite-based waste repositories and storage caverns, and ii) the closure behaviour and stability of boreholes and wells sunk through gypsum sealing horizons.

As already indicated, the creep and densification behaviour of gypsum has also received attention in the field of building materials research (Karni & Karni, 1995; Stoop et al., 1995). Gypsum products, such as plaster and plaster-board, are widely used for interior non-load-bearing purposes in the building industry. These traditional gypsum materials are produced by hydration of calcium sulphate hemihydrate obtained from the calcination of natural gypsum rock. The resulting gypsum products typically exhibit ~65% porosity. This high porosity leads to relatively low strength, low creep resistance and considerable sensitivity to moisture - properties which preclude the use of traditional gypsum products in load-bearing, structural applications. However, building materials researchers have recently started investigating the possibility of producing gypsum materials with low porosity and high strength, by mechanically densifying (i.e. compressing) gypsum powders derived from flue gas desulphurization (FGD) operations at coal burning power plants. Following this route, the energetically inefficient process of calcining gypsum to hemihydrate is avoided, and the resulting dense gypsum products are expected to show significantly improved load-bearing capacity (Stoop et al., 1995). Clearly, a materials-science-based understanding of the densification and deformation behaviour of gypsum aggregates has an essential role to play in these developments.

During the last 30 years, a considerable amount of experimental deformation work has been performed on gypsum single crystals and on polycrystalline gypsum under geologically and geotechnically relevant conditions. In this chapter, the previous experimental work will be reviewed. It will be shown that while valuable data have been obtained, important aspects of the deformation and densification behaviour of polycrystalline gypsum, notably the effects of water in promoting solution transfer phenomena, are insufficiently understood to adequately address the various geological, and engineering problems outlined above. A framework is thus established for the presentation of new fundamental data on the deformation and densification behaviour of polycrystalline gypsum in the subsequent chapters.

1.2 PREVIOUS WORK ON GYPSUM

1.2.1 Crystal structure, stability, and solubility of gypsum

Gypsum ($CaSO_4 \cdot 2H_2O$) possesses a monoclinic crystal structure with point group 2/m. The crystallography and the location of the principle optical directions, is illustrated in Fig. 1.1a,b. Indexing of crystallographic planes and directions refer to the unit A cell of gypsum (unit cell containing the smallest vectors) in which a=0.568 nm, b=1.518 nm, c=6.29 nm and β=113°50' (see Deer et al., 1966). The structure of gypsum (Fig. 1.2) is layered parallel to (010) and consists of double layers of Ca^{2+} and SO_4^{2-} ions separated by layers of water molecules. Between each double layer of Ca^{2+} and SO_4^{2-} ions, the water molecules are located in such a way that they are hydrogen bonded to the oxygens of neighbouring sulphate groups. Each Ca^{2+} ion is coordinated by six oxygens belonging to SO_4 groups and by two water molecules. The perfect (010) cleavage reflects the layered nature of the structure.
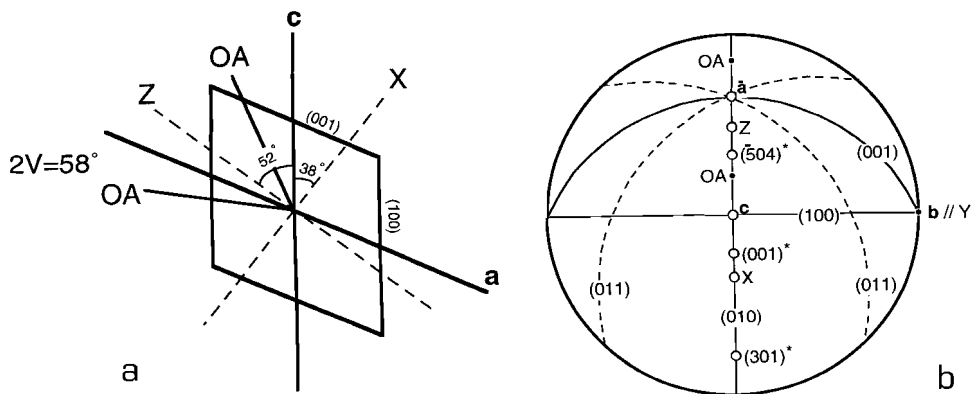
Figure 1.1a. Section parallel to the (010) plane of gypsum showing the crystallographic a and c-axis of the unit A-cell, the optical X and Z directions and the optical axes (O.A.) (after Williams, 1988). b. Upper hemisphere equal angle projection showing important planes and directions in gypsum using unit A-cell indexing. The directions (...)* are given as normals to planes; e.g. (001)* is the direction parallel to the normal on the (001) plane. Open circles are slip directions, O.A. are the optical axes and X, Y and Z are the optical directions.
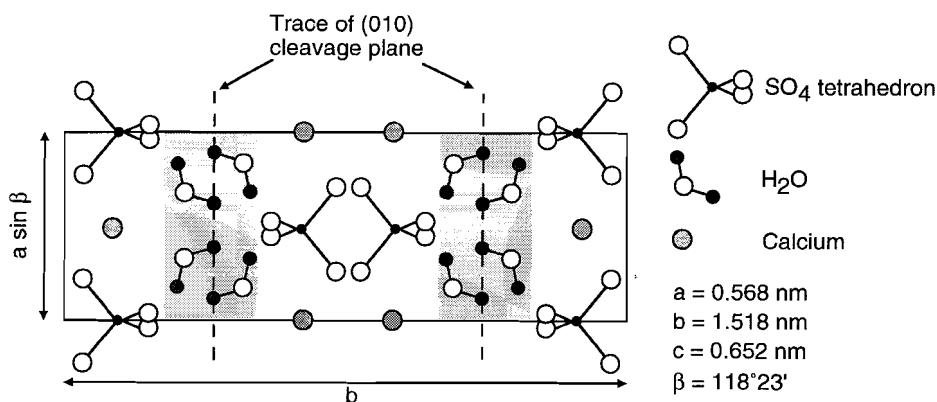
Figure 1.2. Projection of the crystal structure of gypsum perpendicular to the c-axis (c-axis sticking out of the paper) of the unit I-cell of gypsum, showing the calcium sulphate and water layering in the crystal structure parallel to the (010) plane (after Wooster, 1936). In the unit I-cell of gypsum a=.568 nm, b=1.518 nm, c=0.652 nm and β=118°23'.

Gypsum ($CaSO_4 \cdot 2H_2O$) and anhydrite ($CaSO_4$) occur in diverse geological environments, and the equilibrium relations between the two have been studied intensively. To understand the genesis and deformation behaviour of these minerals under crustal conditions, knowledge of the temperature and pressure conditions under which they coexist stably with aqueous solutions is essential. Phase diagrams are shown in Fig. 1.3, illustrating the effects of pressure and temperature. Clearly, gypsum is stable only at relatively low temperatures and pressures. It dehydrates to form anhydrite, via the metastable hemihydrate, following the reaction

$$CaSO_4 \cdot 2H_2O \rightarrow CaSO_4 \cdot \tfrac{1}{2}H_2O + 1\tfrac{1}{2}H_2O \rightarrow CaSO_4 + 2H_2O$$
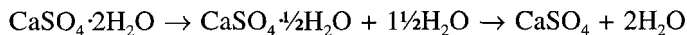
Experimentally obtained values, for the dehydration temperature of gypsum to anhydrite at 1 atm. pressure in pure aqueous solution, range from 38°C (Toriumi et al., 1938) to 63.5°C (Van 't Hoff et al., 1903). Most authors however, obtain values of 40-42°C (e.g. Posnjak, 1938; MacDonald, 1953) or 57-59°C (e.g. Zen, 1965; Hardie, 1967; Blount & Dickson, 1973), both of which agree well with the value of 46°C ± 22°C obtained from thermodynamic calculations (Zen, 1965). In Fig. 1.4, data on the effect of salinity on the boundary between the gypsum and anhydrite

stability fields is plotted for solutions at 1 atm. pressure. Although the data show considerable scatter, it is clear that the presence of sodium chloride decreases the dehydration temperature of gypsum from 40-60°C in pure aqueous solution to ~20°C in NaCl saturated solution (6.1M).
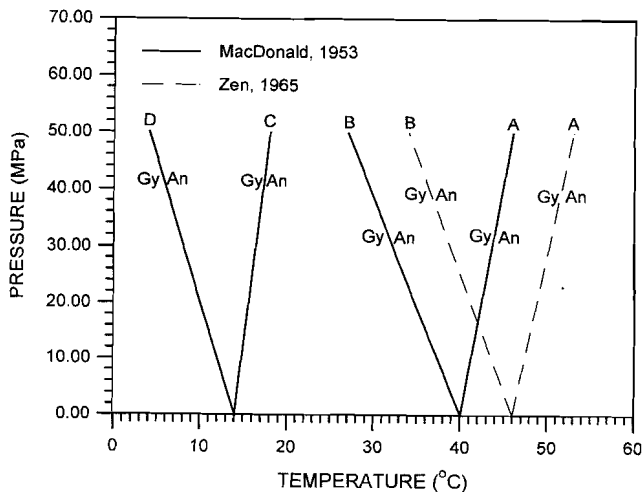
Figure 1.3. The stability fields of gypsum and anhydrite under various conditions. A - Same pressure acting on all phases in the presence of pure water. B - Lithospheric pressure acting on solid phases, hydrostatic pressure acting on pure water. C - Same pressure acting on all phases in the presence of saturated NaCl solution. D - Lithospheric pressure acting on solid phases, hydrostatic pressure acting on saturated NaCl solution. Based on thermodynamic calculations of MacDonald (1953) and Zen (1965).

Moving now to the solubility of gypsum, which is of major importance in any consideration of solution transfer deformation, this has been measured by numerous authors (e.g. Posnjak, 1938; Zen, 1965). In Fig. 1.5, solubility data for atmospheric pressure are plotted versus temperature, making use of extremum solubility curves between which all measured solubilities fall (after Hardie, 1967). In Fig. 1.6, solubility data for gypsum is plotted versus the concentration of various other salts in solution, again at atmospheric pressure (after Shternina, 1960) This shows that, in highly saline aqueous solutions, the solubility of gypsum is increased by up to 2 - 7 times that in pure water, with dissolved NaCl having the least effect and $Mg(NO_3)_2$ the largest effect.
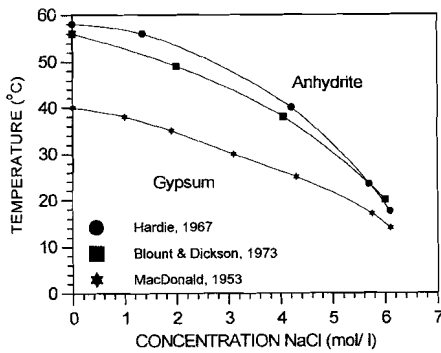
Figure 1.4. Data on the transition temperature of gypsum to anhydrite in aqueous solution at 1 atm. pressure as a function of the concentration of sodium chloride.
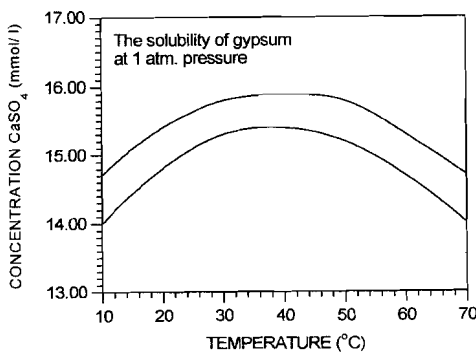
Figure 1.5. Solubility of gypsum as a function of temperature. The two curves represent the minimum and maximum solubilities reported in the literature (after Hardie, 1967).
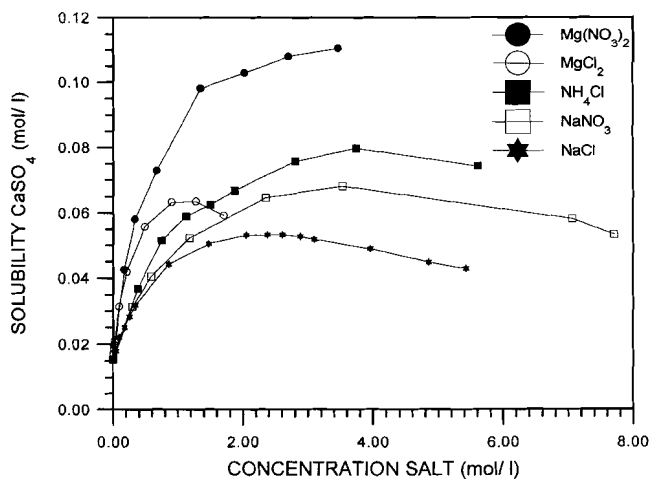
Figure 1.6. The solubility of gypsum as a function of the concentration of various salts (after Shternina, 1960).

1.2.2 Experimental deformation of gypsum single crystals

As early as the last century, translation glide or slip along the perfect (010) cleavage plane was recognized as an important deformation mechanism is gypsum single crystals. By pressing a knife into gypsum single crystals, Mügge (1898) induced glide on the (010) plane in the $(001)^*$, $(301)^*$ and $(\bar{2}05)^*$ directions. The glide directions here are given as normals to planes; e.g. $(001)^*$ is the glide direction parallel to the normal on the (001) plane. By applying a torque to elongated crystals, he also observed that together with glide on (010), glide could also be induced on the (011) and (100) secondary cleavage planes.

More recently, Craker & Schiller (1962) and Williams (1988) performed somewhat better controlled experiments. Craker & Schiller (1962) conducted three point bending tests on gypsum single crystals at room temperature. They found that when the load was applied perpendicular to the (010) cleavage plane, the crystals bent due to slip on the (010) plane. However, when the load was applied in any other direction, the crystals fractured before any detectable bending occurred. Significantly, changes in atmospheric humidity did not effect the observed behaviour. In contrast to the bending tests of Craker & Schiller (1962), Williams (1988) performed axi-symmetric compression experiments on single crystals at low confining pressures (0.1 - 1 MPa), and at room temperature, in order to investigate the stresses needed to initiate glide and rupture on the previously identified slip planes. In all cases both elastic and ductile deformation was observed prior to brittle shear failure. The results are summarized in Table 1.1. Mean critical resolved shear stresses (τ_c, the minimum shear stress needed to initiate detectable yielding by slip) ranged from 0.20 to 0.52 MPa for the different glide directions on the principle (010) slip plane. On (100) in the direction $(\bar{2}05)^*$, and on (011) in the direction $(\bar{5}02)^*$, τ_c was found to be 14.0 and 10.5 MPa respectively. Ultimate shear strengths (τ_u, the shear strength at cataclastic failure on the slip system) ranged from 0.58 to 1.36 MPa on the (010) plane. On the (100) and (011) planes, in the directions $(\bar{2}05)^*$ and $(\bar{5}02)^*$ respectively, the τ_u values were found to be 18.5 and 14.3 MPa. The critical resolved shear stress and ultimate strength of the (100) and (011) planes were measured only in the $(\bar{2}05)^*$ and $(\bar{5}02)^*$ directions respectively, to avoid shear on the (010) principle cleavage plane. The relatively low resistance to slip and rupture on the (010) plane observed by Williams (1988) was ascribed to the weak hydrogen bonding within the H_2O layers and between the H_2O and Ca^{2+} - SO_4^{2-} layers.

In addition to the above work on glide systems, Williams (1986) performed pressure solution experiments on gypsum single crystals at low applied stresses. It was claimed that results could readily be obtained in the time available for laboratory experiments but no results were given.

Slip plane	Slip direction[1]	Slip direction[2]	τ_c (MPa)	τ_u (MPa)	Also observed by
(010)	$(\bar{5}02)^*$	a = [100]	0.52	1.36	
(010)	$(\bar{5}03)^*$	Z = ~$[\bar{4}01]$	0.50	1.26	
(010)	$(\bar{2}05)^*$	c = [001]	0.28	0.69	Mügge, 1898
(010)	$(\bar{5}04)^*$	~$[\bar{2}01]$	0.37	0.88	
(010)	$(103)^*$	X = ~$[\bar{3}04]$	0.27	0.58	
(010)	$(001)^*$	~[102]	0.27	0.70	Mügge, 1898
(010)	$(301)^*$	~$[\bar{2}01]$	0.20	0.64	Mügge, 1898
(100)	$(\bar{2}05)^*$	c = [001]	14.0	18.5	Mügge, 1898
(011)	$(\bar{5}02)^*$	a = [100]	10.5	14.3	Mügge, 1898

Table 1.1: Critical resolved shear strength τ_c, and ultimate shear strength τ_u on three slip planes in single crystals of gypsum measured by Williams (1988). Craker & Schiller (1962) observed slip on the (010) plane of gypsum, but did not identify the slip directions. Indexing of the slip planes and slip directions refer to the unit A cell of gypsum (see Deer et al., 1966).

[1] Slip direction defined as parallel to the normal to the planes given.

[2] Slip direction defined using the crystallographic axes of the unit A-cell of gypsum. Dimensions of unit A-cell; a=0.568 nm, b=1.518 nm, c=0.629 nm and β=113°50'. X and Z are optical directions.

1.2.3 Deformation experiments on polycrystalline gypsum

1.2.3.1 Experiments above the dehydration temperature

Most experimental studies on polycrystalline gypsum rocks have been performed in order to investigate the influence of dehydration reactions on the deformation behaviour of gypsum in its own right, but also viewing gypsum as an analogue for rocks which dehydrate at less easily accessible conditions (Heard & Rubey, 1966; Murrell & Ismail, 1976; Baumann, 1984; Murrell, 1985; Nüesch & Baumann, 1989; Panozzo Heilbronner, 1993; Olgaard et al., 1995; Ko et al., 1995). These experiments have mostly been performed in triaxial testing machines, at temperatures in the range 20°C-470°C, confining pressures of 0.1-552 MPa and constant strain rates in the range $3.3 \cdot 10^{-4}$-$2.8 \cdot 10^{-7}$ s^{-1} (see Table 1.2). The experiments were conducted under both undrained conditions (samples remaining completely sealed during testing; Heard & Rubey, 1966; Murrell & Ismail, 1976; Murrell, 1985; Olgaard et al., 1995; Ko et al., 1995) and drained conditions (sample ends maintained at atmospheric or controlled pressure during testing; Murrell & Ismail, 1976; Baumann, 1984; Murrell, 1985; Nüesch & Baumann, 1989; Panozzo Heilbronner, 1993; Olgaard et al., 1995; Ko et al., 1995).

In all of these studies, the gypsum showed at least a tenfold decrease in strength when dehydration occurred during deformation in undrained experiments. The corresponding samples showed cataclastic deformation accommodated by pressure solution and crystal plasticity, and the weakening effect is believed to be due to enhancement of cataclasis by development of high fluid pressures during dehydration.

In experiments drained to atmospheric pressure, Murrell & Ismail (1976) and Murrell (1985) did not observe any loss of strength during dehydration. However, Baumann (1984), Nüesch & Baumann (1989) and Panozzo Heilbronner (1993) observed a marked decrease in strength under these conditions with a slight tendency for drained samples to be stronger than the undrained samples. This weakening is believed to reflect partial or transient draining resulting from low sample permeability. In the drained experiments performed by Olgaard et al. (1995) and Ko et al. (1995), the pore fluid pressure at the end of the samples was controlled, and the volume of water expelled from the samples was measured. These authors observed a marked decrease in strength just after the onset of dehydration. However, as the cracks accompanying cataclasis began to link, the rock became stronger again, due to a decrease in pore fluid pressure via dilatancy

and a resulting increase in permeability. Eventually, samples became stronger than intact gypsum rock due to progressive conversion into the stronger hemihydrate phase. In the drained experiments performed at confining pressures below 150 MPa, Murrell & Ismail (1976), Baumann (1984), Murrell (1985), Nüesch & Baumann (1989), Panozzo Heilbronner (1993), and Olgaard et al. (1995) report that samples showed brittle failure with deformation generally being localized in narrow faults. However, at high confining pressures, deformation was homogeneous with the sample microstructures showing twinning, kinking, undulatory extinction, flattening of grains, the development of a crystallographic preferred orientation, and minor transgranular fractures, suggesting a combination of crystal plastic flow and cataclasis.

In a somewhat different type of experiment, Shimamoto (1981, 1986) investigated the effect of dehydration of gypsum gouge on frictional sliding in artificially faulted Tennessee sandstone. Initially dry gypsum gouge showed stable sliding at temperatures both below the dehydration temperature (room temperature) and far above the dehydration temperature (300°C), but showed stick-slip behaviour while undergoing dehydration (T=100°C-150°C, effective pressure $\geq$ 30 MPa). In initially wet samples, the stick-slip behaviour seen in the dry samples was not observed and stable sliding occurred at far lower stresses. The slip behaviour of the gouge was inferred to be controlled by its free water content and composition, and by the pore fluid pressure, but the mechanisms of deformation were not addressed further.

Table 1.2: Overview of experimental conditions used in previous triaxial experiments performed on gypsum rocks in order to investigate the effect of gypsum dehydration on deformation behaviour.

AUTHORS	TEMPERATURE (°C)	CONFINING PRESSURE (MPa)	STRAIN RATE (s^{-1})	CONDITIONS	PORE FLUID PRESSURE (at sample ends; MPa)
Heard & Rubey, 1966	26 - 250	200 and 500	$3.3*10^{-4}$ - $3.4*10^{-7}$	U	-
Murrell & Ismail, 1976	20 - 470	0.1 - 552	10^{-5}	U, D_a	0.1
Shimamoto, 1981	20 - 300	150	$5*10^{-5}$	D_a	0.1
Baumann, 1984	20 - 100	0.1 - 200	$8.5*10^{-5}$ - $2.8*10^{-7}$	D_a	0.1
Murrell, 1985	20 - 470	0.1 - 552	10^{-5}	U, D_a	0.1
Shimamoto, 1986	20 - 300	150	$5*10^{-5}$	U, D_a	0.1
Nüesch & Baumann, 1989	20 - 100	0.1 - 200	$8.5*10^{-5}$ - $2.8*10^{-7}$	D_a	0.1
Panozzo Heilbronner, 1993	22 - 140	150	$3*10^{-5}$	D_a	0.1
Olgaard et al., 1995	23 - 150	0.1 - 200	$6*10^{-5}$ - $7*10^{-7}$	D_t	10 - 100
Ko et al., 1995	105 - 150	140 - 200	$2*10^{-5}$ - $4*10^{-5}$	U, D_a, D_t	0.1 - 10

U = Undrained condition (samples remaining completely sealed during testing), D_a = Drained condition with pores vented to atmosphere during testing, D_t = Transiently drained condition (sample ends maintained at constant pore pressure using volumeter system to measure volume of fluid expelled from sample during experiment.)

1.2.3.2 Experiments below the dehydration temperature

While Baumann (1984) and Nüesch & Baumann (1989) conducted some of their experiments above the dehydration temperature, most of their experiments on natural gypsum rock were performed below the dehydration temperature to hemihydrate (see Table 1.2) at pressures ranging from 0.1 to 200 MPa and strain rates in the range $8.5 \cdot 10^{-5}$ - $2.8 \cdot 10^{-7}$ s^{-1}. Under these conditions, Baumann (1984) and Nüesch & Baumann (1989) found that the strength of their natural gypsum samples (no water added) decreased with decreasing confining pressure, increasing temperature, and decreasing strain rate. Microstructural investigation showed that the samples mainly deformed cataclastically at temperatures $\leq$ 40°C, at all strain rates applied. At confining pressures up to 150 MPa, the samples sometimes showed brittle failure at strain rates of $\sim 8.5 \cdot 10^{-5}$ s^{-1}. At higher confining pressures (>150 MPa) brittle failure was suppressed, and the samples exhibited steady state behaviour. The microstructure of these samples showed that cataclasis was accompanied by twinning and dislocation creep, shown by the undulatory extinction of some grains. At higher temperatures (>40°C) and confining pressures >150 MPa, the samples showed steady state creep and microstructural features consistent with plastic deformation (twinning, undulatory extinction, development of kinkbands and a crystallographic preferred orientation) plus evidence for fluid assisted grain boundary migration. Baumann (1984) recalculated the results of his experiments, obtained throughout the entire range of temperatures (20-100°C) and strain rates ($8.5 \cdot 10^{-5}$-$2.8 \cdot 10^{-7}$ s^{-1}) investigated (confining pressure 150 MPa), to a temperature of 40°C using the experimentally obtained activation energy for creep in this entire region (132 kJ/mole), and plotted a "best-fit" through the data (see Fig. 1.7). In field 3 of Fig. 1.7, the mechanical data fitted a power law creep equation of the form

$$\dot{\varepsilon} \;=\; A \cdot \exp(-H/RT) \cdot \sigma^{n} \qquad \textit{with } n \;=\; \sim 4.5 \qquad\qquad (1.1)$$

where, $\dot{\varepsilon}$ is strain rate, A is a constant, H is the activation energy for creep, R is the gas constant, T is absolute temperature, and σ is the differential stress. Baumann (1984) interpreted the corresponding mechanical behaviour as purely dislocation creep, but from the microstructures it was clear that dislocation creep was accompanied or dominated by cataclasis at the lower temperatures, and by fluid assisted grain boundary migration at the higher temperatures.

In an attempt to investigate the effects of water on creep of gypsum at room temperature, and suspecting pressure solution effects, Griggs (1939, 1940)

performed long term dead weight creep experiments on unconfined, natural gypsum samples saturated with water or solution. The applied stresses used fell in the range 10 to 30 MPa. Griggs' results are summarized in Fig. 1.8. Dry samples showed little or no creep ($<1 \cdot 10^{-10}$ s^{-1} at an applied stress of 42 MPa). At the higher stresses (> 30 MPa), the wet samples yielded classical creep curves consisting of primary, secondary and tertiary stages, followed by failure. At low applied stresses, he observed continuously decreasing creep rates. The strain rates obtained in quasi steady state at 10 and 30 MPa were $2 \cdot 10^{-10}$ s^{-1} and $2 \cdot 10^{-8}$ s^{-1} respectively. Griggs (1940) also varied the pore fluid used in his tests. Using a dilute HCl solution (increasing the solubility of gypsum) and a calcium chloride solution (lowering the solubility of gypsum), the observed creep rates were substantially increased, whereas material flooded with oil showed the same behaviour as dry material. Griggs concluded that pressure solution was active, but obtained no detailed kinetics data.

Remaining experimental work on gypsum at temperatures below the dehydration temperature has focused on the engineering properties of polycrystalline gypsum materials under ambient conditions. Recently, Bell (1994) determined the unconfined compressive strength of a number of natural gypsum rocks from the north and midlands of England, obtaining results in the range of 12 to 42 MPa (see Table 2 of Bell (1994) for these values, as well as a range of other engineering properties of natural gypsum rocks). Similarly, work on the compressive and tensile strength of traditional gypsum building products (porosity ~65%) has recently been reported by Karni & Karni (1995). Compressive and tensile strengths were found to range from 1.5 to 20.7 MPa and from 1.1 to 2.5 MPa respectively, decreasing with increasing porosity and increasing moisture/water content. In contrast, tests on dense FGD-Gypsum (porosity 6-20%), prepared by compaction under wet conditions at stresses of 50 - 500 MPa and loading rates 0.8-8.3 MPa s^{-1}, yielded uniaxial compressive strengths ranging from 9.1 to 101.1 MPa (Stoop et al., 1995) The highest strength was obtained in the densest samples, i.e. samples compacted at the highest applied stress (500 MPa) and fastest loading rate (8.3 MPa s^{-1}).
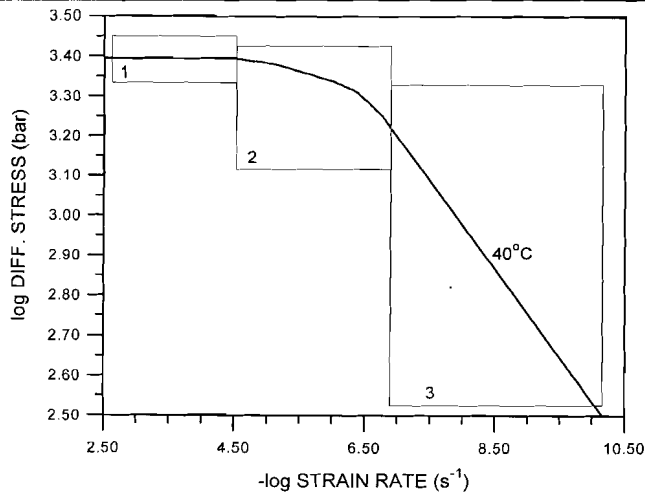
Figure 1.7. Synoptic diagram indicating the different fields of deformation mechanisms reported by Baumann (1984) for natural gypsum tested under drained conditions at confining pressures ranging from 0.1-200 MPa, temperatures from 20-100°C and at strain rates in the range $8.5 \cdot 10^{-5}$ - $2.8 \cdot 10^{-7}$ s^{-1}. The 40°C isotherm is a "best-fit" through all data, recalculated to 40°C using the experimentally obtained activation energy for creep for the entire range (132 kJ/mole). 1 - Cataclasis. 2 - Cataclasis plus dislocation creep. 3 - Dislocation creep plus fluid assisted grain boundary migration.
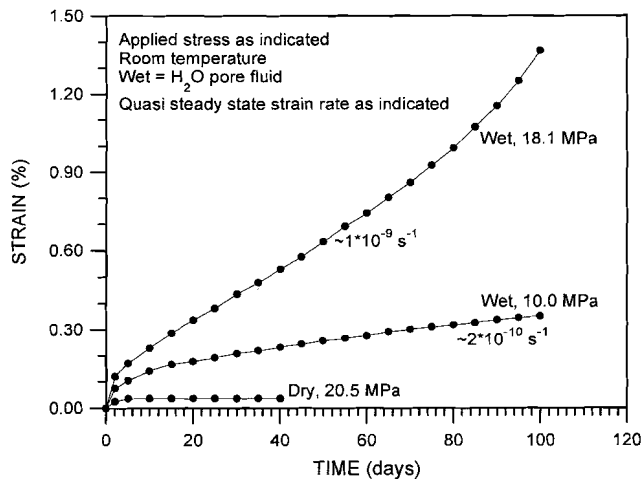
Figure 1.8. Creep curves for unconfined gypsum rock tested in uniaxial compression by Griggs (1940) under wet (i.e. water saturated) and dry (lab dry) conditions. Quasi steady state strain rates ($\dot{\varepsilon}_{ss}$ in s^{-1}) as indicated.

1.3 REMAINING PROBLEMS

The extensive body of work on the effects of dehydration on the mechanical behaviour of gypsum reviewed above clearly demonstrates that dehydration could be responsible for the decollement function of gypsum-rich horizons provided that the fluid pressure can be maintained high. However, the results of Olgaard et al. (1995) and Ko et al. (1995) suggest that high fluid pressure will only be maintained in the early stages of dehydration, unless the gypsum is embedded in fully impermeable rock. The possibility that the decollement action of gypsum horizons is controlled by dislocation and diffusion creep processes within the gypsum, at temperatures below the dehydration temperature, must therefore be taken into account in modelling decollement phenomena. Such processes must also play an important role in gypsum halokinesis, at temperatures below the dehydration temperature.

It is apparent from the above, however, that relatively little is known about plastic and diffusional flow mechanisms in gypsum at temperatures below the dehydration temperature. Although the main slip systems are known and crystal plastic mechanisms are clearly important, Baumann's region 3 flow law (Baumann, 1984, Fig. 1.7) provides an empirical creep equation only with insufficient mechanistic basis to be reliably extrapolated to natural conditions as a dislocation creep law. Most important, however, is the effect of water presumably via some kind of pressure solution process. This drastically enhances creep in gypsum and must therefore dominate under a wide range of geological and engineering conditions i.e. in decollement horizons, during diapirism, in the diagenetic sealing of gypsum caprock formations as proposed by Williams (1986), and in gypsum building materials subjected to moist environments. But no quantitative kinetic description or microphysical understanding of the pressure solution process is available for gypsum rock or building materials. Similarly, the effects of water on the preparation of gypsum building materials by powder compaction are largely unknown.

1.4 AIMS OF THE PRESENT WORK

In view of the problems identified above, this thesis aims to provide fundamental data on the deformation and densification behaviour of polycrystalline gypsum below the dehydration temperature. Emphasis is given to fluid assisted

(pressure solution) creep and related processes in gypsum, with the specific aim of identifying the mechanisms controlling the rate of deformation. In the case of highly soluble salts, such as NaCl, the interfacial reactions of dissolution and precipitation tend to be very rapid (see Scrutton & Grootscholten, 1981), while the opposite tends to be the case in sparingly soluble materials such as gypsum. For this reason, careful attention is given to the kinetics of the interface reactions in gypsum, as these are likely to play an important role in controlling the rate of deformation by fluid assisted processes such as pressure solution creep. Further attention is given to the effect of dissolved NaCl on deformation rates, since crystal growth/dissolution data indicate that NaCl is solution can dramatically influence interfacial reaction rates. Alongside basic experiments designed to address the fundamentals of pressure solution processes in gypsum, high-speed compaction experiments have also been performed with the aim of gaining insight into the mechanisms of compaction and improving the strength and creep resistance properties of compacted gypsum building materials.

1.5 THESIS STRUCTURE

This thesis has been structured in such a way that the independent chapters can be submitted, in future, as individual papers.

CHAPTER 2

CREEP OF WET GYPSUM AGGREGATES UNDER HYDROSTATIC LOADING CONDITIONS[*]

2.1 INTRODUCTION

It is well known that gypsum-dominated evaporite sequences often play an important role in controlling the mechanics of foreland thrust and nappe tectonics, via their action as weak, decollement horizons. Mylonitic decollements of this type occur, for example, under the Jura nappe (Laubscher, 1981; Murrell, 1981; Mugnier & Vialon, 1986; Jordan, 1988, 1991; Jordan et al., 1990), in the foreland thrust belt of the southern Pyrenees (Solé-Sugranes, 1978), in the southern French Alps (Beach, 1981; Malavieille & Ritz, 1989), and in the Greek Hellenides (Underhill, 1988). Gypsum-dominated evaporites are also known to develop large-scale, "halokinetic" structures, such as pillows and diapirs (Gould & De Mille, 1968; Baumann, 1984; Underhill, 1988), some of which are associated with significant oil and gas accumulations, as seen for example in the Sverdrup Basin of arctic Canada (Balkwill, 1978). For these reasons, there has long been interest in developing a microphysically-based understanding of the ductile flow behaviour of polycrystalline gypsum, suitable for quantitative modelling purposes (Baumann, 1984; Williams, 1986, 1988). Data on the deformation and densification behaviour of gypsum are also relevant to modelling i) the evolution of the low permeability and high sealing capacity exhibited by gypsum formations, ii) the mechanical response of gypsum layers present in the neighbourhood of evaporite-based waste repositories and storage caverns, and iii) the closure behaviour and stability of boreholes and wells sunk through gypsum layers.

Despite these areas of interest, relatively little is known about the mechanical behaviour and deformation mechanisms operating in gypsum under either geological or geotechnically relevant conditions. The few experimental studies which have been carried out have shown that crystal plastic mechanisms are of major importance in both single- and polycrystalline gypsum under laboratory conditions

---

[*] *This chapter has been published as: De Meer, S. & Spiers, C.J. 1995. Creep of wet gypsum aggregates under hydrostatic loading conditions. Tectonophysics, vol. 245, p 171-184. Permission to reproduce the paper in this thesis was kindly granted by Elsevier Science B.V.*

(Mügge, 1898; Craker & Schiller, 1962; Heard & Rubey, 1966; Murrell & Ismaïl, 1976; Baumann, 1984; Williams, 1988), and that pressure solution creep may also occur when water is present (Griggs, 1939, 1940; Williams, 1986). By comparison with other soluble salts (see Spiers et al., 1990; Visser & Spiers, 1992), it seems reasonable to suppose that pressure solution and related processes will indeed occur in gypsum under both laboratory and natural conditions. However, the above-mentioned experimental evidence for pressure solution is very limited and the extent to which it may be important in gypsum is therefore unclear.

The present paper documents a preliminary experimental investigation into the compaction creep behaviour of granular gypsum, tested in the presence of saturated $CaSO_4$ solution. The aim was to confirm whether or not pressure solution creep processes occur at measurable rates under laboratory conditions, and if so to gain insight into the detailed mechanism and kinetic controls. To these ends, attention is focused on a comparison of wet versus dry compaction behaviour, and of the observed wet compaction behaviour with theoretical models for grain boundary diffusional pressure solution creep. The results show clear evidence for some kind of pressure solution process. However, in contrast to the behaviour exhibited by more highly soluble salts (e.g. NaCl or $NaNO_3$, see Spiers et al., 1990; Visser & Spiers, 1992), the process is very slow in gypsum, and apparently controlled by interfacial reaction kinetics rather then by grain boundary diffusion.

2.2 EXPERIMENTS

The present experiments consisted of a series of hydrostatic compaction creep tests performed on wet granular gypsum aggregates, at room temperature, following the method used for NaCl by Spiers and Schutjens (1990). The experiments were carried out varying the applied effective pressure (P_e) and sample grain size (d) independently, so that the dependence of compaction creep behaviour on P_e and d could be systematically determined.

2.2.1 Method

Granular gypsum starting material was prepared by sieving crushed natural gypsum (Somerset, U.K.) into controlled grain size fractions of 28-37 μm, 37-50 μm, 50-75 μm, and 105-125 μm. Each fraction was then washed with distilled water to remove any fines attached to the grain surfaces after sieving, and to dissolve

away surface asperities and mechanical damage. An additional grain size fraction with a grain size range of 15-28 μm was prepared by gravitational settling in distilled water (Stokes settling). After wet preparation, each grain size fraction was dried by thinly spreading the material onto a filter paper base placed in a drying cabinet (air circulation type) operated at ambient temperature. The final grain size distribution of individual fractions was then checked optically, and using a Malvern particle sizer, and found still to lie in the ranges given above. Immediately before testing, all fractions were oven-dried for 48 hours at 35 °C to remove any water which may have been taken up during storage.

In setting up the experiments, individual 80 g samples of the various controlled grain size powders were first jacketed in rubber balloons and their starting volume determined by measuring the displaced volume when the jacketed sample was immersed in water. The jacketed samples were then loaded into the servo-controlled, hydrostatic compaction apparatus illustrated in Fig. 2.1, for testing. In the initial stage of all tests, the starting powder was first compacted dry by "ramping" the effective applied pressure (P_e) to a value of 3.9 MPa over a period of 10 minutes, after which the samples were maintained at 3.9 MPa for a further ~90 minutes. During this whole procedure, the pores were vented to atmospheric pressure with valve A open and valve B closed (Fig. 2.1), and volumetric strain was measured by collecting the volume of air expelled through valve A over water, using a measuring cylinder. Note that in each run, the initial "load-ramping" stage led to an essentially time-independent (instantaneous) volumetric compaction of 10-13 per cent with no measurable creep occurring thereafter; this produced a locked compact (Spiers and Brzesowsky, 1993) with a porosity of $\phi_0 = 45.0 \pm 3.0\%$. The dry-compacted samples were then unloaded (P_e reduced to 0.05 MPa), evacuated via valve A and, after closing of valve A, flooded with saturated gypsum solution from the burette measuring system, via valve B (Fig. 2.1). The samples were then reloaded by increasing P_e to the desired test value while the fluid pressure (P_f) was maintained at atmospheric pressure via the burettes (see Fig. 2.1). The compaction creep behaviour of the samples was subsequently monitored as a function of time by measuring the volume of saturated solution displaced from each sample into the burette system. Both constant stress and stress-stepping experiments were performed, using effective pressures in the range $0.4 \leq P_e \leq 3.9$ MPa and samples of each available grain size fraction. Volumetric strains up to 18% were achieved.

Tests were terminated by reducing P_e to zero and extracting the sample, plus embedded high pressure tube (see Fig. 2.1), from the compaction vessel. Each

sample was then removed from its jacket and placed in a bed of laboratory tissue paper. Saturated solution remaining in the pores was then carefully flushed from the sample by directing compressed air through the sample via the embedded tube. Finally, the tube was removed and the samples were impregnated with epoxy resin to allow sectioning and microstructural study.
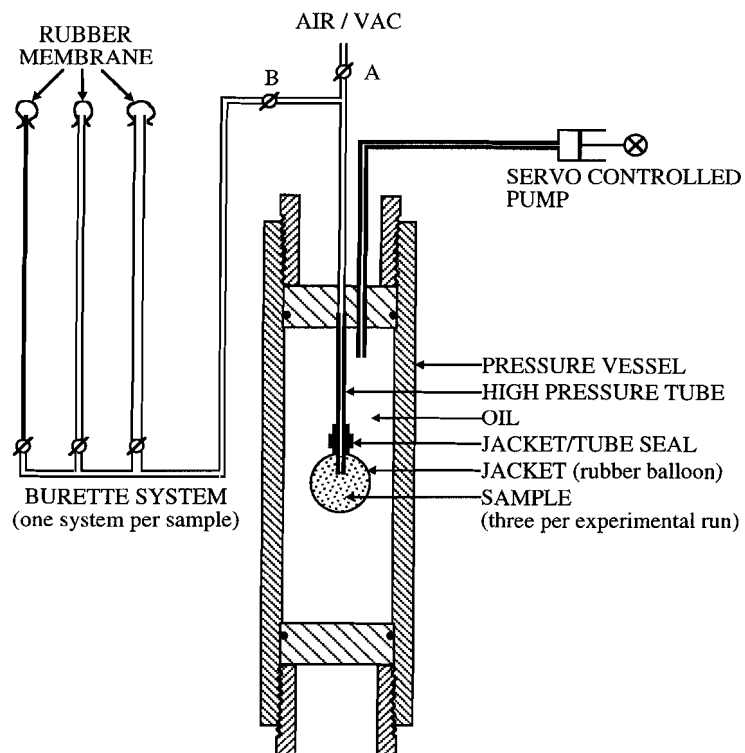
Figure 2.1. Semi-schematic diagram illustrating the hydrostatic compaction apparatus used in the present experiments on wet granular gypsum aggregates. The compaction creep behaviour of each sample was monitored by measuring the volume of saturated gypsum solution expelled from the sample into the burette system.

The complete set of (wet) experiments reported in this paper is listed in Table 2.1, along with the corresponding experimental conditions and variables. For comparative purposes, some of the constant stress experiments (PS-Gyp1, PS-Gyp2) were repeated (in both hydrostatic and uniaxial compaction modes; c.f. Spiers et al., 1990; Spiers & Schutjens, 1990) under entirely dry conditions (i.e. with the sample containing air only), or using dry "evaporating oil" (Shell No. 4919) or silicone oil instead of saturated solution. In the entirely dry hydrostatic experiments, compaction of the samples was measured in terms of the volume of air expelled.

Test/Sample number	Grain size (μm)	Dry compaction pressure (MPa)	Porosity after dry compaction	Wet test type	Applied eff. pressure(s) (MPa)	Final (wet) strain (%)
PS-Gyp1	37 - 50	3.9	44.0 %	CS	2.4	13.3
PS-Gyp2	50 - 75	3.9	45.9 %	CS	2.4	12.4
PS-Gyp3	28 - 37	3.9	43.1 %	SS (5 steps)	0.9, 1.4, 1.9, 1.4, 0.9	12.0
PS-Gyp4	37 - 50	3.9	42.5 %	SS (5 steps)	0.9, 1.4, 1.9, 1.4, 0.9	10.6
PS-Gyp5	50 - 75	3.9	42.1 %	SS (5 steps)	0.9, 1.4, 1.9, 1.4, 0.9	9.8
PS-Gyp6	15 - 28	3.9	47.8 %	SS (7 steps)	0.4, 0.9, 1.4, 1.9, 2.4, 2.9, 3.9	17.6
PS-Gyp7	37 - 50	3.9	45.2 %	SS (7 steps)	0.4, 0.9, 1.4, 1.9, 2.4, 2.9, 3.9	14.8
PS-Gyp8	105 - 125	3.9	46.6 %	SS (7 steps)	0.4, 0.9, 1.4, 1.9, 2.4, 2.9, 3.9	12.4

Table 2.1. List of complete set of wet experiments reported, together with corresponding experimental conditions and variables. All tests were performed at room temperature (20 - 23° C). CS = constant stress test; SS = stress stepping test.

Finally, it should be noted that the experimental apparatus (Fig. 2.1) was operated in such a way that up to three samples could be simultaneously tested, with each one connected to its own burette system. The apparatus allowed

volumetric strains to be measured with a resolution of $\sim 10^{-5}$, and applied (effective) pressures to be measured and controlled to within ~ 0.01 MPa (Spiers and Schutjens, 1990). Volumetric strain rates were calculated as a function of volumetric strain and time, using the 3 point central difference method. Conventional methods of analysis showed that the standard relative error in compaction strain rate was less than 4% in all experiments.

2.2.2 Mechanical results

As already indicated, the initial dry loading stage, to which all samples were subjected, resulted in a more or less instantaneous compaction of the samples by 10-13% during application (ramping) of the load, with little or no creep thereafter. When reloaded after dry compaction, dry and oil-flooded samples (PS-Gyp9, PS-Gyp10) generally showed 0.4-1.0% of instantaneous compaction, but no subsequent creep.

In contrast, the solution-flooded samples showed relatively rapid compaction creep after reloading. The compaction curves obtained for the wet samples, in both constant stress and stress-stepping experiments, are presented in Fig. 2.2a,b. These clearly demonstrate that compaction creep is promoted by increasing effective pressure (P_e) and by decreasing grain size (d), but decelerates with increasing volumetric strain (e_v).

This last trend, i.e. the dependence of creep rate ($\dot{\beta}$) on volumetric strain, is illustrated in Figs. 2.3a-c for a selection of both constant stress and stress-stepping tests. By combining strain rate versus strain data of this kind, obtained from all experimental runs, we have examined how the creep rate of our wet samples, measured at constant strain (here approximately constant porosity), depends on P_e and d, extrapolating the stepping-derived data over small ranges of strain, where necessary. Typical results are shown in Figs. 2.4 and 2.5. From the slopes of the data sets appearing in these figures, it is evident that across most of the range of conditions investigated ($P_e > 0.9$ MPa, $d > 28$-37 μm), the compaction rate ($\dot{\beta}$) at constant strain can be viewed as roughly proportional to P_e raised to the power n$\approx$3 and d to the power m$\approx$-1. Note, however, that at the finest grain sizes investigated ($d \leq 28$-37 μm), $\dot{\beta}$ becomes less sensitive to P_e (n $\rightarrow$ 1.5 at d = 15-28 μm, see Fig. 2.4b) whereas at the lowest stresses ($P_e \leq 0.9$ MPa), $\dot{\beta}$ becomes more sensitive to d (m $\rightarrow$ -3, see Fig. 2.5c).
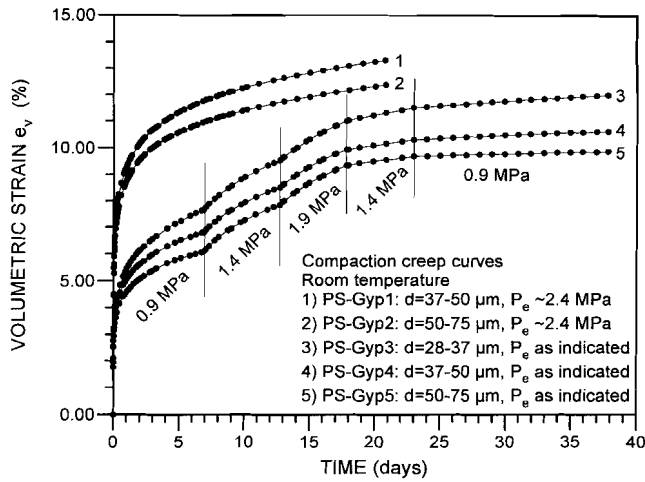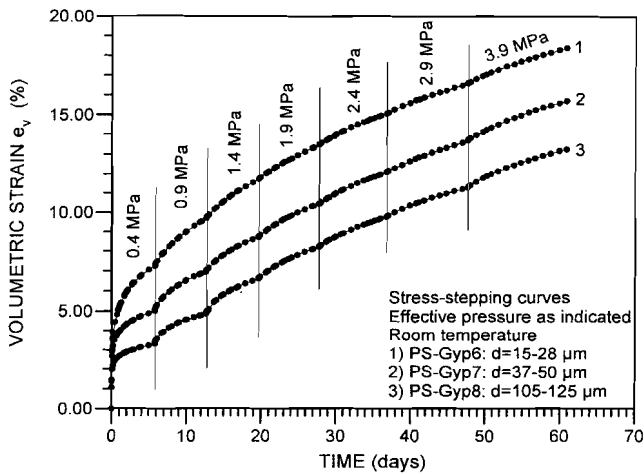
Figure 2.2a,b. The complete set of compaction creep curves obtained in the present wet experiments on gypsum. Note the effects of increasing applied effective pressure (P_e) and decreasing grain size (d) on creep rate.
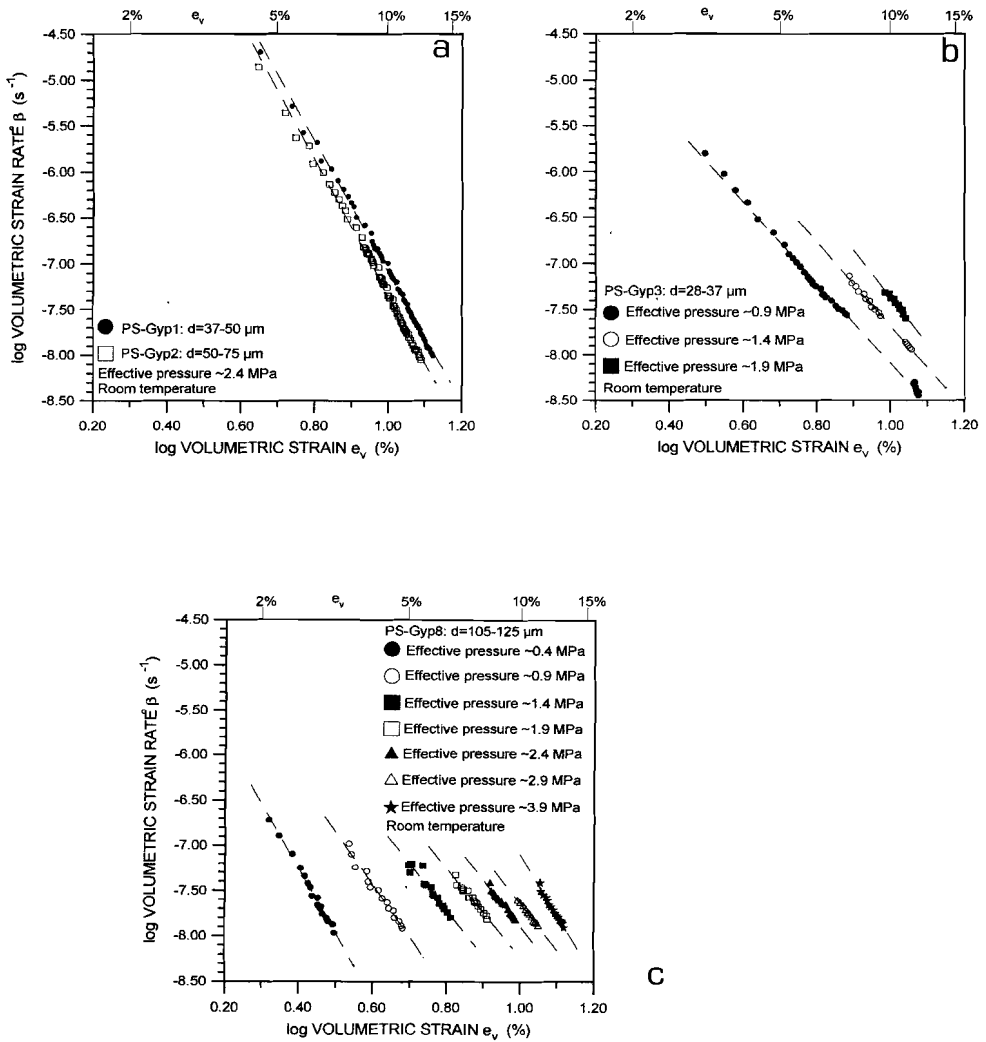
Figure 2.3. Log-log plots of volumetric strain rate ($\dot{\beta}$) versus volumetric strain (e_v) for the constant stress experiments (Fig. a) and two of the stress-stepping experiments (Figures b and c) reported in this study.
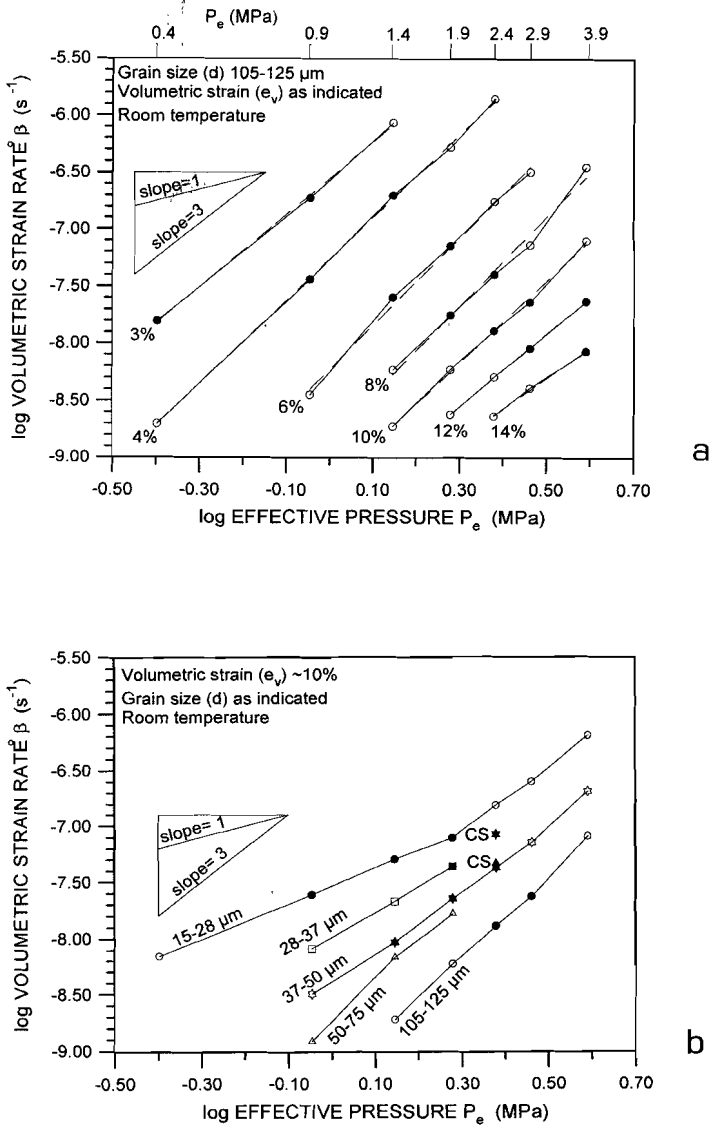
Figure 2.4. Log-log plots of volumetric strain rate ($\dot{\beta}$) versus effective pressure (P_e), a) for a single grain size (d) at different values of volumetric strain (e_v, %), and b) for a fixed value of volumetric strain at different grain sizes. Closed symbols represent measured data points and open symbols represent extrapolated data (see text). All data are from stress-stepping experiments except where marked CS (constant stress).
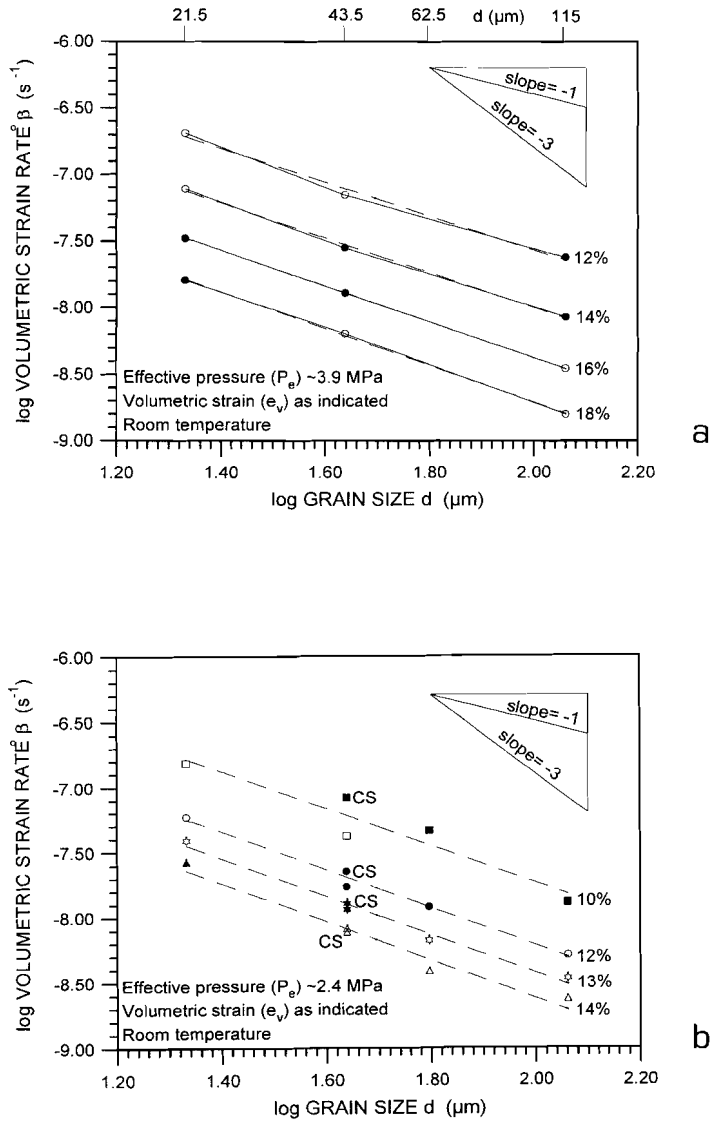
Figure 2.5a and b, caption and Fig. 2.5c see next page.
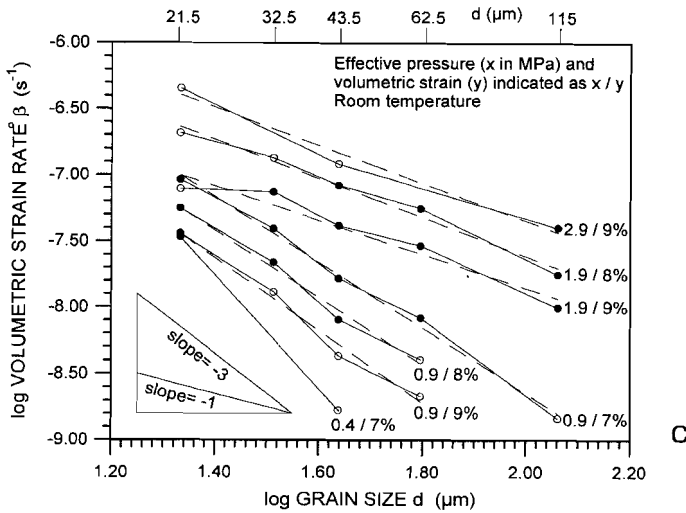
Figure 2.5. Log-log plots illustrating the dependence of volumetric strain rate ($\dot{\beta}$) versus grain size (d), for effective pressures a) of 3.9 MPa, b) 2.4 MPa and c) for various values in the range 0.4 - 2.9 MPa. Volumetric strains (e_v) indicated in %. Closed symbols represent measured data points and open symbols represent extrapolated data (see text). All data are from stress-stepping experiments except where marked CS (constant stress).

2.2.3 Microstructural observations

Microstructural analysis was carried out by means of optical microscopy performed on thin and ultra-thin sections of epoxy-impregnated samples. Examination of the starting material showed the individual grain size fractions to consist of essentially lozenge-shaped grains of reasonably uniform size and aspect ratios of typically 4:2:1. Optical examination of samples, subjected to initial dry compaction only, revealed a highly porous aggregate structure consisting of grains making mostly rather sharp point contacts with their neighbours. Some evidence for plastic grain bending as well as intra- and transgranular cleavage was also observed in these samples (Fig. 2.6). However, a clear change in microstructure was apparent in the wet compacted samples. These showed a marked decrease in porosity, a dramatic increase in blunt as opposed to sharp grain contacts, plus widespread evidence for grain-to-grain indentations, contact truncation, and euhedral

overgrowths within the pores (Fig. 2.7). In addition, the grain contacts in the wet-tested samples were mostly "tight", and no optically visible evidence was found for the development of "necks" by undercutting of contact margins (Pharr & Ashby, 1983; Spiers & Brzesowsky, 1993) or for the development of equilibrium pore configurations. Compared to the samples which underwent dry compaction only, the wet compacted samples did not show any detectable increase in the incidence or amount of plastic deformation (grain bending) or microcracking.
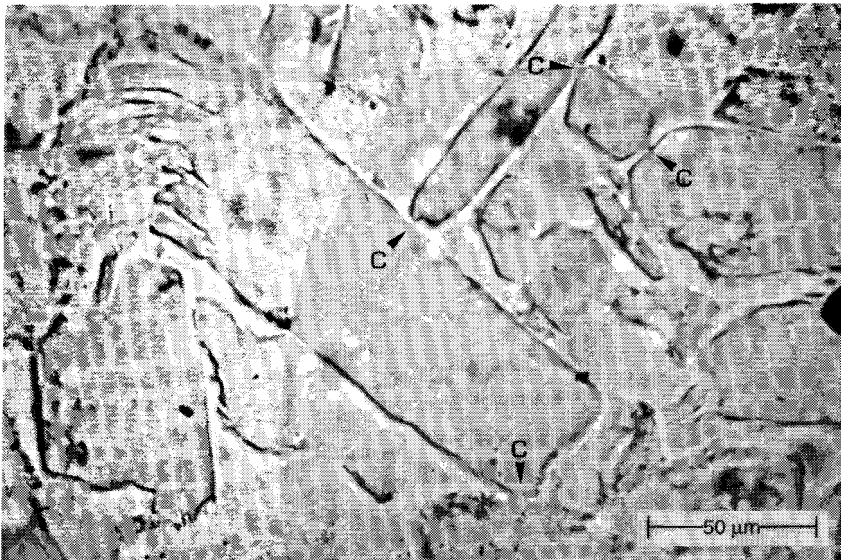
Figure 2.6. Optical microstructure of a sample subjected to initial dry compaction only ($P_e \approx$ 3.9 MPa, d = 50-75 µm) showing a highly porous aggregate structure typical of such samples. Note the rather sharp point contacts between grains (c), plus the evidence for plastic grain bending and brittle cleavage.
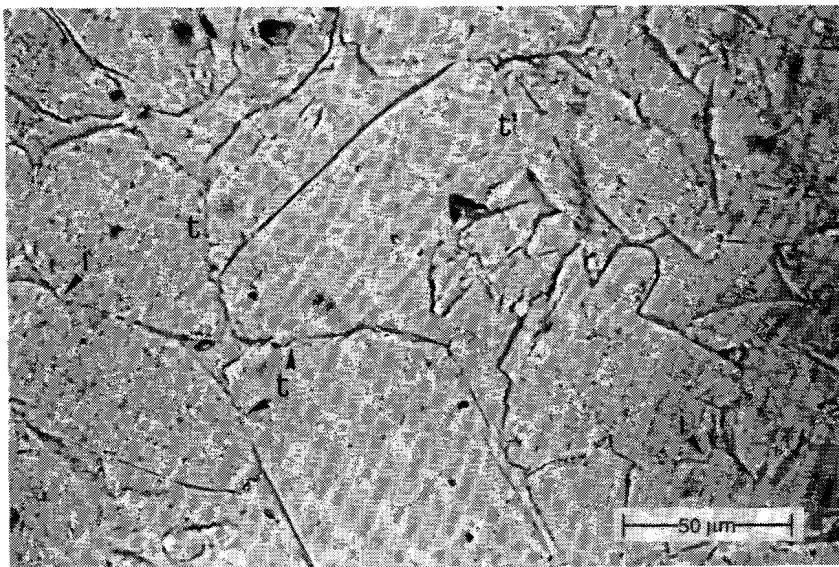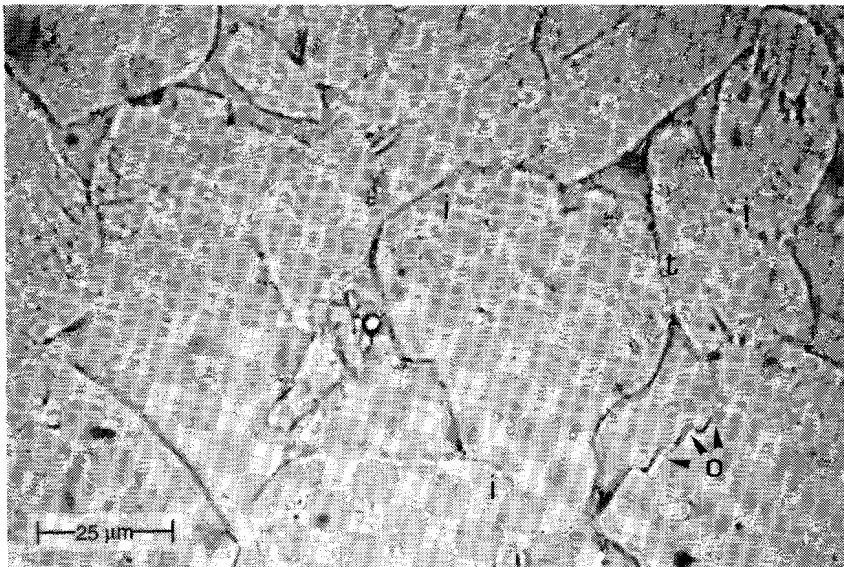
Figure 2.7a, b. Optical microstructure typically exhibited by wet-compacted samples. Note the blunt grain contacts, grain-to-grain indentations (i), contact truncations (t) and overgrowth features (o). a) PS-Gyp7; stress-stepping experiment, $P_e \approx 0.4\text{-}3.9$ MPa, d = 37-50 µm, e_v = 14.8%. b) PS-Gyp2; constant stress experiment, $P_e \approx 2.4$ MPa, d = 50-75 µm, e_v = 12.4%.

2.3 DISCUSSION

2.3.1 Deformation mechanisms during dry compaction

As described under experimental method, initial dry loading of our samples led to a more or less instantaneous compaction of 10-13%, with little or no creep occurring after the full dry compaction stress of P_e = 3.9 MPa was attained. Relating this to the grain bending and brittle/cleavage microstructures observed in samples subjected to this treatment alone, we infer that initial dry compaction occurred by instantaneous (i.e. work hardening) plastic deformation of the grains, plus time-independent grain breakage and rearrangement. Since subsequent reloading was always performed at similar or lower stresses (P_e ≤ 3.9 MPa), the 0.4-1.0% of instantaneous compaction seen in samples reloaded under dry, and oil-flooded conditions, presumably reflects elastic deformation and/or minor additional plasticity, cataclasis and intergranular sliding. Since little or no creep was exhibited by either the dry or oil-flooded samples, time-dependent mechanisms such as dislocation creep or sub-critical microcracking were clearly unimportant under these conditions.

2.3.2 Deformation mechanisms during wet compaction

In contrast to the dry and oil-flooded samples, our wet-tested samples showed relatively rapid, on-going compaction creep, thus proving the operation of some kind of solution- or water-enhanced creep mechanism. Clearly, fluid-lubricated intergranular sliding and/or conventional dislocation creep can be immediately ruled out as the mechanisms of wet creep, since these would also have produced creep in the oil-flooded samples. The remaining mechanisms which can therefore be put forward to explain the observed wet behaviour, in association with intergranular sliding, are:

i)   some kind of fluid-assisted microcracking or contact crushing process (cf. Milliken, 1994);

ii) some kind of intracrystalline water weakening effect;

iii) a plasticity-coupled pressure solution mechanism, involving plastic deformation of grain contacts plus contact undercutting by dissolution (see Pharr & Ashby, 1983; Tada & Siever, 1986; Spiers & Brzesowsky, 1993); or

iv) conventional, grain boundary diffusion type pressure solution (Rutter, 1983;Spiers & Brzesowsky, 1993).

Since the microstructure of the wet-compacted samples shows no detectable increase in microcracking or crystal plasticity (grain bending) compared with samples subjected to initial dry compaction only, despite the similar strains accumulated (around 10-15% in both cases), mechanisms (i) and (ii) above seem unlikely. Mechanism (ii) also seems unlikely on the grounds that the effect of adding solution to our samples is instantaneous, allowing no time for water to diffuse into the grains.

The implication is that the compaction behaviour of our wet samples was controlled by some sort of pressure solution mechanism (i.e. iii or iv above) operating in conjunction with intergranular sliding. The widespread indentation, truncation and overgrowth microstructures developed in the wet-compacted samples provide strong evidence that deformation indeed occurred by dissolution of material within grain contacts and precipitation on pore walls, i.e. by a pressure solution process. In addition, it will be recalled that grain contacts were found to be rather tight, with little or no evidence for grain contact corrosion or undercutting, or for the development of equilibrium pore configurations. It therefore seems likely that deformation of our wet samples was controlled largely by grain boundary diffusional pressure solution rather than by a plasticity coupled mechanism.

2.3.3 Wet creep data vs. pressure solution theory and kinetic constraints

We now compare our wet creep data with micromechanical models for compaction of granular aggregates by grain boundary diffusional pressure solution. Models of this type have been derived by a number of authors (Raj, 1982; Rutter, 1983; Spiers et al., 1989; Spiers & Schutjens, 1990; Spiers & Brzesowsky, 1993; Lehner, 1995) assuming linear kinetic relations for the underlying elementary processes of dissolution, (Fickian) diffusion and precipitation. Allowing the possibility of non-linear dissolution and precipitation kinetics (see Lehner, 1990; Wakai, 1994) and restricting attention to relatively small volumetric strains (<20%), these models can be rewritten in the general form

$$\dot{\beta} = A_x \cdot (P_e^n / d^m) \cdot f_x(e_v) \tag{2.1}$$

where the physical significance and/or values of x, n and m depend on whether the

rate of pressure solution creep is controlled by the kinetics of dissolution within grain boundaries (x = S), of grain boundary diffusion (x = D), or of precipitation on pore walls (x = P). When dissolution or precipitation are rate controlling, m = 1, n reflects the order ($\geq$ 1) of the dissolution or precipitation reaction rate law (expressed as an interfacial velocity vs. potential drop relation), and A_x are temperature-dependent rate coefficients. When diffusion is rate-controlling, m = 3, n = 1 and A_D is a temperature dependent term incorporating the effective grain boundary diffusivity. The $f_x(e_v)$'s are mechanism-specific, geometric structure factors which decrease in magnitude with increasing strain or decreasing porosity.

Turning to our experimental results, it will be recalled that for most of the range of conditions investigated (i.e. P_e > 0.9 MPa, d > 28-37 μm), our wet compaction data show a roughly inverse linear dependence of creep rate ($\dot{\beta}$) on grain size (d), an approximately 3rd order power law dependence on applied effective pressure (P_e), and an inverse dependence on volumetric strain (e_v). This behaviour is consistent with the above models for both dissolution and precipitation controlled pressure solution creep, but is clearly not consistent with that for grain boundary diffusion control.

Now, from the crystal growth and dissolution literature, it is well-known that the kinetics of the dissolution of high purity gypsum are at least two orders of magnitude faster than of precipitation, under comparable conditions (Christoffersen & Christoffersen, 1976; Christoffersen et al., 1982). Indeed, the gypsum dissolution reaction is so fast that it can not be measured directly in practice. In contrast, the kinetics of the precipitation reaction have been measured by numerous authors (Liu & Nancollas, 1970; 1975; Nancollas et al., 1973; Packter 1974; Tadros & Mayes, 1979; Gill & Nancollas, 1980; Van Rosmalen et al., 1981; Christoffersen et al., 1982; Weijnen, 1986). Notably, the results obtained for similar experimental conditions, and for driving forces (or supersaturations) comparable to those estimated for pressure solution in the present experiments (see Appendix 2.1), yield precipitation rate laws of order 2 - 4 (Van Rosmalen et al., 1981; Christoffersen et al., 1982; Packter, 1974). However, the absolute rates of precipitation in high purity systems are some 10^3 to 10^4 too fast to explain the creep rates observed in our experiments. On the other hand, it is well established that the presence of impurities strongly reduces the growth rate of gypsum without affecting the order of the precipitation reaction (Smith & Alexander, 1970; Liu & Nancollas, 1975; Weijnen, 1986).

Combining all of these points, and recognizing that the natural gypsum used in our experiments has an impurity content of up to 3 wt%, we suggest that creep in our wet samples was most probably controlled by precipitation controlled grain boundary diffusional pressure solution. A certain amount of caution is needed, however, since in addition to uncertainties regarding the kinetics of precipitation in our starting material the above pressure solution models are derived for simple solid plus solution systems, and have not yet been rigorously extended to cover the case of solids containing water of crystallization. Nonetheless, for materials such as gypsum, such an extension is unlikely to modify the theoretical results significantly.

2.3.4 Comparison with other salts

In broad terms, the pressure solution behaviour inferred to occur in the present experiments on gypsum is similar to that reported recently for other soluble salts (see Spiers et al., 1990; Visser & Spiers, 1992). There are a number of important differences, however. First, the rates of pressure solution seen in the present compaction tests are typically 3 - 4 orders of magnitude lower than those seen in highly soluble salts, such as NaCl and $NaNO_3$, tested under comparable conditions (Spiers et al., 1990; Visser & Spiers, 1992). Secondly, most highly soluble salts seem to show grain boundary diffusion controlled pressure solution creep (Spiers et al., 1990; Visser & Spiers, 1992), whereas gypsum seems to show interface (probably precipitation) control. In our view, these differences in behaviour probably reflect the simple fact that in highly soluble salts, such as NaCl, interfacial reactions tend to be very rapid (see Scrutton & Grootscholten, 1981), while the opposite tends to be the case in sparingly soluble materials such as gypsum.

2.3.5 Extrapolation to natural conditions

While our results have shown that pressure solution processes can indeed play an important role in gypsum under laboratory conditions, the present data are insufficient, and cover too limited a range of conditions, to warrant any attempt to extrapolate to natural conditions. Further work on both granular aggregates and gypsum rock is needed to address adequately the question of the behaviour of gypsum in nature.

2.4 CONCLUSIONS

In this study, we have investigated the compaction creep behaviour of wet granular gypsum under hydrostatic, room temperature conditions, in an attempt to determine whether or not pressure solution creep processes are important in this material under laboratory conditions. Our results demonstrate that while dry and oil-saturated material show little or no creep under the chosen experimental conditions, samples flooded with saturated gypsum solution creep significantly, thus proving an effect of the solution phase. In addition, the indentation, truncation and overgrowth microstructures developed in our wet-tested samples provide strong evidence for the operation of grain boundary diffusion type pressure solution. Furthermore, most of our wet creep data are broadly consistent with theoretical models for interface reaction controlled creep by this mechanism. Taking into account independent data on the dissolution and precipitation kinetics of gypsum, we suggest that, for most of the range of conditions investigated, compaction of our wet samples is most likely to have occurred by precipitation-controlled grain boundary diffusional pressure solution. Further work is needed for extrapolations to nature.

APPENDIX: Estimation of driving force for pressure solution in the present experiments

From pressure solution theory (e.g. Rutter, 1976, 1983; Raj, 1982; Lehner, 1990; Spiers & Brzesowsky, 1993), it is well established that the driving force for grain boundary diffusional pressure solution in a hydrostatically stressed aggregate of the type tested in the present experiments, is given by differences in the surface chemical potential of the solid developed between grain contacts (dissolution or source sites) and pore walls (precipitation or sink sites). Assuming that changes in the Helmholtz free energy and molar volume (Ω_s) of the solid (in our case gypsum) are negligible within the grains, this potential difference can be written to a first approximation as

$$\Delta \mu_s \approx \Delta \sigma_n \Omega_s \tag{a2.1}$$

where $\Delta\sigma_n$ is the difference in interfacial normal stress (Raj, 1982; Lehner, 1990;

Spiers & Brzesowsky, 1993) between the source and sink sites. For dilute solutions, the mole specific chemical potential of solute (in our case $CaSO_4$) at any point is given by

$$\mu = \mu_0 + RT \ln C \qquad (a2.2)$$

where μ_o is a reference potential, R is the gas constant, T is the absolute temperature, and C is the molar concentration of the solute. Neglecting gradients in the activity of water around grain surfaces, this allows us to express the potential drop $\Delta\mu_s$ between the source and sink sites as

$$\Delta\mu_s = RT \ln C_{gc}/C_{pw} \approx RT\Delta C/C_0 \qquad (a2.3)$$

where C_{gc} and C_{pw} represent the (notional) molar equilibrium concentrations of the solute in solution adjacent to the source (grain contact) and sink (pore wall) sites respectively, where $\Delta C = C_{gc} - C_{pw}$, and where C_o ($\approx C_{pw}$) is the solubility of the unstressed solid in the pore fluid. Making use of equation a2.1, the driving force for pressure solution can hence be written in terms of the "solubility difference"

$$\Delta C/C_0 = \Delta\sigma_n\Omega_s/RT \qquad (a2.4)$$

developed between grain contacts and pore walls.

These quantities, $\Delta\mu_s$ and $\Delta C/C_o$, can be viewed as providing the driving force for the three serial processes of dissolution within the grain contacts, diffusion through the grain boundary fluid, and precipitation on pore walls (see Raj, 1982; Lehner, 1990). In the limiting case of dissolution control, $\Delta\mu_s$ is used entirely in driving the intergranular dissolution reaction and $\Delta C/C_o$ represents the undersaturation developed within the grain contacts. When grain boundary diffusion is rate controlling, $\Delta\mu_s$ is taken up in driving this step and $\Delta C/C_o$ reflects the concentration gradient in grain boundary fluid. On the other hand, when precipitation is rate limiting, $\Delta\mu_s$ represents the corresponding interfacial potential drop and $\Delta C/C_o$ is the supersaturation developed within the pore fluid.

A *minimum* estimate of the total driving force for pressure solution in the present experiments, in terms of both $\Delta\mu_s$ and $\Delta C/C_o$, can now be obtained by inserting into a2.1 and a2.4 the *minimum* values of the average normal stress transmitted across grain boundaries/contacts. In our tests, this is estimated to be of the order of 5 to 10 times the applied effective pressure, since the area fraction of

grain surfaces occupied by grain contacts reached typically up to 1/5 to 1/10 at the maximum strain achieved. Therefore, for the bulk of the range of conditions investigated ($P_e > 0.9$ MPa ≈ 1 MPa) we can write the minimum driving force for pressure solution as

$$(\Delta \mu_s)_{min} = (5 \rightarrow 10) P_e \Omega_s = 370 \rightarrow 740 \quad J \; mole^{-1} \tag{a2.5}$$

or

$$(\Delta C/C_0)_{min} = (5 \rightarrow 10) P_e \Omega_s /RT = 0.15 \rightarrow 0.3 \tag{a2.6}$$

taking $\Omega_s = 7.41 * 10^{-5}$ m^{3}mole^{-1}, R=8.314 JK^{-1}mole^{-1}, and T=293 K. Taking into account the maximum value for P_e used, and the small grain-to-grain contact areas characteristic for the early stages of our tests, we estimate that the *maximum* driving force for pressure solution was of the order of 50 to 100 times the minimum value.

CHAPTER 3

UNIAXIAL COMPACTION CREEP OF WET GYPSUM AGGREGATES

3.1 INTRODUCTION

In the preceding chapter, experiments on the compaction creep behaviour of wet granular gypsum under hydrostatic loading conditions provided strong evidence that grain boundary diffusional pressure solution is an important deformation mechanism in gypsum under laboratory conditions. On the basis of comparison with pressure solution theory and crystal growth data, it was also argued that the gypsum precipitation reaction was likely to be the rate controlling step in the pressure solution process. However, the few results reported (nine experiments) can only be regarded as preliminary. Moreover, considerable discrepancies were noted between the observed rates of pressure solution and those expected on the basis of crystal growth data. In addition, questions were raised regarding the applicability of conventional pressure solution models to hydrated salts such as gypsum. While the results showed that pressure solution is important in gypsum in the laboratory, they were insufficient to extrapolate meaningfully to evaluate the role of pressure solution in natural gypsum, i.e. in decollement zones, halokinetic structures such as pillows and diapirs, and gypsum cap rock formations. Clearly, then, many problems remain unanswered and additional data are needed.

The present chapter documents an experimental investigation into the uniaxial compaction creep behaviour of granular gypsum, tested in the presence of saturated $CaSO_4$ solution, under both chemically closed- and open-system conditions. The term "closed-system" is used here to refer to a simple drained system from which the initially saturated pore fluid solution is merely squeezed out during compaction (as in the experiments of Chapter 2); "open-system" conditions refer to a configuration in which the pore fluid (calcium sulphate solution saturated with respect to the unstressed solid) was flushed through the samples during testing, enabling dissolved material to be removed. The experiments were performed at room temperature and under applied stresses in the range 0.5-2.5 MPa, using grain sizes ranging from 30 to 300 μm. The aim was to confirm whether or not the pressure solution creep processes observed in the hydrostatic experiments would

also occur at measurable rates in uniaxial compaction, and, if so, to obtain a much larger data set enabling a more complete study and characterization of the pressure solution mechanism and kinetic controls operative in the system under investigation. Attention is focused on i) a comparison of wet versus dry uniaxial compaction behaviour, ii) a comparison of the observed wet compaction behaviour with conventional theoretical models for grain boundary diffusional pressure solution creep, and iii) wet behaviour under chemically closed- versus open-system conditions. Simple theoretical arguments are used to demonstrate that such models should apply for sparingly hydrated salts such as gypsum. The results provide clear evidence for the operation of pressure solution processes in the uniaxial tests under both closed-system and open system conditions, with much higher compaction creep rates occurring in the open-system tests. This is shown to support the notion that the rate of pressure solution under closed-system conditions is precipitation controlled.

3.2 BACKGROUND THEORY

In order to determine whether grain boundary diffusional pressure solution is an active mechanism in experiments such as the present, it is essential first to have a relevant theoretical model with which the laboratory results can be compared. In the preceding chapter, the question was raised as to whether conventional theory for pressure solution applies directly to the case of hydrated salts. In the following, an attempt will be made to resolve this question for the case of gypsum $(CaSO_4 \cdot 2H_2O)$.

3.2.1 Driving force for pressure solution in gypsum

To confirm whether or not conventional models for pressure solution creep in simple, two component solid-plus-solution systems (Raj, 1982; Rutter, 1983; Spiers et al., 1989; Lehner, 1990; Spiers & Schutjens, 1990; Spiers & Brzesowsky, 1993) apply to gypsum, a salt containing water of crystallization, it is necessary to evaluate the thermodynamic driving force for pressure solution in gypsum.

From conventional pressure solution theory (e.g. Rutter, 1983; Lehner, 1990; Spiers & Brzesowsky, 1993), it is well established that the driving force for compaction by grain boundary diffusional pressure solution, under closed-system and steady state conditions, is given by differences in the surface chemical potential of the solid $(\Delta\mu_s)$ developed between grain contacts (dissolution or source sites) and

pore walls (precipitation or sink sites). Now, applying the analysis of Paterson (1973; see also Lehner, 1990) to a solid phase containing water of crystallization (formula $X \cdot N_{H2O}$) and its saturated solution, the limiting condition of zero potential drop or zero dissipation, at any representative elementary area within a fluid penetrated grain-to-grain contact or pore wall, is given

$$\mu_x + N\mu_{H_2O} = \mu_s = f^s + \sigma_n \Omega^s \qquad (3.1)$$

where μ_x is the chemical potential of X in solution, N is the number of molecules of water per molecule of solid (for gypsum N=2), μ_{H2O} is the chemical potential of water in the solution phase, μ_s is the (average) potential of the solid within the surface element, f^s is the corresponding Helmholtz free energy of the solid, σ_n is the interfacial normal stress, and Ω^s is the molar volume of the solid. All thermodynamic quantities here are mole specific. For dilute solutions, such as saturated $CaSO_4$ solution (solubility $\approx$ 14 mmole/l = $2.52 \cdot 10^{-4}$ mole fraction), differences in the concentration or activity of water, and hence μ_{H2O}, around grain surfaces are negligible (Christoffersen et al., 1979). Therefore, since differences in the molar volume (Ω^s) and Helmholtz free energy (f^s) of the solid phase (gypsum) are usually negligible within the grains (see Paterson, 1973; Robin, 1978; Raj & Chyung, 1981 for more detail), the driving force for solution transfer of gypsum between source and sink sites can be written

$$\Delta\mu_s = \Delta\mu_x = \Delta f^s + \Delta\sigma_n \Omega^s \approx \Delta\sigma_n \Omega^s \qquad (3.2)$$

where Δf^s and $\Delta\sigma_n$ are the differences in Helmholtz free energy and interfacial normal stress (Raj, 1982; Lehner, 1990; Spiers & Brzesowsky, 1993) between source and sink sites respectively. The present expression for driving force (eq. 3.2) is therefore identical to that used to derive conventional models for grain boundary diffusional pressure solution creep (e.g. Rutter, 1983) in non hydrated solids under closed-system conditions. Hence, from the point of view of driving force considerations, existing models for grain boundary diffusional pressure solution creep can be directly applied to gypsum.

3.2.2 The rate controlling steps of pressure solution

For non-hydrated solids, the potential drop $\Delta\mu_s = \Delta\mu_x$, developed between grain contacts and pores in a stressed granular aggregate under chemically closed-system

conditions, can be viewed as providing the driving force for the three serial processes of dissolution within grain contacts, diffusion through the grain boundary fluid, and precipitation on the pore walls. Since they are serial, the slowest of these processes will be rate-controlling under steady-state conditions (Raj & Chyung, 1981; Raj, 1982). In deriving conventional models for each rate limiting process, it is assumed that all of the driving force ($\Delta\mu_s$) is taken up in driving the rate controlling process in question, with the driving force needed for the other two processes being negligibly small (Raj, 1982; Lehner, 1990; Appendix Chapter 2). The conventional models (see Chapter 2) take the form

$$\dot{\varepsilon} = A_x \cdot \frac{\sigma_e^n}{d^m} \cdot f_x(e_v)$$

(3.3)

where $\dot{\varepsilon}$ is the linear strain rate, σ_e is effective stress, d is grain size and e_v is the volumetric strain. Here the physical significance and/or values of x, n and m depend on whether the rate of pressure solution creep is controlled by the kinetics of dissolution within the grain boundaries (x = S), of grain boundary diffusion (x = D), or of precipitation on pore walls (x = P). When dissolution or precipitation are rate controlling, m=1, n reflects the order (≥ 1) of the dissolution or precipitation reaction rate law (expressed as an interfacial velocity vs. potential drop relation), and A_x are temperature-dependent rate coefficients. When diffusion is rate-controlling, m=3, n=1 and A_D is a temperature-dependent term incorporating the effective grain boundary diffusivity. The f_x's are mechanism-specific, geometric structure factors which decrease in magnitude with increasing strain or decreasing porosity.

In the case of hydrated solids ($X \cdot N_{H2O}$), water is released into stressed grain boundaries when material goes into solution at these sites, and this will cause radial fluid flow out of the contact zone. This flow operates as a parallel concurrent process with grain boundary diffusion, possibly influencing the kinetics of grain boundary transport-controlled pressure solution, compared with the conventional picture. To assess whether this process of grain boundary fluid flow plays an important role during pressure solution creep of gypsum, a calculation of the relative rate of fluid flow vs. rate of diffusion out of grain boundaries will now be made.

For this purpose consider a single grain-to-grain contact zone, with radius a and uniform effective thickness or mean fluid thickness δ, located between two spherical grains surrounded by saturated solution and subjected to an axial force (Fig. 3.1). Regardless of whether the contact zone possesses an island-channel structure (Raj & chyung, 1981; Raj, 1982) or thin-film structure (Weyl, 1959; Rutter, 1976), the applied stress will produce an enhanced potential within the solid in the contact zone causing dissolution within the contact (Lehner, 1990; 1995; Spiers & Brzesowsky, 1993).
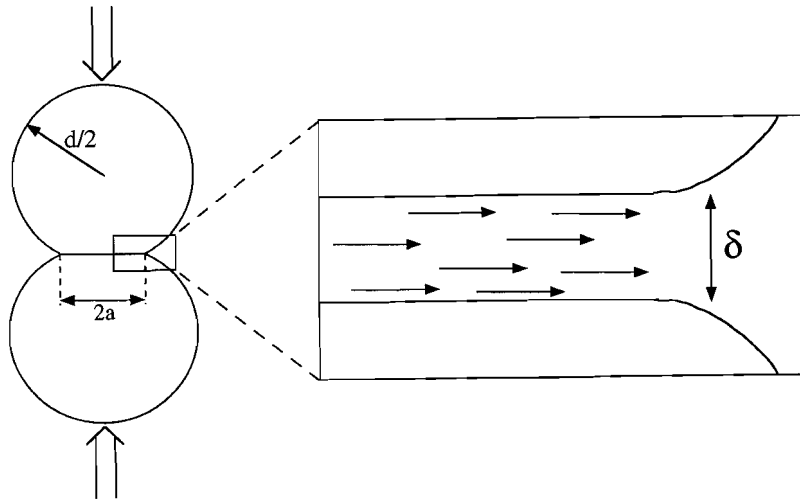
Figure 3.1. Schematic diagram illustrating a single grain-to-grain contact with radius a and uniform effective or mean fluid thickness δ, located between two spherical grains surrounded by saturated solution.

The number of moles of ions then going into solution per second (N_x), and the number of moles of water released per second (N_w) into the grain-to-grain contact, are given by

$$N_x = \frac{v_{diss} \pi a^2}{\Omega^s}$$

(3.4)

and

$$N_w = \frac{Nv_{diss}\pi a^2}{\Omega^s} \qquad (3.5)$$

where v_{diss} is the dissolution velocity, and πa^2 is the grain contact area. If one now assumes that the effective grain boundary thickness (δ) is constant and that the system is always in steady state, then, from the conservation of mass, the velocities of water molecules (U_w) and ions (U_x) at the grain contact periphery (area $2\pi a\delta$) can be expressed as

$$U_w = \frac{Nv_{diss}a}{2C_w\delta\,\Omega^s} \qquad (3.6)$$

and

$$U_x = \frac{v_{diss}a}{2C_x\delta\,\Omega^s} \qquad (3.7)$$

where C_w and C_x are the concentrations (mole/m^3) of water molecules and ions (at the grain contact periphery) respectively. Now,

$$U_x = U_{diff} + U_w \qquad (3.8)$$

where U_{diff} is the velocity of diffusion, hence fluid flow and diffusion are of equal importance in grain boundary transport when

$$U_w = U_{diff} \qquad i.e. \qquad \frac{U_w}{U_x} = \frac{C_xN}{C_w} = \frac{1}{2} \qquad (3.9)$$

Consequently, if $U_w\,/\,U_x = C_x\,N\,/\,C_w \ll 1/2$ grain boundary transport is dominated by diffusion, and if $U_w\,/\,U_x = C_x\,N\,/\,C_w \gg 1/2$ grain boundary transport is dominated by fluid flow. For dilute solutions, as in the case of a saturated gypsum solution, $1/C_w$ is roughly equal to the molar volume of water ($\Omega^{H2O} \approx 1.8\cdot10^{-5}$ m^3/mole at room temperature). For gypsum C_x is approximately equal to the solubility (~14 mole/m^3) so that $U_w\,/\,U_x \approx 5.0\cdot10^{-4}$. Diffusion velocities are thus ~2000 times faster than fluid flow. Hence this calculation shows that, for gypsum, the effect of grain boundary fluid flow can be neglected in relation to diffusion as the rate-controlling step in the grain boundary transport step involved in pressure solution creep.

On this basis, it is inferred that the well-established or conventional models for pressure solution in two component solid-plus-solution systems (equations 3.3) are applicable to grain boundary diffusional pressure solution creep in gypsum at room temperature. They would be less suitable however for describing pressure solution creep in a heavily hydrated salt such as bischofite, where $U_w / U_x = C_x N / C_w \approx$ 0.7. In this case grain boundary transport would be dominated by fluid flow, rather than diffusion, and would be significantly accelerated.

3.3 UNIAXIAL COMPACTION EXPERIMENTS

The experiments consisted of a series of uniaxial compaction creep tests, performed on wet granular gypsum aggregates at room temperature, under either closed- or open-system conditions as defined previously, using initially saturated $CaSO_4$ solution as a pore fluid. The experiments were carried out varying the applied stress (σ_a) and sample grain size (d), so that insight could be gained into the dependence of compaction creep behaviour on these variables. The complete set of (wet) experiments reported is listed in Table 3.1 along with the corresponding experimental conditions and variables. For comparative purposes, some of the closed-system experiments (GY146C and GY267C) were repeated under entirely dry conditions (i.e. with the samples containing air only) or using dry "evaporating" oil (Shell No. 4919) instead of saturated solution.

3.3.1 Starting material

Granular gypsum starting material was prepared by sieving crushed natural gypsum (from the Paris Basin; 95-98wt.% pure) into controlled grain size fractions of 28-37 µm, 37-50 µm, 50-75 µm, 75-105 µm, 105-125 µm, 125-150 µm, and 210-250 µm. Following the procedure outlined in Chapter 2, each fraction was then washed with distilled water to remove any fines attached to grain surfaces, and to dissolve away surface asperities and mechanical damage. Each grain size fraction was subsequently dried by thinly spreading the material onto a filter paper base, placed in an air circulation type drying cabinet operated at ambient temperature. The final particle size distribution of individual fractions was checked optically and using a Malvern particle sizer, and yielded average grain sizes of ~32 µm, ~48 µm, ~74 µm, ~97 µm, ~132 µm, ~160 µm, and ~282 µm for the respective fractions (standard deviation ~23 µm in each case). The average grain shape of the individual fractions

was determined by measuring the ratio of the long axis to short axis of individual crystals using optical microscopy. All fractions yielded comparable axial ratios of 1.6±0.15 with a tendency for this ratio to decrease with increasing grain size.

Table 3.1

Test/Sample number	Average grain size (μm)	Porosity after dry compaction (%)	Wet applied stress (MPa)	Duration of test (days)	Final (wet) strain (%)
GY145C	~160	44.30	2.00	30	5.2
GY146C	~160	44.44	2.50	30	6.3
GY168C	~74	46.18	2.00	28	10.2
GY186C	~32	44.31	0.50	27	8.3
GY187C	~32	45.07	1.01	27	13.7
GY192C	~74	47.00	1.01	21	7.8
GY201O	~160	44.11	2.00	9	4.9
GY203C	~282	45.76	0.50	30	2.3
GY206C	~282	44.95	2.00	30	4.4
GY207C	~282	45.49	2.48	30	5.4
GY208O	~282	44.98	2.48	7	6.4
GY217C	~48	45.26	1.52	30	13.4
GY218C	~48	44.99	2.00	30	13.9
GY220O	~48	45.23	2.48	8	15.5
GY235C	~97	46.78	2.00	30	8.1
GY236C	~97	46.60	2.50	30	9.6
GY237O	~97	45.13	2.48	8	10.3
GY258C	~132	44.42	0.50	35	3.6
GY259C	~132	44.27	1.01	35	4.7
GY260C	~132	45.19	1.52	35	5.9
GY261C	~132	44.43	2.00	35	6.4
GY262C	~132	44.25	2.48	35	6.8
GY263C	~48	46.91	0.50	31	8.3
GY264C	~48	45.66	1.01	31	11.3

Test/Sample number	Average grain size (μm)	Porosity after dry compaction (%)	Wet applied stress (MPa)	Duration of test (days)	Final (wet) strain (%)
GY265C	~48	46.41	1.52	31	13.3
GY267C	~48	45.38	2.50	31	16.1
GY274C	~160	44.64	0.50	26	2.3
GY275C	~282	44.00	1.01	26	2.7
GY276C	~282	44.21	1.52	26	3.4
GY277C	~160	44.65	1.51	26	4.0
GY278C	~74	45.85	2.48	26	9.7
GY285C	~74	46.97	0.50	25	6.2
GY286C	~160	45.29	1.01	25	3.9
GY287C	~74	46.73	1.52	25	9.0
GY288C	~97	46.57	1.51	25	6.3
GY289C	~32	45.93	2.48	25	15.7

Table 3.1. Complete set of wet experiments reported, along with corresponding experimental conditions and variables. The GY...C test/sample numbers are experiments performed under closed-system conditions, the GY...O test/sample numbers are experiments performed under open-system conditions. All samples were compacted dry before wet testing at an applied stress (σ_a) of ~4.0 MPa.

3.3.2 Closed-system experiments

3.3.2.1 Method

The closed-system experiments were conducted using small-scale, dead weight, capillary tube compaction set-ups as illustrated in Fig. 3.2. Five such assemblies were used in all. In setting up individual experiments, the 2 mm diameter glass capillary tube and lower piston plus filter were first mounted in the brass base-block (see Fig. 3.2) and a ~0.04 g sample of the chosen grain size fraction was funnelled into the tube. Samples were weighed out on a Mettler H10W analytical balance with accuracy 0.1 mg. The upper filter paper disk was then placed on top of the granular sample and the upper piston gently inserted into the capillary (Fig. 3.2). The filter paper disks were included in the assembly to prevent grains sliding down or getting stuck between the pistons and the glass capillary tube.

In the initial stage of each experiment, the starting powder was first loaded dry for 15 minutes, using a stress (σ_a) of ~4.0 MPa applied to the top piston using a dead weight of ~1.44 kg. This led to an essentially time-independent (instantaneous) compaction of 10-13%, with no measurable creep occurring thereafter, producing a locked compact with a porosity of (ϕ_o) 46.0 ± 6.0%. Samples with a porosity outside the range 44.0-47.0% were rejected. The initial length, and the length of the samples after dry compaction were measured using a travelling microscope (accuracy 0.01 mm).

After dry compaction, the load on non-rejected samples was adjusted to the desired value for wet testing, and a dial gauge (accuracy 0.01 mm) was carefully placed on top of the dead weight (see Fig. 3.2). Saturated solution or in some cases dry "evaporating" oil (Shell No. 4919) was then added, from above, into the fluid reservoir and introduced into the sample by sucking through the evacuation tube. This was subsequently closed using a clamp, and the fluid reservoir (plastic ring on top of glass capillary tube; see Fig 3.2) was sealed with a drop of silicone oil in order to prevent evaporation. The compaction creep behaviour of the flooded samples was monitored as a function of time (using a stopwatch) by measuring the change in sample length. Note that the saturated solutions for these experiments were prepared using gypsum of the same grain size fraction as the sample under investigation. Constant stress experiments were performed, using applied stresses in the range $0.50 \leq \sigma_a \leq 2.50$ MPa and samples of each available grain size fraction. Strains up to 16% were achieved.

Tests were terminated by removing the load from the samples, after which point the plastic ring, the evacuation tube and the upper piston were removed. Saturated solution remaining in the pores was then carefully flushed from the sample by passing compressed air through the tube and sample. Finally, the sample was carefully pushed out of the capillary tube and vacuum impregnated with blue-stained epoxy resin to allow sectioning and microstructural study.

Clamp stand

Clamps

Dial gauge

Clamps

Dead weight

Weight guide

a
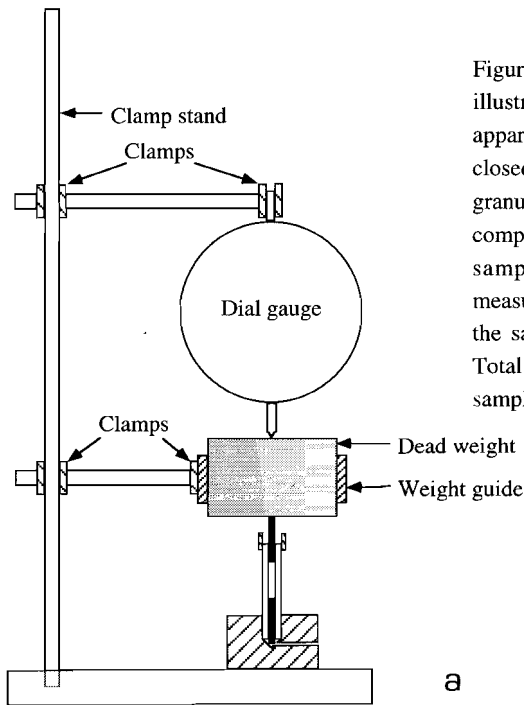
Figure 3.2. Semi-schematic diagram illustrating the uniaxial compaction apparatus used in the present closed-system experiments on wet granular gypsum aggregates. The compaction creep behaviour of the samples was monitored by measuring the change of length of the samples with the dial gauge. a) Total overview of set-up, and b) sample assembly.

Saturated solution

Stainless steel piston

Filter (5 micron grade) paper disks

Stainless steel piston

Brass base

Silicone oil film to prevent evaporation

Plastic ring (reservoir)

Glass capillary tube

Granular sample

Silicone kit seals

Evacuation tube

Clamp

b
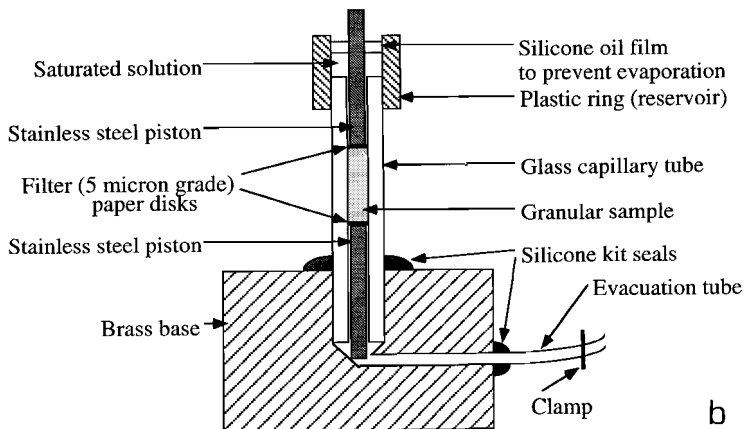
The apparatus and method described above (Fig. 3.2) allowed strains to be measured with a accuracy of ~10^{-4}. Strain rates were calculated as a function of strain and time, using the three point central difference method. Conventional methods of analysis showed that the standard relative error in the compaction strain rate was less than 8% in all experiments.

3.3.2.2 Mechanical results

As already mentioned, the initial dry-loading stage, to which all samples were subjected, resulted in a more or less instantaneous or time-independent compaction of the samples by 10-13%. When reloaded after dry compaction, dry and oil-flooded samples showed hardly any creep. In contrast, the solution-flooded samples showed relatively rapid on-going creep when the liquid was added. A selection of representative compaction creep curves obtained for the solution-flooded samples, are presented in Figs. 3.3a-b. These show that compaction creep is promoted by increasing applied stress (σ_a) and by decreasing grain size (d), but decelerates with increasing strain (e). The dependence of compaction creep rate on strain, is illustrated in Figs. 3.4a-b. By combining strain rate versus strain data of this kind, and interpolating linearly between adjacent data points, it is possible to examine how the creep rate of the wet samples, measured at constant strain (here approximately constant porosity), depends on σ_a and d. Typical results are shown in Figs. 3.5a-b and 3.6a-b. From the slopes of the data shown in these log-log plots, it is evident that, across almost the entire range of conditions investigated ($\sigma_a < 2.50$ MPa), the compaction creep rate at constant strain can be viewed as approximately proportional to σ_a raised to the power p≈1.5 to 3.5 and d to the power q≈-2 to -4. Note however, that at the highest applied stress investigated ($\sigma_a = 2.50$ MPa), the compaction creep rate becomes less sensitive to d (q $\rightarrow$ 1) in experiments using larger grain sizes .
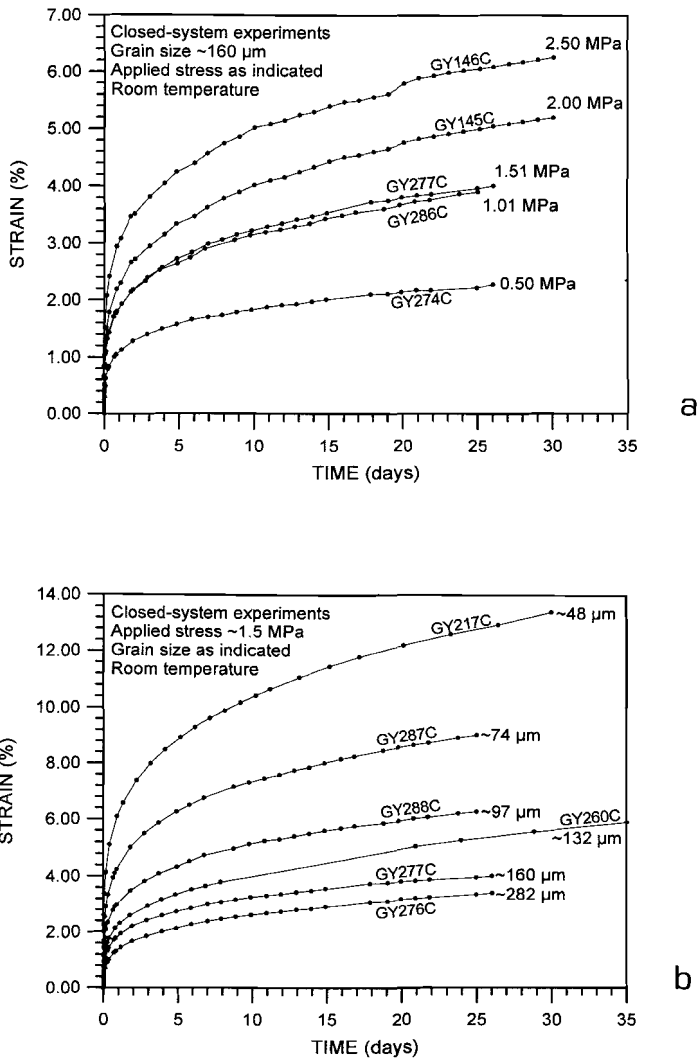
Figure 3.3a-b. Selection of representative compaction creep curves obtained in the wet experiments on gypsum. Note the effects of increasing applied stress (σ_a) and decreasing grain size (d).
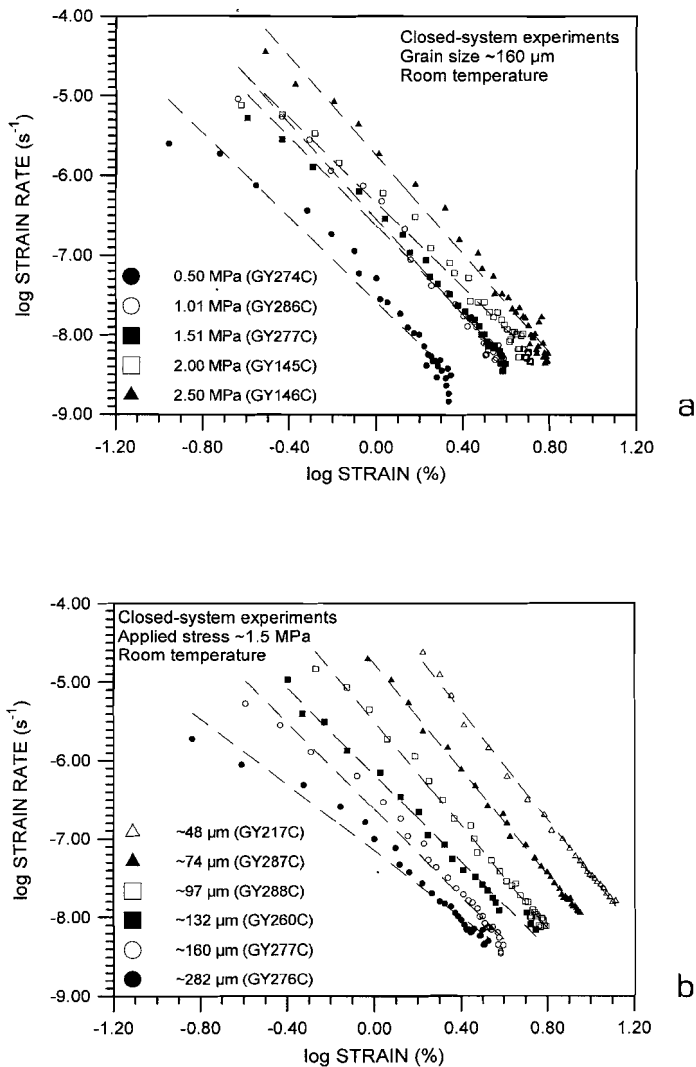
Figure 3.4. Log-log plots of compaction strain rate versus compaction strain constructed from the creep data presented in Fig. 3.3. Note the effects of increasing applied stress (σ_a, Fig. a) and decreasing grain size (d, Fig.b).
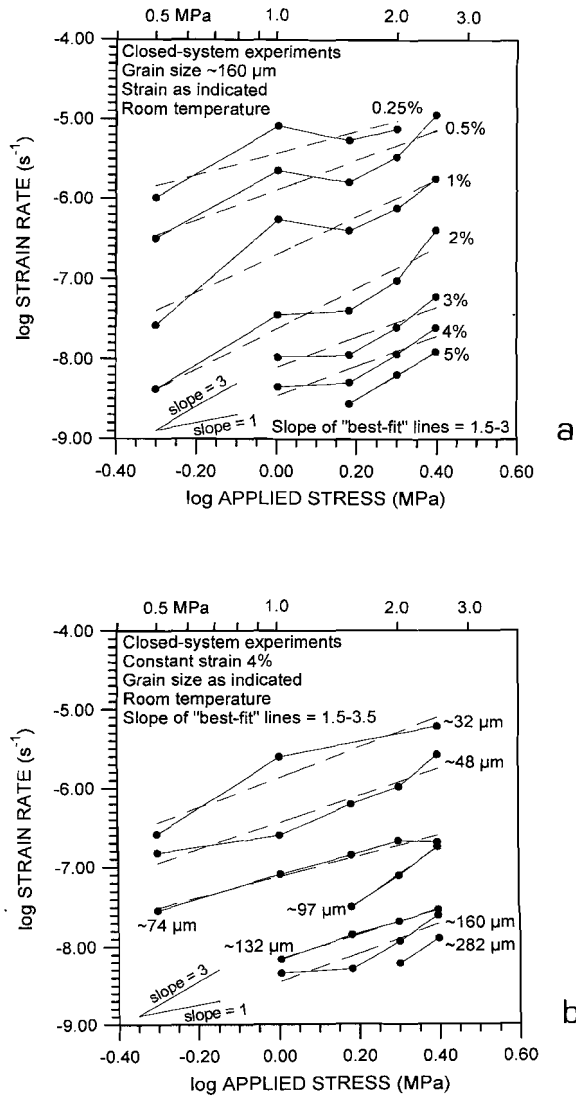
Figure 3.5. Log-log plots of compaction strain rate versus applied stress, a) for a single grain size (~160 μm) at different values of compaction strain (e, %), and b) for a fixed value of compaction strain (4%) at different grain sizes.
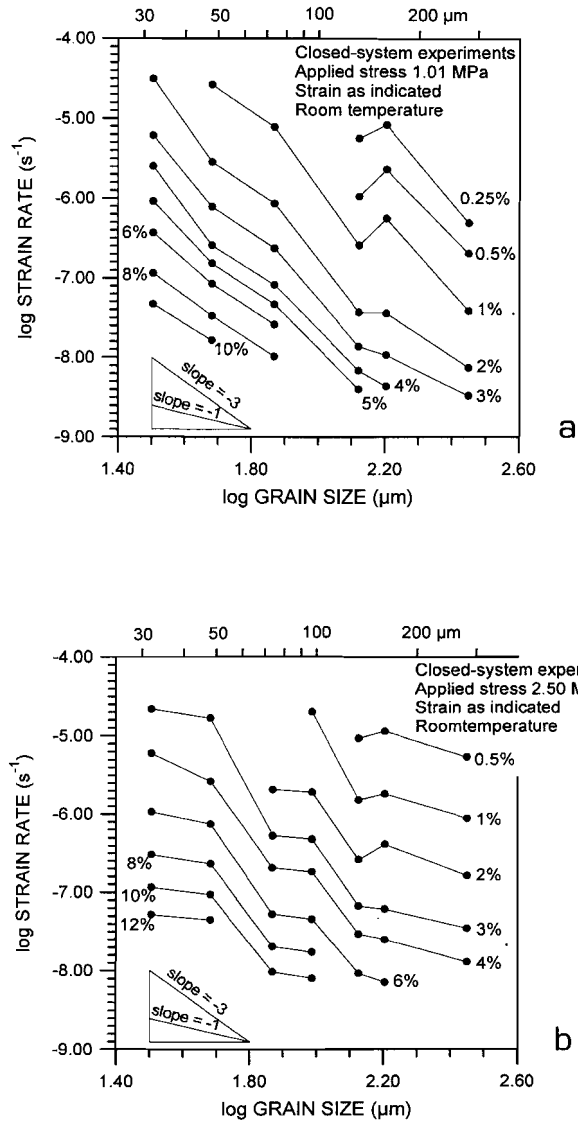
Figure 3.6. Log-log plots illustrating the dependence of compaction strain rate on grain size, for applied stresses a) of 1.01 MPa and b) 2.50 MPa.

3.3.2.3 Microstructural observations

Microstructural analysis was carried out by means of optical microscopy performed on thin sections of the epoxy-impregnated samples. Optical examination of samples subjected to dry compaction only, showed a highly porous aggregate structure, the grains having rather sharp point contacts with their neighbours (Fig. 3.7a). The dry samples also showed evidence for plastic grain bending and intra- and transgranular cleavage. The wet-compacted samples revealed a microstructure characterized by a marked decrease in porosity, an increase in blunt as opposed to sharp grain contacts, plus evidence for grain-to-grain indentations, contact truncation, and euhedral overgrowths within the pores (Fig. 3.7b-c). The grain contacts of the wet-tested samples were generally "tight", showing little or no evidence for irregular corrosion or undercutting of the contact margins (Pharr & Ashby, 1983; Spiers & Brzesowsky, 1993). On the sample scale, a weak grain shape preferred orientation was found to be developed with long axes of the grains aligned normal to the compression direction. No increase in the incidence or amount of plastic deformation or microcracking was observed in the wet compacted samples.
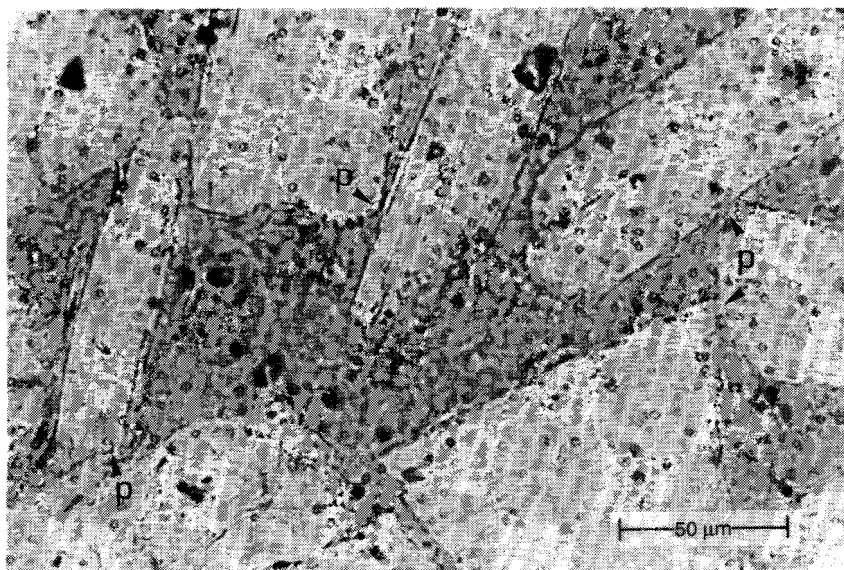
Figure 3.7a Optical microstructure of a sample subjected to initial dry compaction only (σ_a ~4.0 MPa) showing the highly porous aggregate structure typical of such samples. Note the sharp point contacts (p).
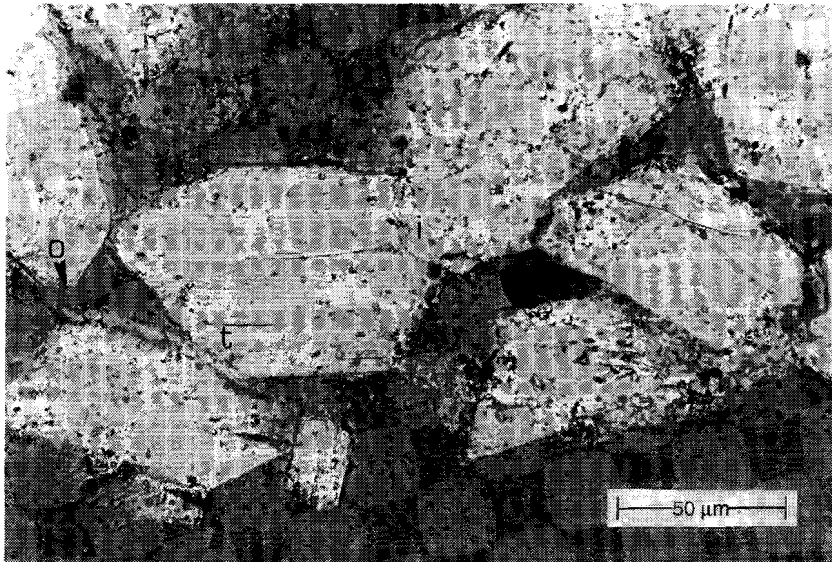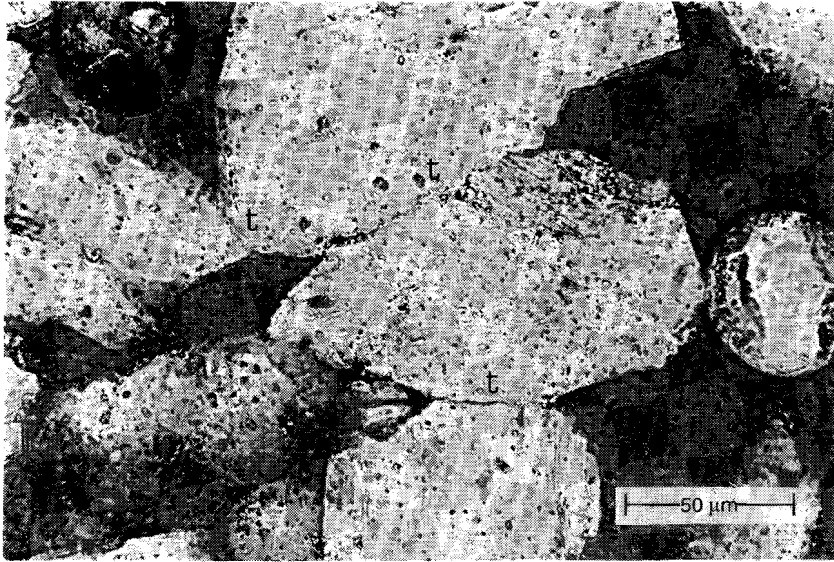
Figure 3.7b,c. Optical microstructures exhibited by wet-compacted samples (Fig. b; GY235C, wet strain 8.1% and Fig. c; GY236C, wet strain 9.6%) under closed-system conditions. Note the blunt contacts, grain-to-grain indentations (i), contact truncation (t) and overgrowth (o) features.

3.3.3 Open-system experiments

3.3.3.1 Method

Four of the closed-system experiments described above were repeated under open-system conditions (see Table 3.1). For this purpose, the experimental set-up (Fig. 3.2) was modified to allow flow of the pore fluid through the sample during deformation (see Figure 3.8). In each open-system test, a saturated gypsum solution was flushed-through from the bottom to the top of the sample using a constant hydrostatic head of ~0.01 MPa. This solution was prepared using loose gypsum of the same grain size as the sample under investigation, and was maintained saturated (with excess gypsum in the solution) during the experimental runs by stirring at a constant rate using a compressed-air-driven stirrer. To achieve a homogeneous supply of fluid to the samples, the lower steel piston in Fig. 3.2 was replaced by a hollow ceramic piston The upper surface of this piston, which makes contact with the aggregate, was covered by a stainless steel filter (mesh size ~50 μm) to prevent powder penetrating into the channels of the piston (Fig. 3.8).

Aside from the above, the open-system experiments were executed using exactly the same procedure as for the closed-system experiments. The samples were first subjected to an applied stress (σ_a) of ~4.0 MPa for 15 minutes, under dry conditions, before loading to the desired value for wet testing. After adjustment of the dead weight for wet testing, the dial gauge was carefully placed on top of the dead weight (Fig 3.8). The wet phase of this experiment was then started by opening the tap to the fluid reservoir, causing fluid flow through the sample. The compaction creep of the samples was subsequently monitored as a function of time (using a stopwatch) by reading the change in sample length from the dial gauge. Constant stress experiments were performed, using applied stresses of ~2.0 and ~2.5 MPa and samples with grain sizes of ~48 μm, ~97 μm, ~160 μm, and ~282 μm, achieving strains up to 15.5%. The experiments were performed at 19.7 ± 0.1°C in a temperature-controlled room. Tests were terminated, by closing the fluid inlet, removing the applied load, extracting the sample and then impregnating the sample (see 3.3.2.1).
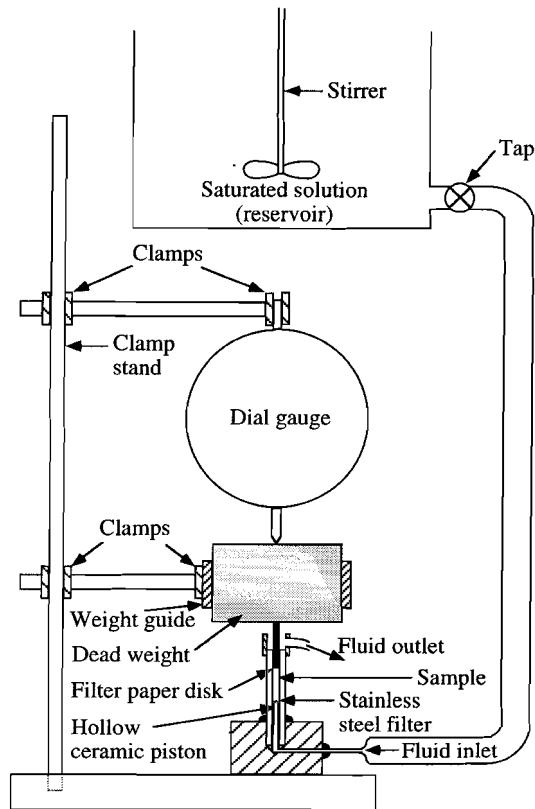
Figure 3.8. Semi-schematic diagram illustrating the uniaxial compaction apparatus used in the open-system experiments on granular gypsum aggregates. The compaction creep behaviour of the samples was monitored by measuring the change in length of the samples with the dial gauge. Note that the saturated solution passed through the samples during testing was prepared using gypsum taken from the same grain size fraction as the sample itself.

.

3.3.3.2 Mechanical results

As in the closed-system experiments, dry loading led to a more or less instantaneous compaction of the samples whereas wet compaction (with solution flowing through the sample) resulted in rapid, on-going creep. The compaction creep curves obtained are presented in Fig. 3.9 and show considerable enhancement of creep compared with closed-system experiments conducted under similar

conditions (c.f. Fig. 3.3a). The curves also demonstrate that creep is promoted by decreasing grain size (d), but decelerates with increasing strain (e). This dependence of compaction strain rate on compaction strain is explicitly represented in Fig. 3.10 for the samples tested at 2.48 MPa. The data have been used to construct a plot of strain rate versus grain size (Fig. 3.11), following the same procedure as described in Section 3.3.2.2. The slopes of the limited data appearing in this log-log plot suggest that at an applied stress (σ_a) of 2.48 MPa, the compaction rate at constant strain can be considered roughly proportional to d raised to the power -m, where m $\approx$ 2.
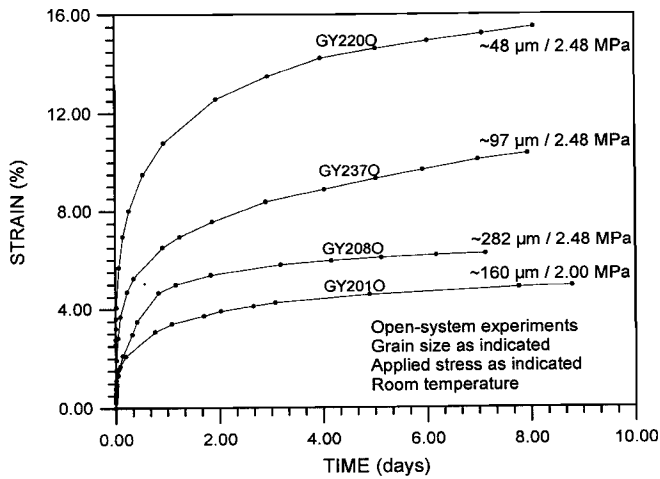
Figure 3.9. Compaction creep curves obtained for the open-system experiments on wet granular gypsum. Note the effect of grain size (d) at constant applied stress (σ_a).
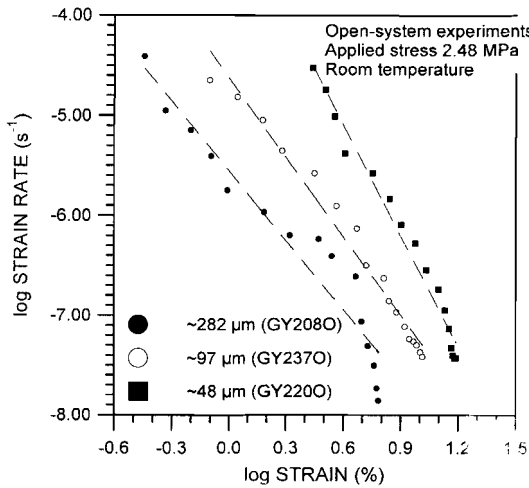
Figure 3.10. Log-log plot of compaction strain rate versus compaction strain illustrating the effect of decreasing grain size (d) in the open-system experiments.
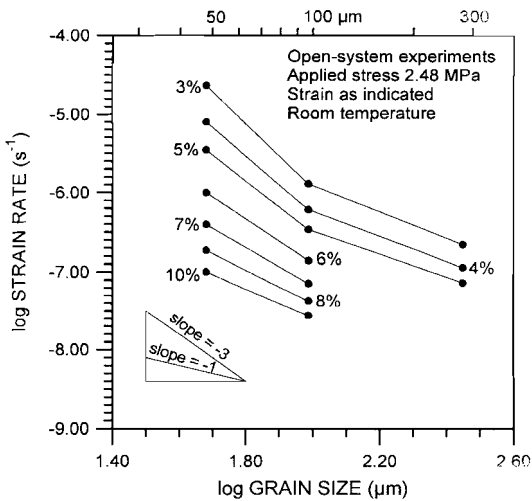
Figure 3.11. Log-log plot of compaction strain rate versus grain size (d) for the open-system experiments performed at an applied stress (σ_a) of 2.48 MPa.

3.3.3.3 Microstructural observations

Like the wet, closed-system samples, the open-system samples showed a marked decease in porosity, an increase in blunt as opposed to sharp grain contacts, plus evidence for grain-to-grain indentations, contact truncations and the development of a weak grain shape preferred orientation. As in closed-system experiments, no detectable increase in the incidence or amount of plastic deformation or microcracking was observed, compared with dry compacted material. However, the samples tested under wet, open-system conditions, also showed some strikingly different features compared to the samples retrieved from

the closed-system runs. Firstly, no overgrowths could be found (Fig. 3.12). Secondly, as opposed to the "tight" grain contacts observed to develop under closed-system conditions, the open-system samples showed occasional open (i.e. voided) grain contacts. Furthermore, occasional evidence was found for the development of "necks" by undercutting of the grain contacts (Fig. 3.12a, b).
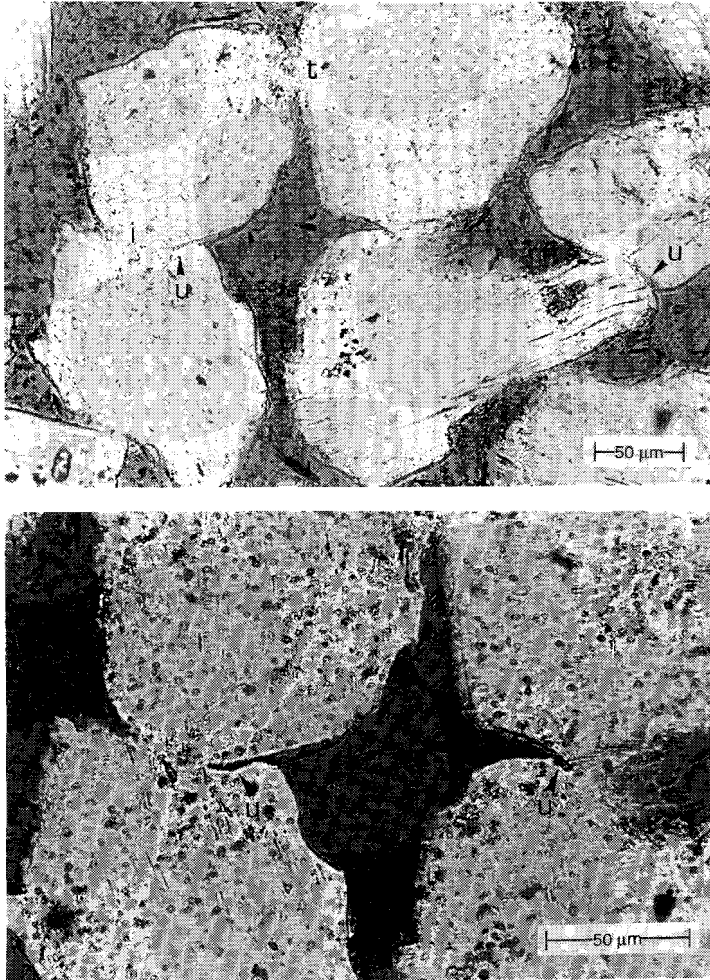
Figure 3.12a,b. Optical microstructure (exp./sample N° GY210O) typically exhibited by samples wet-compacted under open-system conditions. Note the blunt contacts, the grain-to-grain indentations (i), the contact truncation (t) features, and occasional undercutting features (u). Note also the conspicuous absence of overgrowth features on pore walls.

3.4 DISCUSSION

3.4.1 Deformation mechanisms during dry compaction

Since samples subjected to initial dry compaction only, reveal abundant microstructural evidence for grain bending, transgranular cracking, and cleavage development, these features must be related to the 10-13% instantaneous strain built-up observed at this stage. Initial dry compaction is therefore proposed to have occurred by instantaneous (work hardening) plastic deformation of the grains, plus time-independent grain breakage and rearrangement.

3.4.2 Deformation processes during wet compaction under closed-system conditions

In contrast to the dry and oil-flooded samples, the wet-tested samples showed on-going creep under both closed- and open-system conditions, thus providing evidence for the operation of some kind of solution- or water-enhanced creep mechanism. Fluid-lubricated intergranular sliding and/or straight forward dislocation creep can be ruled out as mechanisms of wet creep, since these would also have led to creep in the oil-flooded samples.

Considering the lack of microstructural evidence for significant (additional) plasticity or cataclasis during wet creep, fluid-assisted microcracking processes (such as stress corrosion cracking) or intracrystalline water weakening effects seem unlikely candidates to explain the wet compaction creep behaviour seen in the present closed-system experiments (see also Chapter 2, Section 2.3.2). By elimination, this implies that the closed-system behaviour must have been controlled by some kind of pressure solution mechanism operating in conjunction with intergranular sliding. This is strongly supported by the microstructures developed in the closed-system samples. Indeed the indentation, truncation and overgrowth microstructures developed in these samples provide classical evidence for the operation of a pressure solution process. Moreover, since grain contacts were "tight" with little evidence for grain contact corrosion or undercutting, or for the development of equilibrium pore configurations, it seems likely that deformation in the closed-system experiments was controlled largely by grain boundary diffusional pressure solution, as opposed to a plasticity-coupled mechanism (Spiers & Brzesowsky, 1993) operative on the grain- rather than grain boundary scale.

3.4.3 Comparison with pressure solution theory and kinetic constraints

As already shown, the influence of the water of crystallization of gypsum on the driving force for pressure solution and on grain boundary transport can be neglected, so that the wet creep data of the present closed-system experiments can be justifiably compared with conventional micromechanical models for compaction of granular aggregates by grain boundary diffusional pressure solution (i.e. equation 3.3). For most of the range of conditions investigated (i.e. σ_a < 2.50 MPa), the present closed-system data show an approximately 2nd to 3rd order power law dependence of creep rate on applied stress, a roughly 2nd to 4th order inverse power law dependence of creep rate on grain size, and an inverse dependence on strain. The observed wet behaviour is therefore consistent with neither the interface controlled nor diffusion controlled models for grain boundary diffusional pressure solution creep expressed in equation 3.3.

Turning now to the crystal growth and dissolution literature, it is well known that the kinetics of the dissolution reaction of gypsum are at least two orders of magnitude faster than of the precipitation reaction under comparable conditions (Christoffersen & Christoffersen, 1976; Christoffersen et al., 1982), so that the dissolution reaction is unlikely to be the rate limiting step during pressure solution creep of gypsum. As expressed in the theoretical equation for interface controlled creep (eq. 3.3), the power over the applied stress reflects the order of the dissolution or precipitation reaction rate law. Therefore, taking into account the fast dissolution reaction, the observed 2nd to 3rd order power law dependence of compaction creep rate on applied stress possibly reflects a 2nd to 3rd order precipitation rate law. Precipitation rate laws of this type have been measured in numerous growth experiments on gypsum (Liu & Nancollas, 1970; 1975; Nancollas et al., 1973; Packter, 1974; Barcelona & Atwood, 1978; Tadros & Mayes, 1979; Gill & Nancollas, 1980; Christoffersen et al., 1982; Weijnen, 1986). However, the experimentally observed inverse 3rd to 4th order dependence of creep rate on grain size cannot be explained by precipitation control involving a straight forward precipitation rate law, as this would lead to an inverse linear grain size dependence (eq. 3.3). Furthermore, when used to estimate rates of dissolution at grain contacts under the action of the driving force $\Delta\sigma_n\Omega^s$ (eq. 3.2), the absolute rates of precipitation deduced from crystal growth experiments in high purity systems (or systems with Na$^+$ and Cl$^-$ present) are 2-3 orders of magnitude too fast to explain the creep rates observed in the closed-system experiments. On the other hand, it is

well-established that crystal surface roughness and the presence of impurities can have drastic effects on the absolute growth rate of gypsum, without effecting the order of the precipitation reaction (Smith & Alexander, 1970; Liu & Nancollas, 1975; Nielsen, 1984; 1986; Weijnen, 1986; Sarig, 1994; Van der Eerden, 1994). A possible explanation for the strong grain size dependence observed in the closed-system data might therefore lie in precipitation controlled pressure solution influenced by systematic variations in impurity content and/or surface roughness between the different grain size fractions. Equally feasible, but with no independent support, the observed closed-system results might be explainable by some kind of diffusion controlled model with a stress dependent development of the grain boundary structure. Hence from the closed-system experiments, no definite conclusion can be drawn regarding the rate controlling process operative during compaction of gypsum by pressure solution creep.

3.4.4 Closed- versus open-system experiments

In common with the closed-system experiments, the general nature of the mechanical and microstructural data obtained from the open-system experiments seem to suggest some kind of pressure solution process. However, much higher compaction creep rates occurred in the open-system experiments (see Fig. 3.13). and the microstructures developed in these samples are somewhat modified. The compaction rates are 10-30 times faster in the open-system tests. Moreover, as opposed to the "tight" grain boundaries observed in the closed-system experiments, the open-system experiments showed some rather porous, occasionally undercut grain contacts (contact corrosion) and overgrowths on pore walls were absent.
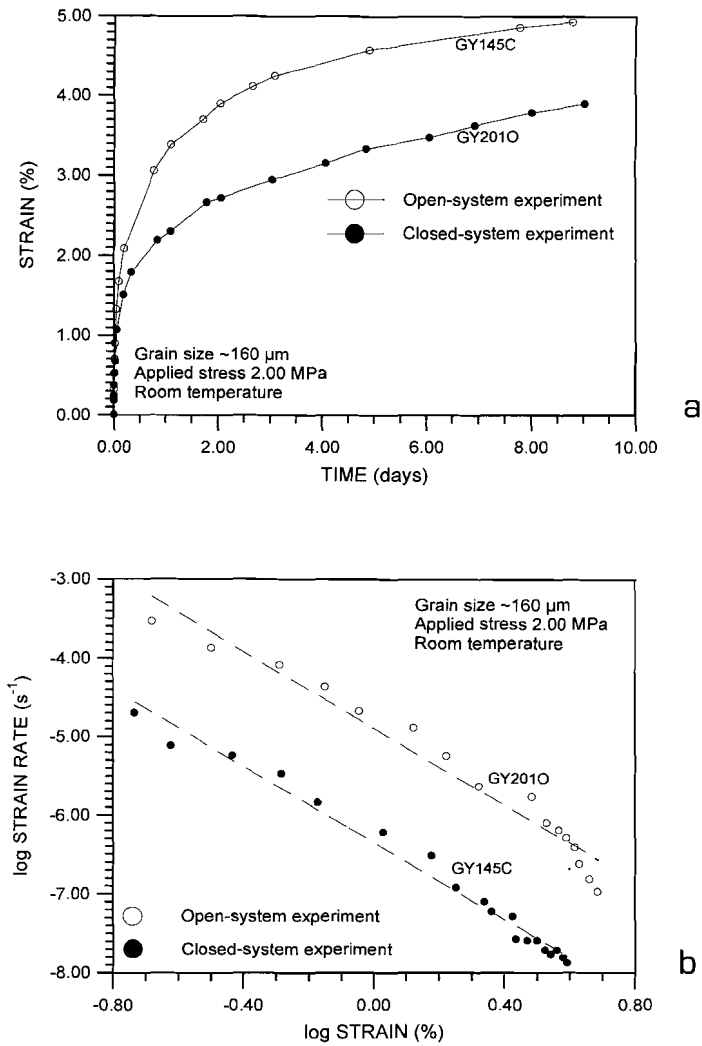
Figure 3.13. Graphs illustrating the difference in compaction creep behaviour between experiments performed under closed- versus open-system conditions. Compaction creep curves (a), and log-log plot of compaction strain rate versus compaction strain (b).

In order to explain these differences let us now consider the question of the driving force and kinetic controls of pressure solution in closed versus open systems of the type investigated here. In Section 3.2.1, it was shown that the expression for the driving force for pressure solution in gypsum, under closed-system steady-state conditions (eq. 3.2), is identical to that used to in conventional models for grain boundary diffusional pressure solution creep, and can be written

$$\Delta \mu_s = \Delta \sigma_n \Omega^s \qquad\qquad (3.2)$$

where $\Delta \mu_s$ and $\Delta \sigma_n$ are the differences in surface chemical potential of the solid and interfacial normal stress which exist between grain contacts (dissolution or source sites) and pore walls (precipitation or sink sites). As shown in Chapter 2 (appendix), this driving force for pressure solution can alternatively be written as a normalized solubility difference

$$\frac{\Delta C}{C_{pw}} = \frac{\Delta \sigma_n \Omega^s}{RT} \qquad\qquad (3.10)$$

developed between stressed grain contacts and pore walls. Here, C_{pw} is the solubility of the stressed solid at pore walls, which is approximately equal to the solubility (C_o) of the unstressed granular solid provided the applied stresses (hence changes in f^s and Ω^s within grains) are not too large.

Consider the simplified grain-to-grain contact geometry illustrated in Fig. 3.14. This grain-to-grain contact with surface A_{gc}, is assumed to possess an interconnected fluid phase and A_{gc} is assumed to remain flat at the scale of the grain contact. Now, during pressure solution creep under steady-state closed-system conditions, the potential drop $\Delta \mu_s$ or equivalent solubility difference ΔC will be taken up driving the serial processes of dissolution at A, grain boundary diffusion from A to B, pore diffusion from B to C and precipitation at C (Fig. 3.14a - Raj, 1982; Rutter, 1983; Lehner, 1990; Appendix, Chapter 2). Thus by analogy with an electrical circuit, a flux of matter is transferred from the dissolving contacts to be precipitated on pore walls, with each kinetic step consuming part of the available driving force ($\Delta \mu_s$, ΔC see Fig. 3.14a). Because the diffusivity of solute through the pore fluid is much larger than the effective grain boundary diffusivity ($D_{pore} \gg D_{gb}$), the pore fluid solution is assumed to be in equilibrium, and the potential drop for pore fluid diffusion from B to C is neglected in relation to the other potential drops. In the limiting cases of dissolution, grain boundary diffusion and precipitation control, this

means that the entire potential drop $\Delta\mu$ or solubility difference ΔC will appear across whichever of the processes of dissolution, grain boundary diffusion and precipitation is the slowest, thus leading to the potential and concentration distributions depicted in Figs. 3.14b, c, d (see also Schutjens, 1991).

General case
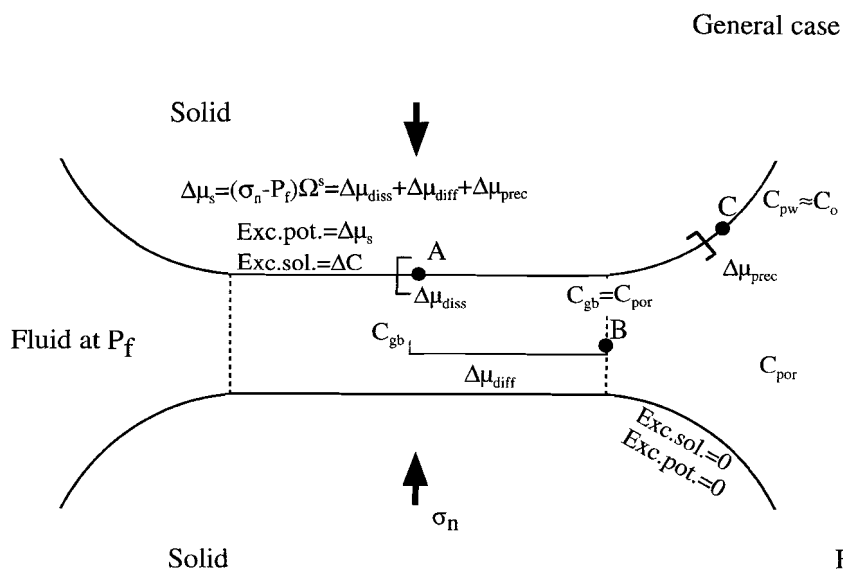
Fig. 3.14a

Figure 3.14. Schematic grain-to-grain contact between two grains undergoing pressure solution under closed-system, steady state conditions. The grain contact is assumed to possess an interconnected fluid phase (either island-channel structure or thin film), and is assumed to remain flat at the scale of the contact. The chemical potential difference between the solid at the grain-to-grain contact and the pore wall ($\Delta\mu_s$), or similarly the solubility difference ΔC (excess solubility at the grain-to-grain contact), drives dissolution at A, diffusion through the grain boundary fluid from A to B, pore diffusion from B to C (neglected in further considerations, see text), and precipitation at C (Fig. a). Figs. b-d (next pages): Chemical potential differences and solubility differences in the limiting cases of dissolution-controlled, grain boundary diffusion-controlled and precipitation-controlled pressure solution. Refer to text for explanation. In these figures $\Delta\mu_{diss}$, $\Delta\mu_{diff}$ and $\Delta\mu_{prec}$ are the potential drops associated with the dissolution, diffusion and precipitation steps. C_{pw} is the solubility of the solute at the pore walls, C_{gb} and C_{por} are the concentrations of the solute in the grain boundary fluid and pore fluid, C_o is the solubility of the unstressed solid, σ_n is the normal stress across the contact at A, P_f is the pore fluid pressure and Ω^s is the molar volume of the solid.

Dissolution control

Solid

$C_{pw} \approx C_o$

Exc.pot.$=\Delta\mu_s$
Exc.sol.$=\Delta C$

A

$\Delta\mu_{prec}=0$

$\Delta\mu_{diss}=(\sigma_n-P_f)\Omega^s$

C

Fluid at P_f

$C_{gb}=C_{pw}$

B

$C_{por}=C_{pw}$

$\Delta\mu_{diff}=0$

Exc.sol.=0
Exc.pot.=0

σ_n

Solid

Fig. 3.14b

Diffusion control

Solid

$C_{pw} \approx C_o$

Exc.pot.$=\Delta\mu_s$
Exc.sol.$=\Delta C$

A

$\Delta\mu_{prec}=0$

C

$\Delta\mu_{diss}=0$

$C_{gb}=C_{por}$

Fluid at P_f

$C_{gb}=C_{pw}+\Delta C$

B

$C_{por}=C_{pw}$

$\Delta\mu_{diff}=(\sigma_n-P_f)\Omega^s$

Exc.sol.=0
Exc.pot.=0

σ_n

Solid

Fig. 3.14c

Precipitation control
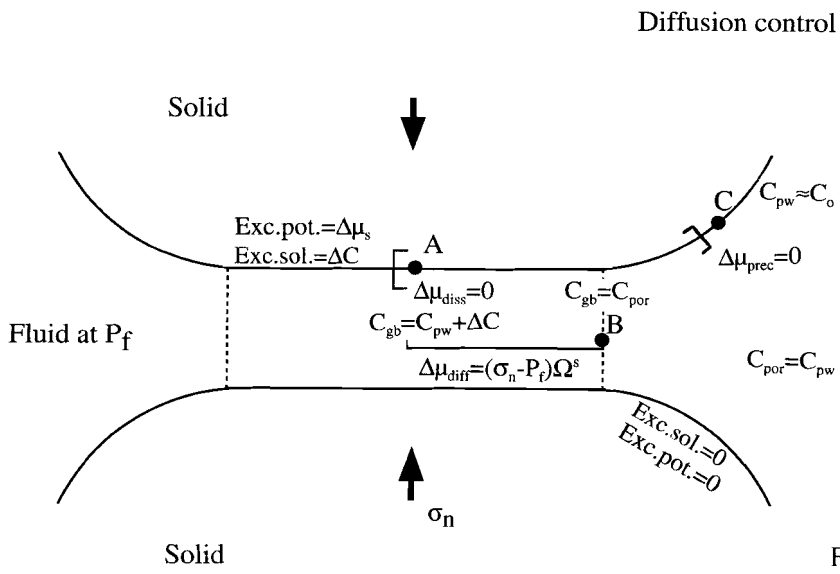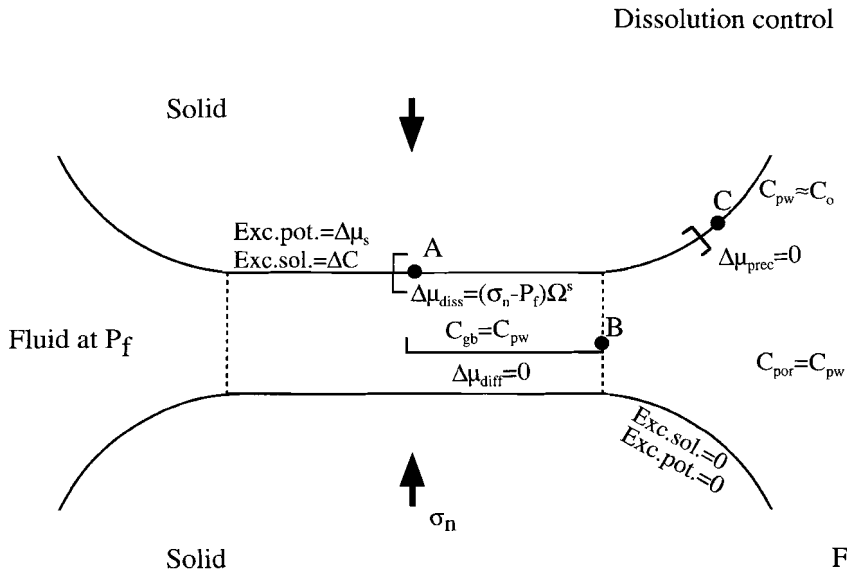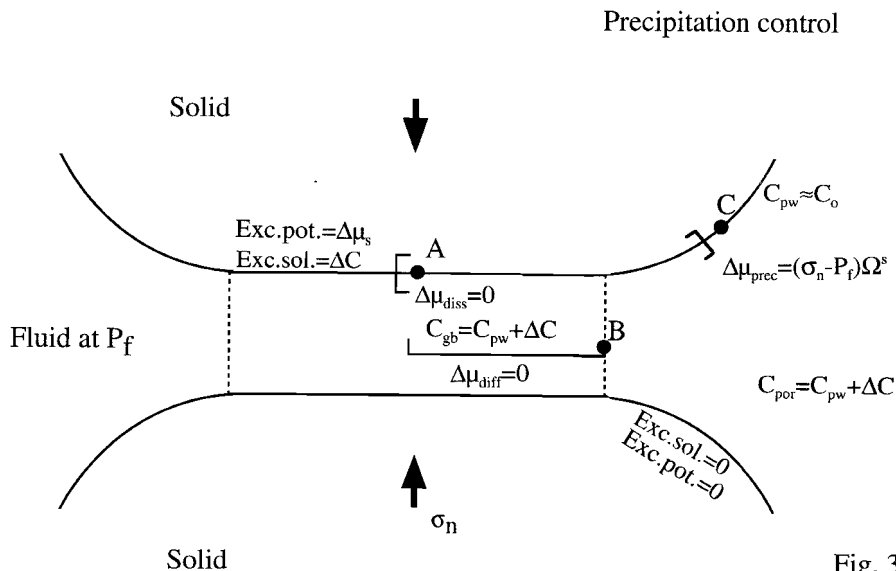
Fig. 3.14d

Referring to Figs. 3.14a-d, it now becomes possible to assess the effect of open-system conditions, i.e. of flushing the pores with a solution maintained at or near the concentration C_o (solubility of loose, unstressed, granular gypsum). Since $C_o \approx C_{pw}$ at relatively low applied stress, it is clear from Figs. 3.14b and c that, when closed-system creep is controlled by dissolution or grain boundary diffusion, rapid flushing of the pores with a solution of input concentration C_o will cause little change compared with closed system. Firstly, dissolution or grain boundary diffusion will remain rate limiting· for deformation with more or less unchanged driving force for and rate of transport from contacts to pores. Moreover, since precipitation on pore walls is relatively easy in this situation, it will continue as long as the rate of fluid flow is not too high. If the flow rate is very high, the solute concentration in the pores will be slightly undersaturated with respect to the grain contacts ($C_o < C_{pw} + \Delta C$) so that contacts might become somewhat undercut, causing a slight increase in creep rate, and precipitation might be inhibited due to mass removal from the system.

On the other hand, when precipitation is rate controlling under closed-system conditions (Fig. 3.14d), flushing at rapid rates with a solution with $C_o \approx C_{pw}$ can be expected to have much bigger effects. In essence, the supersaturation $\Delta C/C_o$ tending to develop in the pores will be flushed away by the moving fluid ($C_{pw} + \Delta C \rightarrow C_o \approx C_{pw}$), so that precipitation will be prevented and the driving forces $\Delta \mu_s$ and ΔC for

compaction deformation will appear across the easier dissolution and grain boundary diffusion steps, i.e. one of these relatively easy processes will become rate controlling. The result will be twofold. Firstly, a drastic increase in creep rate will occur as the faster dissolution or grain boundary diffusion steps take control. This implies order of magnitude increases in creep rate ($\dot{\varepsilon}$) and a change in dependence of creep rate on stress (σ) and grain size (d). Secondly, the microstructure will be modified as precipitation is prevented and as the grain contacts again tend to be undercut by the slightly undersaturated pore fluid (producing an additional acceleration of creep rate).

These last described mechanical and microstructural effects, i.e. a large increase in creep rate, absence of overgrowths and minor undercutting, are clearly visible in the open-system experiments presented here. It therefore seems likely that the closed-system experiments were rate limited by precipitation controlled grain boundary diffusional pressure solution creep. Nonetheless, as mentioned above, the precipitation reaction kinetics needs to show a strong grain size dependence to fully explain the observed wet behaviour.

3.4.5 Comparison with hydrostatic balloon experiments

The results obtained from the hydrostatic balloon experiments of Chapter 2 (chemically closed-system), show close similarities with those obtained from the uniaxial closed-system tests described in the present chapter. In particular the pressure solution microstructures developed in both types of experiments are very much alike.

The dependence of compaction creep rate on applied stress obtained in the two test types is also similar and it has been proposed that creep in both cases is controlled by the kinetics of pore wall precipitation. However, the hydrostatic experiments show an inverse linear dependence of compaction creep rate on grain size, whereas the uniaxial experiments show an inverse 2nd to 4th order relation. Secondly, the creep rates observed in the hydrostatic experiments are one to two orders of magnitude slower than those observed in the closed-system uniaxial experiments.

These discrepancies could of course reflect some difference in rate controlling mechanism, but in view of the evidence presented for precipitation control in both cases, the following explanations seem more likely: i) differences in the testing methods; ii) increased grain boundary sliding and preferred orientation development

in the uniaxial tests; iii) differences in the surface structure of the granular gypsum materials used causing differences in precipitation kinetics; or iv) differences in the chemical composition (impurity content) of the materials used causing differences in precipitation kinetics.

Although it is known that uniaxial compaction geometry can produce higher creep rates than hydrostatic compaction (see Paterson, 1995), this effect is not enough to explain the observed one to two orders of magnitude difference in creep rates. Wall friction in the uniaxial tests can also be excluded as an explanation for the difference in creep rate, as this would tend to slow-down the uniaxial compaction creep rates. No preferred explanation can presently be selected from possibilities ii-iv. However, it is relevant to recall that the precipitation kinetics of gypsum have been shown to be highly sensitive to trace impurities (e.g. Smith & Alexander, 1970; Liu & Nancollas, 1973b; weijnen, 1986). Notwithstanding their high purity (95-98wt.% pure), the natural gypsum materials used for the experiments, undoubtedly differ in trace impurity content (inorganic and organic); the gypsum used for the hydrostatic balloon experiments came from Somerset, England, while the present uniaxial tests were performed on gypsum from the Paris Basin, France.

3.4.6 Creep equation for natural gypsum

The present experiments provide a much larger body of data, upon which to base a creep law for gypsum, than obtained in Chapter 2. However, while a precipitation controlled creep law of the form

$$\dot{\epsilon} = A \cdot \frac{\sigma^n}{d^m}$$

with n=2-3 and m=2-4 would seem appropriate, an empirical fitting exercise is of little value for extrapolation to nature without a) further confirmation of the rate controlling process, and b) a theoretically-based, quantitative description of this process. These topics and the formulation of a creep law for natural gypsum form the subject of future chapters.

3.5 CONCLUSIONS

In this chapter, the compaction creep behaviour of wet granular gypsum has been investigated in both chemically closed- and open-systems under conditions favouring pressure solution creep (σ_a = 0.5-2.5 MPa, d = 32-282 μm and room temperature). The results demonstrate that whereas dry and oil-saturated material show little or no creep under the chosen experimental conditions, samples flooded with saturated gypsum solution creep significantly. In addition, the indentation and truncation microstructures present in samples compacted under both closed- and open-system conditions, plus overgrowths present in samples compacted under closed-system conditions, provide classical evidence for the operation of grain boundary diffusional type pressure solution. It was shown that the water of crystallization present in gypsum influences neither the driving force for pressure solution nor the rate limiting steps of pressure solution creep. Therefore, conventional models for grain boundary diffusional pressure solution creep are applicable, in theory, to the compaction creep of wet granular gypsum. However, the mechanical results obtained for the closed-system tests show that $\dot{\varepsilon} \propto \sigma_a^{2-3}/d^{2-4}$. This behaviour does not fully match any of the existing models for dissolution, diffusion or precipitation controlled pressure solution. However, independent data on the dissolution and precipitation kinetics of gypsum suggest that the precipitation reaction is most likely to be the rate limiting process. Additional information on the rate limiting step under closed-system conditions, was provided by the open-system experiments (i.e. with through-flowing solution saturated with respect to the unstressed sample). In such experiments, precipitation can no longer control the rate of deformation, so that either dissolution or grain boundary diffusion will take over as the rate limiting process if fluid flow rates are high enough. This should strongly enhance the compaction creep rate. Indeed, a 10 to 30 times increase in compaction creep rate was observed in the open-system tests, confirming that creep in the closed-system experiments probably occurred by precipitation controlled grain boundary diffusional pressure solution.

CHAPTER 4

KINETICS OF PRECIPITATION OF GYPSUM AND IMPLICATIONS FOR PRESSURE SOLUTION CREEP

4.1 INTRODUCTION

The experiments reported in Chapters 2 and 3, on the creep behaviour of wet gypsum aggregates under both hydrostatic and uniaxial compaction conditions, provided strong evidence for deformation by grain boundary diffusional pressure solution creep. In addition, it was inferred that the kinetics of gypsum precipitation on pore walls probably controlled the rate of deformation. However, kinetic descriptions for the gypsum precipitation reaction, derived from the crystal growth literature, are only partially consistent with the observed deformation behaviour. In particular, although the stress-strain rate relationships obtained in the pressure solution experiments are consistent with the order of the precipitation reaction obtained in crystal growth experiments, the absolute deformation rates were found to be 2 to 4 orders of magnitude slower than expected from the crystal growth data. Furthermore, it was inferred in Chapter 3 that the kinetics of crystal growth would have to show an inverse dependence on grain size (i.e. the initial size of the "seed" crystals constituting the compacted aggregate) in order to explain the observed non-linear dependence of pressure solution strain rate on grain size.

Now, as pointed out in Chapter 3, most crystal growth experiments on gypsum have been performed using highly pure seed crystals plus analytical quality Na_2SO_4 and $CaCl_2$ solutions to create a supersaturated gypsum solution. Thus in most growth experiments, Na^+ and Cl^- were present in the system. However, the absolute precipitation rate of gypsum is known to be highly sensitive to impurities and to Na^+ in solution (e.g. Smith & Alexander, 1970; Liu & Nancollas, 1973b; 1975; Brandse et al., 1977; Kushnir, 1980; Weijnen, 1986). Furthermore, the compaction creep experiments reported in Chapters 2 and 3 were performed on natural (impure) gypsum, using saturated pore fluid solutions prepared from the same gypsum. It therefore seems likely that the rate-discrepancies between the pressure solution experiments of Chapter 2 and 3 and independent crystal growth data can be explained in terms of differences in solution and solid phase (seed) composition. To

satisfactorily explain pressure solution phenomena in gypsum however, this remains to be quantitatively demonstrated, as does any grain size / seed-size (or related) dependence of precipitation reaction rates in the granular gypsum material used in the compaction experiments of Chapter 3.

The present chapter aims to resolve these questions by reporting crystal growth experiments performed using seed crystals and supersaturated solutions prepared from natural gypsum powders identical to those used in the wet compaction experiments of Chapter 3. For orientational purposes, the chapter is opened with a summary of previous studies of kinetics of gypsum crystal growth. The new crystal growth experiments carried out using natural gypsum are then described. These were performed using supersaturations or driving forces similar to the lower end of the range calculated for the pressure solution tests of Chapters 2 and 3 (i.e. supersaturations of S=10-80%), and using gypsum grain size fractions in the range ~30 to ~300 μm as seed crystals. The results are combined with a theoretical model for precipitation controlled pressure solution to predict rates of creep by this mechanism. Reasonable agreement is obtained with the pressure solution creep data of Chapter 3, at least to within 1.5 order of magnitude.

4.2 PREVIOUS WORK ON THE KINETICS OF GYPSUM PRECIPITATION

Gypsum precipitation is an unwelcome problem associated with many industrial processes. It is of particular importance in the following areas:

i)   during the desalination of sea water by evaporation techniques where scale formation on heat transfer surfaces may significantly reduce thermal efficiency,

ii)   in waste water treatment,

iii) in phosphoric acid production, and

iv)   in off-shore oil recovery, where sea water is used for well-stimulation.

For these reasons, numerous investigations have been carried out on the crystallization of calcium sulphate dihydrate (gypsum), the kinetics of crystal growth, and the mechanisms of crystal growth.

In the kinetics experiments performed, the rate of precipitation was measured as a function of time, either by

i)   recording the change of electrical conductivity of the solution (McCartney & Alexander, 1958: Smith & Alexander, 1970; Van Rosmalen et al., 1981; Christoffersen et al., 1982; Nielsen, 1986; Weijnen, 1986),

ii)   recording the change of concentration of calcium in solution using a Ca-

selective electrode (Liu & Nancollas, 1970; Christoffersen et al., 1979; Kushnir, 1980).

iii) in-situ microscopic observations (Liu & Nancollas, 1973a; Tadros & Mayes; 1979; Bosbach & Rammensee, 1994), or

iv) analyzing aliquots of the filtered solution for calcium ions by EDTA titration (Liu & Nancollas, 1973b; 1975; Nancollas et al, 1973; Packter, 1974; Brandse et al., 1978; Barcelona & Atwood, 1978; Gill & Nancollas, 1979; Weijnen, 1986).

Several of these investigations have been done using spontaneous crystallization techniques, in which Na_2SO_4 or $NaNO_3$ solution and $CaCl_2$ solution were added drop-wise to a saturated $CaSO_4$ solution (McCartney & Alexander, 1958; Smith & Alexander, 1970; Packter, 1974; Gill & Nancollas, 1980; Cody & Cody, 1988; 1991). After an initial "surge" of precipitation during which nucleation took place, gypsum crystals grew following a rate equation showing a second order dependence of growth rate or velocity on supersaturation. An exception is the work of Packter (1974), who inferred that the crystallization rate was a fourth order process.

However, most studies of gypsum precipitation kinetics have been performed by means of seeded growth. In these experiments, a constant mass or volume of gypsum crystals is added to a supersaturated $CaSO_4$ solution, and the rates of precipitation measured as a function of time using the same techniques as mentioned above. The supersaturated solutions used in these experiments were prepared by

i)   mixing Na_2SO_4 with $CaCl_2$ solutions (Liu & Nancollas, 1970; 1973a; 1973b; 1975; Smith & Alexander, 1970; Barcelona & Atwood, 1978; Tadros & Mayes, 1979; Kushnir, 1980),

ii) mixing K_2SO_4 or Li_2SO_4 with $CaCl_2$ solutions (Kushnir, 1980), or

iii) dissolving the more soluble hemihydrate (Nancollas, et al., 1973; Brandse et al., 1977; Christoffersen et al., 1979; 1982; Van Rosmalen et al., 1981; Nielsen, 1986; Weijnen, 1986; Bosbach & Rammensee, 1994).

The bulk of these studies were performed in order to investigate the effect of additives on the growth kinetics and morphology of gypsum crystals, with the aim of assessing whether unwanted precipitation of gypsum in industrial processes could be retarded or stopped completely. Through these experiments, a wide variety of polymers, organic compounds, acids and especially phosphonates (e.g. (A)MDP (amino-)methane-biphosphonic acid, HEDP 1-hydroxy-ethylidene-1,1-biphosphonic acid) have been found to greatly decrease or completely block the growth of

gypsum (McCartney & Alexander, 1958; Smith & Alexander, 1970; Liu & Nancollas, 1973b; 1975; Barcelona & Atwood, 1978; Tadros & Mayes, 1979; Weijnen, 1986). This effect is caused by preferential adsorption of the phosphonates at active growth sites (e.g. Weijnen, 1986). On the other hand, the rate of crystallization is increased when NaCl, KCl or LiCl are present in the solution due to the formation of complexed $(Na,K,Li)SO_4^-$ ion pairs. These ion pairs make the otherwise strongly repulsed sulphate more available to the negatively charged surfaces of the gypsum crystal (Brandse et al., 1977; Kushnir, 1980). Regardless of the presence or absence of additives, however, most seeded growth studies (Liu & Nancollas, 1970; 1973a; Nancollas et al., 1973; Christoffersen et al., 1979; 1982; Van Rosmalen, 1981; Nielsen, 1986; Weijnen, 1986) have yielded a second order growth rate description (i.e. a second order relation between growth velocity and driving force or supersaturation) for most of the range of supersaturations investigated ($3\% \leq S \leq 200\%$). In a few cases where no additives were present (Liu & Nancollas, 1973a; Brandse et al., 1977; Christoffersen et al., 1982), the order of the kinetic relation was found to increase towards 3 or 4 at high supersaturations ($S \geq \sim 40\text{-}80\%$). Barcelona & Atwood (1978) who performed their crystal growth experiments in natural sea water at supersaturations 15-90%, observed a third order rate dependence on supersaturation.

4.3 EXPERIMENTS

4.3.1 Aims and approach

The present experiments consisted of a series of seeded growth tests performed using natural gypsum seed crystals deposited in a supersaturated solution prepared from the same starting material. The experiments were carried out at room temperature using supersaturations up to a maximum attainable value of 80% or S=0.8. The supersaturation S is defined henceforth as

$$S = \frac{(C - C_o)}{C_o} \qquad (4.1)$$

where C is the concentration of the supersaturated solution, and C_o is the (apparent) seed crystal solubility, determined at the end of each experimental run. The progress of the precipitation reaction (i.e. the changing concentration of solute), was

monitored by measuring the change of electrical conductivity of the solution as a function of time. The grain size fraction used for the seed crystals was varied from experiment to experiment, so that any dependence of the precipitation rate on grain size could be systematically determined.

4.3.2 Seed crystals and preparation of supersaturated solutions

The seed crystals for the present experiments were taken from the same grain size batches used for the uniaxial compaction creep experiments on wet granular gypsum aggregates reported in Chapter 3. The grain size fractions with final average crystal sizes of ~32 μm, ~48 μm, ~97 μm, ~160 μm, and ~282 μm were used (see Chapter 3). The specific surface area of the individual fractions was measured using N_2 gas adsorption, i.e. using the technique developed by Brunauer, Emmett and Teller (BET-technique). The BET results, and chemical analysis data obtained for the different grain size fractions are given in Table 4.1. Note that individual fractions were 96.5 - 98.6% pure $CaSO_4 \cdot 2H_2O$. Washing of the various fractions using water, during preparation (see Chapter 3) ensured that the content of highly soluble salts was below detection (Table 4.1).

Supersaturated solutions were made by dissolving the more soluble hemihydrate ($CaSO_4 \cdot \frac{1}{2}H_2O$), prepared by dehydrating the natural gypsum material. To achieve this, the gypsum starting material (from the Paris Basin, see Chapter 3) was crushed in a Herzog disk mill to a grain size of approximately 2-5 μm and subsequently dehydrated to the equivalent mass of hemihydrate (calculated assuming 100% purity) by heating in an oven at 110°C. The very fine grained hemihydrate powder produced was then dissolved in doubly distilled water. Undissolved crystals in the supersaturated solution were filtered off using a vacuum filter system plus 0.4 μm Poretics membrane filters. The process of dissolving and filtering the hemihydrate was repeated 5 times, to achieve the highest possible starting concentration of $CaSO_4$ in solution ($C_{init} \leq 0.0244M$).

Table 4.1: BET-specific surface data, X-ray fluorescence (XRF) analyses, and thermogravimetric (TGA) analyses for the different seed-sizes used in the present growth experiments.

		~32 μm	~48 μm	~97 μm	~160 μm	~282 μm
Specific surface (m²/g)		0.36	0.39	0.16	0.10	0.07
H_2O (TGA)	%	20.17	19.98	20.20	20.30	20.45
SiO_2	%	<2.78	<2.78	<2.78	<2.78	<2.78
Al_2O_3	%	<1.08	<1.08	<1.08	<1.08	<1.08
Fe_2O_3	%	<0.92	<0.92	<0.92	<0.92	<0.92
MnO	%	<0.023	<0.023	<0.023	<0.023	<0.023
MgO	%	<0.24	<0.24	<0.24	<0.24	<0.24
Na_2O	%	<0.10	<0.10	<0.10	<0.10	<0.10
K_2O	%	<0.10	<0.10	<0.10	<0.10	<0.10
Sr	ppm	806.5	464.0	360.2	351.7	361.7
TiO_2	%	<0.02	<0.02	<0.02	0.02	<0.02
P_2O_5	%	0.02	<0.02	<0.02	0.03	<0.02
Cl	ppm	<148.8	<148.8	<148.8	357.3	<148.8
$CaSO_4 \cdot 2H_2O$	%	96.5	95.6	96.6	97.1	97.8

The amount of gypsum was calculated using the loss of weight, due to dehydration of gypsum, determined by TGA analyses.

4.3.3 Experimental procedure

The kinetics experiments performed are listed in Table 4.2 and were carried out using the apparatus illustrated in Fig. 4.1. The conductivity meter forming the central element of this system was a Knick conductometer with a resolution of $1 \cdot 10^{-5}$ Sm^{-1} which is approximately equivalent to a concentration change of $8 \cdot 10^{-5}$ M. The temperature of the solution was measured with a type K (chromel-alumel) thermocouple yielding a resolution of 0.1°C. Both signals were logged using a 16-bit A/D converter situated in an Epson QX-16 microcomputer.
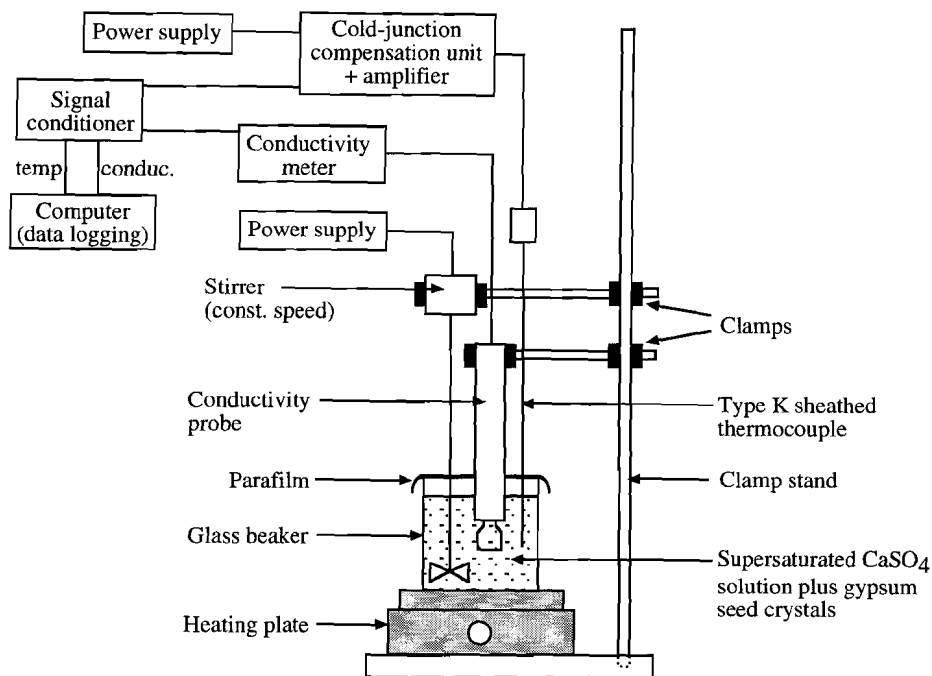
Figure 4.1. Schematic diagram illustrating the conductivity measurement set-up used for the present crystal growth experiments on gypsum. The change of $CaSO_4$ concentration in solution and the solution temperature were measured using a Knick conductometer and chromel-alumel thermocouple respectively. The corresponding signals were logged versus time using an Epson-QX16 microcomputer.

Before setting-up any individual experiment, the glass beaker, stirrer, thermocouple, and conductivity probe were first cleaned with Decon soap and thoroughly rinsed with distilled water.Careful decontamination is essential for meaningful conductivity measurements. The conductivity probe was then calibrated using 0.01M to 0.0001M $CaSO_4$ solutions, to obtain an experiment specific conductivity - concentration relation (Fig.4.2). These were prepared by dissolving a calculated mass of the same natural gypsum used for the growth experiments assuming 100% purity. After re-cleaning the apparatus, 200 ml of supersaturated solution was poured into the glass beaker, and the conductivity probe, thermocouple, and stirrer were immersed in the solution. The stirrer was then switched-on, and adjusted to operate at a constant speed of approximately 200 rpm

(same for all experiments). Two grams of the chosen fraction of seed crystals, measured on an analytical balance (Mettler H10W, accuracy of 0.1 mg), were then added to the supersaturated solution, and the glass beaker was sealed with a plastic (parafilm) sheet to prevent evaporation. Immediately after addition of the seed crystals, logging of the conductivity and temperature signals was started. In the first half hour of each experiment, the data was logged every 30 s, then every 120 s, and, after three hours every 600 s until the end of the test (total running time ~ 15 hours).

Table 4.2: Complete set of crystal growth experiments reported.

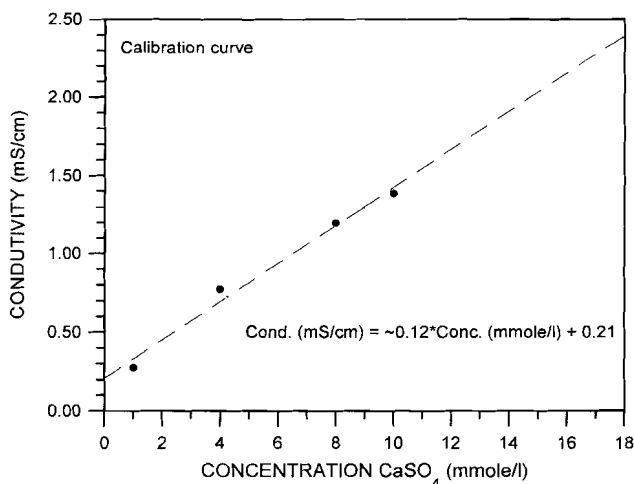| Experiment/ Sample N°	Grain size (μm)	Specific surface (m²/g)	Initial conc. $CaSO_4$ (mmole/l)	Initial supersaturation	Final conc. $CaSO_4$ (mmole/l)
GY334G	~282	0.07	19.79	0.56	13.78
GY335G	~48	0.39	24.42	0.80	13.71
GY336G	~97	0.16	22.14	0.49	13.48
GY337G	~160	0.10	18.01	0.33	13.52
GY338G	~32	0.36	20.37	0.48	12.68

Figure 4.2. Typical calibration curve showing the relation between conductivity and $CaSO_4$ concentration.

Tests were terminated by measuring the temperature dependence of the final (asymptotic) conductivity value (also used to determine C_o for each test). This was done by heating the beaker plus contents to ~45°C and allowing it to cool down again to room temperature, after each experimental run. This enabled the raw conductivity data to be corrected for temperature-change effects. The crystals were finally filtered off using the vacuum filter system, dried at 40°C in air, and stored under dry conditions for subsequent study by scanning electron microscopy (SEM).

4.3.4 Data processing

The raw data files (conductivity, temperature, time records), obtained for each test, were first processed to correct the conductivity data to a constant reference temperature of 22 °C (average temperature during the experimental runs). This was done using the conductivity dependence on temperature determined at the end of each experiment. The test-specific conductivity calibration data were then used to calculate the $CaSO_4$ concentration (C in mol/l) and supersaturation (S) of the solution, the driving force for precipitation ($\Delta\mu$), and the derivatives of C and S as a function of time, t. These quantities were computed assuming the starting materials to consist of pure $CaSO_4 \cdot 2H_2O$. This is considered reasonable in view of the ~95-98% purity of the gypsum used and the extremely low soluble salt concentration. The driving force for precipitation was calculated using the dilute solutions relation (e.g. Christoffersen et al., 1979)

$$\Delta\mu = RT\ln\frac{C}{C_o} \approx RT\frac{C-C_o}{C_o} = RTS \qquad (4.2)$$

where, R is the gas constant (R=8.314 $JK^{-1}mole^{-1}$), and T is the absolute temperature (T=295 K). The concentration change rate was obtained using

$$\frac{dC}{dt} = X\frac{d\kappa}{dt} \qquad (4.3)$$

(where X is the test-specific calibration coefficient linking concentration to conductivity, and $d\kappa/dt$ is the conductivity change rate), calculating the rate of change of conductivity ($d\kappa/dt$) as a function of time using a least squares fit method applied over a moving interval. The interval chosen was 50 μS/cm which is five times the resolution of the Knick conductometer. Conventional error analysis reveals

that the total standard error in dκ/dt ranges from ±2% at the beginning of the experiments to ±25% at the end of the experiments. Data with errors > ± 10% were rejected.

4.4 RESULTS

4.4.1 Quantitative data

As illustrated in Fig. 4.3, for all the seed-size fractions used, the conductivity and supersaturation dropped very fast at the start of the experiments, after which they asymptotically decreased to a more or less constant value. Corresponding log-log plots of concentration change rate (dC/dt) versus driving force for precipitation are shown in Fig. 4.4. These show that for much of the driving force range investigated, the gypsum precipitation rate expressed as dC/dt is proportional to the driving force squared (slope of 2 in Fig. 4.4), except for the ~282 μm seed crystals which shows that dC/dt is almost linearly proportional to the driving force (slope = 1). However, there is a tendency at high driving forces (logΔμ >3) for the precipitation rate (expressed as dC/dt) to be proportional to the driving force with a power greater than two. In addition, at the start of the experiments some clear differences can be observed between the different seed fractions (Fig. 4.4). For the smaller seed crystals used (~32 μm and ~48 μm), the precipitation rate (dC/dt) started to decrease immediately from the beginning of the experiment, while for the larger seed crystals (~160 μm and ~282 μm) the quantity dC/dt first increases before it starts to decrease. The data obtained from the experiment with ~97 μm seed crystals lies intermediate between these two trends. To illustrate any systematic grain size effects, Figure 4.4 was used to construct a plot of concentration change rate (dC/dt) versus grain size (d) at constant driving force (Δμ); see Fig. 4.5. This shows that dC/dt is roughly the same for all the seed-sizes used.
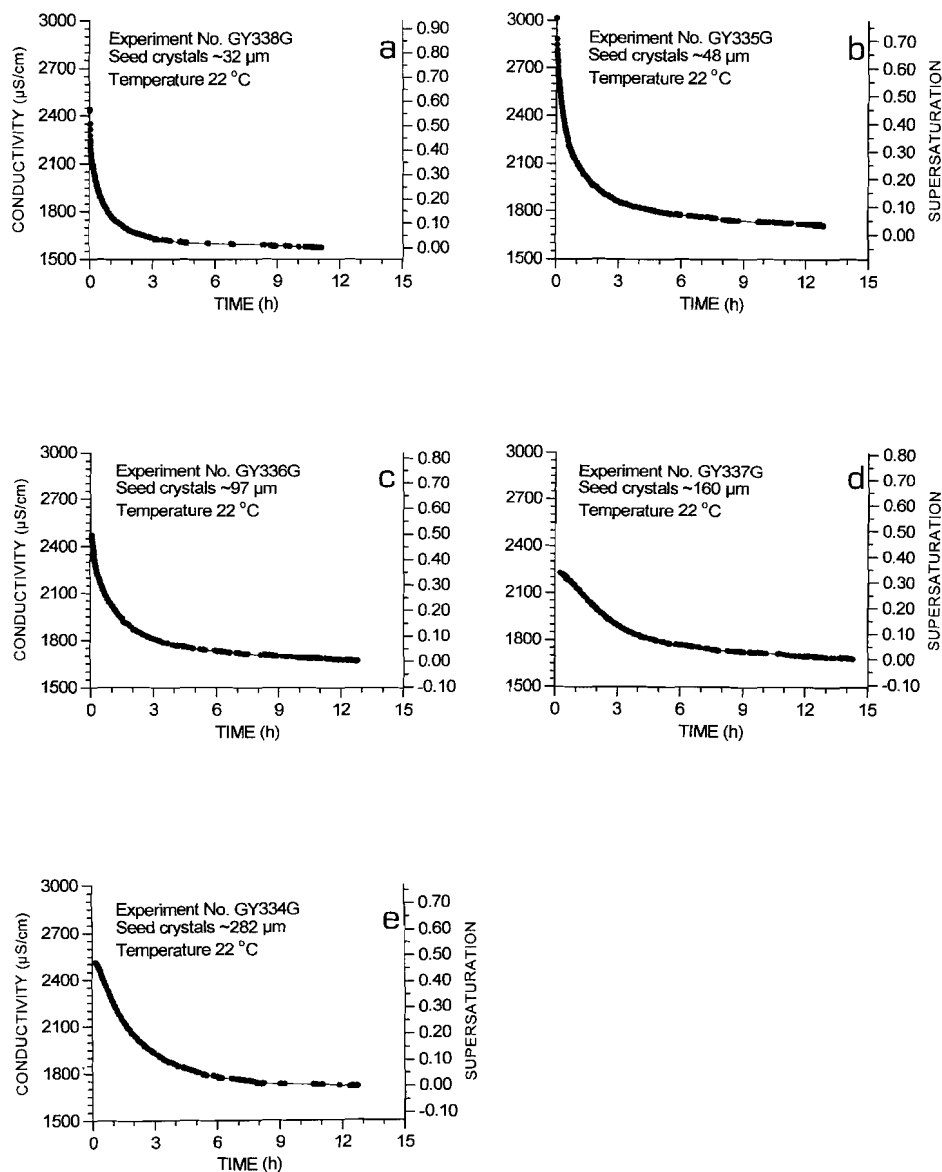
Figure 4.3a-e. Conductivity (κ), corrected to 22 °C, and supersaturation (S) versus time data obtained for all seed sizes used in the present experiments.
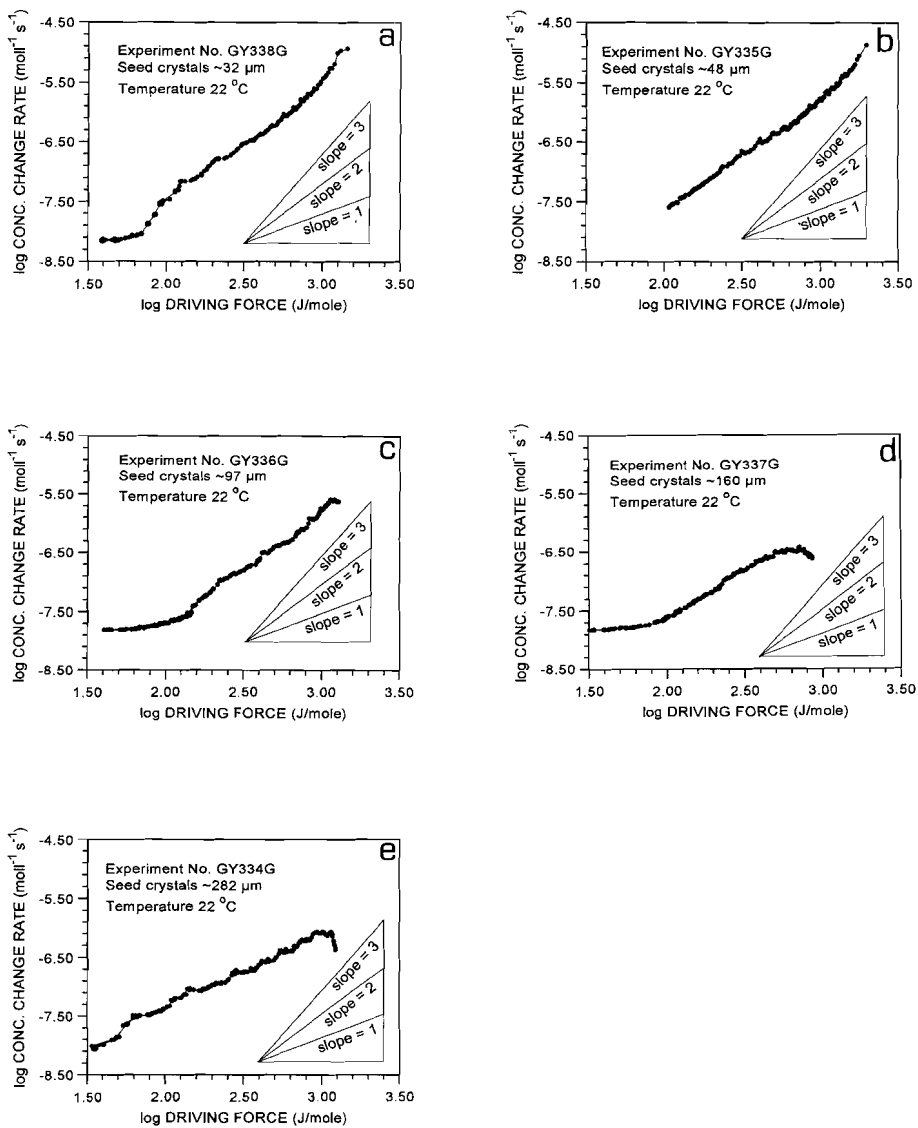
Figure 4.4a-e. Log-log plots of concentration change rate (dC/dt) versus driving force (Δμ) for all seed sizes investigated.
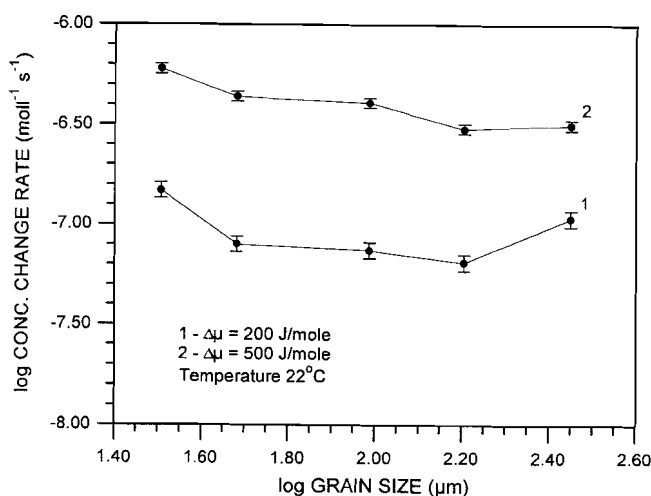
Figure 4.5. Log-log plot of concentration change rate (dC/dt) versus grain size (d) for two different values of driving force ($\Delta\mu$). Data displayed for all seed sizes investigated (i.e. all grain size fractions).

4.4.2 SEM observations

Both the starting seed crystals and final filtrate were studied using scanning electron microscopy (SEM). Figures 4.6a-e show the ~32 μm, and ~282 μm starting materials, and the final products of the growth experiments performed using the ~32 μm, ~97 μm, and ~282 μm seed crystals. The ~32 μm starting seed crystals (Fig 4.6a) have a subangular, non-uniform shape with many fines attached to their surfaces, while the ~282 μm starting seed crystals (Fig. 4.6b) are subrounded and have reasonably uniform shape with fewer fines attached to their surfaces. The intervening starting fractions were found to exhibit intermediate shapes and general appearance. In contrast, the final filtrate materials (Figs. 4.6c-e) are strikingly different from the starting material, though far from uniform from experiment to experiment. The experiments performed with the ~32 μm and ~48 μm seed crystals (test N°s GY338G and GY335G) show that the grains grew to become approximately euhedral (Fig. 4.6c). However, the material produced in the ~97 μm test (N° GY336G - Figure 4.6d) shows that, besides euhedral growth of the seed crystals, nucleation and growth of fine acicular grains took place as well, at some

stage of the experiment. This nucleation and growth is even more pronounced in the experiments performed using the ~160 μm and ~282 μm starting material (test Nᵒs GY337G and GY334G), although there is also clear evidence for euhedral overgrowth on the seed crystals (Fig. 4.6e).

Fig. 4.6a

Fig. 4.6b

Fig. 4.6c

GY338g-32   00008   30μm

Fig. 4.6d

GY336g-97   00022   100μm
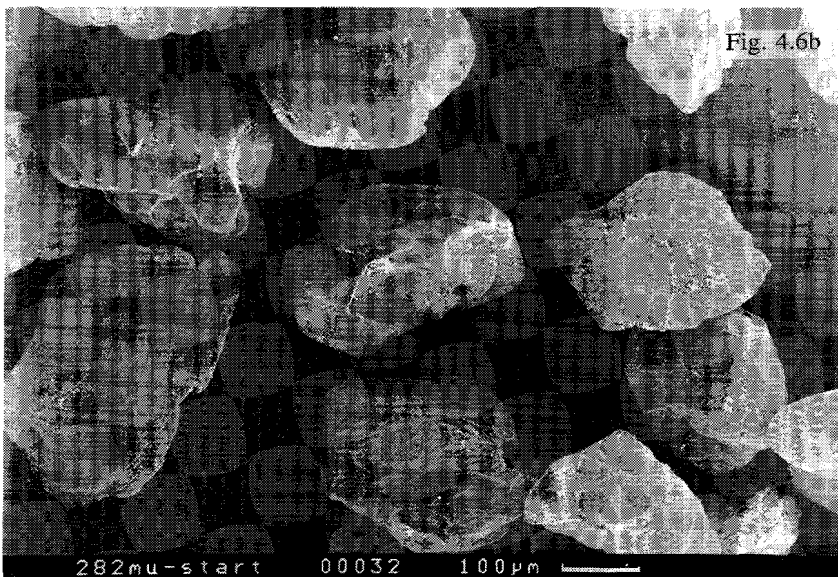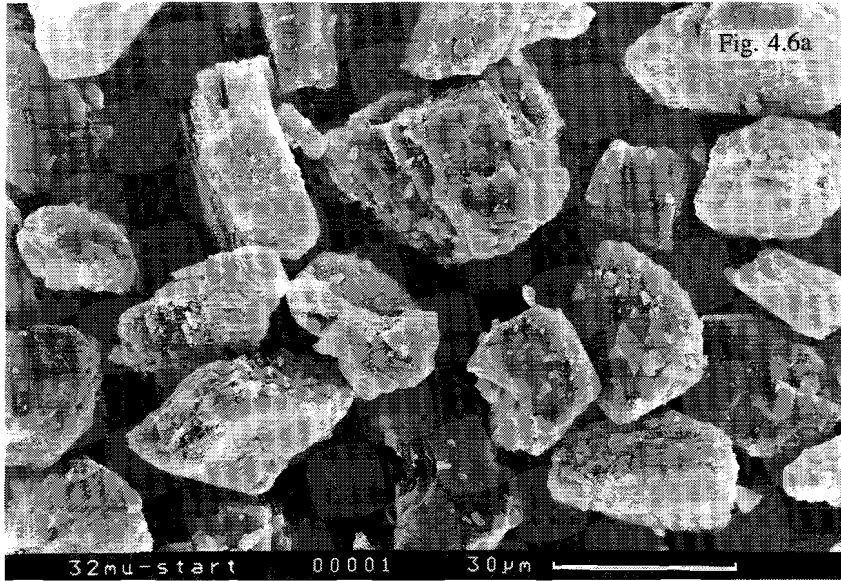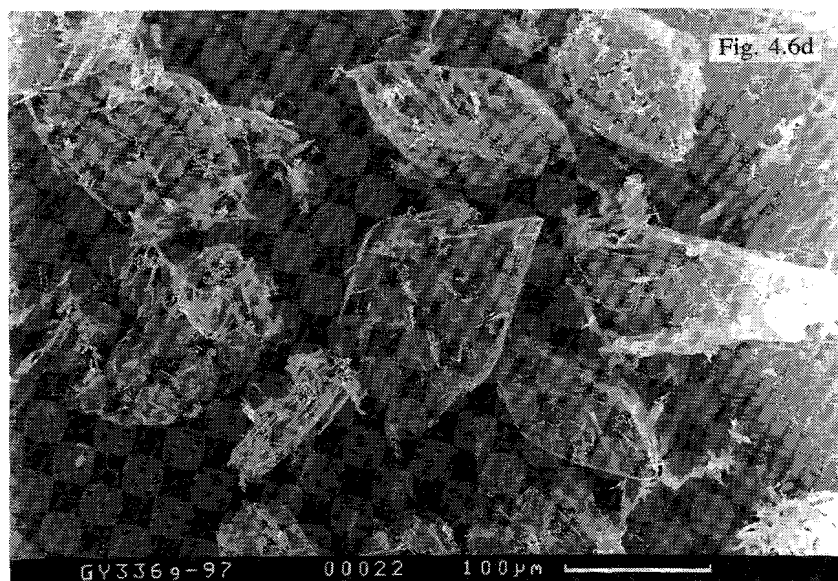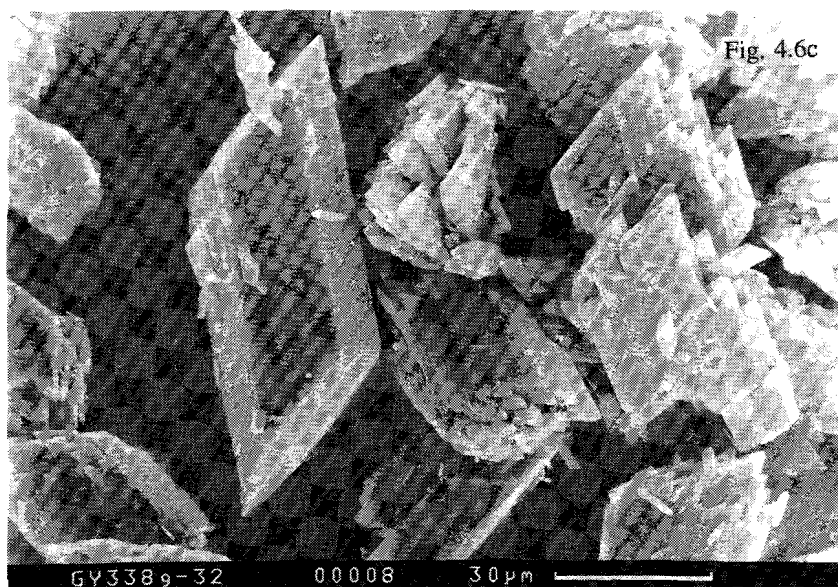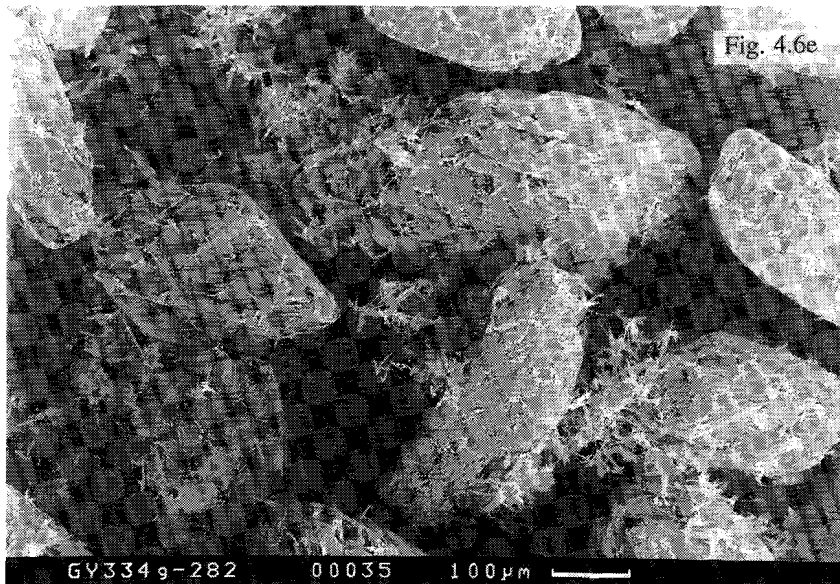
Figure 4.6. Secondary electron images of the starting material (a, b) and final filtrates (c-e). a) ~32 µm starting seed crystals (page 88), and b) ~282 µm starting seed crystals (page 88). Note the differences in shape, roundness and concentration of fines attached to the surfaces. c-e) Final products obtained using ~32 µm (c, page 89), ~97 µm (d, page 89), and ~282 µm (e, this page) seed crystals respectively (experiment No's GY338G, GY336G and GY334G). Fig. c shows the approximately euhedral shape of gypsum crystals obtained in the experiments using the 32 and 48 µm starting material. Fig. d shows that besides overgrowth of the seeds (~97 µm), small acicular crystals formed during the experiment. In the experiments using the 160 and 282 µm starting material the amount of small crystallites formed is very large, although there is also clear evidence for overgrowth on the seeds (Fig. e).

4.5 DISCUSSION

4.5.1 Growth rate versus rate of nucleation

Focusing first in the SEM observations, it is believed that the heating of the solution plus contents at the end of each experiment to 45°C, plus subsequent cooling to room temperature, did not influence the microstructure of the resulting material significantly, since the solubility of the gypsum in this temperature range changes by only 3%. From the SEM images described above, it is thus inferred that,

besides growth of the seed crystals during each experimental run, spontaneous nucleation from the solution also took place. This spontaneous nucleation was unimportant at 32 and 48 μm, but became more and more prominent, the larger the seed crystals used.

On this basis, the different trends observed in the plots of concentration change rate (dC/dt) versus driving force (Δμ) presented in Fig. 4.4 are inferred to be related to varying amounts of spontaneous nucleation from solution. Thus, in the experiments done using the ~32 μm and ~48 μm seed crystals, little or no spontaneous nucleation occurred, and the steady decrease in supersaturation (i.e. driving force) observed in Fig. 4.4a,b is believed to be more or less entirely due to precipitation on the seed crystals. The initial increase in dC/dt and subsequent decrease in dC/dt with decreasing Δμ, observed in the experiments using the larger grain size fractions, is suggested to be caused by spontaneous nucleation and subsequent precipitation on both the nuclei and seed crystals. Nucleation is presumably favoured in the courser seed size experiments because the reduced seed surface area in these experiments makes seed growth less competitive.

From the above, it is clear that the mean seed or crystal overgrowth rate (v_p) can be calculated only for the ~32 μm and ~48 μm seed crystals. This precipitation rate was calculated as a function of driving force (Δμ), assuming that all precipitation occurred on the seed crystals, using the equation (Nielsen & Toft, 1984)

$$v_p = \frac{\Omega_s}{A} \cdot \frac{dn}{dt} = \frac{\Omega_s \, V_{liq}}{A} \cdot \frac{dC}{dt} \qquad (4.4)$$

where, Ω_s is the molar volume of gypsum (Ω_s=7.42·10⁻⁵ m³/mole), A is the specific surface of the seed crystals, n is the cumulative number of moles of material precipitated on the seeds, and V_{liq} is the volume of solution used. The v_p versus Δμ data thus obtained for the ~32 μm and ~48 μm seed crystals are presented in Fig. 4.7. Noting the log-log nature of this plot, the slopes of both the 32 and 48 μm curves show that the growth rate is roughly proportional to the driving force to the power x=3-4 in the region logΔμ >3 (Δμ >1 kJ/mole), and x≈2 in the region logΔμ <3 (Δμ <1 kJ/mole). Figure 4.7 was also used to construct a plot of growth rate (v_p) versus grain size (d) for fixed values of Δμ (Fig. 4.8).
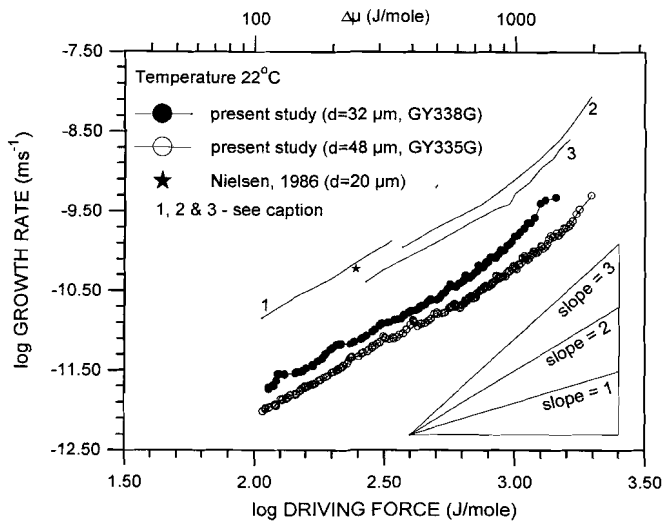
Figure 4.7. Log-log plot of growth rate (v_g) versus driving force ($\Delta\mu$) comparing the seed growth rate data obtained in the present study with growth rate data obtained by previous authors under similar experimental conditions (i.e in experiments using NaCl-free solutions).
1 - Christoffersen et al. (1982) and Weijnen (1986), d=10-200 μm but not accurately known.
2 - Van Rosmalen et al. (1981), d= not given. 3 - Brandse et al. (1977), d≈50 μm.
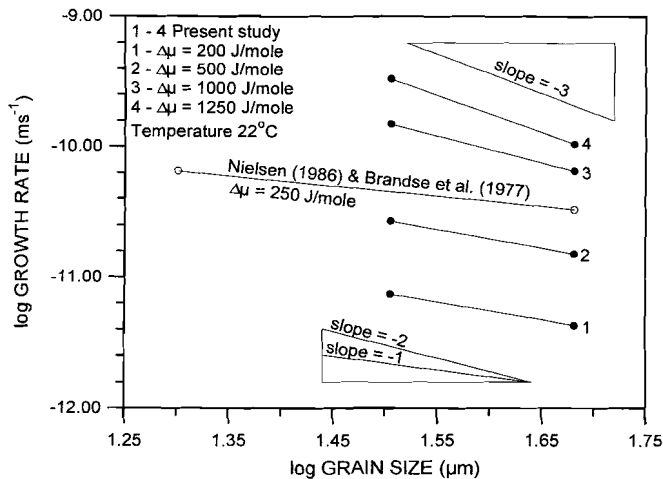
Figure 4.8. Log-log plot of growth rate (v_g) versus grain size (d) for four different values of driving force ($\Delta\mu$) in the present experiments (d=32 and 48 μm - closed symbols), and for a driving force of 250 J/mole for the combined data of Nielsen, 1986 (d=20 μm) and Brandse et al., 1977 (d≈50 μm - open symbols).

Though the data are few, this suggests an inverse 1st to 2nd order dependence of growth rate on grain size for $\Delta\mu$ <1 kJ/mole, and an inverse 2nd to 3rd order dependence of growth rate on grain size for $\Delta\mu$ >1 kJ/mole. The growth rate for the present experiments can thus be expressed empirically as

$$v_p = L_{1,2} \cdot \frac{(\Delta\mu)^a}{d^b} \qquad (4.5)$$

where $L_{1,2}$ are rate coefficients (constant at constant temperature), a=2 and b=1-2 at $\Delta\mu$< ~1 kJ/mole, a=3-4 and b=2-3 at $\Delta\mu$> ~1 kJ/mole. Note however that caution is needed with regard to the value of b, since data is available for only two grain sizes.

4.5.2 Comparison with previous studies

In Figures 4.7 and 4.8 the results of previous seed growth experiments, conducted under the same conditions (i.e. in NaCl-free solutions) as those reported here (Brandse et al., 1977; Van Rosmalen et al., 1981; Christoffersen et al., 1982; Nielsen, 1986; Weijnen, 1986), have been combined with the results of the present study in a single plot of growth rate versus driving force (Fig. 4.7), and a plot of growth rate versus grain size at constant driving force (Fig. 4.8). Figure 4.7 shows that below a driving force of ~1 kJ/mole, the growth rate is proportional to the driving force squared, implying second order growth kinetics, for all the different studies. This has previously been explained as being due to spiral growth at surface steps produced by screw dislocations (e.g. Christoffersen et al., 1982; Nielsen, 1986; Sarig, 1994). Above a driving force of ~1 kJ/mole, the results of Brandse et al. (1977), Van Rosmalen et al. (1981) and and the results of the present study show that the growth rate is approximately proportional to the driving force raised to the power 3 to 4, implying third to fourth order growth kinetics. This type of behaviour has previously been explained by surface nucleation growth processes (e.g. Nielsen, 1986; Sarig, 1994). In addition, Figure 4.8 shows that by combining the data of Brandse et al. (1977) and Nielsen (1986) for which the seed crystal sizes are accurately known, an approximately similar dependence of growth rate on grain size ($v_p \propto 1/d^{-1}$) is obtained as for the present experiments at a low driving force ($\Delta\mu \approx 250$ J/mole).

In addition to the above observations on the order of the growth kinetics, it can

be seen from Fig. 4.7 and 4.8 that the absolute rates of growth obtained in the present study, are one order of magnitude slower than those obtained by the other authors cited, for comparable seed sizes. This is most probably a reflection of the use of natural gypsum as a starting material in the present study, whereas previous work used analytical reagent. The natural gypsum contains up to 5wt% impurities which, as mentioned before, mostly reduce the growth rate of gypsum (McCartney & Alexander, 1958; Smith & Alexander, 1970; Liu & Nancollas, 1973b; 1976; Barcelona & Atwood, 1978; Tadros & Mayes, 1979; Weijnen, 1986). Significantly, the reduction in absolute growth rate, seen in both the present experiments and in previous work on the effects of added impurities (Liu & Nancollas, 1970; 1973a; Nancollas et al., 1973; Christoffersen et al., 1979; 1982; Van Rosmalen, 1981; Nielsen, 1986; Weijnen, 1986), does not effect the kinetic order of the growth reaction.

4.5.2 Comparison with pressure solution experiments

The growth kinetics data obtained in the present experiments will now be inserted into a theoretical model for precipitation controlled pressure solution creep, thus predicting creep rates which can directly be compared to the pressure solution creep data reported in Chapter 3. Two extreme types of precipitation controlled pressure solution creep models can be considered: one in which the rate of deformation is controlled by growth on the pore walls only (c.f. seeded growth), and one in which the deformation is rate limited by nucleation and growth of crystallites forming in suspension in the pore fluid. Although the results obtained for the present experiments indicate that for the larger grain sizes both growth and nucleation occur, no evidence was found for nucleation in the pressure solution experiments of Chapter 3. This is thought to be a reflection of the ratio of the surface area of the granular solid phase (A_s) to the volume of liquid (V_{liq}), which is very different for the two types of tests. The growth experiments yield a value for A_s/V_{liq} of ~0.7 - 3.6 m^{-1}, while in the pressure solution experiments A_s/V_{liq} ~150 - 800 m^{-1}. Thus much more surface was available in the pressure solution experiments than in the growth experiments, presumably leading to dominant growth rather than nucleation, as seen in the growth experiments using the largest grain sizes. On this basis, only the crystal growth data obtained for the 32 μm and 48 μm seed crystals will be used to predict pressure solution creep rates, assuming rate limitation by growth on pore walls (seeded growth).
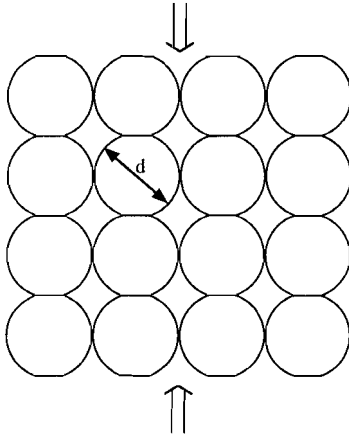
Figure 4.9. Idealized aggregate (simple cubic pack of spherical grains) undergoing uniaxial compaction.

For precipitation controlled grain boundary diffusional pressure solution creep, it follows from theory (e.g. Raj, 1982; Lehner, 1990) that all the driving force is used to drive the precipitation step, with the driving force for dissolution and diffusion being negligibly small. For simplicity, we shall here consider the case of uniaxial compaction by precipitation controlled pressure solution, in an idealized aggregate consisting of a simple cubic pack of spherical grains (see Fig. 4.9). In a granular aggregate of this type, deforming to small strains by pressure solution creep, the areas (per grain) of contact dissolution (A_d) and pore wall precipitation (A_p) can be written in the form

$$A_d = Z \cdot A_t \tag{4.6}$$

$$A_p = (1 - Z) \cdot A_t \tag{4.7}$$

where, A_t is the total surface area per grain, and Z is the ratio of grain contact area to total grain surface area. For a system in which there is negligible removal of dissolved solid via the pore fluid phase, it follows from the conservation of mass that

$$v_d \cdot A_d = v_p \cdot A_p \tag{4.8}$$

where v_d and v_p are the velocities of dissolution at grain contacts and precipitation on pore walls respectively (see Fig. 4.9). Assuming that strains are small (e.g.

<15%), the dissolution velocity at grain contacts is related to the pressure solution strain rate ($\dot{\varepsilon}$) normal to the contact by

$$v_d \approx \frac{\dot{\varepsilon}\, d}{2} \tag{4.9}$$

where d is grain size. Combining equations 4.6-4.9, the linear strain rate can thus be written

$$\dot{\varepsilon} = \frac{2v_p}{d} \cdot \frac{(1-Z)}{Z} \tag{4.10}$$

Now, from crystal growth theory, the velocity of precipitation can be expressed as a function of the driving force for precipitation, in the form

$$v_p = f(\Delta\mu) = k_a^{+} \cdot (\Delta\mu)^{n} \tag{4.11}$$

where, k_a^{+} is an apparent precipitation rate coefficient (T-dependent), and n is the order of the net precipitation reaction. By combining eq. 4.10 with eq. 4.11, the creep rate for a granular aggregate undergoing uniaxial compaction by grain boundary diffusional pressure solution creep with rate control by precipitation on the pore walls (c.f. seed crystals) is hence given

$$\dot{\varepsilon} = \frac{2k_a^{+}(\Delta\mu)^{n}}{d} \cdot \frac{(1-Z)}{Z} \tag{4.12}$$

For the prediction of creep rates by this mechanism, the precipitation rate data obtained in the ~32 μm and ~48 μm growth experiments will now be inserted into 4.12 as follows. In the pressure solution experiments of Chapter 3 only small strains were achieved (<15%) so that grain contact areas and the ratio $Z=A_d/A_t$ were small. On the basis of microstructural observations made on samples deformed by 8 - 10% (Chapter 3), a value of 0.1 is chosen as a representative value for Z. For a fixed value of strain, the driving force for pressure solution can now be approximated (Rutter, 1983; Lehner, 1990; Spiers & Brzesowsky, 1993; Paterson, 1995; Shimizu, 1995) using

$$\Delta\mu = (\sigma_n - P_f) \cdot \Omega_s \tag{4.13}$$

where, σ_n is the average normal stress transmitted across dissolving grain contacts

(refer Fig. 4.9), P_f is the pore fluid pressure, and Ω_s is the molar volume of the solid. With increasing strain at constant applied stress (σ_a), σ_n decreases, and thus the driving force $\Delta\mu$ decreases as well. For the chosen idealized pack and small strains, the effective normal stress (σ_n - P_f) is related to σ_a by the equation

$$\sigma_n - P_f = \frac{\sigma_a \cdot d^2}{Z \cdot A_t} \approx \frac{\sigma_a}{\pi Z} \qquad (4.14).$$

For strains of 8 - 10% and corresponding Z-value of 0.1, (σ_n - P_f) thus takes a value of ($10\sigma_a/\pi$). Inserting this into 4.13, for chosen stresses σ_a, the resulting values for $\Delta\mu$ can be used to obtain corresponding values of v_p from Fig. 4.7, which can in turn be inserted into eq. 4.10 to predict creep rates. Alternatively, creep rates can be predicted by directly inserting $\Delta\mu$ from 4.13 into eq. 4.12, together with the appropriate values for the apparent precipitation reaction rate constant (k_a^+) and the precipitation reaction order (n) obtained from Fig. 4.7.

In Figures 4.10 and 4.11, the predicted creep rates and experimentally obtained creep rates (Chapter 3) are plotted versus applied stress (σ_a) and grain size (d) respectively.
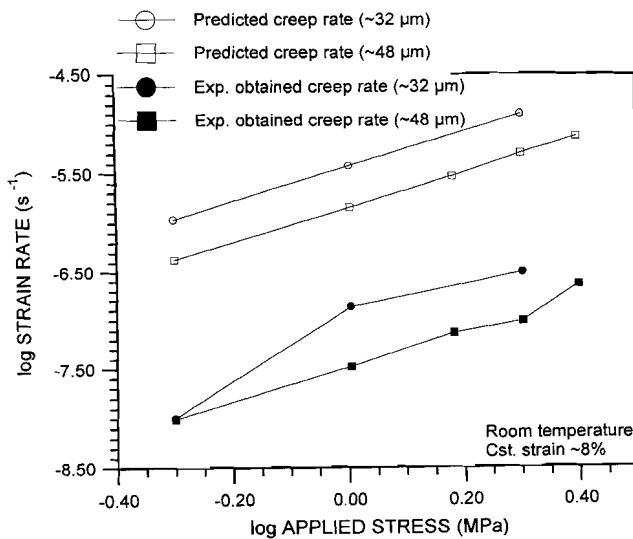
Figure 4.10. Log-log plot of compaction strain rate ($\dot{\varepsilon}$) versus applied stress (σ_a) showing experimentally obtained creep rates and creep rates predicted by inserting the present crystal growth data into a model for precipitation controlled pressure solution.
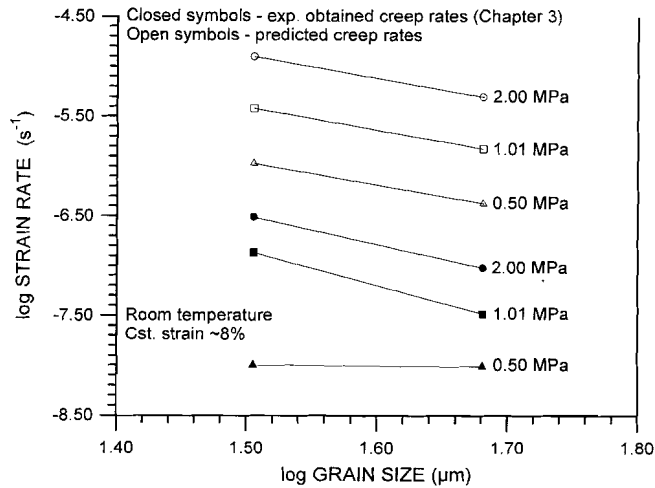
Figure 4.11. Log-log plot of compaction strain rate ($\dot{\varepsilon}$) versus grain size (d) showing experimentally obtained creep rates and creep rates predicted by inserting the present crystal growth data into a model for precipitation controlled pressure solution.

The dependence of creep rate on applied stress and grain size are found to be very similar. Both experimentally obtained and predicted creep rates show a roughly 2nd order dependence of creep rate on applied stress, and an inverse 2nd to 3rd order dependence on grain size. However, both figures show that the predicted creep rates are roughly 30 - 50 times faster than the experimentally obtained creep rates. In view of the approximation and uncertainties associated with the present rough model for pressure solution (e.g. in estimating Z), this is considered to be reasonably good agreement, confirming that pressure solution in the gypsum studied is precipitation controlled. However, the observed 1.5 order of magnitude difference in predicted and observed rates may have additional implications. One possibility is that the higher A_s/V_{liq} ratios characterizing the pressure solution experiments may lead to higher impurity content in solution in the compaction tests than in the growth experiments, and hence lower than predicted strain rates. Otherwise, the substantial difference in creep rates might be explained by the fact that in the pressure solution experiments the grains are under stress, contrary to the growth experiments where the grains (i.e.seeds) are stress free. This could conceivably effect the growth mechanisms. As already pointed out, gypsum grows by spiral

growth at steps produced by screw dislocations (2nd order rate equation) at relatively low supersaturations (S<40-80% - e.g. Van Rosmalen, 1981; Christoffersen et al., 1982; Weijnen, 1986), and probably by surface nucleation growth processes (>2nd order rate equation) at relatively high supersaturations (S>40-80%; - e.g. Packter, 1974; Christoffersen et al., 1982; Weijnen, 1986). However, the extent to which these growth mechanisms might be effected by stressing the solid grains is beyond speculation at present.

4.6 CONCLUSIONS

In this chapter, the growth of gypsum using seed crystals and solutions prepared from natural gypsum has been investigated in order i) to determine the kinetic order of the precipitation reaction, ii) to determine the absolute rates of crystal growth, iii) to determine the dependence of growth rate on the size of the seed crystals, iv) to predict pressure solution creep rates using the obtained growth rates, and v) to compare the predicted rates with the creep rates observed in the pressure solution experiments reported in Chapter 3. Due to spontaneous nucleation from the solution when using the large seed crystals (d>48μm, small specific surfaces), the calculated growth rates of the large seed crystals are erroneous. The remaining results (32, 48 μm seed crystals) demonstrate that at low driving forces (Δμ < 1 kJ/mole) precipitation follows second order reaction kinetics, while at higher driving forces (Δμ > 1 kJ/mole) the order of reaction is 3 - 4, which is in good agreement with previously performed studies. The dependence of growth rate on seed crystal size could only be obtained using the 32 and 48 μm seed-size fractions. Nonetheless, the data suggest a roughly inverse 1-2nd order dependence of seed crystal size on growth rate at low driving forces (Δμ < 1 kJ/mole) which is also reasonably consistent with previous data, and an inverse 2-3rd order dependence of seed crystal size on growth rate at higher driving forces (Δμ > 1 kJ/mole) However, the absolute rates of crystal growth are found to be one order of magnitude lower than those obtained in previous work, which can most likely be attributed to the impurity content of the natural gypsum used. The obtained growth rates were used to predict grain boundary diffusional pressure solution creep rates with rate limitation by growth on pore walls (seeded growth). The predicted creep rates were found two be roughly 30-50 times faster than the creep rates observed in the pressure solution experiments of Chapters 3. However, the predicted creep rates and experimentally obtained creep rates show a closely similar dependence of creep

rate on applied stress and grain size. It is therefore concluded that the pressure solution process is almost certainly controlled by the precipitation reaction, with the absolute rate discrepancies probably reflecting the different solid/fluid ratios characterizing the pressure solution and growth experiments.

CHAPTER 5

INFLUENCE OF PORE-FLUID SALINITY ON PRESSURE SOLUTION CREEP IN GYPSUM

5.1 INTRODUCTION

In the preceding chapters on the compaction creep behaviour of wet granular gypsum in hydrostatic loading (Chapter 2) and uniaxial compaction mode (chapter 3), it has been shown that grain boundary diffusional pressure solution is an important deformation mechanism in natural gypsum under laboratory conditions. On the basis of a comparison of the observed mechanical behaviour with pressure solution theory and crystal growth data, it has also been inferred that the gypsum precipitation reaction is most probably the rate limiting step in the pressure solution process (Chapters 2-4). However, while the dependence of deformation rate on applied stress and grain size was found to be broadly consistent with that expected for gypsum precipitation control, the absolute rate of pressure solution creep obtained in the deformation tests is a) 2 - 3 orders of magnitude slower than that expected on the basis of most crystal growth data for pure gypsum, and b) 30 - 50 times slower than expected from the crystal growth experiments of Chapter 4, performed using natural gypsum seed crystals and solution.

Now, from the crystal growth literature, it is well-known that dissolved organic material (undoubtedly present in the natural gypsum used) very strongly reduces the growth rate of gypsum (McCartney & Alexander, 1958; Smith & Alexander, 1970; Liu & Nancollas, 1973b; 1976; Barcelona & Atwood, 1978; Tadros & Mayes, 1979; Weijnen, 1986), whereas the presence of sodium- or potassium chloride in solution strongly increases the growth rate (Brandse et al., 1977; Kushnir, 1980) without changing the order of the reaction (Liu & Nancollas, 1970; 1973a; Nancollas et al., 1973; Christoffersen et al., 1979; 1982; Van Rosmalen, 1981; Nielsen 1986; Weijnen, 1986). Furthermore, most crystal growth experiments reported in the literature have been performed using analytical grade gypsum, often with sodium- or potassium chloride present in solution. It is therefore of interest to determine the influence of pore fluid salinity on pressure solution creep in gypsum, in order to assess how far such effects can account for the observed discrepancies

between pressure solution and crystal growth rates. Moreover, if the precipitation reaction does indeed control the rate of pressure solution creep in gypsum, as inferred so far, then the addition of sodium or potassium chloride to the pore fluid phase should lead to an increase in creep rate which parallels the effect of these salts upon the kinetics of the precipitation reaction. Data on the influence of pore fluid salinity on creep rate thus offers an additional test of the mechanism controlling the rate of pressure solution in gypsum. Lastly, besides providing important information regarding the rate limiting step, data on the effect of pore fluid salinity on pressure solution in gypsum are highly relevant to the behaviour of gypsum in geological situations, since gypsum is almost always associated with other evaporite minerals such as halite, with the result that pore fluid compositions will be generally be highly saline (Balkwill, 1978; Laubscher, 1981; Murrell, 1981; Mugnier & Vialon, 1986; Jordan, 1988; 1991; Jordan et al., 1990).

In view of the above points, this chapter reports uniaxial compaction creep experiments on wet granular gypsum, performed under conditions favouring pressure solution creep, and designed to systematically determine the effect of increasing NaCl concentration within the pore fluid phase. The tests were carried out on the same natural gypsum as that used in the uniaxial compaction experiments reported in Chapter 3, and at the same drained ("closed-system") conditions, i.e. at room temperature and at applied stresses nominally in the range 1 - 4 MPa, using grain size fractions ranging from ~50 to ~300 μm. The pore fluids used were saturated with respect to the individual gypsum fractions used, varying the NaCl concentration in the range 0.01 to 6.1M. The results show that while the mechanical behaviour and microstructures developed are very similar to those observed in experiments with no NaCl, addition of NaCl to the pore fluid produces a significant increase in creep rate, the systematics of which are closely consistent with rate limitation by the precipitation reaction step.

5.2 EXPERIMENTS

As indicated above, the present experiments consisted of uniaxial compaction creep tests, performed on wet granular gypsum aggregates at room temperature. The test were done in the presence of sodium chloride solutions, saturated with respect to the gypsum sample material. The experiments were carried out varying the applied stress (σ_a), sample grain size (d), and molarity (x) of the NaCl-bearing pore fluid (hence the solubility (C_o) of $CaSO_4$) independently, so that the dependence of

compaction creep behaviour on σ_a, d and x could be systematically investigated.

5.2.1 Method

The gypsum test materials and experimental method employed here were exactly the same as those used for the closed-system uniaxial compaction experiments on granular gypsum plus saturated solution reported in Chapter 3. The granular gypsum test material was prepared by crushing, sieving, washing and drying natural gypsum rock (95-98wt% pure $CaSO_4 \cdot 2H_2O$) from the Paris Basin (for details see section 3.3.1). Samples of this, with grain sizes of ~48 μm, ~74 μm, ~132 μm, ~160 μm, and ~282 μm, were tested using small scale, dead-weight capillary tube set-ups of the type illustrated in Fig. 5.1 (see also Section 3.3.2.1). Pore fluid solutions with molar NaCl concentrations of 0.01, 0.1, 1.0, 3.4 and 6.11M (saturated NaCl solution at room temperature) were prepared using analytical grade NaCl (Merck N° 6404), subsequently saturating the solution with respect to $CaSO_4$ using gypsum of the same grain size fraction as the sample under investigation.

In initiating individual experiments, a ~0.04g sample of the chosen grain size fraction was first placed into the apparatus and loaded dry using an applied stress (σ_a) of ~4 MPa for ~15 minutes. The resulting dry compaction was essentially time-independent with no measurable creep occurring thereafter. To eliminate any effects of the porosity attained at this stage, only samples with a porosity of 45.5 ± 1.5% after dry compaction were used for subsequent wet testing. This was carried out by first adjusting the applied stress to a value in the range $1.01 \leq \sigma_a \leq 4.05$ MPa, then flooding the sample with the desired pore fluid as indicated in Fig. 5.1 (caption). All experiments lasted for 5 days, and final wet strains up to 18% were achieved.

After terminating individual tests by removing the load, the pore fluid remaining in the sample was carefully flushed out by passing compressed air through the capillary tube apparatus plus sample. The sample was then carefully pushed out of the capillary tube, and vacuum-impregnated with blue-stained epoxy resin to allow sectioning and microstructural study.

Figure 5.1a-b. Semi-schematic diagram illustrating the uniaxial compaction apparatus used in the present experiments on wet granular gypsum with saline pore fluids. The compaction creep behaviour of the samples was monitored by measuring the change of length of the samples with the dial gauge. a) Total overview of set-up, and, b) sample assembly. Samples were flooded by drawing the solution phase from the reservoir into the sample using the evacuation tube located in the base.
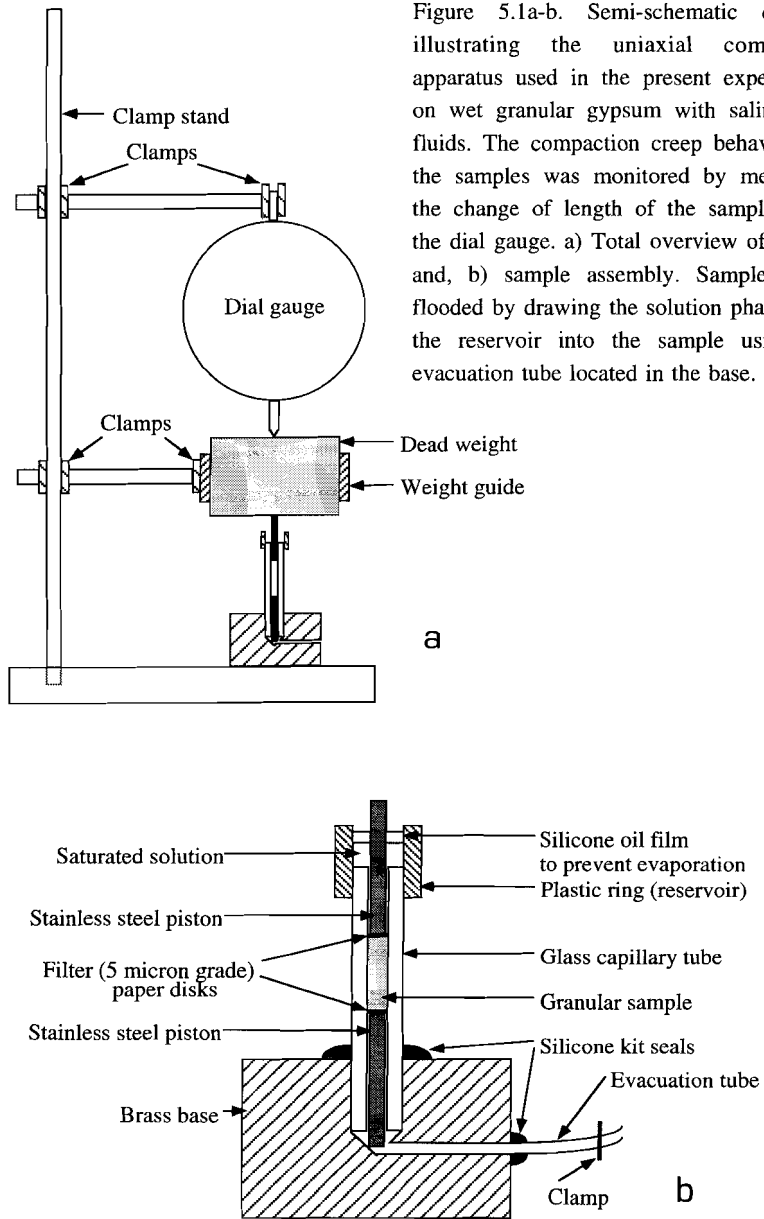
The complete set of experiments reported in this chapter is listed in Table 5.1 along with the corresponding experimental conditions and variables. For comparative purposes, the tests reported in Chapter 3 for similar conditions but without added NaCl, are also listed in Table 5.1. Note that most of the experiments were carried out at a wet creep stress of ~1.5 MPa, varying the pore fluid salinity and sample grain size independently. The effect of stress on creep behaviour was investigated using ~74 μm grain size material plus pore fluid with a 1M concentration of NaCl.

The capillary tube set-ups used allowed compaction strains (e_v) to be measured with a resolution of ~10^{-4}. Strain rates were calculated as a function of strain and time, using the three point central difference method. Conventional methods of analysis showed that the standard relative error in the compaction strain rate was less than 8% in all experiments.

Table 5.1

Experiment/ Sample N°	Grain size (μm)	Wet applied stress (MPa)	NaCl conc. (mole/l)	Starting porosity (%)	Final strain achieved (%)	Duration (days)
GY260C	~132	1.52	0	45.19	5.88	35
GY265C	~48	1.52	0	46.41	13.32	31
GY276C	~282	1.52	0	44.21	3.41	26
GY277C	~160	1.51	0	44.65	4.00	26
GY287C	~74	1.52	0	46.73	9.02	25
GY295C	~132	1.52	0.01	44.60	3.24	5
GY296C	~132	1.53	0.1	44.13	4.34	5
GY297C	~132	1.56	1.0	44.00	5.85	5
GY298C	~132	1.54	3.4	44.02	6.25	5
GY299C	~132	1.57	6.11	43.45	5.57	5
GY300C	~48	1.52	0.01	46.31	12.16	5
GY302C	~48	1.56	1.0	45.86	17.33	5
GY303C	~48	1.56	3.4	45.28	18.06	5
GY304C	~48	1.57	6.11	45.89	16.30	5

Experiment/ Sample N°	Grain size (μm)	Wet applied stress (MPa)	NaCl conc. (mole/l)	Starting porosity (%)	Final strain achieved (%)	Duration (days)
GY305C	~282	1.52	0.01	44.74	2.74	5
GY306C	~282	1.53	0.1	44.71	3.39	5
GY307C	~282	1.56	1.0	44.50	3.71	5
GY308C	~282	1.57	3.4	45.00	3.98	5
GY309C	~282	1.56	6.11	45.13	3.52	5
GY313C	~160	1.52	0.01	44.19	2.88	5
GY314C	~160	1.53	0.1	44.14	3.62	5
GY315C	~160	1.56	1.0	44.32	4.90	5
GY316C	~160	1.57	3.4	44.74	5.16	5
GY317C	~160	1.56	6.11	44.75	4.80	5
GY318C	~74	1.52	0.01	46.55	6.08	5
GY319C	~74	1.53	0.1	44.77	7.40	5
GY320C	~74	1.56	1.0	45.60	11.64	5
GY321C	~74	1.57	3.4	46.04	10.98	5
GY322C	~74	1.56	6.11	45.59	10.86	5
GY324C	~74	1.01	1.0	45.59	8.56	5
GY325C	~74	2.03	1.0	45.23	11.25	5
GY326C	~74	2.49	1.0	44.36	14.02	5
GY327C	~74	4.05	1.0	45.57	15.76	5

Table 5.1. Complete set of experiments reported on the effect of pore fluid salinity, along with corresponding experimental conditions and variables. All samples were compacted dry before wet testing at an applied stress (σ_a) of ~4.0 MPa producing a porosity at this stage of 45.5±1.5% (similar to the experiments of Chapter 3). The first five tests/samples listed were presented previously in Chapter 3. Note that all experiments/samples are uniquely identified by corresponding experimental conditions.

5.2.2 Mechanical data

As mentioned above, the initial dry-loading, to which all samples were subjected, resulted in a more or less instantaneous (time-independent) compaction of the samples. The solution-flooded samples, however, showed rapid on-going (time-dependent) creep when the fluid was added. In Figs. 5.2a-g, all of the wet compaction creep curves obtained are presented. From careful inspection of these figures it is clear that at constant stress (~1.5 MPa) and for any given grain size, compaction creep is promoted by increased concentrations of NaCl, at least up to concentrations of 3.4M. Higher concentrations (6.11M) seem to have a decreased effect. It is also apparent that compaction creep is promoted by increasing applied stress (σ_a - Fig. 5.2f) and by decreasing grain size (d - Fig. 5.2g), at constant NaCl concentration. Under all conditions, creep decelerates with increasing strain (e_v). The dependence of compaction creep rate on strain typically observed is illustrated in Figs, 5.3a-c for a range of stresses, grain sizes and pore fluid salinities; note the highly consistent slope of these data, with a value around 3. Using this kind of strain rate versus strain data, it is possible to depict how the creep rate of the wet samples, measured at constant strain, depends on applied stress (σ_a), grain size (d) and NaCl content (x) of the pore fluid (see also Chapters 2, 3). Representative results are shown in Figs. 5.4, 5.5a-b and 5.6a-b. Figure 5.4 shows that, for the conditions indicated, the compaction creep rate at constant strain is approximately proportional to σ_a raised to the power p≈2 (on average). In addition, at ~1.5 MPa applied stress, across the entire range of NaCl concentrations used (0M - 6.11M), the compaction creep rate can be viewed as approximately proportional to d to the power q=-3 to -4, with a tendency for the creep rate to become less sensitive to d (q → -1) in experiments using the largest grain sizes (Fig. 5.5a-b). Figure 5.6a-b shows the dependence of compaction creep rate on the NaCl content of the pore fluid. At the applied stress investigated (~1.5 MPa), it can be seen that across the entire range of grain size fractions used, the creep rate increases with increasing NaCl content of the pore fluid, at least up to 3.4M. At an NaCl concentration of 3.4M in the pore fluid, creep rates are increased by up to 50 times compared to experiments performed at similar conditions with NaCl-free pore fluids. Higher concentrations seem to have a decreased effect on creep rates.
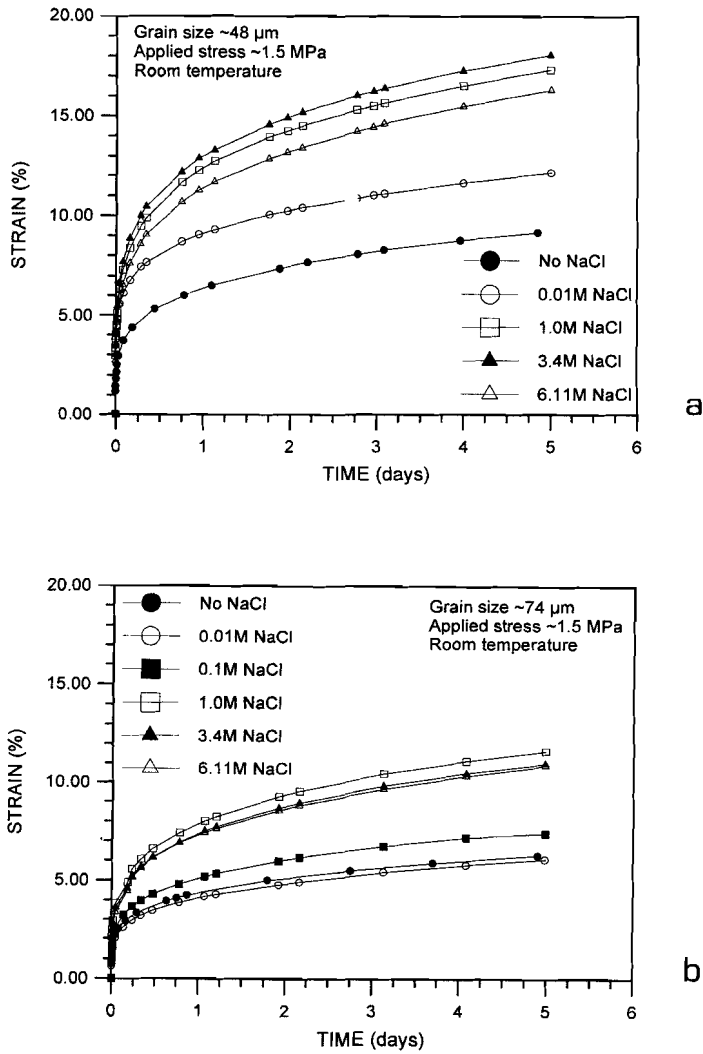
Figure 5.2a-g (this and nest two pages). The complete set of compaction creep curves obtained in the wet experiments on gypsum with saline pore fluids. Note the effect of increasing pore fluid salinity (x, Fig. a-e) for samples with grain sizes of respectively a) ~48 μm. b) ~74 μm, c) ~132 μm, d) ~160 μm, and e) ~282 μm. Also note the effects of increasing applied stress (σ_a, Fig. f) and decreasing grain size (d, Fig. g). Individual experiments are uniquely identified by the experimental conditions.

Grain size ~132 µm
Applied stress ~1.5 MPa
Room temperature

c

No NaCl
0.01M NaCl
0.1M NaCl
1.0M NaCl
3.4M NaCl
6.11M NaCl

No NaCl
0.01M NaCl
0.1M NaCl
1.0M NaCl
3.4M NaCl
6.11M NaCl

Grain size ~160 µm
Applied stress ~1.5 MPa
Room temperature

d

No NaCl
0.01M NaCl
0.1M NaCl
1.0M NaCl
3.4M NaCl
6.11M NaCl

Grain size ~282 µm
Applied stress ~1.5 MPa
Room temperature

e

STRAIN (%)

TIME (days)
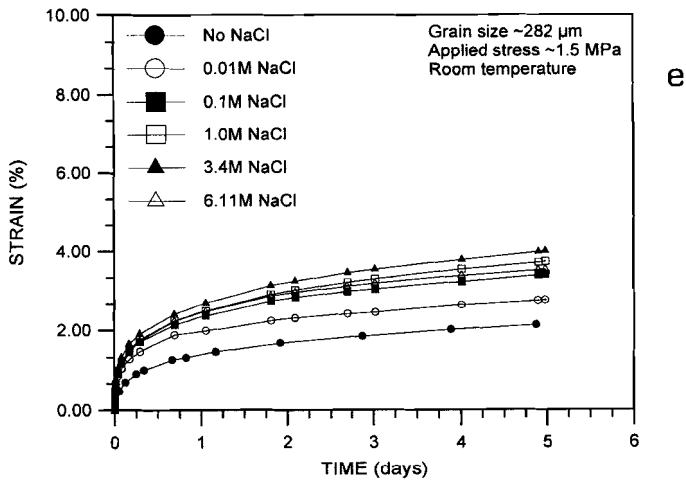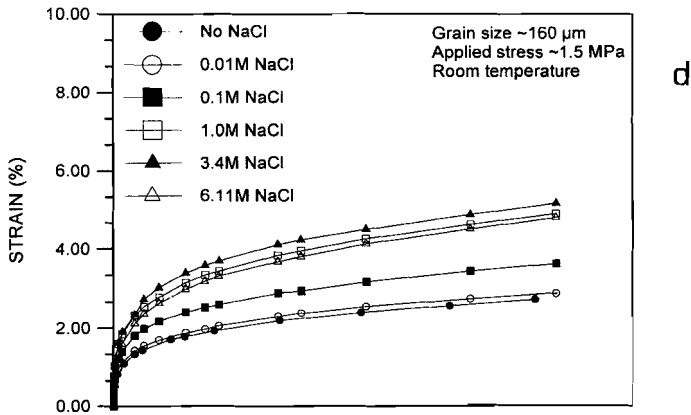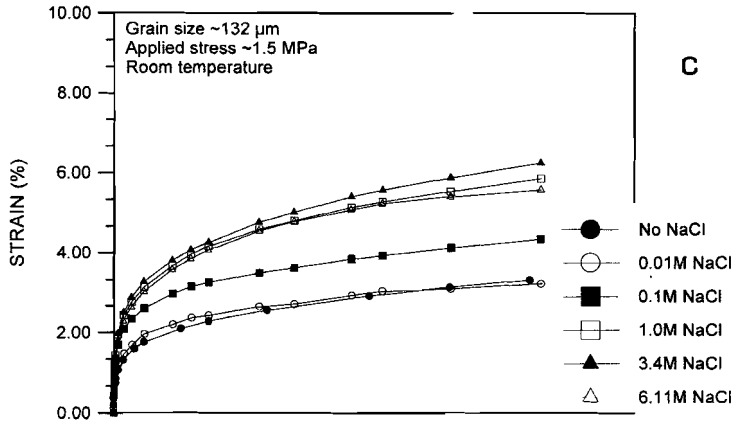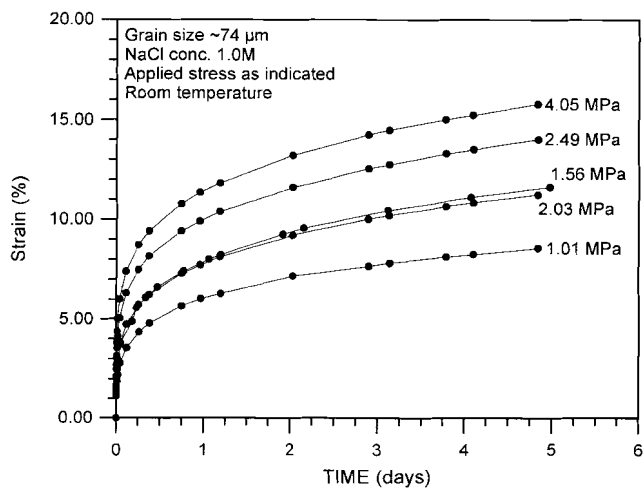
f
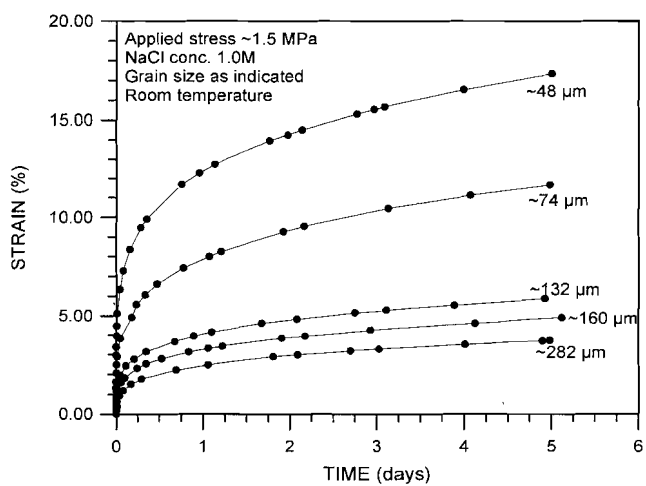
g
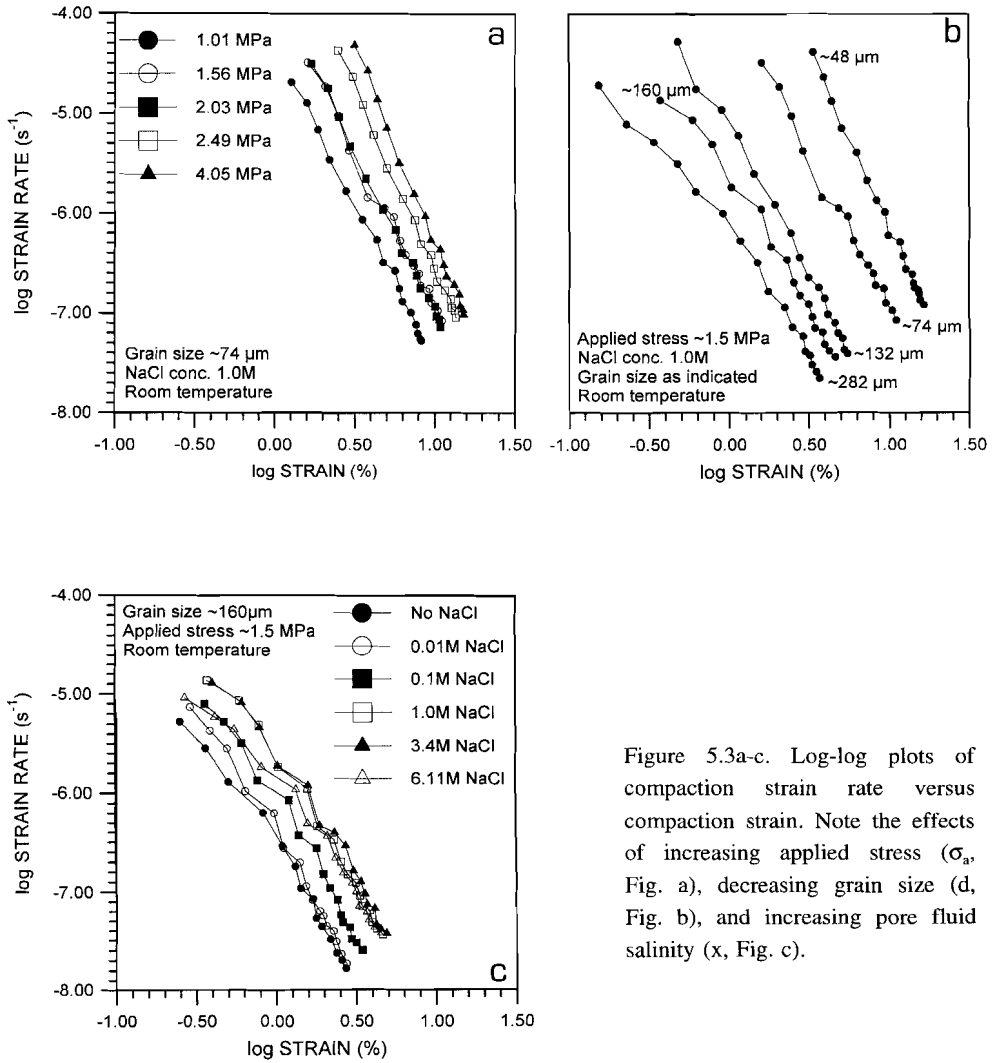
Figure 5.3a-c. Log-log plots of compaction strain rate versus compaction strain. Note the effects of increasing applied stress (σ_a, Fig. a), decreasing grain size (d, Fig. b), and increasing pore fluid salinity (x, Fig. c).
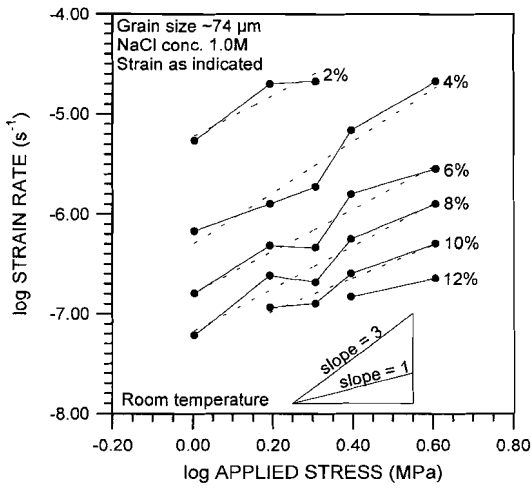
Figure 5.4. Log-log plot of compaction strain rate versus applied stress for a constant grain size (d) and constant NaCl concentration (x) in the pore fluid at different values of compaction strain (e_v, %).
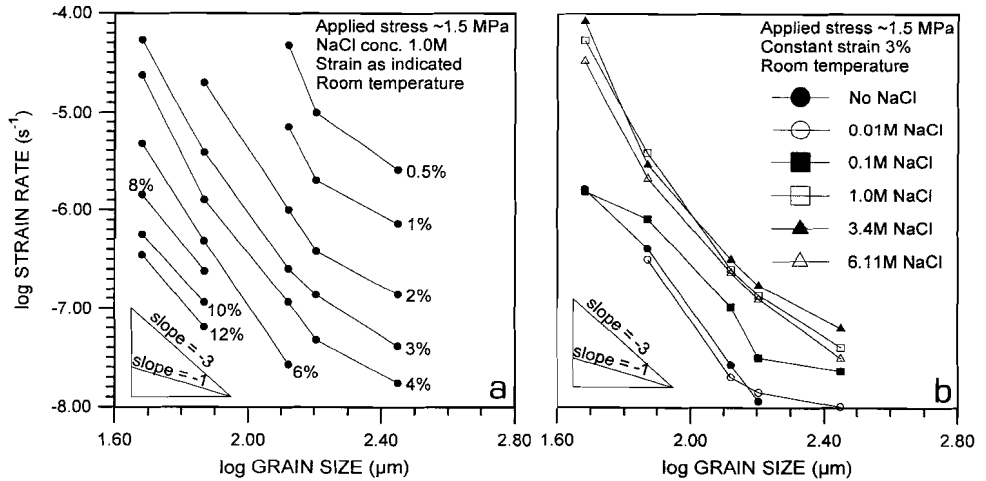
Figure 5.5a-b. Log-log plots illustrating the dependence of compaction strain rate on grain size for a) experiments with a constant NaCl concentration (x) in the pore fluid of 1.0M at different values of compaction strain (e_v, %), and b) a constant compaction strain of 3% and increasing concentrations of NaCl (x) in the pore fluid, both at a constant applied stress (σ_a) of ~1.5 MPa.
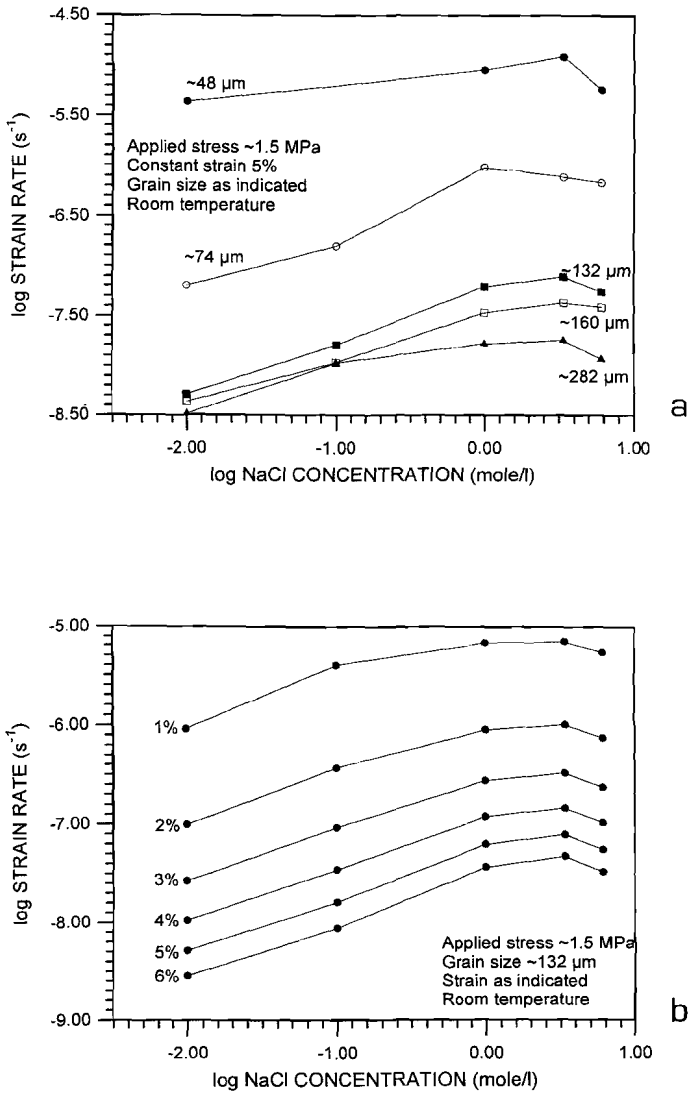
Figure 5.6a-b. Log-log plots of compaction strain rate versus NaCl concentration in the pore fluid for a) a compaction strain (e_v) of 5% at different grain sizes, and b) a single grain size (~132 µm) at different values of compaction strain (e_v, %), both at a constant applied stress (σ_a) of ~1.5 MPa.

5.2.3 Microstructural observations

Microstructural examination was carried out by means of optical microscopy performed on thin sections of the epoxy-impregnated samples. As the present experiments were performed with the same starting material, and following exactly the same dry compaction procedure as for the experiments reported in Chapter 3, no additional microstructural observations were carried out on dry-compacted samples. For an illustrated description of the microstructure of dry-compacted samples, the reader is referred to Section 3.3.2.3. In brief, these samples show a highly porous structure characterized by point contacts between grains, plastic grain bending and minor intra- and transgranular cleavage. The wet-compacted samples (Fig. 5.7a-c) show a marked decrease in porosity, many blunt grain-to-grain contacts, plus widespread evidence for grain-to-grain indentations, contact truncation, and euhedral overgrowths within the pores. The grain contacts are usually tight, showing little or no evidence of any contact undercutting or "corrosion" effects (Pharr & Ashby, 1983; Spiers & Brzesowsky, 1993). In comparison with dry-compacted samples, the wet-compacted samples show no visible increase in the amount of plastic deformation or microcracking. On the sample scale, however, a weak preferred orientation was observed in the wet tested samples, with the long axes of the gypsum particles tending to align themselves normal to the axial compression direction.

Fig. 5.7a
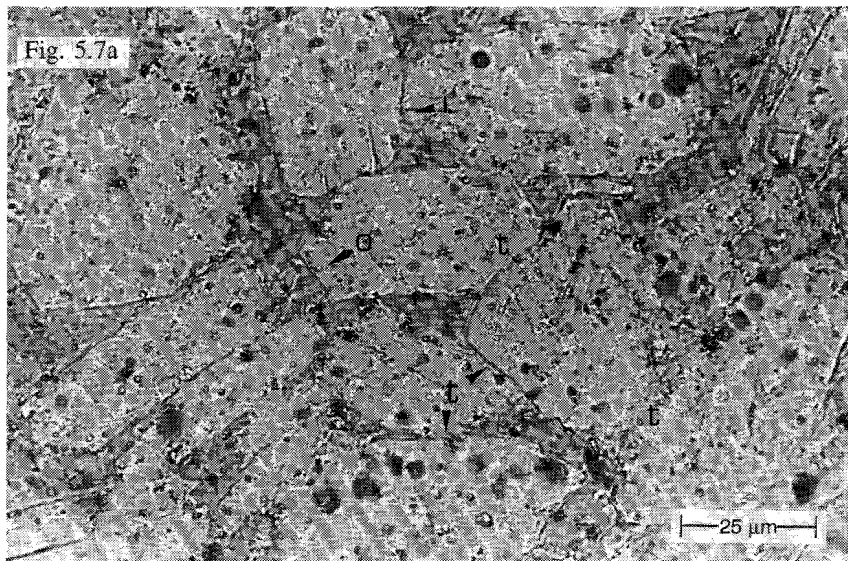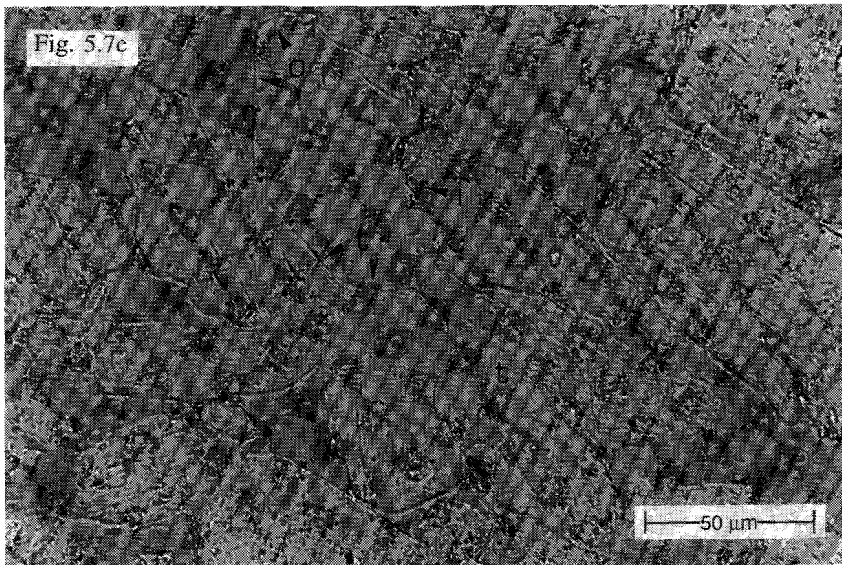
Figure 5.7. Optical microstructures exhibited by samples compacted in the presence of saline pore fluids. Note the blunt contacts, grain-to-grain indentations (i), contact truncation (t) and overgrowth features (o). a) Experiment/sample N° GY303C, b) experiment/sample N° GY317C and c) experiment/sample N° GY327C.

5.3 DISCUSSION

5.3.1 Comparison with NaCl-free experiments

The results obtained for the present compaction experiments with NaCl added to the pore fluid, show good agreement with the results of the otherwise identical NaCl-free experiments of Chapter 3, in terms of the trends seen in mechanical behaviour and the microstructures developed.

In the case of the NaCl-free experiments, the compaction creep rate could be viewed as approximately proportional to the applied stress (σ_a) raised to the power 2.5 (on average), while for the present experiments with added NaCl the compaction creep rate was found to be approximately proportional to σ_a squared (Fig. 5.4). In both sets of experiments, the compaction creep rate roughly proportional to the grain size (d) raised to the power -3 to -4, becoming less sensitive to d (power $\rightarrow$ -1) towards the larger grain sizes (d > 160 µm). However, the absolute creep rates obtained in the experiments with NaCl added to the pore fluid were up to 50 times faster than in the NaCl-free tests, as shown by Figs. 5.3c, 5.5b and 5.8. With regard to the microstructures characterizing the two types of compaction experiments, both showed the development of indentation, truncation, and overgrowth microstructures in the pores. Little or no evidence was found for contact corrosion or undercutting of the grains, or the development of an equilibrium pore configuration. Recalling that the growth rate of gypsum increases with nutrient salinity, with no change in the order of the growth reaction (Brandse et al., 1977; Kushnir, 1980), it thus seems likely that the present compaction experiments carried out in the presence of $CaSO_4$ saturated solutions, with added NaCl, involved the same deformation mechanism as the compaction experiments without added NaCl reported in Chapter 3. In other words, it seems likely that compaction in the present tests also occurred by grain boundary diffusional pressure solution creep (plus intergranular sliding) with the precipitation reaction as the process controlling the rate of deformation.
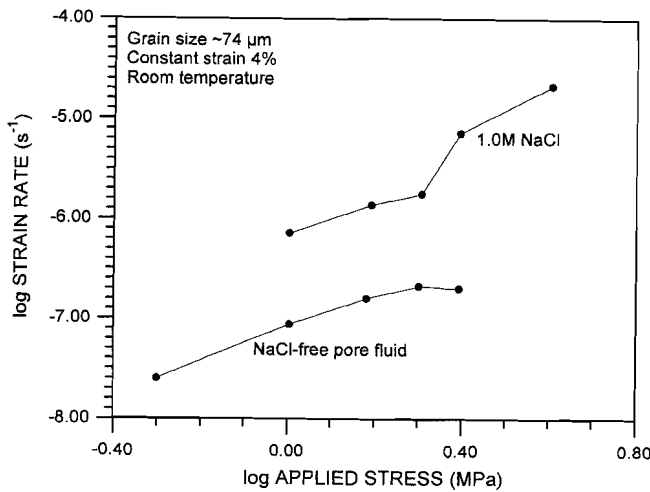
Figure 5.8. Log-log plot of compaction strain rate versus applied stress for samples with a grain size (d) of ~74 μm at a constant value of compaction strain (e_v=4%). Note the increase of compaction strain rate at constant applied stress observed in samples compacted in the presence of a saline pore fluid (1.0M NaCl) compared with samples compacted using NaCl-free pore fluid (Chapter 3).

5.3.2 Comparison with theory and crystal growth data

In order to gain deeper insight into the rate controlling mechanism of pressure solution in the present experiments, attention is now focused on a comparison of the results with models for pressure solution and with crystal growth data. Consider first the theoretical equations for grain boundary diffusional pressure solution. For the case of uniaxial compaction creep (rate $\dot{e}$), these are given

$$\dot{e} = B_x \cdot \frac{\sigma_e^n}{d^m} \cdot f_x(e_v) \qquad (5.1)$$

where the physical significance and/or values of x, n and m depend on whether the rate of pressure solution creep in controlled by the kinetics of dissolution within the grain boundaries (x=S), of grain boundary diffusion (x=D), or of precipitation on the pore walls (x=P), B_x are temperature-dependent rate coefficients, σ_e is the

applied effective stress, and the f_x's are mechanism specific geometric structure factors which decrease in magnitude with increasing strain (e_v) or with decreasing porosity. Now for the diffusion controlled case and present experimental configuration, this takes the form

$$\dot{\varepsilon} = \frac{A D C_o \delta \Omega_s \sigma_a}{R T d^3} \qquad\qquad (5.2)$$

where, A is a geometrical constant, D is the diffusivity of the solute in the intergranular solution phase, C_o is the solubility of the solid, δ is the effective grain boundary width, Ω_s is the molar volume of the solid, R is the gas constant, and T is absolute temperature. As already indicated in the introduction section, gypsum is more soluble in NaCl solutions than in pure water, and in Fig. 5.9 the solubility of gypsum as a function of the concentration of NaCl in solution is presented (after Shternina, 1960). Using the values for C_0 taken from Fig. 5.9 plus the experimental data on compaction strain rate versus NaCl content of the pore fluid (Fig. 5.6a), a plot of compaction strain rate versus C_0 can be constructed (Fig. 5.10). This shows that across the entire range of grain sizes investigated, the compaction creep rate is approximately proportional to C_o raised to the power 3, with a tendency for the power to become smaller at the largest grain size used (d $\approx$ 282 μm). If the rate of compaction by pressure solution creep was controlled by the diffusion step, the compaction creep rate would be linearly proportional to the solubility (see eq. 5.2), Fig. 5.10 clearly shows that this is not the case. Thus diffusion can be rejected as the rate controlling mechanism of pressure solution in the present experiments.

From the crystal growth literature, it is well known that the growth rate of gypsum for a given driving force is considerably increased in solutions containing alkali metal ions (Brandse et al., 1977; Kushnir, 1980). This is probably true also for the much faster dissolution reaction, so that this is unlikely to control rates of pressure solution. The increase in growth rate caused by salts in solution is explained by the existence of an excess negative charge on the crystal surface of gypsum (Kushnir, 1980). In the presence of for instance Na^+ ions, a significant number of SO_4^{2-} ions in solution will be complexed in the form of $NaSO_4^-$ ion pairs. Owing to its lower negative charge, the $NaSO_4^-$ ion is expected to be less repelled by the negative surface of the gypsum, that way making the sulphate more available to the surface, and thus increasing the growth rate (Brandse et al., 1977; Kushnir, 1980).
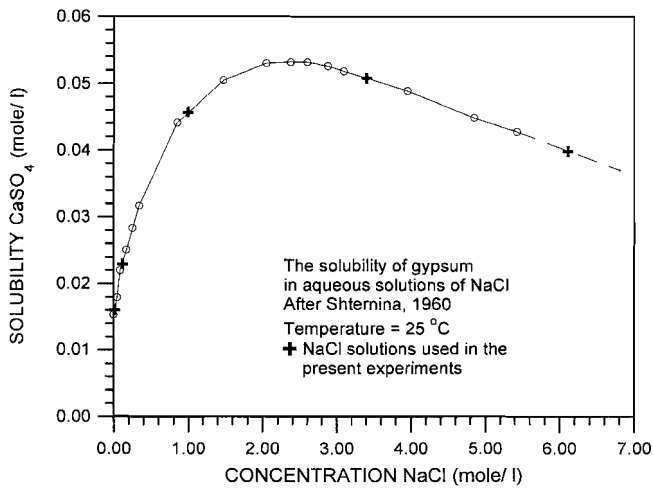
Figure 5.9. The solubility of gypsum in aqueous solutions as a function of the NaCl concentration of the solution, at 25°C (after Shternina, 1960).
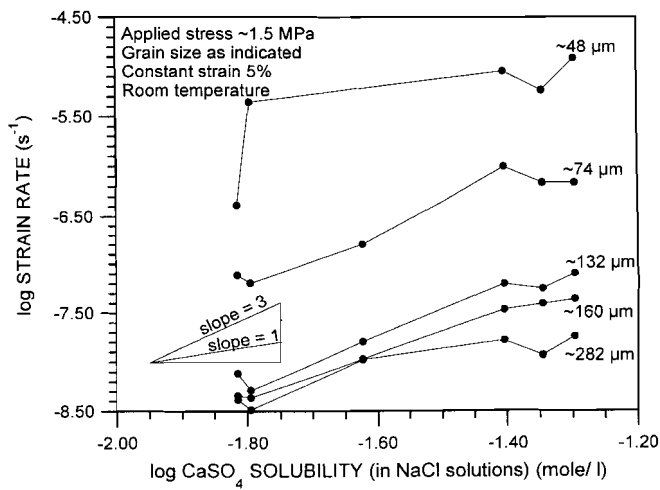
Figure 5.10. Log-log plot of compaction strain rate versus gypsum solubility (C_o) in NaCl solutions, for a fixed value of compaction strain (e_v=5%) at different grain sizes (d).

In Fig. 5.11, available data on the growth rate of gypsum are plotted versus driving force for seeded growth in NaCl-bearing and NaCl free solutions. The data of Brandse et al. (1977) are re-plotted in Fig. 5.12 to illustrate explicitly the dependence of growth rate on NaCl content at constant driving force.
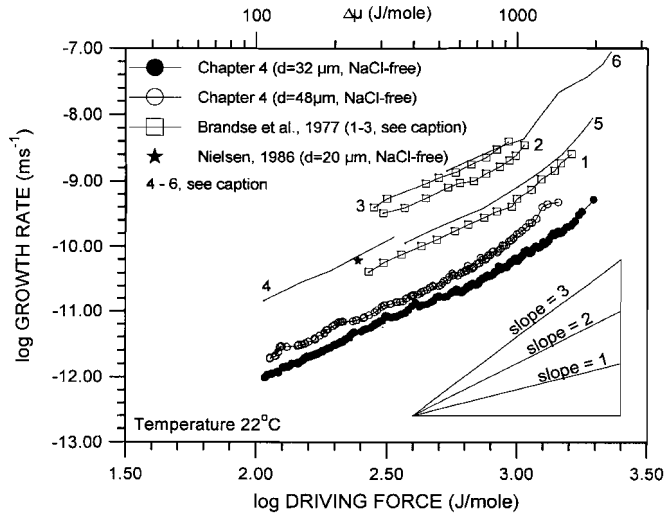
Figure 5.11. Log-log plot of growth rate (v_p) versus driving force ($\Delta\mu$) comparing the seed growth rate data obtained in Chapter 4 (using NaCl-free solutions) with growth rate data obtained by previous authors for experiments using both NaCl-free and NaCl-bearing solutions. Curves 1 - 3 are from Brandse et al. (1977) obtained for growth in solutions containing 0.0M, 0.5M and 1.0M NaCl respectively (grain size ~50 μm). Curve 4 is from Christoffersen at al. (1982) and Weijnen (1986) and was obtained for growth in NaCl-free solutions (grain size 10-200 μm). Curve 5 by Van Rosmalen et al. (1981) is for growth in NaCl-free solutions (grain size not specified), and curve 6 by Liu & Nancollas (1973) was obtained for growth in NaCl-bearing solutions (NaCl concentration and grain size not specified).
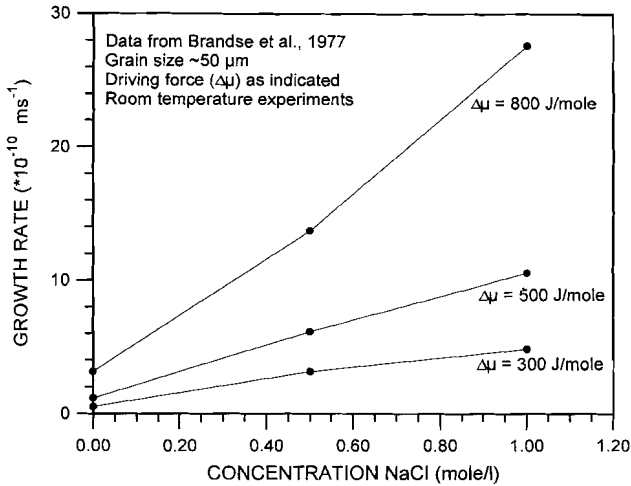
Figure 5.12. Growth rate versus concentration NaCl in solution at different values of driving force ($\Delta\mu$) for the results obtained by Brandse et al. (1977).

The above growth rate data are now used to predict creep rates for precipitation controlled pressure solution creep in the presence of NaCl-bearing pore fluid, which can be compared with the present experimental results. This is done using the equation for (seeded) growth controlled pressure solution creep derived in Chapter 4 assuming uniaxial compaction geometry, a simple cubic packing of spherical grains and small strains ($e_v \leq 15\%$) (c.f. equation 5.1 above). This is written (see Section 4.5.2)

$$\dot{\varepsilon} = \frac{2v_p}{d} \cdot \frac{(1-Z)}{Z} \tag{5.3}$$

or

$$\dot{\varepsilon} = \frac{2k_a^+(\Delta\mu)^n}{d} \cdot \frac{(1-Z)}{Z} \tag{5.4}$$

where, $\dot{\varepsilon}$ is the strain rate, v_p is the precipitation or growth velocity on pore walls, k_a^+ is the apparent precipitation reaction rate constant, $\Delta\mu$ is the driving force for precipitation, n is the order of the precipitation rate law, d is grain size, and Z is the

ratio of grain-to-grain contact area to total grain surface area $(Z=A_d/A_t)$. For precipitation control, the driving force for precipitation is approximated using

$$\Delta \mu = (\sigma_n - P_f) \cdot \Omega_s \tag{5.5}$$

where σ_n is the average normal stress transmitted across the dissolving grain contacts and P_f is the pore fluid pressure. With increasing strain (hence increasing Z) at constant applied effective stress (σ_a), σ_n decreases, and thus the driving force $\Delta \mu$ decreases as well. For the chosen idealized aggregate consisting of a simple cubic pack of spherical particles, the effective normal stress $(\sigma_n - P_f)$ is related to σ_a by the equation

$$\sigma_n - P_f \approx \frac{\sigma_a \cdot d^2}{Z \cdot A_t} \approx \frac{\sigma_a}{\pi Z} \tag{5.6}.$$

For a compaction strain of 8-10% and a corresponding value of ~0.1 for the ratio of contact area to total area (Z), $(\sigma_n - P_f)$ thus takes a value of $(10\sigma/\pi)$. Inserting this into 5.5, for chosen stress (σ_a) the resulting value for $\Delta \mu$ can be used to obtain corresponding values of v_p from Fig. 5.11, which can then be inserted into 5.3 to predict creep rates. Alternatively, creep rates can be predicted by directly inserting $\Delta \mu$ from 5.5 into eq. 5.4, together with the appropriate values for k_a^+ and the precipitation reaction order (n) obtained from Fig. 5.11.

In figures 5.13a-b, the predicted and experimentally obtained creep rates (present chapter) are plotted versus NaCl concentration (x) in the pore fluid and applied stress (σ_a) respectively. Figure 5.13a shows that the increase in compaction strain rate with increasing NaCl content of the pore fluid observed in the present experiments, is very similar to the increase in strain rate predicted using the data of Brandse et al. (1977) on growth of gypsum in saline solutions. Both the experimentally obtained creep rates and predicted creep rates show a roughly 10-20 times increase in compaction creep rate between experiments performed with NaCl-free pore fluids and experiments carried out in the presence of pore fluids containing 1.0M NaCl. Thus the effect of NaCl on ϵ is consistent with the accelerating effect of alkali ions such as sodium, potassium and lithium on the growth rate of gypsum (Brandse et al., 1977; Kushnir, 1980). Figure 5.13b demonstrates that both the experimentally obtained and creep rates predicted from crystal growth data show an approximately 2nd order dependence of creep rate on applied stress.
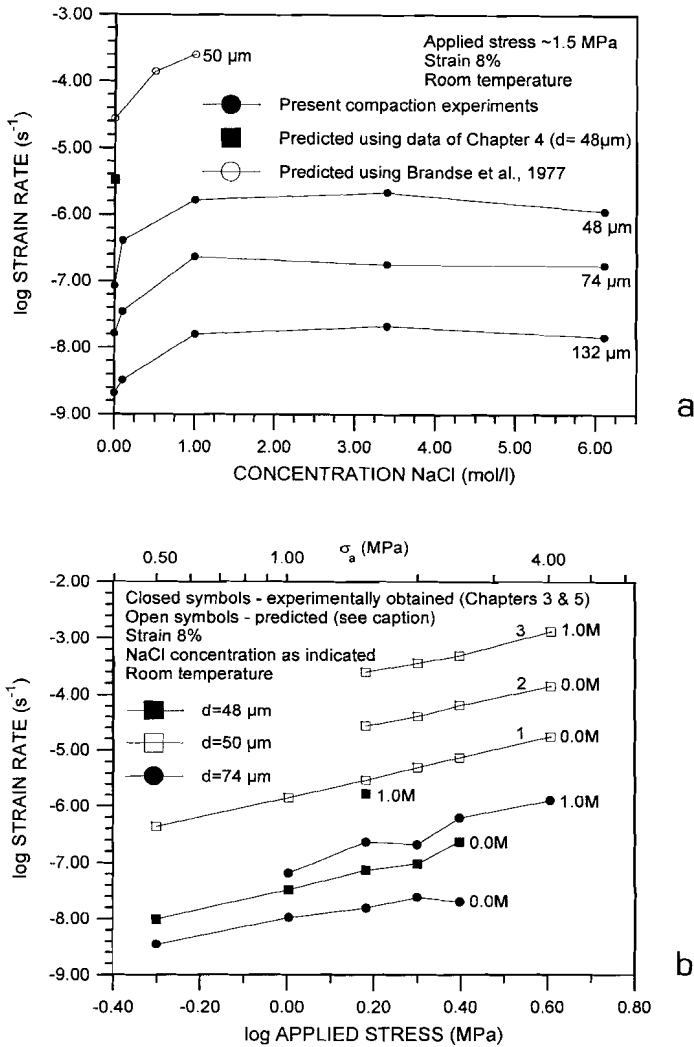
Figure 5.13a-b. Log-log plots of compaction strain rate versus concentration NaCl in the pore fluid (Fig. a) and versus applied stress (Fig. b) showing experimentally obtained creep rates (Chapter 3 and present chapter) and creep rates predicted by inserting the crystal growth data of Chapter 4 and the crystal growth data of Brandse et al. (1977) into a model for precipitation controlled pressure solution. Curve 1 is predicted using the crystal growth data of Chapter 4, and curves 2, 3 are predicted using the crystal growth data of Brandse et al. (1977) for growth experiments performed in solutions with 0.0 and 1.0 molar concentrations of NaCl respectively.

On this basis it is inferred that, both in the compaction tests with NaCl-free and NaCl-bearing pore fluids, pressure solution in the gypsum studied is precipitation controlled. However, figures 5.13a and b show that i) the creep rates predicted using the data of Chapter 4 are roughly 30-50 times faster than the experimentally obtained creep rates, and ii) the creep rates predicted using the crystal growth data of Brandse et al. (1977) are roughly 2-3 orders of magnitude faster. In Chapter 4 the decelerating effect of impurities on the growth rate of gypsum has been argued. In view of this, the above-mentioned discrepancies in creep rate may be due to compositional differences of the solid (i.e. gypsum grains used) and the solution phase (i.e. pore fluid used). Brandse et al. (1977) performed their growth tests with analytical reagents, whereas in the present compaction experiments both the solid and solution phases were prepared using natural gypsum (impurity content up to 5wt.%). Furthermore, the higher solid to fluid ratio (A_s/V_{liq}) employed in the pressure solution experiments, compared with the crystal growth experiments of Chapter 4, may lead to higher impurity content in solution in the compaction tests, and hence to lower than predicted strain rates.

5.3.3 Pressure solution creep in gypsum under natural conditions

As pointed out in the introduction, gypsum is associated with other evaporite minerals such as halite in most geological situations (balkwill, 1978; Laubscher, 1981; Murrell, 1981; Mugnier & Vialon, 1986; Jordan, 1988; 1991; Jordan et al., 1990). The result of this is that pore fluid compositions will be generally be highly saline. Therefore, a creep law based on the present experiments performed with highly saline pore fluids should apply to geological situations. Rough extrapolation of the data, for a solution containing 1M NaCl to a dense gypsum rock deforming at geological strain rates of 10^{-14} s^{-1} (average) or 10^{-10} s^{-1} (shear zone), predicts stresses in the range 0.01 to 1 MPa. Further attention to the importance of pressure solution creep in gypsum under natural conditions and to deriving a realistic flow law will be given in Chapter 7.

5.4 CONCLUSIONS

The compaction creep behaviour of granular gypsum, in the presence of sodium chloride-bearing pore fluids, has been investigated. The results yield mechanical behavioural trends consistent with those observed in experiments in which no NaCl was added to the saturated calcium sulphate solution pore fluid phase (Chapter 3). In addition, microstructural features such as indentations, truncation, and overgrowths microstructures are present in all samples and are similar to the microstructures observed in samples compacted in NaCl free-pore fluid. These findings suggest that the samples compacted in the presence of NaCl-bearing fluids deformed by the same mechanism inferred for the NaCl-free experiments, i.e. grain boundary diffusional pressure solution creep with rate limitation by the precipitation reaction. The observed compaction creep rates, however, are up to 50 times faster than for compaction with NaCl-free pore fluids. This is nonetheless consistent with the effect of NaCl concentration on growth rate reported in the literature, where it is well-established that alkali ions such as sodium, potassium and lithium increase the growth rate of gypsum by one to two orders of magnitude (Brandse et al., 1977; Kushnir, 1980). Accordingly it is concluded that pressure solution in laboratory experiments on gypsum is indeed precipitation controlled, under both saline and non-saline conditions. In geological environments, gypsum is almost always associated with occurrences of halite. Therefore, the results of the present experiments on NaCl-bearing systems are highly relevant to natural conditions.

CHAPTER 6

DENSIFICATION BEHAVIOUR OF FGD-GYPSUM
AT RAPID LOADING RATES

6.1 INTRODUCTION

The preceding chapters have focused on the determination of the rate
controlling process and kinetics of pressure solution creep in polycrystalline gypsum
aggregates. The experiments performed to this end mostly consisted of uniaxial
compaction creep tests, accessing strain rates as low as 10^{-9} s^{-1}. The results obtained
are relevant to understanding both the long term creep behaviour of gypsum rock
under geological conditions and the slow creep behaviour of (wet) gypsum building
materials. In contrast, this chapter presents an investigation into the densification
behaviour and mechanisms of densification operative during uniaxial compaction of
granular gypsum at very rapid loading rates, i.e. during essentially "instantaneous"
compaction, under both dry and wet conditions. In this case, the results are relevant
to the <u>fabrication</u> of new gypsum building materials.

For many years, gypsum products have been widely used in non-load-bearing
applications in the building industry. Examples include plaster, plasterboard, and
gypsum building blocks used in non-load-bearing interior walls, all of which are
manufactured in vast quantities in the developed world. These traditional gypsum
materials are produced by the hydration of calcium sulphate dihydrate, obtained by
calcination of natural gypsum rock, and typically exhibit ~65% porosity. Their high
porosity leads to relatively low strength (Karni & Karni, 1995), low creep resistance
and considerable sensitivity to moisture, and makes them unsuitable for use in load-
bearing structural applications. However, building materials researchers have
recently begun to investigate the possibility of producing low porosity gypsum
products, with high strength, by mechanically densifying gypsum powders derived
from flue gas desulphurization (FGD) facilities operating at coal burning power
stations and other industrial plants (Stoop et al., 1995). The proposed method
possesses the advantages that FGD-gypsum is available in large quantities as a
waste product or secondary raw material, and that the energetically inefficient

process of calcining gypsum to hemihydrate is avoided. The densified FGD-gypsum products are expected to show higher strength and improved resistance to creep, perhaps enabling them to be used in load-bearing building applications.

At present, there is almost no microphysically based understanding of the time-independent or instantaneous densification of granular gypsum, that is of the mechanisms leading to rapid densification. In particular, the effects of water, salt impurity content, loading rate, temperature and very high stresses on the preparation of gypsum building materials by mechanical compaction are largely unknown, as are the effects of the process variables on the properties of the final product (Stoop et al., 1995). Materials-science-based investigations of the densification behaviour of gypsum aggregates at high loading rates, and of the properties of the products, thus have an essential role to play in assessing/optimizing the potential of pressed FGD-gypsum for load-bearing applications within the building industry. As discussed in preceding chapters, the few experimental data which are available for gypsum demonstrate that polycrystalline material can deform by crystal plastic mechanisms (e.g. Heard & Rubey, 1966; Baumann, 1984; Williams, 1988) and by pressure solution creep. Taking these findings into account, and bearing in mind the solubility of the material, dislocation glide and/or creep, fluid-assisted recrystallization, pressure solution creep, stress-corrosion-cracking mechanisms, and time-independent cataclastic processes can all be expected to occur in gypsum under conditions relevant to the pressing and performance of FGD-gypsum building materials.

The aims of the work reported in the present chapter were to elucidate the principal densification mechanisms operating in granular gypsum during high-speed uniaxial compaction, and to determine the most favourable conditions for densification (i.e. those which produce the densest samples, as dense samples are expected to show the highest strength and resistance to creep). With these aims in mind, the mechanical behaviour and microstructural development were investigated by means of uniaxial densification experiments performed under conditions of varying applied stress, temperature, water content, salt impurity content, and loading rate. The results show that dislocation glide/creep mechanisms, fluid-assisted recrystallization, and time-(in)dependent cataclastic processes are all active during densification, and that high densities can be obtained under relatively easily accessible conditions.

6.2 EXPERIMENTAL PROCEDURE

The experiments consisted of a series of densification tests performed on Flue Gas Desulphurization gypsum (FGD-gypsum) using an Instron-1362 materials testing machine plus a pair of one-dimensional (1-D) compaction dies. The experiments were carried-out at applied stresses (σ_a) in the range 25-530 MPa, temperatures (T) of 20-150°C, water contents of ~0-5wt.%, salt impurity contents of the fluid phase in molar concentrations in the range 0-1.0M, and loading rates in the range 10^4-10^7 Pa s^{-1}. The complete set of experiments reported in this chapter is listed in Table 6.1, along with the corresponding conditions and variables.

6.2.1. Starting material

The gypsum used in the present experiments, was produced as a by-product of the Babcock-Kawasaki flue gas desulphurization process used at coal-burning power plants. The material was kindly provided by the gypsum building materials company Gyproc Benelux N.V. Thermo-gravimetric analysis (TGA) and inductivily-coupled-plasma atomic absorption spectrometry (ICPAAS) of the FGD-gypsum show that it is at least 95wt.% pure $CaSO_4 \cdot 2H_2O$ (see Table 6.2). The particle size distribution of the FGD-gypsum was determined optically, and using a Malvern particle sizer yielding similar results. The grain size was found to be more or less normally distributed, with a median size of ~48 μm (Table 6.2 and Fig. 6.1a-b). The shape of the grains is euhedral to subrounded and many elongated grains are present (~25vol.%) with aspect ratios of up to 5.

Table 6.1. Complete set of experiments reported. The Experiments/samples N° GY...B were performed using the ~22 mm diameter room temperature compaction die. Experiments/samples N° GY...D were performed in the ~15 mm diameter compaction die which could be operated at temperatures above ambient. All tests were performed under drained conditions.

Experiment/ Sample N°	Applied stress (MPa)	Water content (wt.%)	Temperature (°C)	Loading rate (MPa s^{-1})	Starting porosity (%)	Weight loss (% of original total weight)	Final porosity (%)
GY048B	27.5	0	room	1.3	43.75	0	27.44
GY049B	27.2	0	room	1.3	45.10	0	29.68
GY050B	53.9	0	room	1.3	44.95	0	23.71
GY051B	80.2	0	room	1.3	44.81	0	19.94
GY052B	106.9	0	room	1.3	44.99	0	17.83
GY053B	133.2	0	room	1.3	45.03	0	16.04
GY054B	160.0	0	room	1.3	44.95	0	14.91
GY055B	186.2	0	room	1.3	44.85	0	13.58
GY056B	212.9	0	room	1.3	44.63	0	12.83
GY057B	239.4	0	room	1.3	45.17	0	12.22
GY058B	252.7	0	room	1.3	45.44	0	11.60
GY071B	27.0	5.0	room	1.3	46.91	0	22.75
GY072B	26.9	5.0	room	1.3	47.86	0	23.94
GY073B	53.1	5.0	room	1.3	47.86	0	17.29
GY074B	80.3	5.0	room	1.3	44.98	0	12.53

Experiment/ Sample N°	Applied stress (MPa)	Water content (wt.%)	Temperature (°C)	Loading rate (MPa s⁻¹)	Starting porosity (%)	Weight loss (% of original total weight)	Final porosity (%)
GY075B	106.6	5.0	room	1.3	44.82	0	10.01
GY076B	133.4	5.0	room	1.3	46.67	0	9.21
GY077B	159.7	5.0	room	1.3	46.77	0	8.54
GY078B	186.2	5.0	room	1.3	47.30	0	7.69
GY079B	212.8	5.0	room	1.3	48.32	0	7.18
GY080B	239.2	5.0	room	1.3	48.09	0	7.02
GY081B	252.7	5.0	room	1.3	45.91	0	6.14
GY098B	252.7	3.0	room	1.3	45.83	0	5.43
GY099B	239.8	3.0	room	1.3	45.57	0	5.96
GY100B	212.8	3.0	room	1.3	46.45	0	6.48
GY101B	186.4	3.0	room	1.3	45.33	0	7.01
GY102B	159.7	3.0	room	1.3	45.45	0	7.35
GY103B	133.6	3.0	room	1.3	46.12	0	8.87
GY104B	106.6	3.0	room	1.3	45.25	0	10.18
GY105B	80.2	3.0	room	1.3	45.38	0	12.68
GY106B	53.6	3.0	room	1.3	45.24	0	15.48
GY107B	27.1	3.0	room	1.3	45.86	0	23.13

Experiment/ Sample N°	Applied stress (MPa)	Water content (wt.%)	Temperature (°C)	Loading rate (MPa s^{-1})	Starting porosity (%)	Weight loss (% of original total weight)	Final porosity (%)
GY111B	252.6	1.0	room	1.3	44.27	0	5.21
GY112B	252.7	0.5	room	1.3	44.24	0	6.97
GY115B	252.9	1.5	room	1.3	43.58	0	4.92
GY116B	252.7	2.0	room	1.3	45.27	0	4.80
GY117B	133.2	2.0	room	1.3	45.27	0	8.49
GY118B	253.0	2.5	room	1.3	45.60	0	4.64
GY119B	27.3	2.0	room	1.3	46.04	0	22.36
GY120B	133.2	2.5	room	1.3	45.06	0	8.86
GY121B	133.5	1.5	room	1.3	45.36	0	8.88
GY122B	27.2	2.5	room	1.3	45.55	0	21.94
GY123B	133.2	1.0	room	1.3	45.66	0	9.98
GY124B	27.0	1.0	room	1.3	45.10	0	23.63
GY125B	27.1	1.5	room	1.3	45.43	0	22.84
GY126B	133.1	0.5	room	1.3	44.91	0	11.78
GY127B	27.0	0.5	room	1.3	44.94	0	26.11
GY128B	252.9	2.5 + 0.001M CaCl$_2$	room	1.3	46.61	0	4.77

Experiment/ Sample N°	Applied stress (MPa)	Water content (wt.%)	Temperature (°C)	Loading rate (MPa s^{-1})	Starting porosity (%)	Weight loss (% of original total weight)	Final porosity (%)
GY129B	252.8	2.5 + 0.01M CaCl$_2$	room	1.3	45.91	0	4.83
GY130B	252.9	2.5 + 0.002M CaCl$_2$	room	1.3	46.02	0	4.99
GY131B	252.9	2.5 + 0.1M CaCl$_2$	room	1.3	46.14	0	4.49
GY132B	253.0	2.5 + 1.0M CaCl$_2$	room	1.3	45.65	0	4.81
GY133B	252.8	OIL	room	1.3	46.96	0	10.28
GY134B	252.8	2.5	room	0.13	45.82	0	6.11
GY135B	252.1	2.5	room	6.6	45.69	0	4.12
GY136B	252.7	2.5	room	0.013	45.96	0	6.60
GY137B	252.7	2.5 + 0.001M Na$_2$SO$_4$	room	1.3	45.64	0	4.79
GY138B	252.9	2.5 + 0.002M Na$_2$SO$_4$	room	1.3	45.98	0	4.92
GY139B	252.7	2.5 + 0.01M Na$_2$SO$_4$	room	1.3	45.69	0	5.07
GY140B	252.8	2.5 + 0.1M Na$_2$SO$_4$	room	1.3	46.06	0	5.00

Experiment/ Sample N°	Applied stress (MPa)	Water content (wt.%)	Temperature (°C)	Loading rate (MPa s⁻¹)	Starting porosity (%)	Weight loss (% of original total weight)	Final porosity (%)
GY141B	253.0	2.5 + 1.0M Na$_2$SO$_4$	room	1.3	45.56	0	4.71
GY152D	56.7	0	26	2.8	44.36	0	25.10
GY153D	56.6	0	40	2.8	42.77	0	24.89
GY154D	57.0	0	50	2.8	41.11	0	24.64
GY155D	56.3	0	60	2.8	44.34	0	24.86
GY156D	56.5	0	70	2.8	43.79	0	24.45
GY157D	56.8	0	80	2.8	44.47	0	24.01
GY158D	56.3	0	90	2.8	42.66	0	23.70
GY159D	56.7	0	100	2.8	42.57	0	22.89
GY160D	56.7	0	110	2.8	41.85	0.89	21.96
GY161D	56.4	0	120	2.8	43.92	3.47	20.35
GY162D	56.4	0	130	2.8	43.56	13.59	31.40
GY163D	56.7	0	140	2.8	43.09	15.24	36.21
GY164D	56.8	0	150	2.8	41.74	15.34	38.28
GY170D	278.4	0	24	2.8	44.15	0	11.97
GY171D	279.2	0	40	2.8	45.10	0	12.27
GY173D	279.1	0	60	2.8	44.65	0	11.64

Experiment/ Sample N°	Applied stress (MPa)	Water content (wt.%)	Temperature (°C)	Loading rate (MPa s^{-1})	Starting porosity (%)	Weight loss (% of original total weight)	Final porosity (%)
GY174D	279.0	0	50	2.8	42.15	0	12.01
GY175D	278.5	0	70	2.8	44.79	0	11.29
GY177D	278.3	0	80	2.8	44.60	0	10.24
GY178D	278.2	0	90	2.8	43.29	0	8.50
GY179D	278.9	0	100	2.8	44.26	0	5.77
GY180D	278.2	0	110	2.8	43.18	1.81	3.51
GY181D	278.8	0	120	2.8	44.82	8.90	5.07
GY182D	278.8	0	130	2.8	44.04	15.19	9.11
GY183D	278.8	0	140	2.8	42.84	14.73	5.56
GY185D	279.0	0	150	2.8	44.84	15.16	25.98
GY209D	528.4	0	room	2.8	44.33	0	8.52
GY210D	528.0	0	room	2.8	44.02	0	8.36
GY211D	528.4	0	room	2.8	45.24	0	7.80
GY212D	56.5	0	room	2.8	44.99	0	25.74
GY213D	140.0	0	room	2.8	45.19	0	18.03
GY214D	278.8	0	room	2.8	44.56	0	13.06
GY241D	529.3	2.5	50	2.8	44.90	0	3.56

Experiment/ Sample N°	Applied stress (MPa)	Water content (wt.%)	Temperature (°C)	Loading rate (MPa s⁻¹)	Starting porosity (%)	Weight loss (% of original total weight)	Final porosity (%)
GY242D	528.3	2.5	60	2.8	45.21	0	3.79
GY243D	528.5	2.5	40	2.8	45.56	0	3.84
GY244D	528.7	2.5	70	2.8	45.13	0	3.38
GY245D	529.5	2.5	80	2.8	43.96	0	3.27
GY246D	529.1	2.5	90	2.8	44.26	0	2.78
GY247D	528.3	2.5	100	2.8	44.88	0	2.14
GY248D	528.8	2.5	110	2.8	45.71	0	1.73
GY250D	528.8	2.5	130	2.8	47.22	11.12	20.07
GY251D	529.0	2.5	120	2.8	45.97	1.34	2.41

Table 6.2. Grain size analyses (Malvern Particle Sizer), Thermo-gravimetric analyses (TGA) and chemical analyses (ICPAAS) of the FGD-gypsum starting material (7 samples taken from 50 kg batch). D10, D50 and D90 are respectively the 10th, 50th (median) and 90th percentile. The gypsum content was calculated using the TGA data.

[1] The ICPAAS equipment was not calibrated for high CaO content, therefore these values are unreliable.

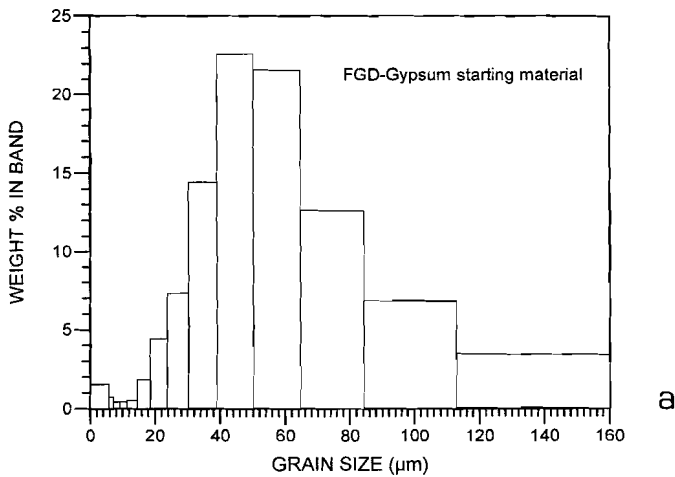|	
Median grain size (D50) (particle sizer)	43 - 48 µm
D90 (particle sizer)	81 - 89 µm
D10 (particle sizer)	21 - 23 µm
SO_3 content (ICPAAS)	45.53 - 47.70 wt.%
CaO content (ICPAAS)	37.25 - 42.36 wt.%[1]
Free water (TGA)	< 0.05 wt.%
Bound water (TGA)	19.9 - 20.6 wt.%
$CaSO_4 \cdot 2H_2O$	95.2 - 98.5 wt.%

Figure. 6.1. Grain size distribution of the FGD-gypsum starting material measured using a Malvern particle sizer. The median grain size of the starting material is ~48 µm (Fig. b, next page).
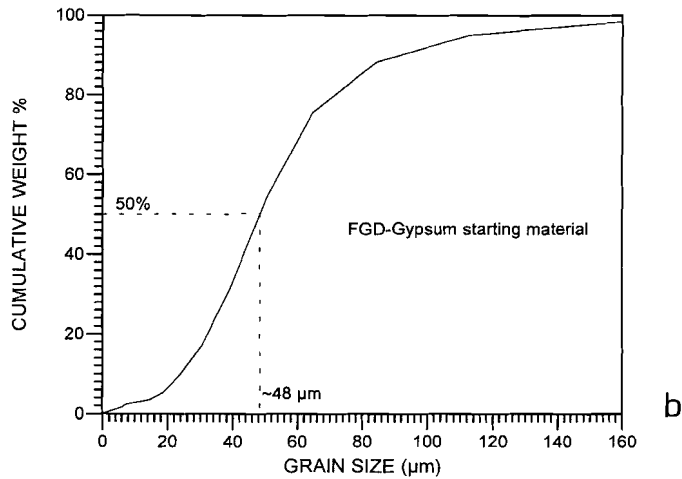
6.2.2 Sample preparation

Dry experiments were conducted on FGD-gypsum as received (free water content <0.05wt.%). In such tests, a fixed mass of gypsum powder, ~4.4 g or ~2.1 g depending on the diameter of the compaction die used, was simply funnelled into the pre-lubricated compaction die.The two different sample masses used yielded a fixed initial sample aspect ratio of ~1.5 : 1.

Wet samples were prepared in two ways depending on the water content required. For samples containing 3.0-5.0wt.% H_2O, a fixed amount of dry FGD-gypsum powder (~4.4 g) was funnelled into the pre-lubricated compaction die. The equivalent of 3.0 or 5.0wt% water (~130 μl or ~220 μl) was then added to the powder, using a high precision pipette with an accuracy of 1 μl. After addition of the water, a period of 10 minutes was allowed to pass before testing, in order to obtain a homogeneous distribution of the water throughout the sample. The compaction die was sealed with plastic foil (parafilm) during this period to prevent evaporation.

Wet samples containing 0.5-2.5wt.% H_2O were prepared outside the compaction die. Gypsum powder (~2.1 or ~4.4 g) was funnelled into an 8 ml plastic container of known weight. The container plus gypsum powder were then weighed using a Mettler H10W analytical balance (accuracy 0.1 mg) and ~5wt.% water was added. The container was then placed in an ultrasonic bath for 10 minutes to obtain a homogeneous distribution of the water throughout the sample. Water was then

allowed to evaporate from the sample, by exposing it to air at room temperature, until the desired weight was reached. During this evaporation period, the samples were occasionally shaken manually in order to try to maintain a homogeneous distribution of the water. Finally, the gypsum powder plus the desired amount of water were funnelled into the pre-lubricated compaction die.

Some tests were performed with oil instead of water for control, and some experiments were carried out with Na_2SO_4 or $CaCl_2$ added to the pore fluid.

6.2.3 Apparatus and method

The densification experiments were performed using an Instron-1362 materials testing machine equipped with a 100kN load cell, plus two different, 1-D compaction dies. (Fig. 6.2). The first, a cylindrical compound vessel with an internal diameter of ~22 mm, an external diameter of 140 mm and a height of 90 mm (Fig.6.2b), was suitable for use at room temperature and to a maximum stress of ~250 MPa. The second, with an internal diameter of ~15 mm, was designed to operate at temperatures up to 250 °C and applied stresses up to ~530 MPa (Fig. 6.2c). When using this die, sample temperature was controlled using a CAL 9900 PID temperature controller, and measured using type K (chromel-alumel) thermocouples (accuracy ±0.1°C). All experiments were performed under drained conditions.

In setting up individual experiments using either die, the vessel base-assembly was first mounted onto the Instron loading ram as indicated in Fig. 6.2. The upper-surface of the bottom piston, the lower o-ring (15 mm die), and the sample area of the compaction die were then smeared with a very thin layer of HTP-paste (molybdenum disulphide grease, manufactured by Dow Corning), and the die and bottom piston were located onto the base-assembly. The granular gypsum sample was then funnelled into the die, and a porous 2mm thick stainless steel plate was placed on top (15 mm die). The face of the upper piston and the upper piston o-ring (15 mm die) were then lubricated with HTP-paste, and the piston assembly was carefully pushed into the compaction die to just touch the sample. Finally a steel spacer was placed on top of the upper piston, and the Hewlett Packard linear variable differential transformer (LVDT) was attached to the Instron loading column to measure displacement of the top piston into the die (Fig. 6.2).
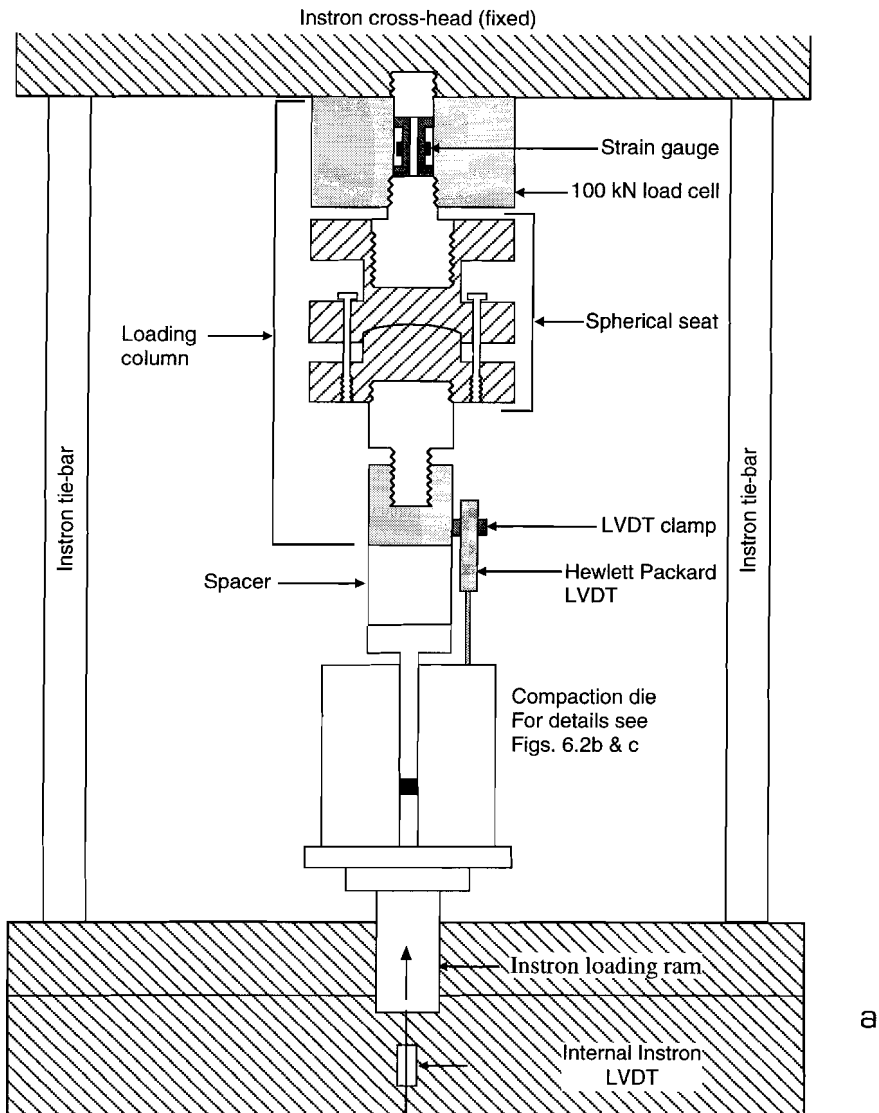
Figure 6.2. Semi-schematic diagram, illustrating a) the Instron-1362 materials testing machine set-up as used for the present experiments, and b,c) the two compaction die assemblies used. Applied load, displacement (measured using the internal Instron LVDT and external Hewlett Packard LVDT), and temperature signals were recorded as a function of time using a 6 channel chart recorder, the pen positions of which were logged on a Olivetti microcomputer using a 16 bit A/D converter.

Instron loading column — Hewlett Packard LVDT — Upper spacer — Push-out piston — Compaction die (compound vessel) — Upper piston — Sample — Lower piston — Push-out block — Lower spacer — Instron loading ram — **b**

Seal — Instron loading column — Hewlett Packard LVDT — Upper piston thermocouple — Spacer — Pore fluid inlet/outlet — Cooling — Heat shield — Ceramic insulation block — Insulation material — Sheated heating element — Upper piston — Furnace mantle — O-ring — Porous steel plate — Control thermocouple — Sample — Lower piston — O-ring — Vessel — Monolux insulation plate — Base assembly — Cooling — Base plate — Lower piston thermocouple — Instron loading ram — **c**

In starting room temperature experiments, a small compressive load of 0.1% (equivalent to ~0.27 or ~0.56 MPa applied stress, depending on the compaction die used) of the total 100 kN range of the Instron was applied to the sample, taking the corresponding position to represent the zero displacement position. Data logging of the load cell, displacement (LVDT) and temperature signals was then started (see Section 6.2.4), and the sample was loaded at the desired rate to the chosen load and maintained there for 30 minutes. This was done using the ramp function generator and load-control option of the Instron-1362 machine. The sample was then unloaded to 0.1% of the total range, still using the load-control option of the Instron. Finally, the sample was completely unloaded using the Instron position-control option to lower the compaction die plus pistons away from the upper loading column. For tests carried out at temperatures higher than ambient, the 15 mm vessel plus sample were heated to the desired temperature after application of the initial small load (0.1%) and before beginning the main loading sequence. Cooling of the 15 mm apparatus was started after unloading of the sample to the initial small load of 0.1%, by switching off the furnace while continuing the flow of water through the cooling plates (Fig. 6.2c).

In order to remove samples from the die after unloading, the upper piston was removed and replaced by a steel rod with the same length as the compaction die. The die was then lifted onto a hollow, cylindrical steel spacer placed between the die and the base assembly. The Instron was then used to carefully push out the lower piston and sample. Each sample was then weighed immediately to determine any mass loss due to water expulsion or dehydration. The sample was subsequently dried at 40°C for 24 hours, weighed again and impregnated under vacuum with blue-dyed epoxy-resin to allow sectioning and microstructural study. All samples were impregnated within one week after test completion. Some samples were cut in half, of which one half was impregnated within one week after testing, and the other half was stored wet (sealed with plastic foil) at room temperature and atmospheric pressure for a period up to one year. This was done to study microstructural changes as a function of age.

6.2.4 Data acquisition and processing

The following output signals were produced during all experiments:
-   Instron load cell output (100 kN load cell, accuracy 0.5% of indicated load).
-   Internal Instron LVDT output (full scale range 10 mm, accuracy 0.1% of full

scale).

- External Hewlett Packard LVDT output (linear full scale range 12.7 mm, accuracy 0.1% of full scale).

In experiments performed at elevated temperatures using the 15 mm vessel, the following output signals were also produced:

- Compaction die control temperature (measured with a type K (chromel-alumel) thermocouple, accuracy ± 0.1°C).
- Temperature above the sample (see Fig. 6.2c; measured ~3 mm above the sample with a type K thermocouple, accuracy ± 0.1°C).
- Temperature below the sample (see Fig. 6.2c; measured ~3 mm below the sample with a type K thermocouple, accuracy ± 0.1°C).

The raw data signals were recorded as a function of time using a 6 channel recorder, the pen positions of which were logged by an Olivetti microcomputer using a 16 bit A/D converter. A specially developed computer programme (DASAEHPT, by Peach, Brzesowsky and Den Brok) supervised the logging. The raw data were processed, calculating axial strain, axial strain rate (using the 3-point central difference method), and porosity versus time from the displacement-time records obtained for each experiment. Since expelled fluid volume was not measured during the tests, syn-deformational sample porosity was calculated assuming no decomposition of the gypsum. In the case of samples later observed to have decomposed to hemihydrate (T > 110°C), only final porosity data are presented. These were calculated using the weight change of the samples to arrive at the gypsum / hemihydrate / porosity ratio. All final (fully unloaded) porosity data presented in this chapter were determined from mass and volume measurements on the samples.

6.3 RESULTS

6.3.1 Mechanical data

The porosity versus time curves obtained in all experiments showed essentially the same 3-stage form, corresponding to the loading up, the constant load, and the controlled unloading stages of the experiments. Typical examples are shown in Figs. 6.3a, 6.4a, 6.5, 6.6a, 6.7a and 6.8a, which also illustrate the effect of applied stress (Figs. 6.3a, 6.7a), temperature (Figs. 6.4a, 6.8a), and water content (Fig. 6.6a).

The behaviour of <u>dry samples</u> densified at room temperature is illustrated in Fig. 6.3a. This shows that after samples attained the desired stress for testing little or no further reduction of porosity occurred (flat portion of the curves). The final porosities (porosities after unloading) of dry samples obtained during densification at room temperature, across the entire range of applied stresses investigated (~27-530 MPa), are illustrated in Fig. 6.3b. Clearly, with increasing applied stress the final porosities of the samples decreased reaching values around 9-10% at 500 MPa. In contrast to densification of dry samples at room temperature, densification of dry samples at elevated temperatures showed time dependent porosity reduction during the constant load stage of the experiments (Fig. 6.4a). Furthermore, the final porosity of the samples decreased with increasing temperature (Fig. 6.4a). However, at temperatures above 110°C the final (true) porosities of the dry samples increased with increasing temperature. This is illustrated in Fig. 6.4b, which shows the final (true) porosities obtained across the complete range of temperatures studied (~25-150°C) at two different applied stresses.
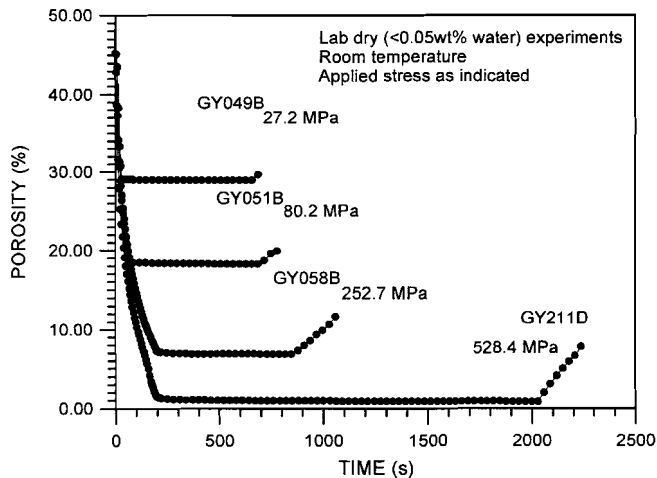

Figure 6.3a. Typical porosity (φ) versus time curves obtained for dry samples densified at room temperature. Note the three test stages of loading up, constant load and unloading which are clearly visible in this plot.
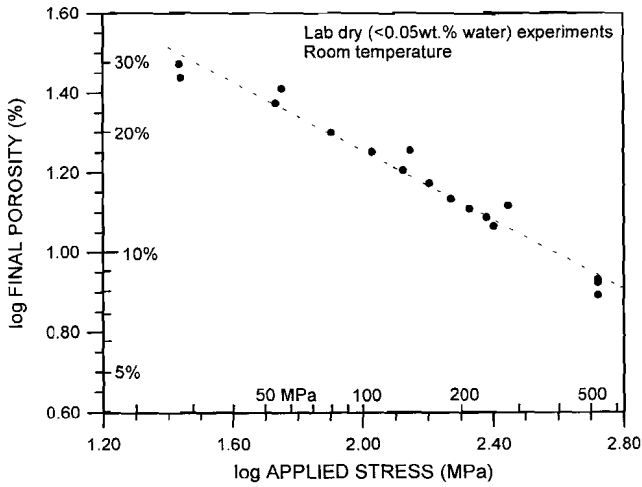
Fig.6.3b. Log-log plot of final porosity (porosity determined from sample mass before testing and from the mass and volume after testing) versus applied stress for dry samples densified at room temperature across the entire range of stresses investigated (~25-530 MPa). Note the effect of increasing applied stress on the final porosity achieved.
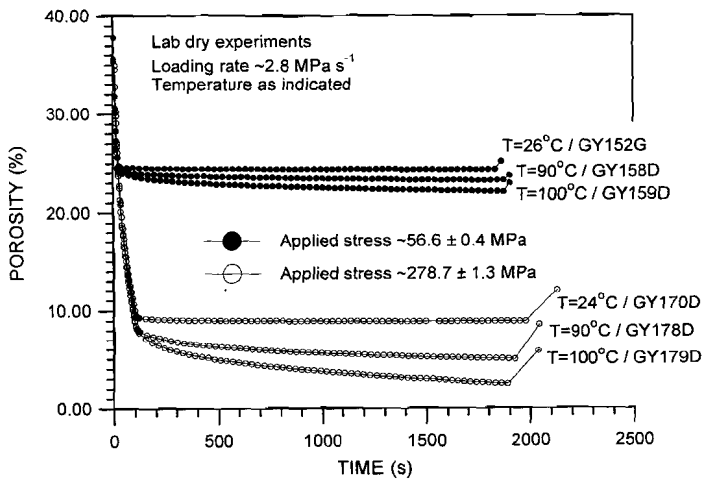

Figure 6.4a. Typical porosity (ϕ) versus time curves obtained for dry samples densified at elevated temperatures up to 100°C. The curves are plotted for two different values of applied stress (σ_a), all clearly reflecting the three stage character of the tests.
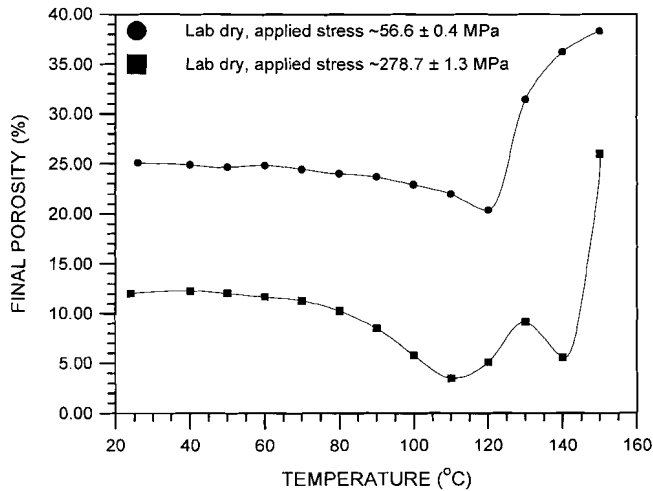
Fig. 6.4b. Final porosity (porosity determined from sample mass before testing and from the mass and volume after testing) versus temperature for dry samples densified at applied stresses of respectively ~57 and ~280 MPa and across the entire range of temperatures studied (~25 - 150°C). Note the decrease of final porosity with increasing temperatures up to ~110°C, and subsequent increase in final porosity at temperature above 110°C.

The underline influence of adding a fluid (oil or water) on densification behaviour at room temperature is illustrated in Fig. 6.5. This shows that samples with oil and water attained a lower final porosity (porosity after unloading of the samples) than dry material densified under similar conditions (applied stress ~253 MPa, loading rate ~1.3 MPa s^{-1} and room temperature), though the effect of water was considerably greater than oil. Furthermore, samples containing oil underwent little or no porosity reduction during the constant load stage of the experiment, whereas those containing water showed time-dependent porosity reduction during this stage of the test. The behaviour obtained with increasing amounts of added water at room temperature is illustrated in Fig. 6.6a. The final porosities of samples densified wet at applied stresses of ~27, ~133 and ~253 MPa, at room temperature and for all water contents investigated (0-5wt.% water) is illustrated in Fig. 6.6b. This shows that, up to a water content of ~2.5wt.% the final porosities of samples decreased with increasing amount of water added. However, addition of more than ~2.5wt.% water seemed to have slightly increase the final porosities of the samples.
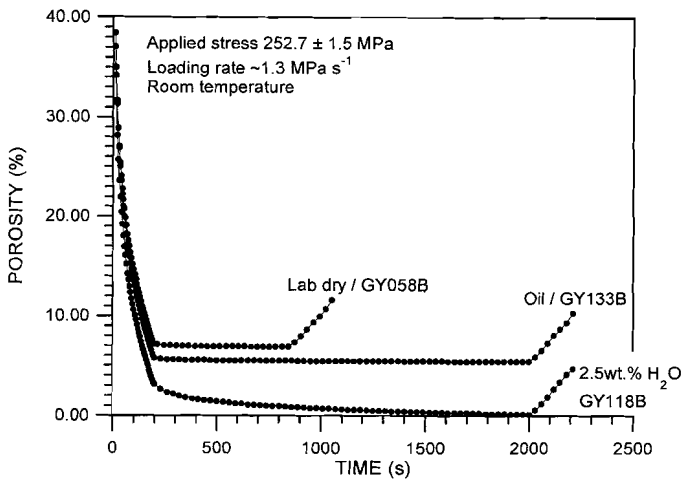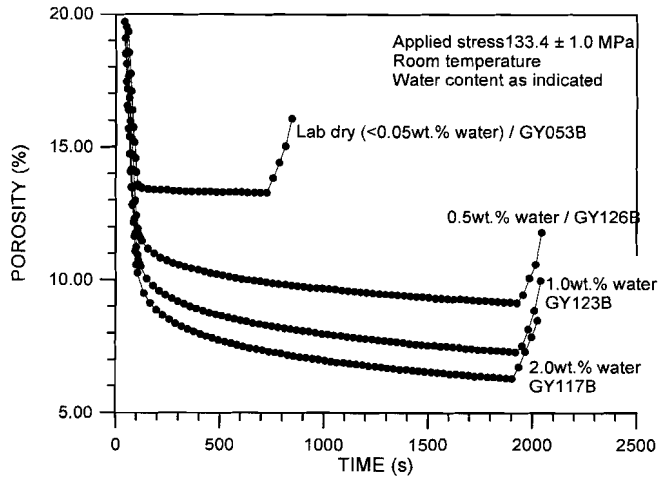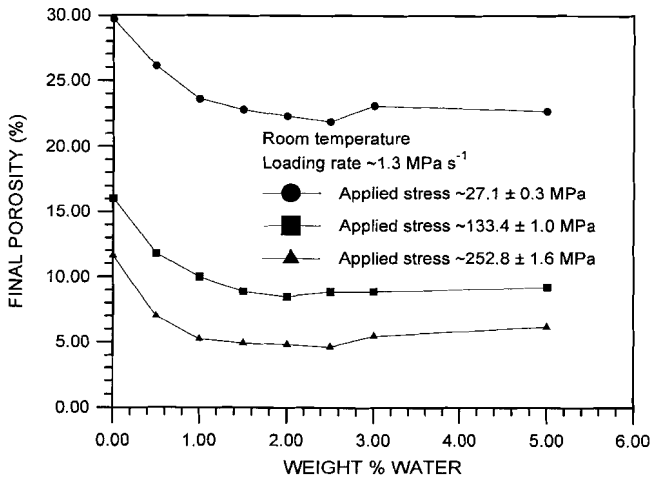
Figure 6.5. Porosity (ϕ) versus time curves for a dry sample, a sample containing oil, and a wet sample (2.5wt.% H$_2$O) densified at similar experimental conditions, showing the influence of pore fluids. The three stages of loading, constant load and unloading are clearly apparent in this plot.

Like the dry samples, the wet samples also revealed decreasing final porosities with increasing applied stress at room temperature (Fig. 6.7a,b). However, as already mentioned (see Figs. 6.5 and 6.6a), the wet samples showed strongly enhanced initial porosity reduction as well as time-dependent porosity reduction during the constant load stage of the experiments (Fig. 6.7a) contrary to the dry samples. As in the case of dry samples, wet samples also revealed a decreasing final porosity with increasing temperatures up to 110°C, and increasing final porosities at higher temperatures (110-150°C - see Fig. 6.8a,b). Wet test performed at elevated temperatures also showed time dependent porosity reduction during the constant load stage of the experiments (Fig. 6.8a).

Final porosity versus loading rate data are plotted in Fig. 6.9a for samples containing 2.5wt.% water densified at room temperature. Tests investigating the effect of loading rate were performed only for these samples. The observed decrease of porosity was in fact achieved during the constant load stage of the experiments. At the end of the loading-up stage all samples possessed roughly similar porosities of ~2.9±0.3% (including elastic effects); however, the amount of subsequent porosity reduction during the constant load stage increased with increasing loading rates used during the loading-up stage (Fig. 6.9b).

Figure 6.6. a) Typical porosity (ϕ) versus time curves obtained for samples densified with varying amounts of water at constant applied stress (~133 MPa) and room temperature. Note the effect of increasing water content. b) Final porosity (porosity determined from sample mass before testing and from the mass and volume after testing) versus water content data obtained at three different values of applied stress (σ_a). Note that the lowest final porosities were obtained in samples containing ~2.0-2.5wt.% H_2O.
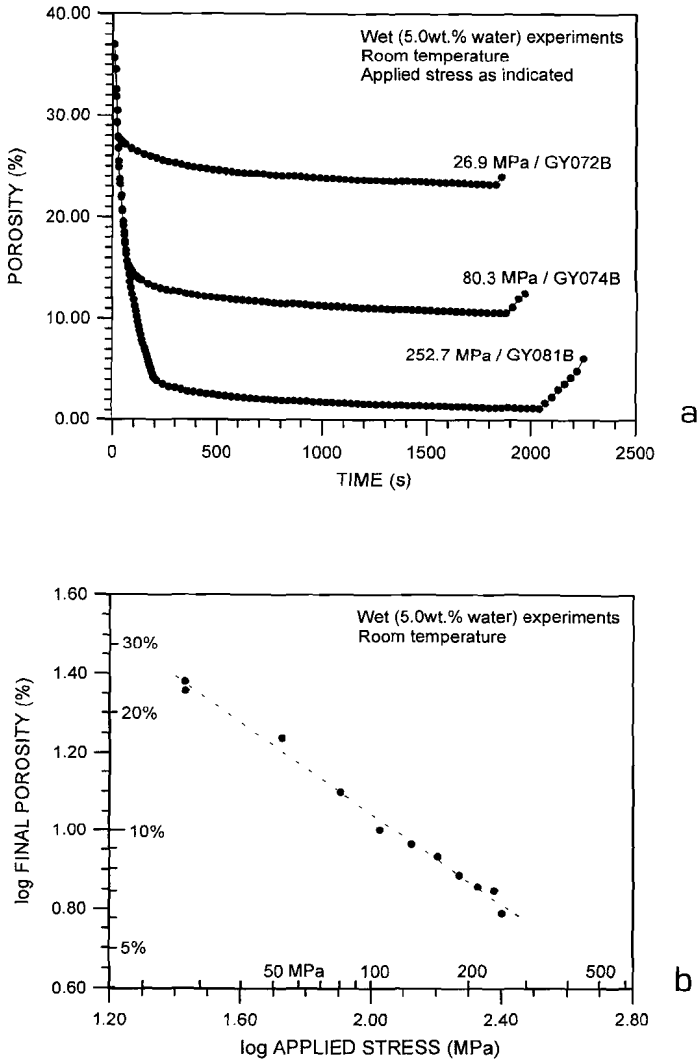
Figure 6.7. a) Porosity (φ) versus time curves for wet (5.0wt.% water) samples densified at room temperature, showing the influence of increasing applied stress. b) Log-log plot of final porosity (porosity determined from sample mass before testing and from the mass and volume after testing) versus applied stress for wet samples (5.0wt.% water) densified at room temperature across the entire range of stresses investigated (~25- 253 MPa). Note the effect of increasing applied stress on the final porosity achieved.
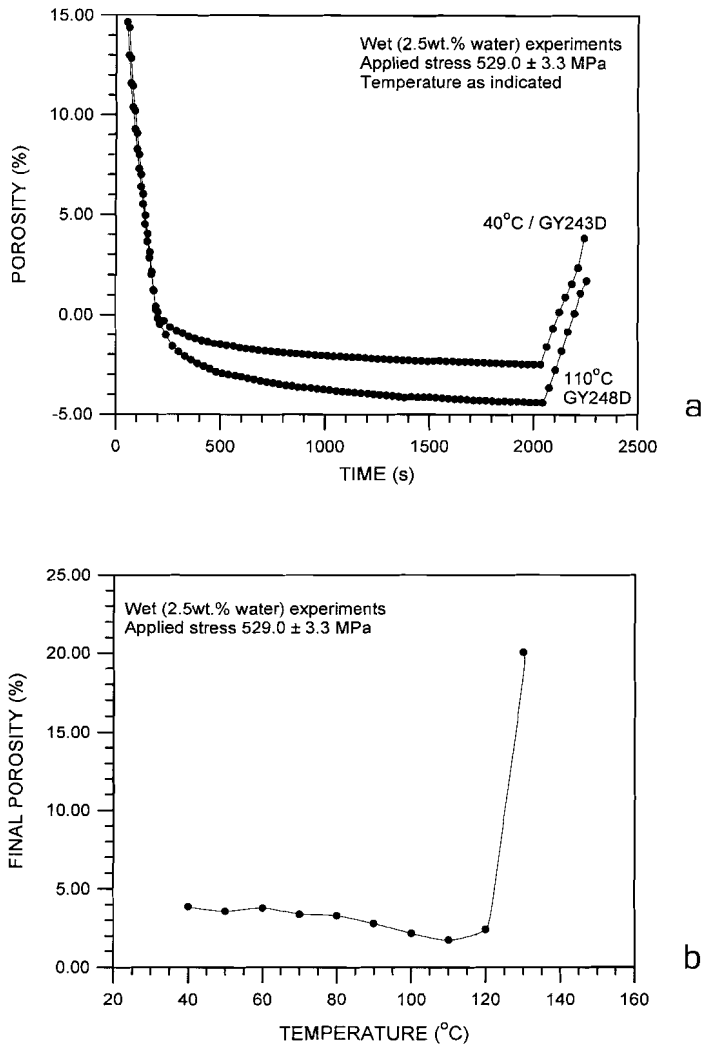
Figure 6.8. a) Typical porosity (ϕ) versus time curves obtained for wet (2.5wt.% water) samples densified at elevated temperatures and constant applied stress (~530 MPa). b) Final porosity (porosity determined from sample mass before testing and from the mass and volume after testing) versus temperature for wet samples (2.5wt.% water) densified at a constant applied stress of ~530 MPa and across the entire range of temperatures studied (40 - 130°C). Note that the final porosity of the samples decreases with increasing temperatures up to 110°C, but increases dramatically at temperature above 110°C.

Figure 6.9. a) Final porosity (porosity determined from sample mass before testing and from the mass and volume after testing) versus log loading rate for wet samples (2.5wt.% water) densified at a constant applied stress (~253 MPa) and at room temperature. Note that the final porosity of the samples decreases with increasing loading rates. b) Porosity reduction during the constant load stage of the experiments versus time, showing the influence of loading rate on reduction of porosity during the constant load stage of the experiments.

The influence of salt impurity content within the fluid phase on densification was investigated using samples with a water content of 2.5wt.% at an applied stress of ~253 MPa, at constant loading rate (~1.3 MPa s^{-1}) and at room temperature (see Table 6.1). The results showed that Na_2SO_4 and $CaCl_2$ in molar concentrations in the range 0.001 - 1.0M did not significantly influence the final porosity the samples obtained (Fig. 6.10); the final porosities obtained for all concentrations were statistically indistinguishable from that obtained for samples with 2.5wt.% pure water added (see Fig. 6.6b, sample N° GY118B).
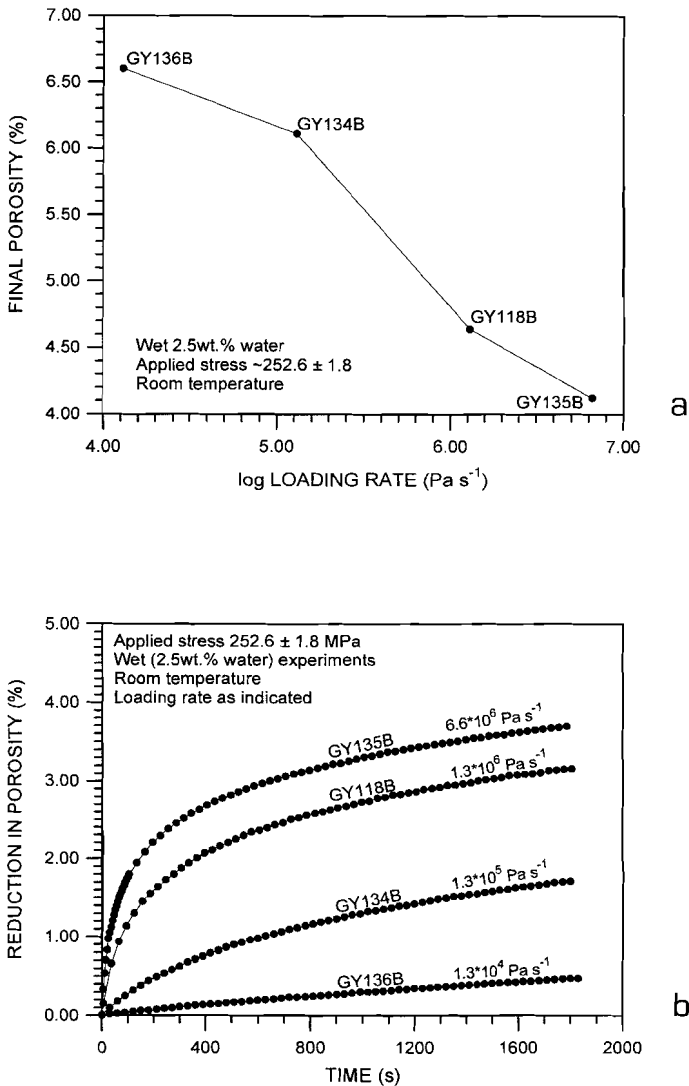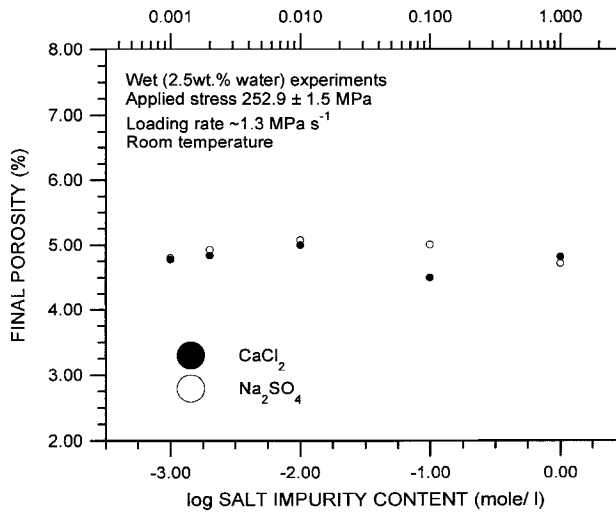

Figure 6.10. Final porosity (porosity determined from sample mass before testing and from the mass and volume after testing) versus log salt impurity content within the fluid phase, for wet samples (2.5wt.% water) densified at a constant applied stress of ~253 MPa and at room temperature. No significant differences can be observed between the final porosities achieved.

6.3.2 Microstructural observations

Microstructural analysis was carried out by means of optical microscopy on thin and ultra-thin sections of epoxy-impregnated samples. Examination of the FGD-gypsum starting material revealed that the grains are euhedral to subrounded in shape. About ~75% are roughly equiaxed but many elongated grains (~25%) with aspect ratios of up to 5 are also present (Fig. 6.11). When viewed in cross polarized light, many grains show twinning and/or undulatory extinction. It will be recalled from Section 6.2.1 that the median grain size is ~48 μm.
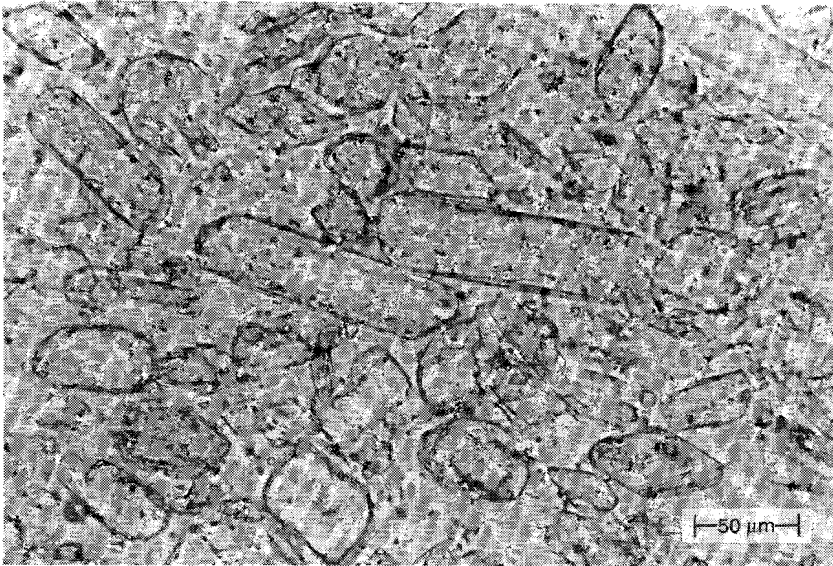
Figure 6.11. Optical micrograph of the FGD-gypsum starting material, showing the variability in shape of the grains, which range from euhedral to subrounded. About 75% are equiaxed. Many elongated grains are also present (~25%), these have aspect ratios of up to 5.

Figures 6.12a-c show the microstructure of samples densified dry at room temperature and increasing applied stresses. At the lowest applied stresses (~27 MPa), many trans-/intragranular microcracks are developed in the elongated grains. Some slightly bent grains and undulatory extinction are also observed (Fig. 6.12a, exp./sample N° GY049B). At stresses above ~150 MPa, elongate grains having orientations more or less parallel to the compaction direction are kinked; furthermore almost every grain exhibits undulatory extinction, some subgrains are developed and some grain size reduction has occurred (Fig. 6.12b, exp./sample N° GY054B). At the highest stresses (> ~200 MPa), elongate grains are no longer present, all grains are equiaxed and the grain size is uniform and reduced to ~25 μm (Fig. 6.12c, exp./sample N° GY057B); in cross polarized light all grains show intense undulatory extinction.

Fig. 6.12a

Fig. 6.12b
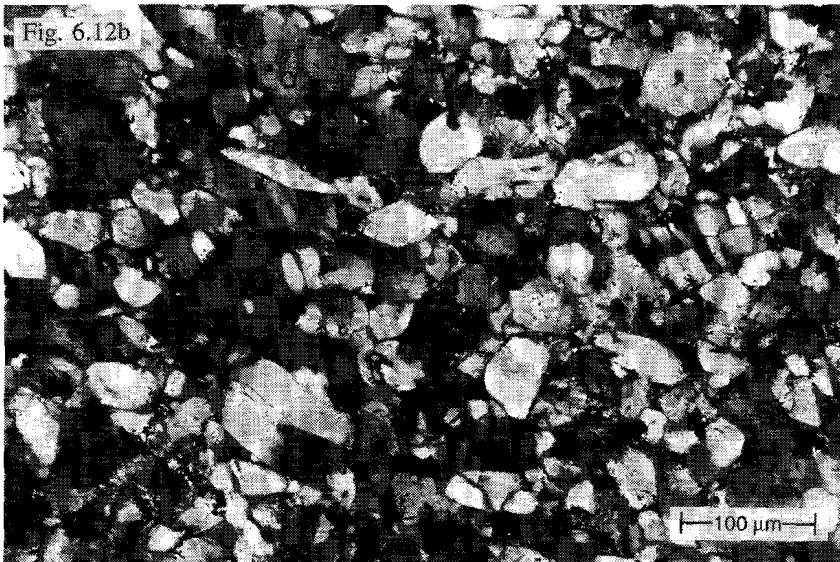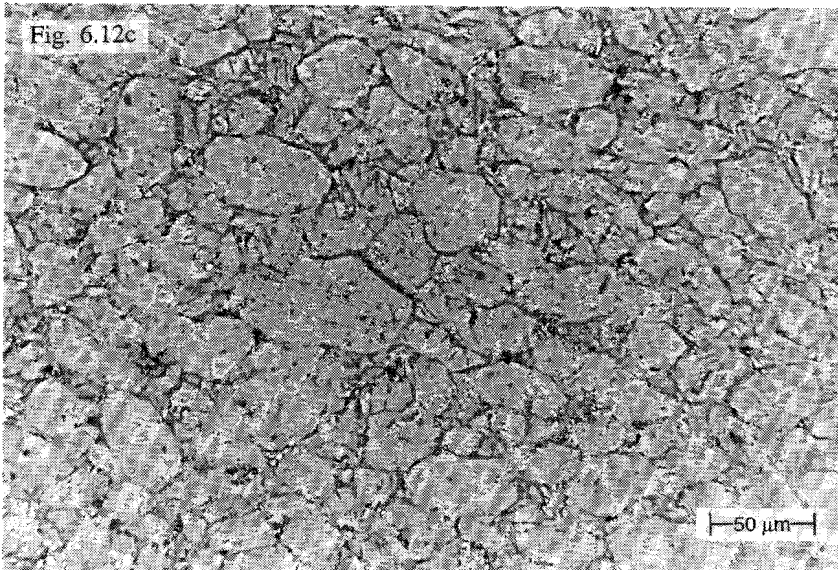
Figure 6.12. Microstructure of dry samples densified at room temperature. a) Sample densified at ~27.2 MPa showing many trans-/intragranular cracks, some slightly bent grains and undulatory extinction (exp./sample N° GY049B); b) sample densified at ~160.0 MPa showing kinked grains, undulatory extinction, the local development of subgrain structures, and grain size reduction (exp./sample N° GY054B); c) sample densified at ~239.4 MPa showing significant grain size reduction and elimination of elongate grains (exp./sample N°GY057B).

The microstructure of dry samples densified at elevated temperatures, but below the dehydration temperature (i.e. below 110°C), is very similar to the microstructure of dry samples densified at room temperature. Thus all samples tested dry up to 90 or 100° C show trans-/intragranular cracks, kinking of elongated grains, undulatory extinction, the development of subgrains and significant grain size reduction, particularly at the higher stresses. At temperatures close to the dehydration temperature (90-100°C), the microstructure is slightly different; at these temperatures some grains start to show lobate or serrated grain boundaries (Fig. 6.13, exp./sample N° GY178D).
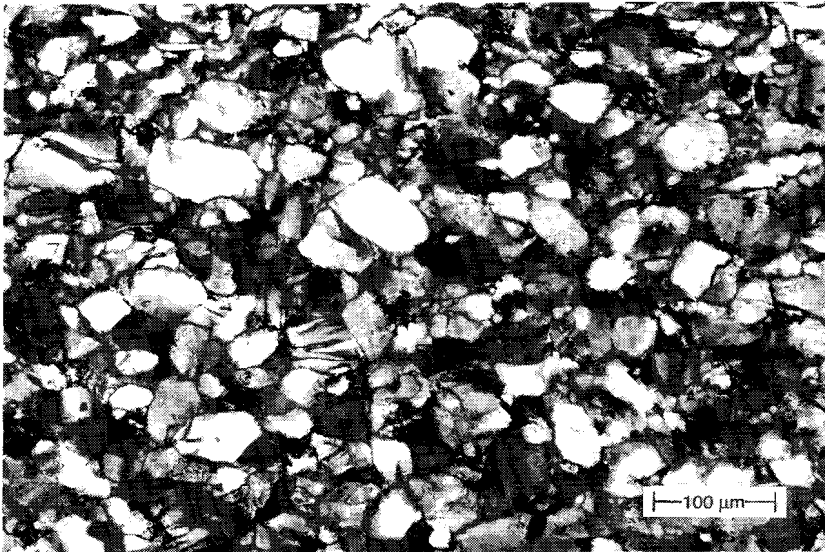
Figure 6.13. Microstructure of a dry sample densified at an applied stress of ~280 MPa and at a temperature of 90°C, showing that some grains start to develop lobate or serrated grain boundaries near the dehydration temperature (exp./sample N° GY178D).

Wet experiments performed at room temperature exhibit broadly the same microstructural features and trends with increasing applied stress as described above for the dry experiments. As in the dry samples, wet samples densified at $\sigma_a \geq 150$ MPa with less than 2.0wt.% water show kinked grains, undulatory extinction, grain size reduction, and minor serration of grain boundaries (Fig. 6.14a, exp./sample N° GY115B). However, when using water contents $\geq$ 2.0wt.%, there is less grain size reduction and elongated grains are preserved even at the highest applied stresses (~530 MPa). These grains are aligned in a direction perpendicular to the loading direction (Fig. 6.14b, exp./sample N° GY118B). Furthermore, with increasing applied stress (>100 MPa) and water content (>2.0wt.%), grains show more and more lobate or serrated grain boundaries and grain-to-grain interpenetrations or indentations (Fig. 6.14c, exp./sample N° GY118B). The microstructure developed in samples tested with salts dissolved in the solution phase (Table 6.1) could not be distinguished from the microstructure developed in samples densified with pure water under otherwise identical conditions. Similarly no effect of loading rate was observed on the microstructure of samples tested wet (2.5wt.% water) at room temperature (Table 6.1).

Fig. 6.14a

⊢—50 µm——⊣

Fig. 6.14b

⊢—100 µm—⊣
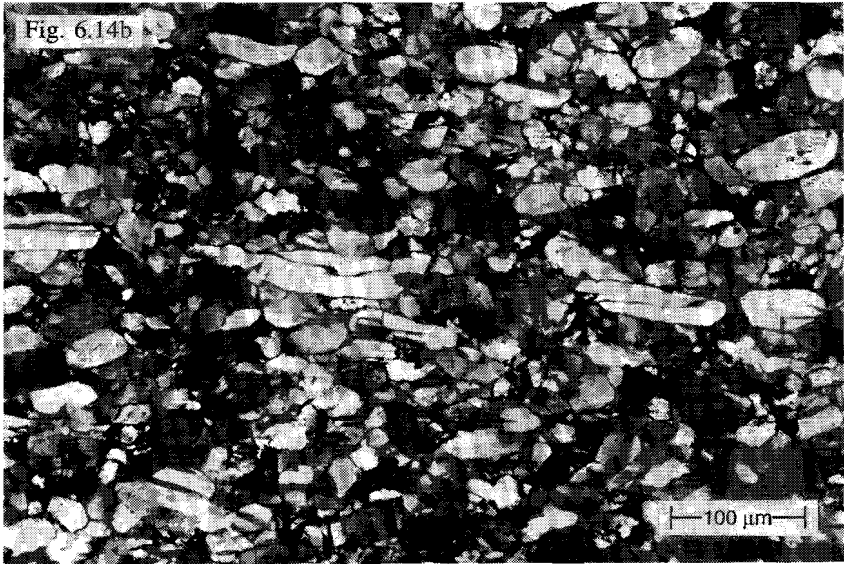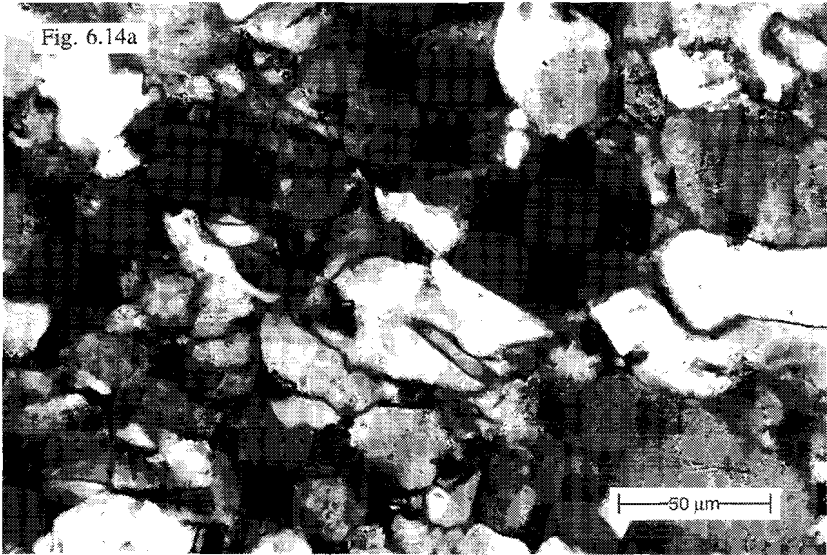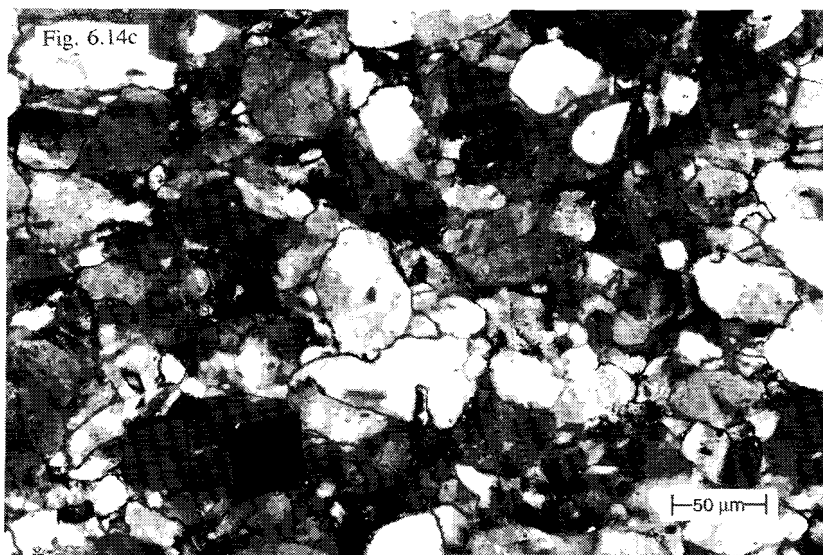
Figure 6.14. Microstructure of wet samples densified at room temperature. a) The microstructure of a sample densified with 1.5wt.% water at ~250 MPa, showing kinked grains, undulatory extinction and minor grain boundary migration (exp./sample N° GY115B). b) Microstructure of a sample densified with 2.5wt.% water at ~250 MPa, showing the alignment of surviving elongated grains perpendicular to the loading direction (exp./sample N° GY118B). c) Microstructure of a wet sample (2.5wt.% water) densified at an applied stress of ~250 MPa and at room temperature showing abundant lobate grain boundaries and grain-to-grain interpenetrations/indentations (exp./sample N° GY118B).

It will be recalled from Table 6.1 that wet tests at elevated temperatures were performed only on samples containing 2.5wt.% water. The microstructure of these samples, densified at temperatures below the dehydration temperature (<110°C), show no detectable changes in microstructure compared with that obtained in wet samples at room temperature. All samples show undulatory extinction, cracks, some grain-to-grain interpenetration/indentations, lobate or serrated grain boundaries, the development of some subgrains, and alignment of elongated grains perpendicular to the loading direction.

At temperatures above the dehydration temperature (≥110°C), the microstructure of dry and wet samples is indistinguishable. In dry and wet samples densified at 110°C, some of the gypsum grains start to show a mantle of hemihydrate (Fig. 6.15a, exp./sample N° GY180D). All remaining gypsum grains show undulatory extinction, kink bands, microcracks, grain-to-grain indentations and/or lobate grain boundaries and some subgrain development. At 120°C, ~50vol.% of the gypsum is dehydrated to hemihydrate with gypsum remaining in grain cores (Fig. 6.15b, exp./sample N° GY181D). Gypsum is completely dehydrated to hemihydrate at temperatures above 120°C, producing a microstructure with a strong preferred orientation of hemihydrate grains aligned perpendicular to the compression direction (Fig. 6.15c, exp./sample N° GY185D).

As mentioned in Section 6.2.3, some samples densified wet at room temperature (GY116B-GY118B) were cut in half after completion of the experiments. Like all other samples, the microstructure of one half was studied within a week after completion of the tests, while the microstructure of the other half was studied after a sealed storage period of one year. Using optical microscopy, no visible microstructural differences could be observed between these halfs. All show roughly similar amounts of plastic deformation (undulatory extinction), cracks, grain-to-grain indentations and lobate or serrated grain boundaries.

Fig. 6.15a

├─50 μm─┤
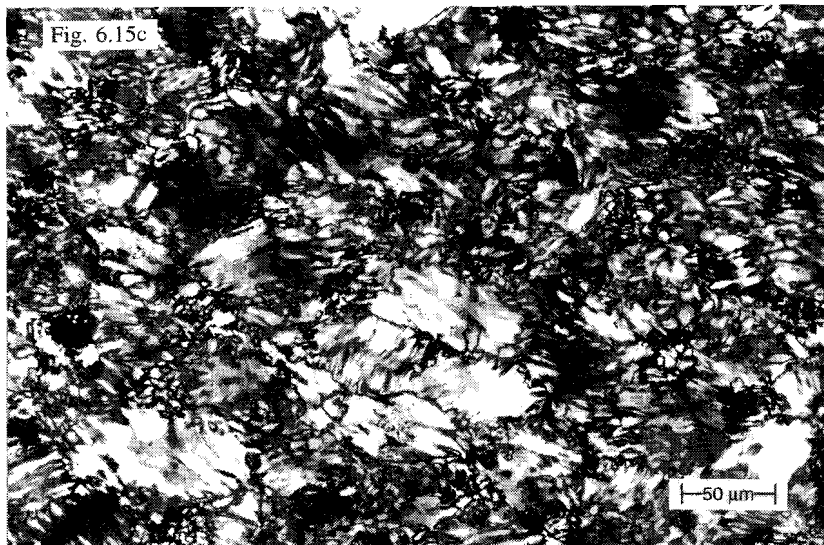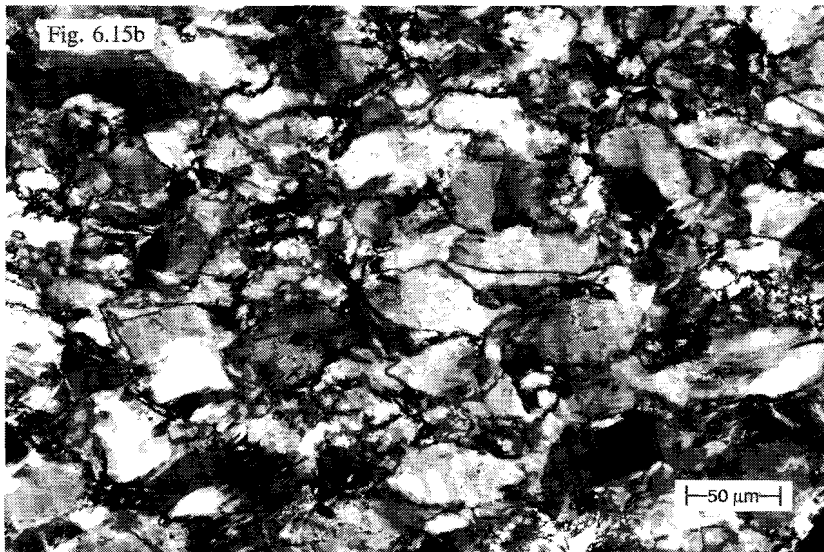
Figure 6.15. Microstructure of dry samples densified at an applied stress (σ_a) of ~280 MPa. a) Sample densified at ~110°C showing some gypsum grains with a mantle of hemihydrate (exp./sample N° GY180D); b) sample densified at ~120°C in which ~50vol.% of the gypsum is dehydrated to hemihydrate (exp./sample N° GY181D); c) sample tested at ~150°C showing complete dehydration of gypsum to hemihydrate (exp./sample N° GY185D).

6.4 DISCUSSION

6.4.1 Dry versus wet behaviour at room temperature

The results reported above for the dry and wet samples densified at room temperature are markedly different. Porosity reduction during the initial loading phase, was more efficient in runs where fluid was present, either oil or water, than dry runs, and more efficient in samples containing water than samples containing a similar amount of oil. Thus both fluids presumably had a physical lubricating effect facilitating intergranular sliding, therefore resulting in denser samples. In addition, initial loading in the presence of water must have activated some kind of fluid assisted mechanism of deformation, such as pressure solution or stress corrosion cracking at grain contacts, which would also facilitate intergranular sliding. Wet densification not only led to a greater initial reduction in porosity, it was also shown that samples exhibited time-dependent deformation after the full stress was reached during wet densification, contrary to the behaviour of dry and oil-saturated samples which no longer deformed after the full stress was attained. This proves the operation of some type of fluid-assisted creep mechanism in the wet samples, such as pressure solution, dislocation creep accompanied by fluid-assisted recrystallization, or "stress corrosion cracking".

Taking into account the microstructural studies it is inferred that dry densified samples deformed by a coupled process of grain scale cataclasis accompanied by time-independent plastic deformation (i.e. distortion of the crystal lattices by dislocation glide) and intergranular sliding rearrangements, resulting in the observed transgranular cracks, grain size reduction, bending of the grains and undulatory extinction, plus kinked grains at applied stresses above ~150 MPa. The microstructures observed in the wet densified samples indicate that in addition to microcracking and plastic deformation, diffusive mass transfer processes were operating. In particular, the lobate grain boundaries exhibited by nearly all the grains provide microstructural evidence for partial recrystallization by grain boundary migration (Urai, 1983; Urai et al., 1986). Since this was restricted to the wet samples, the mechanism was presumably one of fluid-assisted grain boundary migration. In addition, the evidence found for indentations in wet samples suggests the operation of pressure solution.

Synthesizing on the basis of the above points, it is inferred that initial densification of the wet samples involved intergranular sliding, grain fracture and

plasticity, as in the dry samples. However, these processes were (almost certainly) accompanied by lubrication, dissolution and perhaps fluid-assisted cracking of grain contact asperities, leading to i) increased intergranular sliding, ii) reduced transgranular fracture and grain size reduction, and iii) the survival of a significant number of elongated grains plus their rotation into the observed preferred orientation (normal to compression). During the relatively long constant load stage of the tests, it is proposed that densification creep in the wet samples occurred largely by a combination of pressure solution creep and dislocation creep involving recovery by fluid assisted grain boundary migration. In the dry samples, none of the above-mentioned fluid enhanced processes were active, with the result that densification was dominated by cataclasis plus work hardening plastic deformation and intergranular sliding, with no measurable time dependent effects.

6.4.2 Dry versus wet behaviour at elevated temperatures

In contrast to the experiments performed at room temperature, where only wet samples showed time-dependent behaviour, at elevated temperatures both the dry and wet samples showed time-dependent behaviour during the constant load stages of the tests, at least at temperatures up to 110°C (see Figs. 6.4a and 6.8a). At temperatures above 60°C, the dry samples clearly showed significant time-dependent behaviour. In the following, the behaviour observed above and below the "dehydration temperature" will be addressed separately, as will the effect of the different variables investigated.

6.4.2.1 Behaviour at temperatures below 110°C

Two mechanisms can be put forward to explain the time-dependent behaviour seen in dry material in this region. Firstly, at elevated temperatures it is likely that the densification of dry samples involved an increasing amount of time-dependent crystal plastic deformation (i.e. dislocation creep processes), since these are known to be enhanced at elevated temperatures (Baumann, 1984). However, from the microstructure of the dry samples it was not clear whether recovery controlled plastic deformation was more important at elevated temperatures than at room temperature. The dry samples, densified at all temperatures up to 110°C, show roughly the same amount of undulatory extinction, kinking and subgrain development. Secondly, because the dry experiments in the range 60-110°C were performed outside the stability field of gypsum (Marsal, 1952; MacDonald, 1953), it

is likely that small amounts of gypsum dehydrated to hemihydrate in these experiments. During dehydration, small amounts of water produced in the dry samples would probably be sufficient to wet or partially wet the grain boundaries thus enabling the same time-dependent deformation mechanisms seen in the wet samples to become operative, i.e. pressure solution and/or plastic deformation with fluid-assisted recrystallization. It is well established that only 0.05wt.% water is needed to cause these effects in rocksalt (Urai et al., 1986; Spiers et al., 1989). At temperatures $\geq$ 90°C the microstructure of the initially dry samples revealed lobate grain boundaries which clearly suggests the operation of the fluid-assisted grain boundary migration mechanism seen in the wet samples.

Focusing now on the behaviour of the wet samples densified at temperatures up to 110°C, these show no significant changes in microstructural development with temperature. All show plastic deformation, cracks, pressure solution and/or fluid-assisted grain boundary migration and the development of subgrains at elevated temperatures, but as for the dry samples, it was not clear whether recovery controlled plastic deformation was more important at elevated temperatures than at room temperature. Pursuing the argument given above regarding the effect of temperature on plasticity in gypsum, the observed relationship between run temperature and final porosity (i.e. the finding that the higher the temperature the lower the final porosity, see Fig. 6.8) was probably due to temperature effects promoting dislocation creep processes as well as solution transfer.

6.4.2.2 Behaviour at temperatures above 110°C

At high temperatures (>110°C), the dry and wet samples undergo partial or complete dehydration to hemihydrate. The resulting final (true) porosity of completely dehydrated dry and wet samples was relatively high (up to ~26% in the dry samples densified at an applied stress of ~280 MPa and up to ~20% in the wet samples densified at an applied stress of ~530 MPa). As mentioned in the experimental method (Section 6.2.3), the volume of water expelled from the samples was not measured, therefore, the porosity versus time behaviour of significantly dehydrated (T>110°C) samples could not be obtained from the deformation experiments. The microstructures of dry and wet samples densified at temperatures in the range 110°C - 150°C are indistinguishable. The partially dehydrated samples reveal that dehydration started on grain boundaries, resulting in aggregates consisting of grains with a deformed gypsum core and hemihydrate mantle. Still existing gypsum-gypsum grain contacts show lobate grain boundaries,

suggesting the operation of a fluid-assisted grain boundary migration mechanism. The reduced compaction (i.e. high final (true) porosities) observed in the partially and completely dehydrated samples, is suggested to be caused by the fact that hemihydrate is far stronger than gypsum itself (Olgaard et al., 1995).

6.4.3 Effects of varying water content

The experimental results clearly showed that samples densified in the presence of 2.0wt.% to 2.5wt.% H_2O reached the lowest final porosities (e.g. see Fig. 6.6b). In samples densified with less than 2.0wt.% H_2O, it is possible that not all grain boundaries or pore wall surfaces were wetted. This would result in diffusive mass transfer processes such as pressure solution and fluid-assisted recrystallization being restricted to the wetted regions, so that these samples did not attain the maximum density (lowest porosity) possible. This is supported by the microstructural observation that samples with <2wt.% water showed more kinking and less grain boundary migration than samples with higher water content. In samples densified with more than ~2.5wt.% H_2O densification was probably impeded by the process of squeezing water out of the sample. For example, 5.0wt.% H_2O fills 11.6% porosity, so that densification to values below this porosity requires the removal of water from the sample. Using 2.5wt.% water, an equivalent porosity of 5.6% is filled with water, which is very similar to the final porosity values achieved at room temperature using 2.5wt.% water. This water content is therefore inferred to be most effective in obtaining the densest samples because it represents the optimum "trade off" between water expulsion effects and water-enhanced deformation mechanisms.

6.4.4 Effects of loading rate

As mentioned in the results section (Section 6.3.1) the effects of loading rate were studied only using samples with 2.5wt.% water, at an applied stress of ~253 MPa and at room temperature. The results showed that for these conditions the final porosity of the densified samples decreased with increasing loading rate (see Fig. 6.9). This effect cannot be attributed directly to the initial loading stage itself, as the samples attained a roughly similar porosity (~2.9±0.3%) at the end of this stage, regardless of the rate, provided other variables were held constant. The differences in final porosity were attained not during initial loading then, but during the subsequent constant load stage (see Fig. 6.9b). However, the differences in

mechanical behaviour of the samples during the constant load stage must be a result of the loading rate applied, when all other variables (applied stress, water content, and temperature) are kept constant. Furthermore, the microstructure of the samples, which were studied after they had gone through the whole cycle of loading, constant load and unloading, did not reveal detectably different features. An unambiguous explanation for the observed behaviour is not available at present, but a possibility might be that of increasingly adiabatic deformation-heating at high loading rates.

6.4.5 Effects of salt impurity content

Samples tested at room temperature with Na_2SO_4 and $CaCl_2$ in solution (2.5wt.%) show similar mechanical behaviour, final porosities obtained (~4.8% at 253 MPa), and microstructure to those of samples densified with no salt added to the pore fluid at otherwise identical conditions. During the constant load stage of the experiments the samples exhibited a time-dependent decrease in porosity which was not detectably faster than samples with pure water. It is proposed that densification creep of the samples occurred by a combination of pressure solution creep and dislocation creep involving recovery by fluid-assisted grain boundary migration during the constant load stage of the tests.

6.4.6 Optimum conditions for (useful) densification

The obtained results showed that wet compaction was more effective than dry compaction, and most effective using a water content of ~2.5wt.% at otherwise identical conditions of applied stress, temperature and loading rate. Furthermore, densification was most effective using the highest applied stresses of ~530 MPa allowing final values of 5% to be achieved for 2.5wt.% water at room temperature. In addition, denser samples were obtained at elevated temperatures, but below temperatures at which partial or complete dehydration occurs (i.e. at temperatures below 110°C). Also, high loading rates (~6.6 MPa s^{-1}) resulted in denser samples. Therefore, to produce gypsum products with high density, it is suggested that densification should be carried out on samples containing ~2-2.5wt.% water, at temperatures of 100-110°C, using the highest possible applied stresses and loading rates. Dense gypsum products produced at these conditions can be expected to have porosities < 2% and on the basis of the compressive strength versus density data of

Stoop et al. (1995) should have sufficient strength to be used in load-bearing applications in building industry.

6.4.7 Effect of aging

Microstructural study of the samples (GY116B-GY118B) which were set aside for aging revealed that no visible changes occurred during the storage period of one year. Samples studied within a week after completion of the tests and samples studied after wet storage show plastic deformation, cracks, subgrain development and the operation of diffusive mass transfer processes (i.e. pressure solution and recrystallization by fluid-assisted grain boundary migration). As no visible microstructural changes occurred, it is suggested that the observed fluid-assisted recrystallization mechanism is dynamic rather than static.

6.3.8 Determination of elastic stiffness of densified samples

The effective axial stiffness of the densified samples could be determined from the elastic recovery behaviour shown by the samples during the unloading stage of the experiments (see Figs. 6.3a, 6.4a, 6.5, 6.6a, 6.7a and 6.8a). For uniaxial loading/unloading, the effective axial stiffness can be defined as

$$C = \frac{\sigma_1}{\varepsilon_1} \tag{6.1}$$

where σ_1 and ε_1 are the stress and elastic strain parallel to the loading direction respectively. In order to correctly calculate the effective axial stiffness for the FGD-gypsum used, the elastic distortion of the pistons and upper spacer (see Fig. 6.2) must be taken into account. This was done using a value of $2.1 \cdot 10^{11}$ Pa for the Young's modulus of the hardened steel components. The calculated effective axial stiffness $C = 1.3 \cdot 10^{10} \pm 0.2 \cdot 10^{10}$ Pa, for wet samples with final porosities of ~5%, agrees well with the value of Youngs Modulus for polycrystalline gypsum rock of $C = 1.0 \cdot 10^{10}$ Pa reported by Baumann (1984). Since the present samples are undoubtedly anisotropic, no attempt was made to calculate the bulk modulus.

6.4 CONCLUSIONS

The aims of the present chapter were to determine the principle densification mechanisms in gypsum under both dry and wet conditions, and to investigate the conditions at which the most dense gypsum samples could be obtained. Dense gypsum is expected to show the highest strength and resistance to creep, and hence is a potential material for load-bearing applications in building industry (Stoop et al., 1995).

The starting material, flue gas desulphurization gypsum (FGD-gypsum) produced as a by-product at coal-burning power plants, was uniaxially densified at applied stresses in the range ~25-530 MPa, with water contents of 0wt% to 5.0wt.%, at temperatures ranging from ambient to ~150°C, with salt impurity contents within the fluid phase ranging from 0 to 1.0 mole/l, and at loading rates in the range ~$1.3 \cdot 10^4$-$6.6 \cdot 10^6$ Pa s^{-1}. At room temperature, after the full load was reached, the dry samples did not show further reduction in porosity, whereas the wet samples did show a time-dependent porosity reduction. Microstructural investigation showed that at room temperature conditions the dry samples mainly densified by a cataclastic mechanism accompanied by plastic deformation. Both cataclasis and plastic deformation became more intense with increasing applied stress. At applied stresses >150 MPa many of the elongated grains became intensely kinked. At applied stresses >200 MPa elongated grains were fractured resulting in grain size reduction, and producing a microstructure consisting of grains of roughly similar size and aspect ratios close to one. Wet samples also densified by cataclastic and plastic deformation mechanisms, however, these were accompanied by diffusive mass transfer processes. Fluid-assisted grain boundary migration and possibly pressure solution related processes took place during densification of the wet samples.

At elevated temperatures, both the dry and wet samples showed time-dependent porosity reduction after the full stress was reached. At temperatures below 90°C the dry samples deformed by cataclastic and plastic deformation mechanisms. Above this temperature fluid-assisted grain boundary migration, caused by the release of water during the dehydration reaction of gypsum to hemihydrate, became important. At elevated temperatures, the wet samples densified by the same mechanisms identified in the wet samples under room temperatures conditions. The microstructure of wet samples densified at room temperature, did not change with age.

It was shown that the densest samples (~1.5% porosity) were obtained by compaction of wet material (~2.0-2.5wt.% H_2O), at the highest applies stress (~530 MPa), at temperatures close to the dehydration temperature of gypsum to hemihydrate (~100-110°C), and using the highest loading rate (~6.6·10^6 Pa s^{-1}). Dense gypsum of this kind is expected to have sufficient compressive strength to be used in load-bearing applications in building industry.

CHAPTER 7

GENERAL CONCLUSIONS AND SUGGESTIONS FOR FURTHER WORK

This thesis has investigated the creep behaviour of and deformation mechanisms operative in polycrystalline aggregates of natural gypsum deformed in uniaxial and hydrostatic compaction modes in the presence of saturated $CaSO_4$ solution. Furthermore, to gain insight into the kinetics of grain scale solution transfer processes the kinetics of gypsum precipitation have also been investigated. In addition, the time-independent densification behaviour of dry and wet gypsum has been investigated by means of uniaxial compaction tests performed at high loading rates. In this case FGD-gypsum was used, i.e. gypsum produced as a by-product of the Babcock-Kawasaki flue gas desulphurization process used at coal-burning power plants.

The purpose of this final chapter is to draw together general conclusions, based on findings presented in the preceding chapters and to examine the implications of these for the creep behaviour of gypsum under geological conditions, and for the preparation and performance of (FGD) gypsum building materials. In addition, questions which remain unanswered are identified and suggestions are made for further research.

7.1 DEFORMATION BEHAVIOUR OF GYPSUM UNDER LABORATORY CONDITIONS

7.1.1 Pressure solution creep in gypsum

The indentation, truncation and overgrowth microstructures developed in samples compacted wet (i.e. in the presence of saturated $CaSO_4$ solution $\pm$ NaCl) in the hydrostatic and uniaxial compaction experiments reported in Chapters 2, 3 and 5, have provided classical evidence for the operation of some kind of pressure solution creep mechanism in wet gypsum under laboratory conditions. The microstructures showed no detectable contribution to creep by microcracking or crystal plasticity, and neither dry-tested nor oil-flooded samples showed measurable

creep. Thus, pressure solution must have been the dominant deformation mechanism in wet samples, presumably in conjunction with intergranular sliding/rearrangement. Furthermore, under simple, drained test conditions (chemically closed system) grain boundaries were found to be tight on the optical scale, and no evidence was found for grain contact corrosion or undercutting, or neck growth. It is therefore concluded that deformation of the wet samples occurred by grain boundary diffusional pressure solution (Rutter, 1976; Raj, 1982; Lehner 1990; Spiers & Brzesowsky, 1993) as opposed to any grain-scale contact undercutting or corrosion process coupled to grain-scale plasticity (i.e. plasticity coupled pressure solution; Spiers & Brzesowsky, 1993). The internal grain contact structure could not be observed and may have been an island-channel structure or thin film.

The mechanical data obtained in the simple drained experiments (chemically closed) of Chapters 2, 3 and 5 have shown that the compaction creep rate of the wet material tested can be described in terms of a second to third order power law dependence on applied stress, and an inverse dependence on grain size. In the hydrostatic compaction experiments (Chapter 2) this inverse dependence was roughly linear, whereas a third to fourth order inverse dependence on grain size was obtained in the uniaxial compaction experiments (Chapters 3, 5). This behaviour is not consistent with conventional models for <u>diffusion-controlled</u>, grain boundary diffusional pressure solution creep (Raj, 1982; Rutter, 1983; Spiers et al., 1989; Lehner, 1990; Spiers & Schutjens, 1990; Spiers & Brzesowsky, 1993), as these would predict the compaction creep rate to be linearly proportional to applied stress and inversely proportional to grain size cubed. The observed stress dependence of creep rate and an inverse linear grain size dependence are consistent with models for <u>interface-reaction-controlled</u> grain boundary diffusional pressure solution creep, when allowing for the possibility of non-linear dissolution and precipitation kinetics (Lehner, 1990; Wakai, 1994). However, to be explainable in terms of interface reaction limited models, the non-linear effect of grain size obtained in the uniaxial compaction tests (Chapters 3, 5) would require grain size dependent interface kinetics.

From previous crystal growth and dissolution studies, it is well-known that the kinetics of dissolution of gypsum are <u>at least</u> two orders of magnitude faster than of precipitation under comparable conditions (Christoffersen & Christoffersen, 1976; Christoffersen et al., 1982), making dissolution an unlikely candidate for interface controlled pressure solution. By contrast, the kinetics of the precipitation reaction have been measured by numerous authors (e.g. Liu & Nancollas, 1973a; 1973b;

Packter, 1974; Brandse et al., 1977; Kushnir, 1980; Van Rosmalen et al., 1981; Christoffersen et al., 1982; Weijnen, 1986) and yield precipitation rate laws of order 2 (spiral growth at low driving forces) to 4 (surface nucleation at high driving force). This is consistent with the present data on the stress dependence of creep rate (Chapters 2, 3, 5), suggesting that the rate of pressure solution creep in gypsum could be controlled by the precipitation reaction. However, pressure solution creep rates predicted using the above-mentioned crystal growth data on high purity gypsum have been found to be 2 to 3 orders of magnitude faster than the creep rates obtained experimentally in Chapters 3 and 5. On the other hand, it is well established that the presence of organic and inorganic impurities can dramatically reduce the growth rate of gypsum without significantly effecting the order of the precipitation reaction (e.g. Smith & Alexander, 1970; Liu & Nancollas, 1975; Weijnen, 1986). Furthermore, many of the above mentioned crystal growth studies have been performed with NaCl present in solution, which has a strong accelerating effect on absolute growth rate, again without changing the reaction order (Brandse et al., 1977; Kushnir, 1980). This raises the question of whether the differences between the observed pressure solution creep rates (Chapters 2, 3, 5), and those predicted on the basis of precipitation reaction control, can be explained by differences in composition between the solids and solutions used in crystal growth experiments and those used in the present closed-system compaction tests.

In order to investigate further whether precipitation control can explain the observed pressure solution behaviour in gypsum under closed-system conditions (Chapters 2, 3, 5), crystal growth data are clearly needed for the gypsum and solution phases actually used in the compaction creep experiments, to eliminate effects of compositional differences. In addition, data on any grain size dependence of growth kinetics are needed, for comparison with the dependence of creep rate on grain size observed in the uniaxial compaction experiments (Chapters 3, 5). These points formed the motivation for the experimental investigation of the kinetics of precipitation of gypsum reported in Chapter 4, conducted using the same natural gypsum and same grain size fractions and conditions employed in the uniaxial compaction tests of Chapter 3. In agreement with previous data, the (seed) crystal growth results obtained showed a second order dependence of growth velocity on driving force at low driving forces ($\Delta\mu < 1$ kJ/mole), attributed to a spiral growth mechanism (c.f. Christoffersen et al., 1982; Nielsen, 1986; Sarig, 1994); at higher driving forces, a third order growth relation was obtained, probably reflecting surface nucleation control (c.f. Packter, 1974; Christoffersen et al., 1982; Nielsen,

1986; Weijnen, 1986; Sarig, 1994). Notably, the absolute growth rates measured were roughly 1 - 2 orders of magnitude slower than literature values. In addition, when coupled with literature data (Brandse et al., 1977; Nielsen, 1986), limited evidence was found for an inverse dependence of growth rate on grain size. Most importantly, when the growth data were inserted into a pressure solution model assuming precipitation control, the dependence of compaction creep rate on stress and grain size reported in Chapter 3 was closely reproduced, though the predicted rates were about 30-50 times too fast. Considering the approximate nature of the model used, however, and uncertainties regarding pore fluid impurity content in the creep tests (where the solid/fluid ratio was very high in comparison with the growth experiments), this is considered to represent reasonable agreement.

For still further testing of the hypothesis that pressure solution in the compaction creep experiments was precipitation controlled, data on the influence of pore fluid salinity (NaCl concentration) reported in Chapter 5, and on the effect of pore fluid flushing (Chapter 3), have important implications. First consider the experiments on the effect of dissolved NaCl (Chapter 5). These have demonstrated that the pressure solution rate in gypsum increases strongly with NaCl concentration according to a relation which closely parallels the dependence of gypsum precipitation rate on NaCl concentration obtained by compiling previous crystal growth data (that of Brandse et al., 1977). This effect supports precipitation control but rules out diffusion controlled pressure solution, since theory for this mechanism (Rutter, 1983; Lehner, 1990; Spiers & Schutjens, 1991), coupled with data on the solubility of gypsum in NaCl solutions (Shternina, 1960), predicts only a minor effect of NaCl concentration on compaction creep rate.

Consider now the open-system compaction experiments of Chapter 3, in which $CaSO_4$ solution, saturated with respect to unstressed gypsum sample material, was flushed through the sample under test. These showed a 1 - 2 orders of magnitude acceleration of pressure solution creep rate compared with the "closed-system" experiments - an effect which is only to be expected if large pore fluid supersaturations develop in the closed-system case, i.e. if the pressure solution under these conditions is precipitation limited (see Chapter 3 for detailed arguments).

Combining all of the points above, it is concluded that the samples tested under wet, "closed-system" conditions compacted by grain boundary diffusional pressure solution creep with rate limitation by the pore wall precipitation reaction. This appears to be spiral growth controlled at low driving forces ($\dot{\varepsilon} \propto \sigma^2$) and probably

surface nucleation controlled at driving forces > 1 kJ/mole ($\dot{\epsilon} \propto \sigma^3$), and exhibits an as yet unexplained grain size dependence. The absolute reaction rates and hence pressure solution creep rates are highly sensitive to impurities which can strongly inhibit creep (e.g. organic impurities) or strongly enhance it (e.g. NaCl). An observation, which remains inconsistent with this picture, is the inverse linear dependence of creep rate on grain size reported in the hydrostatic compaction experiments of Chapter 2. In view of the extremely limited (mostly extrapolated) data showing this relation, and the lack of more detailed information on the effect of grain size on precipitation kinetics reported in Chapter 4, this is not considered a serious shortcoming, though is does warrant further hydrostatic experiments.

7.1.2 Time-independent densification processes in FGD-gypsum

From the microstructural observations and the mechanical behaviour reported in the high-speed, uniaxial densification experiments of Chapter 6, it can be inferred that dry granular FGD-gypsum (grain size ~48 μm) densifies by grain scale cataclasis (i.e. microcracking) and "instantaneous" or work hardening plastic deformation of the grains (i.e. grain bending and kinking) when compressed uniaxially at room temperature, at stresses in the range 25-530 MPa, and loading rates of 1.3 MPa s^{-1}. The resulting microstructure consists of grains of uniform reduced size (~25 μm) and roughly equiaxed shape. At temperatures above ~90°C the above deformation processes are accompanied by fluid assisted grain boundary migration and possibly pressure solution, caused by water which is produced by the dehydration reaction of gypsum to the hemihydrate phase. Maximum densities reached in the dry material are 88% at σ = 280 MPa, T = 20°C and 96% at σ = 280 MPa, T = 90°C.

Below the temperature at which a large amount of gypsum dehydrates to hemihydrate (<110°C), densification of FGD-gypsum in the presence of small amounts of added water (1-5%), occurs by microcracking, plastic deformation with fluid-assisted grain boundary migration and probably pressure solution. Cataclastic grain size reduction is reduced compared with dry samples. Furthermore, a significant grain shape preferred orientation is developed due to alignment of surviving elongate grains perpendicular to the loading direction. At temperatures > 110°C, dehydration to the stronger hemihydrate phase inhibits densification. Densification is most effective in wet samples containing ~2 - 2.5wt.% H$_2$O, at high applied stresses (>500 MPa), temperatures close to the dehydration temperature of gypsum to hemihydrate (~100°C), and using high loading rates (>5 MPa s^{-1}). At these

conditions almost fully dense, indurated samples, with porosities as low as 1-2% can be obtained. This residual porosity reflects the volume of added water. The presence of dissolved salts in the added water has no influence on densification.

Compaction creep effects are measurable in wet samples at all temperatures, when maintained at full load, and can be utilized to slightly improve final density. These effects are presumably due to pressure solution, plasticity enhanced by fluid assisted recrystallization, and fluid escape effects. Minor compaction creep occurs in dry material at temperatures > 90°C, presumably due to dislocation creep and effects of water released by dehydration.

7.2 PRESSURE SOLUTION EQUATIONS FOR GYPSUM

Having shown that pressure solution in gypsum under laboratory conditions is controlled by the precipitation reaction, an attempt is now made to develop pressure solution creep laws for gypsum by combining the crystal growth data handled in Chapter 4, and the compaction creep data obtained in Chapters 2, 3 and 5, with theoretical models for precipitation controlled grain boundary diffusional pressure solution.

7.2.1 Equations for compaction of porous gypsum aggregates

Our starting point is to consider a conventional model for precipitation controlled grain boundary diffusional pressure solution, in which the possibility of non-linear precipitation kinetics is allowed for (see Lehner, 1990; Wakai, 1994). As discussed in Chapters 2, 4 and 5, such models take the form

$$\dot{\varepsilon} = B_p \cdot \frac{\sigma_e^n}{d} \cdot f_p(e_v) \tag{7.1}$$

where $\dot{\varepsilon}$ is the compaction strain rate, B_p is a rate coefficient reflecting the precipitation reaction rate coefficient (including any dependence of this on temperature or other variables), σ_e is the applied effective stress, n reflects the order of the precipitation reaction rate law, d is grain size, and $f_p(e_v)$ is a geometric structure factor which decreases in magnitude with increasing volumetric strain e_v (i.e. with decreasing porosity) as grain contact and pore wall areas change. We shall now derive an simple explicit version of this model, pertaining to the case of

uniaxial compaction of a simple drained system (chemically closed). This is done following Spiers et al. (1989) assuming

i) a simple cubic packing of spherical grains surrounded by "saturated solution" at pressure P_f (see Fig. 7.1),

ii) dissolution occurs on horizontal grain boundaries only (refer Fig. 7.1),

iii dissolving grain contacts remain planar throughout compaction and overgrowing pore walls remain spherical,

iv) strains are small ($e_v \leq \sim15\%$), and

v) grain contacts have an island-channel or thin film structure (Weyl, 1959; Rutter, 1976; 1983; Robin, 1978; Raj & Chyung, 1981; Lehner, 1990; Spiers & Schutjens, 1990).

Now, from purely kinematic requirements, and assuming that all mass dissolved at grain contacts (area A_s) is precipitated on the corresponding portion of pore wall (area A_p), it follows from Fig. 7.1 that

$$\dot{\varepsilon} = \frac{-\dot{x}}{x} \approx \frac{2v_p}{d} \cdot \frac{(1-Z)}{Z} \tag{7.2}$$

where $\dot{\varepsilon}$ is the uniaxial compaction strain rate, v_p is the velocity of precipitation on pore walls, and Z is the grain specific ratio of contact area to total grain surface area. However, from crystal growth theory,

$$v_p = f(\Delta\mu) = k^*(\Delta\mu)^n \tag{7.3}$$

where $\Delta\mu$ is the driving force for precipitation, and n is the order of the precipitation rate law (assuming a typical power law). But from pressure solution theory (Lehner, 1990; Spiers & Brzesowsky, 1993; see also Chapter 3), the driving force for grain boundary diffusional pressure solution under steady state closed-system conditions, is given by differences in the surface chemical potential of the solid (μ_s) developed between grain contacts (dissolution or source sites) and pore walls (precipitation of sink sites). This can be written to a first approximation as

$$\Delta\mu_s = (\sigma_n - P_f)\Omega^s \tag{7.4}$$

where σ_n is the normal stress transmitted across an element of grain contact and Ω^s is the molar volume of the solid.
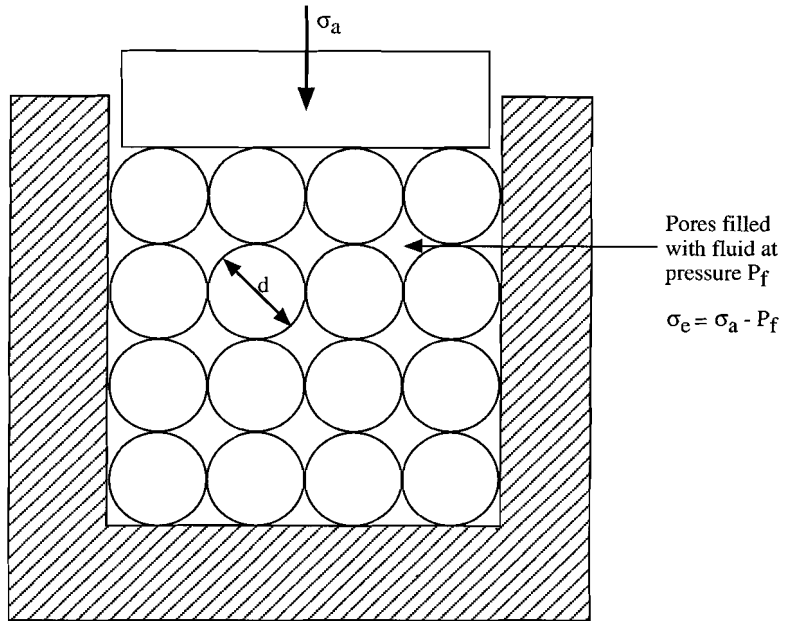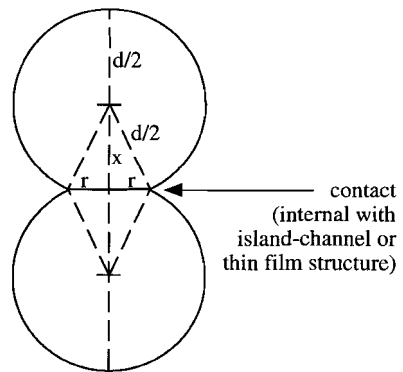
Figure 7.1. Geometry of the simple cubic pack of spherical grains used in deriving the present equations for precipitation controlled pressure solution in porous gypsum aggregates. The small strain approximations are reasonably justified provided that e_v is less than about 15%.

When precipitation is rate controlling, all of the driving force is dissipated in driving the precipitation reaction, so that $\Delta\mu = \Delta\mu_s$, the dissipation by dissolution and diffusion being negligible (Raj, 1982; Lehner, 1990). Since contacts are assumed flat in the present model, the dissolution velocity and hence σ_n will be uniform over grain contacts. Thus σ_n is equal to the average normal stress supported by individual grain contacts and is given (c.f. Spiers & Brzesowsky 1993)

$$\sigma_n = \frac{\sigma_e d^2}{A_s} + P_f = \frac{2\sigma_e}{\pi Z} + P_f \quad with \quad Z = \frac{A_s}{A_t} \tag{7.5}$$

where σ_e is the applied effective stress, $A_s = \pi d^2 Z/2$ and $A_t = \pi d^2/2$ (refer Fig. 7.1). Combing the above equations for σ_n, $\Delta\mu$, $\Delta\mu_s$ and v_p with eq. 7.2 and the approximation $Z \approx e_v$ (Fig. 7.1) now leads to the result

$$\dot{\varepsilon} = \frac{2^{n+1} k^* (\Omega^S)^n}{\pi^n} \cdot \frac{\sigma_e^n}{d} \cdot \frac{1}{e_v^{n+1}} \tag{7.6}$$

which is an explicit form of 7.1. Here, the term $(1 - Z) \approx (1 - e_v)$ is neglected as, at small strain, $(1 - e_v) \approx 1$. Note however, that the exponent to e_v appearing in equation 7.6 is sensitive to the small strain assumption made and cannot be regarded as very accurate.

Now, from the crystal growth experiments reported in Chapter 4, the velocity of (Paris basin) gypsum precipitation from a simple aqueous solution at room temperature follows empirical relations of the form

$$v_p = L \cdot \frac{(\Delta\mu)^a}{d^b} \tag{7.7}$$

where the rate coefficient L and exponents a and b depend on growth mechanism. At low driving forces, that is for $\Delta\mu \leq 1$ kJ/mole or equivalently here for $2\sigma_e\Omega^s/\pi e_v \leq 1$ kJ/mole, where the growth is inferred to be one of spiral growth, fitting of 7.6 to the data presented in Chapter 4 yields

$$v_p = 1 \cdot 10^{-23} \cdot \frac{(\Delta\mu)^2}{d^{1.5}} \tag{7.8}.$$

Here the exponent to $\Delta\mu$ of 2 is consistent with theoretical models for spiral growth

(Nielsen, 1986; Sarig, 1994), but the exponent to d is a purely empirical fit. At higher driving forces, where surface nucleation is believed to be the growth rate controlling mechanism,

$$v_p = 2 \cdot 10^{-32} \cdot \frac{(\Delta \mu)^3}{d^{2.8}} \tag{7.9}$$

where the exponents a=3 and b=2.8 have (rounded) empirical values. Note that, by equating (7.8) and (7.9) and applying (7.4) and (7.5) it follows that the implied boundary between the two growth velocity (mechanism) fields is given at room temperature by

$$\Delta \mu = \frac{2 \sigma_e \Omega^s}{\pi e_v} = 5 \cdot 10^8 \cdot d^{1.3} \quad or \quad \sigma_e^* = \frac{(5 \cdot 10^8) \pi e_v d^{1.3}}{2 \Omega^s} \tag{7.10}$$

where σ_e^* is the applied effective stress on the field boundary.

Making use of the above semi-empirical relations for v_p (7.8, 7.9) in eq. (7.2) and recalling that $Z \approx e_v$ and $(1 - e_v) \approx 1$, the following creep equations are obtained for precipitation controlled pressure solution creep of gypsum in uniaxial compaction mode (drained, chemically closed system):

i) For the spiral growth controlled field (i.e. when $\sigma_e < \sigma_e^*$)

$$\dot{\varepsilon} = A_{sp} \cdot \frac{\sigma_e^2}{d^{2.5}} \cdot \frac{1}{e_v^3} \tag{7.11}$$

where $A_{sp} = 8 \cdot 10^{-23} (\Omega^s)^2 / \pi^2 \approx 4.5 \cdot 10^{-32}$. Assuming the theoretical temperature-dependence for spiral growth rate in eq. 7.8 (Arhenius-type), and using the activation energy for growth of gypsum in this field reported in the literature (Liu & Nancollas, 1970; 1973; Nancollas et al., 1973), this creep equation can be rewritten

$$\dot{\varepsilon} = 1.25 \cdot 10^{13} \cdot A_{sp} \cdot \exp(\frac{-\Delta H}{RT}) \cdot \frac{\sigma_e^2}{Td^{2.5}} \cdot \frac{1}{e_v^3} \tag{7.12}$$

where ΔH is the activation energy ($\Delta H = 60 \pm 8$ kJ/mole), R is the gas constant (R = 8.314 J/Kmole), and T is absolute temperature.

ii) For the surface nucleation field (i.e. when $\sigma_e > \sigma_e{}^*$)

$$\dot{\varepsilon} = A_{sn} \cdot \frac{\sigma_e^3}{d^{3.8}} \cdot \frac{1}{e_v^4} \qquad (7.13)$$

where $A_{sn} = 32 \cdot 10^{-32} (\Omega^s)^3 / \pi^3 \approx 4.2 \cdot 10^{-45}$.

Focusing on room temperature conditions, equations 7.11 and 7.13 above closely reflect the stress, grain size and strain dependencies observed in the compaction creep experiments on (Paris Basin) gypsum reported in Chapters 3 and 5 for the relevant stress ranges (see eq. 7.10). Furthermore, good agreement is obtained between the absolute experimental strain rates and those predicted by 7.11 and 7.13, simply by adjusting the values of A_{sp} and A_{sn} by a factor of 10^{-1}, for creep in the absence of dissolved NaCl (Chapter 3 data), and a factor $10^0 = f(s)$ for creep with a saline pore fluid of NaCl concentration s=1M (Chapter 5 data). This is illustrated in Fig. 7.2 for the spiral growth controlled field and is interpreted to reflect the previously discussed point that the absolute growth rate of gypsum is strongly effected by impurities, without changing the order of the growth velocity relation (i.e. without changing the basic mechanism, presumably).

On this basis, it is proposed that equation 7.11 (also 7.12) and 7.13 provide a satisfactory description of the uniaxial compaction creep behaviour of gypsum by precipitation controlled pressure solution, with the recommended (adjusted) value ranges for A_{sp} and A_{sn} given in Table 7.1.

7.2.2 Equation for dense gypsum

The above approach and assumptions are now applied in order to derive equations for the axi-symmetric creep of dense gypsum or gypsum rock by precipitation controlled pressure solution. To start, consider the idealized "dense" aggregate represented in Fig. 7.3 and subjected to the axi-symmetric stress state defined $\sigma_1 > \sigma_2 = \sigma_3$.
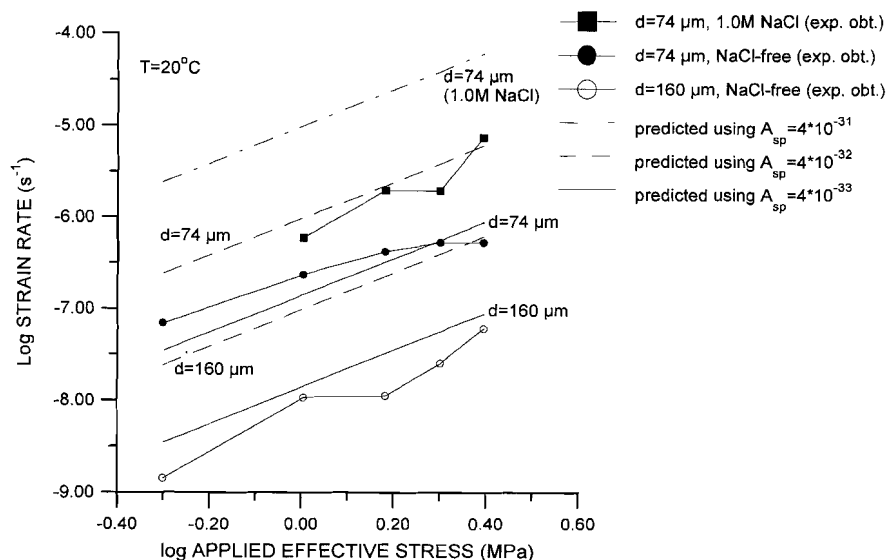
Figure 7.2. Log-log plot of compaction strain rate versus applied effective pressure showing experimentally obtained data (Chapters 3 and 5) and rate data predicted using eq. 7.11. This plot shows that good agreement between experimental data and predicted data is obtained by simply adjusting the values of A_{sp} (see text for explanation).

Table 7.1: Recommended values for A_{sp} and A_{sn} in the precipitation controlled pressure solution creep equations (eq. 7.11-13 and 7.16-18).

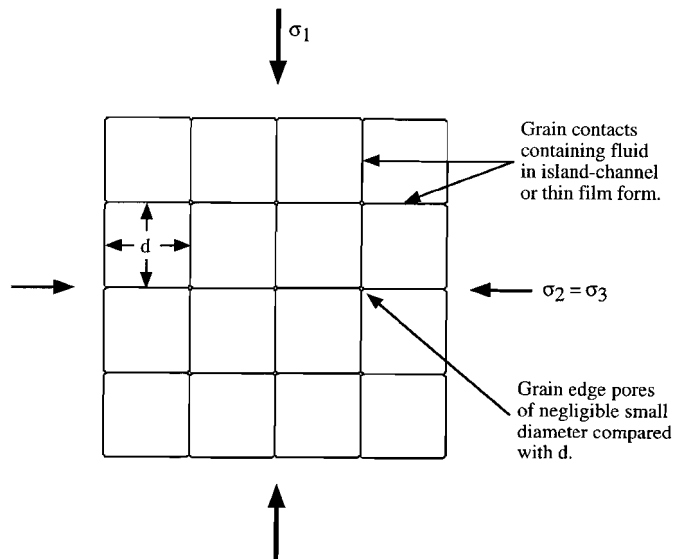|	A_{sp}	A_{sn}
Natural gypsum (Somerset) non saline fluid (Chapter 2)	$(4 \pm 2) \cdot 10^{-34}$	$(4 \pm 2) \cdot 10^{-47}$
Natural gypsum (Paris Basin) non saline fluid (Chapter 3)	$(4 \pm 2) \cdot 10^{-33}$	$(4 \pm 2) \cdot 10^{-46}$
Natural gypsum (Paris Basin) 1M NaCl (Chapter 5)	$(4 \pm 2) \cdot 10^{-32}$	$(4 \pm 2) \cdot 10^{-45}$
Natural gypsum (Paris Basin) 3M NaCl (chapter 5)	$(4 \pm 2) \cdot 10^{-32}$	$(4 \pm 2) \cdot 10^{-45}$
Analytical grade gypsum non saline fluid	$(2 \pm 1) \cdot 10^{-30}$	$(2 \pm 1) \cdot 10^{-43}$
FGD gypsum non saline fluid	$(4 \pm 2) \cdot 10^{-34}$	$(4 \pm 2) \cdot 10^{-47}$

Figure 7.3. Simple pack of cubic grains with grain edge pores of negligibly small diameter compared with grain size (d). This geometry is used to derive precipitation controlled pressure solution equations for dense gypsum.

In such a situation, the difference in normal stress between horizontal and vertical grain boundaries will give rise to a difference in the surface chemical potential (μ_s) of the solid between these sites, given $\Delta\mu_s = (\sigma_1 - \sigma_2)\Omega^s = \sigma_d\Omega^s$ (see Raj & Chyung, 1981; Raj, 1982). This will cause material to dissolve from the horizontal contacts and to precipitate at the vertical ones, giving creep. If the velocity of dissolution is v_s and of precipitation is v_p, kinematic and mass balance requirements for the configuration in Fig. 7.3 imply

$$\dot{\varepsilon}_a = \frac{2v_s}{d} = \frac{4v_p}{d} \tag{7.14}$$

where $\dot{\varepsilon}_a$ is the axial creep rate. Now, in the case of precipitation controlled creep, all of the driving force ($\Delta\mu_s$) will be used to drive the precipitation reaction on vertical grain boundaries. Assuming that this reaction can again be described by a crystal growth law of the form $v_p = k^*(\Delta\mu)^n$ where $\Delta\mu$ is the potential drop driving the reaction, equation 7.14 now modifies to the axi-symmetric steady-state creep

equation

$$\dot{\varepsilon}_a = \frac{4k^*(\Omega^s)^n(\sigma_d)^n}{d}$$ (7.15).

From Chapter 4, it is known, however, that k^* and n for gypsum depend on the growth mechanism and that k^* depends on grain size, as expressed in eqs. 7.8 for spiral growth and 7.9 for surface nucleation control. Assuming that these relations are valid for the precipitation reactions occurring on the vertical grain boundaries in dense gypsum, insertion of them into eq. 7.14 yields the following precipitation controlled pressure solution creep equations for dense gypsum:

i) For the spiral growth controlled field (low driving force or stresses)

$$\dot{\varepsilon}_a = 5 \cdot A_{sp} \cdot \frac{\sigma_d^2}{d^{2.5}}$$ (7.16)

or, including the temperature-dependence for spiral growth incorporated in (7.12)

$$\dot{\varepsilon}_a = 6.25 \cdot 10^{13} \cdot A_{sp} \cdot \exp(\frac{-\Delta H}{RT}) \cdot \frac{\sigma_d^2}{Td^{2.5}}$$ (7.17)

with $\Delta H = 60 \pm 8$ kJ/mole and R = 8.314 J/Kmole.

ii) For the surface nucleation field (higher driving forces or stresses)

$$\dot{\varepsilon}_a = 7.75 \cdot A_{sn} \cdot \frac{\sigma_d^3}{d^{3.8}}$$ (7.18)

In the above, $A_{sp} = 8 \cdot 10^{-23}(\Omega^s)^2/\pi^2 \approx 4.5 \cdot 10^{-32}$ and $A_{sn} = 32 \cdot 10^{-32}(\Omega^s)^3/\pi^3 \approx 4.2 \cdot 10^{-45}$. However, following the same arguments pursued for compaction creep, these may be assigned any of the recommended values given in Table 7.1. As for compaction creep, the boundary between the above two fields at room temperature can be obtained by equating 7.8 with 7.9 or 7.16 with 7.18. This yields $\Delta\mu = \sigma_d\Omega^s = 5 \cdot 10^8$ $d^{1.3}$ or $\sigma_d^* = 5 \cdot 10^8$ $d^{1.3}/\Omega^s$ where σ_d^* is the differential stress on the field boundary. Thus the spiral growth field is the region $\sigma_d \le \sigma_d^*$ and the surface nucleation field is $\sigma_d > \sigma_d^*$.

7.3 BEHAVIOUR OF GYPSUM IN NATURE

7.3.1 Deformation mechanisms maps

In order to evaluate the importance of pressure solution creep of dense gypsum rock in nature, the above constitutive equations (7.16 - 7.15) have been used to construct deformation mechanism maps (Fig. 7.4 a-d). In these maps the flow law for gypsum

$$\dot{\varepsilon}_a = 4.5 \cdot \exp(\frac{-\Delta Q}{RT}) \cdot \sigma_d^{4.5} \tag{7.19}$$

as proposed by Baumann (1984) has been used to define the dislocation creep field. In this equation $\dot{\varepsilon}_a$ is the axial strain rate, σ_d is the differential stress, and ΔQ is the apparent activation energy for dislocation creep ($\Delta Q = 132kJ/mole$). Figures 7.4a and 7.4b are deformation mechanism maps for the two "extreme" cases of pure gypsum with highly saline pore fluid (Fig. 7.4a, $A_{sp} = 4 \cdot 10^{-32}$ and $A_{sn} = 4 \cdot 10^{-45}$ - see Table 7.1) and for impure gypsum with NaCl-free pore fluids (Fig.7.4b, $A_{sp} = 4 \cdot 10^{-33}$ and $A_{sn} = 4 \cdot 10^{-46}$ - see Table 7.1) at 20°C. Recognizing that natural gypsum has grain sizes typically in the range 0.1 to 3mm (Jordan, 1994) and taking extreme natural strain rates of 10^{-15} s^{-1} and 10^{-9} s^{-1}, appropriate for all situations ranging from bulk orogenic rates, diapiric rates and highly localized intra-decollement deformation, these figures predict that gypsum should deform by spiral growth controlled pressure solution creep under near-surface conditions (~20°C). The figures also show that under these conditions, dislocation creep is expected to become important only in the coarsest, most impure gypsum, with low salinity pore fluid and at rapid strain rates (e.g. decollement rates), and that surface nucleation controlled pressure solution is unlikely to occur.

In order to be able to construct deformation mechanism maps at elevated temperatures for which gypsum is still stable or metastable, the temperature-dependence of both pressure solution creep laws must be known. However, that for pressure solution creep controlled by surface nucleation is unknown, so as a first approximation it is assumed here to be the same as for spiral growth controlled pressure solution (see eq. 7.17). Using this approach, deformation mechanism maps have been drawn for a maximum likely natural temperature of 60°C, again for pure gypsum with highly saline NaCl-bearing pore fluids (Fig. 7.4c), and for impure

gypsum with NaCl-free pore fluids (Fig. 7.4d). The results show a slight expansion of the dislocation creep field, but at 60°C pressure solution creep controlled by spiral growth is still predicted to be the dominant deformation mechanism in nature. The complete set of maps (Figs. 7.4a-d) shows that at all temperatures in the range 20-60°C, flow stresses in gypsum undergoing natural deformation by spiral growth controlled pressure solution will mostly be of the order of only 0.1-10 MPa, with a max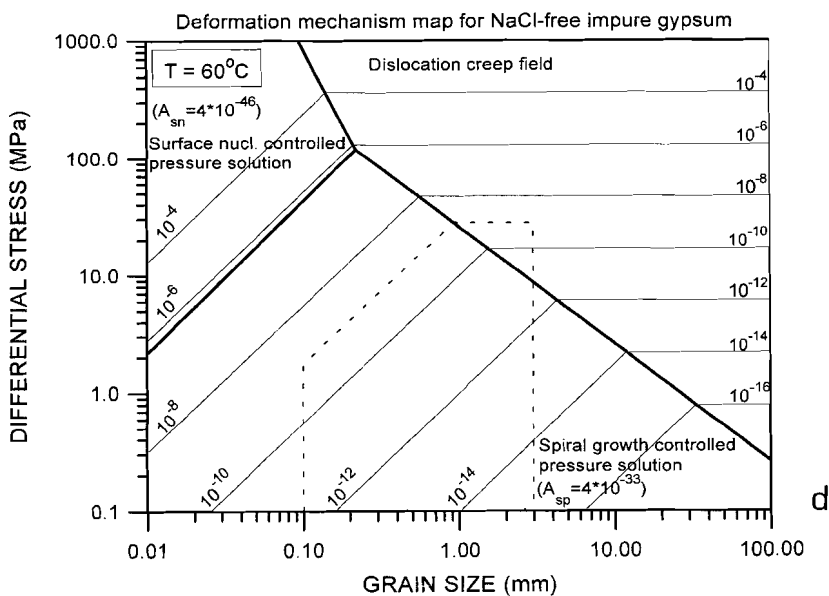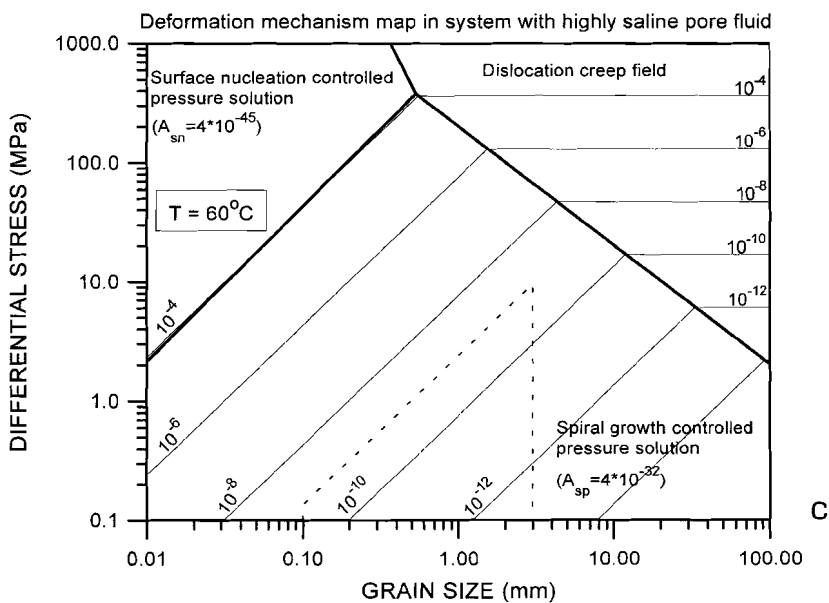imum of 100 MPa possible, due to dislocation creep, under very extreme conditions (coarse, impure gypsum with non-saline pore fluid, at strain rates $> 10^{-11}$ s^{-1}).

Figure 7.4 (next two pages).

a) Deformation mechanism map for high purity gypsum rock with highly saline grain boundary pore fluid phase ([NaCl]=1M; A_{sp}=4·10^{-32}, A_{sn}=4·10^{-45} according to Table 7.1). Temperature 20°C. Contours give strain rates (s^{-1}). Dashed box indicates the strain rate and grain size field relevant for flow of gypsum in nature ($\dot{\varepsilon}$=10^{-15}→10^{-9} s^{-1}, d=0.1-3.0 mm). Note that this map depicts the maximum expected pressure solution strain rates and hence maximum extent of the pressure solution field.

b) Deformation mechanism map for impure gypsum rock (comparable to Paris Basin gypsum) with NaCl-free grain boundary fluid (A_{sp}=4·10^{-33}, A_{sn}=4·10^{-46} following Table 7.1). Temperature 20°C. Contours give strain rates (s^{-1}). Dashed box indicates strain rate and grain size field relevant for natural gypsum flow. This map predicts the minimum expected pressure solution strain rates and hence minimum extent of the pressure solution field.

c) Deformation mechanism map for high purity gypsum rock with highly saline grain boundary fluid; T=60°C. Parameters A_{sp}, A_{sn} as for 7.4a.

d) Deformation mechanism map for impure gypsum rock (c.f. Paris Basin) with NaCl-free grain boundary fluid T=60°C. Parameters A_{sp}, A_{sn} as for 7.4b.

Deformation mechanism map for system with highly saline pore fluid

a

Deformation mechanism map for NaCl-free impure gypsum

b

Deformation mechanism map in system with highly saline pore fluid

Deformation mechanism map for NaCl-free impure gypsum
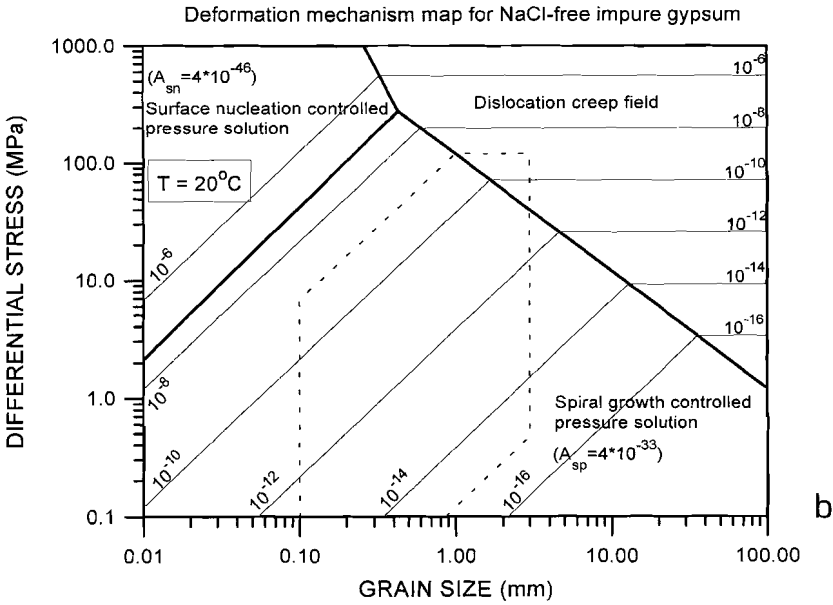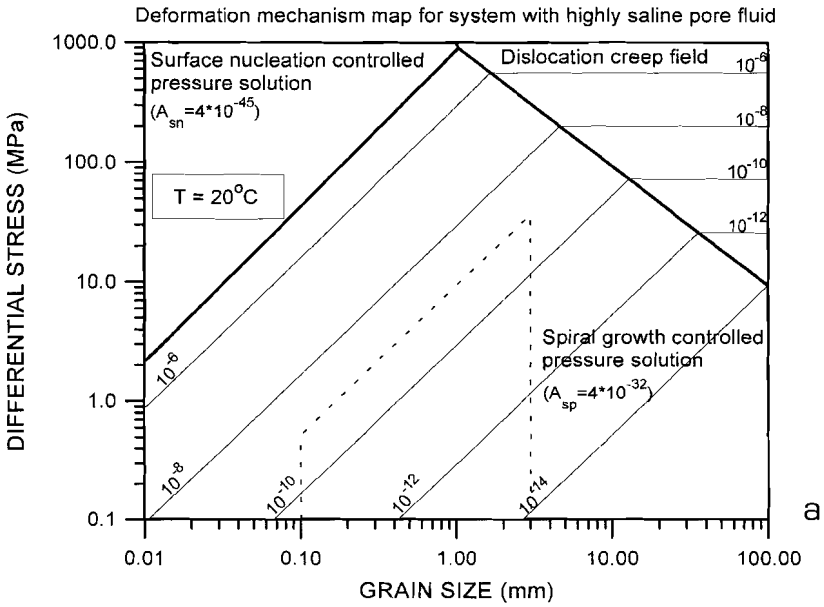
7.3.2 Strength of the upper crust

In Figure 7.5 a strength profile diagram for the upper crust, in a Jura mountains (decollement) type of setting, is constructed (c.f. Jordan, 1994). For the strength of Jura gypsum (grain size d=0.1-1mm), the spiral growth pressure solution creep equation (eq. 7.17) developed in this chapter and the dislocation creep flow law (eq. 7.19) of Baumann (1984) have been used. The parameter A_{sp} for the pressure solution equation has been chosen for the realistic situation of impure gypsum with highly saline grain boundary fluid (A_{sp} = $4 \cdot 10^{-32}$ refer Table 7.1). The data of Nüesch (1991), Müller & Briegel (1978) and Müller et al. (1981) have been used to plot the strength of shales and anhydrite. The figure shows that under almost all conditions, pressure solution is "weaker" than dislocation creep and should dominate in the gypsum. The gypsum is also weaker than anhydrite and shale (at depths > a few 100 m). Indeed the pressure solution creep model predicts that gypsum has hardly any strength at low strain rates (< 1 MPa at 10^{-14} s^{-1}). Even at relatively high creep rates (10^{-10} s^{-1}), the strength of gypsum is very low ($\leq$ 4 MPa) for the small grain sizes (0.1 mm). Thus gypsum could easily dominate decollement flow at stresses around 1 MPa.

Figure 7.6 confirms that the strain rates predicted by the pressure solution creep model are almost always smaller than those predicted by the dislocation creep flow law of Baumann (1984) under Jura conditions. The box shown indicates the relevant conditions of strain rate for decollement of the Jura mountains quoted by Jordan (1994). This also suggests that pressure solution creep should have been the dominant deformation mechanism in the Jura mountain gypsum decollement horizons with flow stresses of around 0.1-1 MPa. Further work is needed on this to assess in how far the predominance of pressure solution is supported by microstructural observations on natural Jura samples.
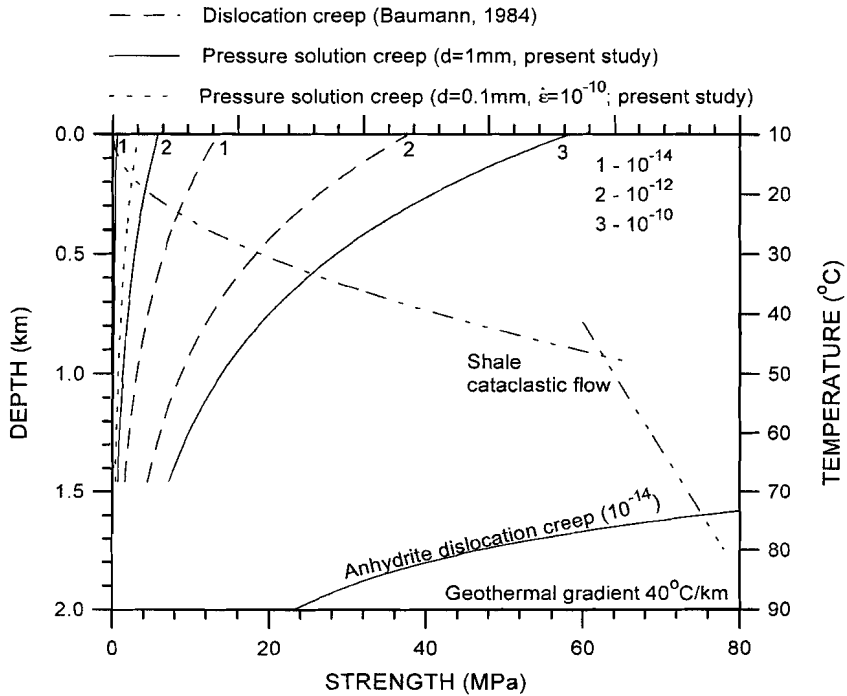
Figure 7.5 Strength profile diagram drawn for upper crustal conditions corresponding to a Jura Mountains type of setting. Pressure solution creep rates are calculated using the spiral growth controlled pressure solution equation applied for impure gypsum with saline grain boundary fluid ($A_{sp}=4\cdot10^{-33}$).
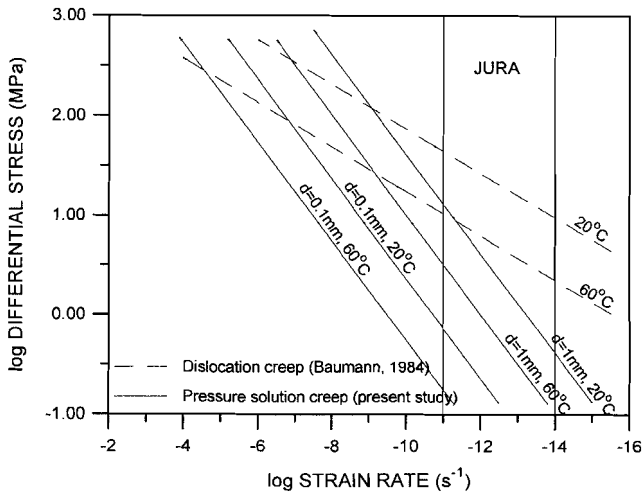
Figure 7.6. Deformation mechanism map for natural gypsum (impure, saline pore fluid - 1M NaCl) drawn in stress versus strain rate space for spiral growth controlled pressure solution creep ($A_{sp}=4 \cdot 10^{-33}$) plus dislocation creep.

7.4 IMPLICATIONS FOR BUILDING MATERIALS RESEARCH

The high speed densification experiments reported in Chapter 6 of this thesis have shown that it is technically easy to densify FGD-Gypsum mechanically to very low porosities (1-5%), notably if a few percent of water are present. The wet-pressed products are well-indurated, and have quite high compressive fracture strength (up to ~100 MPa, Stoop et al., 1995) which renders them superficially suitable for structural applications. Dry-compacted products have low compressive strength and are not suitable (Heijnen & Stoop, pers. comm., 1995).

However, to assess fully the suitability of dense, wet-pressed, FGD-Gypsum as a structural building material, the question of pressure solution creep clearly needs to be considered. These materials are not only prepared with water present, but may become damp in specific building applications. For this reason, the relevant pressure solution creep model (i.e. the low stress, spiral growth model, eq. 7.17) has been used to predict creep rates of dense gypsum building materials, produced by rapid densification of FGD-gypsum, for stresses appropriate to load-bearing applications. This was done bearing in mind that the FGD-gypsum starting material used in the

densification experiments of Chapter 6 has been shown to exhibit pressure solution compaction creep rates (uniaxial tests not reported in this thesis) which were one order of magnitude slower than creep rates observed in the uniaxial compaction experiments on natural (Paris Basin) gypsum reported in Chapter 3. On this basis, an appropriate value for the kinetic coefficient A_{sp} is $4 \cdot 10^{-34}$ (c.f. Table 7.1). The model predicts creep rates (Fig. 7.7) which are far too fast to sanction use of dense FGD-gypsum building products in structural load-bearing applications.
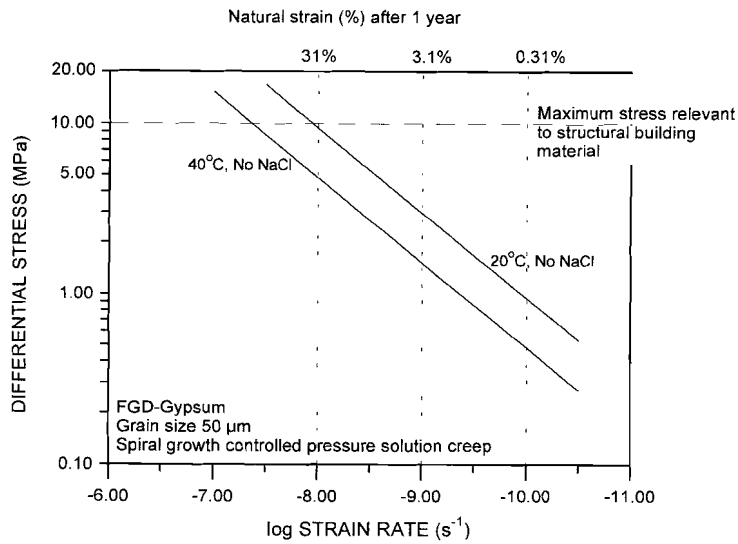

Figure 7.7.Predicted pressure solution creep behaviour of dense FGD-gypsum material at stresses characteristic of load-bearing applications in the building industry. The pressure solution creep mechanism for these conditions is the spiral growth process. The corresponding creep eq. (7.17) has been applied with $A_{sp}=4 \cdot 10^{-34}$, estimated from experiments on FGD-gypsum.

7. 5 SUGGESTIONS FOR FURTHER WORK

The experiments reported in this thesis have shown that grain boundary diffusional pressure solution creep is indeed an important mechanism of compaction under laboratory conditions, and that the rate of deformation is controlled by the precipitation reaction. Under natural conditions, it has been shown that spiral growth controlled pressure solution should be the dominant mechanism in gypsum. It has also been shown that nearly fully dense gypsum materials can be obtained by rapidly densifying damp FGD-gypsum powders mechanically, and the potential of the products as load-bearing building materials has been considered. However, it will be apparent to the reader that a number of questions remain unanswered and that some new questions have been raised. In the following, suggestions for further work are proposed.

i) The results of the uniaxial and hydrostatic compaction experiments reported in Chapters 2 and 3 of this thesis, while exhibiting clear evidence for precipitation controlled pressure solution, are not entirely consistent. Notably the hydrostatic experiments (Chapter 2) showed considerably slower creep (1-2 orders) and an inverse linear grain size dependence which is not seen in the uniaxial tests of Chapters 3 (and 5), and is not predicted from crystal growth data (Chapter 4). While there is good reason to expect that the hydrostatic creep tests were slower due to a different starting material impurity content, the inverse linear grain size dependence is unexplained. On the other hand, the amount of data obtained on the influence of grain size under hydrostatic conditions was very limited and largely extrapolated (see Chapter 2). Clearly then, a more extensive investigation of hydrostatic compaction creep of wet gypsum is needed, paying careful attention to grain size and impurity effects.

ii)   In Chapter 4, on the precipitation of gypsum on "natural" gypsum, data were obtained indicating a grain size dependence of growth rate. The data, when coupled with models for precipitation controlled pressure solution predicted creep behaviour which agrees well with the uniaxial creep results of Chapter 3 (closed-system) to within 1 - 2 orders of magnitude, and shows identical trends. The same trends were also found in the uniaxial compaction experiments with saline pore fluid (Chapter 5). However, the amount of crystal growth data presented in Chapter 4, particularly on the effect of grain size on growth rate, are limited and more experiments are

needed to consolidate the present description of this effect and to gain insight into the mechanistic reason for it. In these growth experiments, care should be taken to use not only the same gypsum solid as used in the creep experiments, but also solutions of the same chemical composition as the pore fluids used in the pressure solution creep experiments, i.e. solutions prepared using similar solid-fluid ratios. The substantial difference in volume ratio of solid to liquid between the present pressure solution experiments (Chapter 3) and crystal growth experiments (Chapter 4) might be a cause for compositional differences in the solutions and for the observed 1-2 order rate discrepancies. Ideally, new growth experiments should be make use of a calcium specific electrode as well as electrical conductivity to measure the progress of the precipitation reaction.

iii)   The amount of evidence for the operation of precipitation controlled pressure solution creep in gypsum presented in this thesis is substantial. However, ultimate proof for rate limitation by the precipitation reaction could be obtained from compaction creep experiments in which the axial electrical conductivity (κ) of the fluid-saturated sample is measured in-situ, i.e. during compaction creep. Bearing in mind Archie's law and the near linear relation between bulk fluid conductivity and solute concentration (see Chapter 4, Fig. 4.2), the conductivity of the sample at fixed porosity is, of course, related to the $CaSO_4$ concentration (C) in the pore fluid via a linear relation

$$\kappa = K \cdot C \tag{7.20}$$

Now, as demonstrated in Chapter 3, during precipitation controlled pressure solution in a simple drained compaction experiment, the pore fluid will develop a supersaturation given (using 7.5) as

$$\frac{\Delta C}{C_o} = \frac{\sigma_n^e \Omega^s}{RT} \approx \frac{2\sigma_e \Omega^s}{\pi e_v RT} \tag{7.21}$$

where C_o is the solubility of the unstressed solid, σ_n^e is the effective grain contact normal stress, σ_e is the applied effective stress, Ω^s is the molar volume of the solid, R is the gas constant (R=8.314 $JK^{-1}mole^{-1}$) and T is absolute temperature. Thus, at constant aggregate structure (i.e. approximately constant strain (e_v) in samples with similar starting porosities), σ_n^e and hence ΔC and therefore the sample conductivity

κ should be linearly related to differences in applied (effective) stress. In contrast, when either dissolution or diffusion controls the rate of pressure solution creep, the concentration of $CaSO_4$ in the pore fluid will remain roughly constant (independent of the stress applied, see Chapter 3 Section 3.4.4). However, if pressure solution creep is rate limited by the precipitation reaction, the concentration of $CaSO_4$ in the pore fluid is linearly related to the stress applied as shown above, and in a plot of κ versus applied stress at constant strain, the slope of the lines obtained will be simply related to the quantity Ω_s/RT. This offers an excellent test for precipitation control.

iv)   The question was raised in Chapter 2 of this thesis whether conventional models of pressure solution creep (Raj, 1982; Rutter, 1983; Spiers et al. 1989; Spiers & Schutjens, 1990; Spiers & Brzesowsky, 1993; Lehner, 1995) can be applied to gypsum, since these models have not previously been rigorously extended to cover the case of solids containing water of crystallization. In Chapter 3, simple theoretical arguments were used to demonstrate that the conventional models do apply for gypsum. However, it was shown that for heavily hydrated salts, such as bischofite, conventional models are less applicable. To describe pressure solution creep in heavily hydrated salts, rigorous new models should be derived incorporating the effect of water of crystallization on the thermodynamic driving force for pressure solution creep, and particularly on the rate controlling processes which also include the flow of water out of grain boundaries. These models should then be tested by performing experiments on materials such as bischofite, carnalite or alums. Parallel arguments apply for pressure solution in silicate minerals plus a silicate partial melt phase. Similar effects should occur in these systems as in hydrated salts plus solution, and should obviously be investigated too since they might have important implications for melt migration in the upper mantle, for example.

v)   The presently derived creep models for spiral growth controlled pressure solution creep in dense gypsum indicate that this mechanism will dominate the creep of gypsum under natural conditions. Further microstructural work on natural deformed gypsum rocks (e.g. Jura gypsum) is needed to confirm/validate this conclusion.

vi)   In building materials research community, it is expected that dense (FGD) gypsum products will show improved strength and resistance to creep over conventional, porous gypsum products, that way enabling (FGD) gypsum to be used in load-bearing applications in the building industry. In Chapter 6 it was shown that highly indurated almost fully dense gypsum samples can be obtained by directly densifying damp gypsum powders. However, predictions using the pressure solution creep equations developed in this thesis show that creep is likely to be a problem under wet conditions. Nonetheless, additional experiments are needed to directly determine the strength of dense FGD material and particularly their resistance to creep.

REFERENCES

Balkwill, H.R. 1978. Evolution of Sverdrup basin, arctic Canada. AAPG Bull., vol. 62(6), p 1004-1028.

Barcelona, M.J. & Atwood, D.K., 1978. Gypsum-organic interactions in natural seawater: Effect of organics on precipitation kinetics and crystal morphology. Marine Chem., vol. 6, p 99-115.

Baumann, W. 1984. Rheologische Untersuchungen an Gips. Eclogae Geol. Helv., vol. 77, p 301-325.

Beach, A., 1981. Some observations on the development of thrust faults in the Ultradauphinois Zone, French Alps. In: K.R. McClay (Editor), Thrust and Nappe Tectonics. Geol. Soc. London, Spec. Publ., vol. 9, 329-334.

Bell, F.G. 1994. A survey of the engineering properties of some anhydrite and gypsum from the north and midlands of England. Engineering Geology, vol. 38, p 1-23.

Blount, C.W. & Dickson, F.W. 1973. Gypsum-anhydrite equilibria in systems $CaSO_4$-H_2O and $CaSO_4*H_2O$. Am. Min., vol. 58, p 323-331.

Bosbach, D. & Rammensee, W. 1994. In situ investigation of growth and dissolution on the (010) surface of gypsum by scanning force microscopy. Geoch. et Cosmoch. Acta, vol. 58, p 843-849.

Brandse, W.P., Van Rosmalen, G.M. & Brouwer, G. 1977. The influence of sodium chloride on the crystallization rate of gypsum. J. Inorg. Nucl. Chem., vol. 39, p 2007-2010.

Christoffersen, J. and Christoffersen, M.R. 1976. The kinetics of dissolution of calcium sulphate dihydrate in water. J. Cryst. Growth, vol. 35, p 79-88.

Christoffersen, J., Christoffersen, M.R., Van Rosmalen, G.M. & Marchee, W.G.J. 1979. The affinity of crystal growth and dissolution in aqueous solution with special reference to calcium sulphate dihydrate. J. Cryst. Growth, vol. 47, p 607-612.

Christoffersen, M.R., Christoffersen, J., Weijnen, M.P.C. and Van Rosmalen, G.M. 1982. Crystal growth of calcium sulphate dihydrate at low supersaturation. J. Cryst. Growth, vol. 58, p 585-595.

Cody, R.D. & Cody, A.M., 1988. Gypsum nucleation and crystal morphology in analog saline terrestrial environments. J. Sed. Pet., vol. 58, p 247-255.

Cody, A.M. & Cody, R.D. 1991. Chiral habit modifications of gypsum from epitaxial-like adsorption of stereospecific growth inhibitors. J. Cryst. Growth, vol. 113, p. 508-519.

Craker, W.E. & Schiller, K.K. 1962. Plastic deformation of gypsum. Nature, vol. 193, p 672-673.

Dabbagh, A.E., Hoetzl, H. & Schier, H. 1984. South Tihamah and Farasan Islands; Farasan Islands. Quaternary Period in Saudi Arabia, vol. 2, p 212-220.

Davis, D.M. & Engelder, T. 1985. The role of salt in fold-and-thrust belts. Tectonophysics, vol. 119, p 67-88.

Doglioni, C. 1984. Triassic diapiric structures in the central Dolomites (Northern Italy). Eclogae Geol. Helv., vol. 77, p 261-285.

Gill, J.S. & Nancollas, G.H. 1980. Kinetics of growth of calcium sulphate dihydrate at heated metal surfaces. J. Cryst. Growth, vol. 48, p 34-40.

Gould, D.B. & De Mille, G. 1968. Piercement structures in Canadian arctic islands. In: J. Braunstein and G.D. O'Brien, Diapirsm and diapirs. AAPG memoir, vol. 8, p 183-214.

Griggs, D.T. 1939. Creep of rocks. J. Geol., vol. 47, p 225-251.

Griggs, D.T. 1940. Experimental flow of rocks under conditions favouring recrystallization. Geol. Soc. Am. Bull., vol. 51, p 1001-1022.

Hardie, L.D. 1967. The gypsum-anhydrite equilibrium at one atmosphere pressure. Am. Min., vol. 52, p 171-200.

Heard, H.C. & Rubey, W.W. 1966. Tectonic implications of gypsum dehydration. Geol. Soc. Am. Bull., vol. 77, p 741-760.

Jordan, P.G. 1988. Deformationsverhalten der Keuper Evaporit des Belchen-Tunnels (Faltenjura, Schweiz). Erlanger Geol. Abh., vol. 116, p 53-66.

Jordan, P.G. 1991. Development of asymmetrical shale pull-aparts in evaporite shear zones. J. Struc. Geol., vol. 13(4), p 399-409.

Jordan, P.G. 1994. Evaporite als Abschierhorizonte: Eine gefügekundlich-strukturgeologische Untersuchung am Beispiel de Nordschweizer Trias. Beitrage zur Geologischen Karte der Schweiz, vol. 164, pp 79.

Jordan, P.G. Noack, T. & Widmer, T. 1990. The evaporite shear zone of the Jura Boundary Thrust - New evidence from Wisen well (Switzerland). Eclogae Geol. Helv., vol. 83(3), p 525-542.

Karni, J. & Karni, E. 1995. Gypsum in construction: origin and properties. Materials and Structures, vol. 28, p 92-100.

Ko, S.C., Olgaard, D.L. & Briegel, U. 1995. The transition from weakening to strengthening in dehydrating gypsum: Evolution of excess pore pressures. Geoph. Res. Letters, vol. 22, p 1009-1012.

Kupfer, D.H. 1989. Gypsum dehydration, agent of salt diapirism. AAPG Bull., vol. 73(9), p. 1186.

Kushnir, J., 1980. Effect of the Ca/SO_4 ratio on the growth rate and crystal habit of gypsum. In: Hsue, K.J. (ed.). Int. Assoc. Sedimentologists, 1st European meeting, Bochum 1980., p 239-241.

Laubscher, H.P. 1981. The 3D propagation of décollement in the Jura. In: K.R. McClay (Editor), Thrust and Nappe Tectonics. Geol. Soc. London, Spec. Publ., vol. 9, p 311-318.

Lehner, F.K. 1990. Thermodynamics of rock deformation by pressure solution. In: D.J. Barber and P.D. Meredith (Editors), Deformation Processes in Minerals, Ceramics and Rocks. Unwin Hyman, London, pp 296-333.

Lehner, F.K. 1995. A model for intergranular pressure solution in open systems. In: C.J. Spiers and T. Takeshita (Editors), Influence of fluids on deformation processes in rocks. Tectonophysics, vol. 245, p 153-170.

Liu, S.T. & Nancollas, G.H. 1970. The kinetics of crystal growth of calcium sulphate dihydrate. J. Crystal Growth, 6, p 281-289.

Liu, S.T. & Nancollas, G.H. 1973a. Linear crystallization and induction-period studies of the growth of calcium sulphate dihydrate crystals. Talanta, vol. 20, p 211-216.

Liu, S.T. & Nancollas, G.H. 1973b. The crystal growth of calcium sulphate dihydrate in the presence of additives. J. Coll. Int. Sci., vol. 44, p 422-429.

Liu, S.T. & Nancollas, G.H. 1975. A kinetic and morphological study of the seeded growth of calcium sulphate dihydrate in the presence of additives. J. Coll. Interf. Sci., vol. 52, p 593-601.

Liu, S.T. & Nancollas, G.H. 1976. A kinetic and morphological study of the seeded growth of calcium sulphate dihydrate in the presence of additives. J. Coll. Int. Sci., vol. 52-3, p 593-601.

MacDonald, G.J.F. 1953. Anhydrite-gypsum equilibrium relations. Am. J. Sci., vol. 251, p 884-898.

Malavieille, J. & Ritz, J.F. 1989. Mylonitic deformation of evaporites in décollements: examples from the Southern Alps, France. J. Struc. Geol., vol. 11(5), p 583-590.

Marsal, D. 1952. Der Einfluss des Druckes auf das System $CaSO_4$-H_2O. Heidelberger Beitr. Min. Petrogr., Bd. 3, p 289-296.

McCartney, E.R. & Alexander, A.E.. 1958. The effect of additives upon the process of crystallization. I. Crystallization of calcium sulfate. J. Coll. Sci., vol. 13, p 383-396.

Milliken, K.L. 1994. The widespread occurrence of healed microfractures in siliciclastic rocks: Evidence from scanned cathodoluminescence imaging. In: P.P. Nelson and S.E. Laubach (Editors), Rock Mechanics, Models and Measurements. Proceedings of the North American Rock Mechanics Symposium, Austin, TX. A.A. Balkema, Rotterdam, pp 825-832.

Mügge, O. 1898. Über Translationen und verwandte Erscheinungen in Krystallen. Neues Jahrb. Min. Geol. Pal., Bd. 1, p 71-154.

Mugnier, J.L. & Vialon, P. 1986. Deformation and displacement of the Jura cover on its basement. J. Struc. Geol., vol. 8 (3/4), p 373-387.

Murrell, S.A.F. 1981. The rock mechanics of thrust and nappe formation. In: K.R. McClay (Editor), Thrust and Nappe Tectonics. Geol. Soc. London, Spec. Publ., vol. 9, p 99-109.

Murrell, S.A.F. 1985. Aspects of relationships between deformation and prograde metamorphism that causes the evolution of water. Adv. Phys. Geoch., vol. 4, p 211-241.

Murrell, S.A.F. & Ismail, I.A.H. 1976. The effect of decomposition of hydrous minerals on the mechanical properties of rocks of high pressure and temperature. Tectonophysics, vol. 31, p 201-218.

Nancollas, G.H., Reddy, M.M. & Tsai, F. 1973. Calcium sulphate dihydrate crystal growth in aqueous solution at elevated temperatures. J. Cryst. Growth, vol. 20, p 125-134.

Nielsen, A.E. 1984. Electrolyte crystal growth mechanisms. J. Crystal Growth, vol. 67, p 289-310.

Nielsen, A.E. 1986. Mechanisms and rate laws in electrolyte crystal growth from aqueous solution. In: Geochemical processes at mineral surfaces, J.A. Davis and K.F. Hayes (Editors), ACS Symp. Ser. 323, p 600-614.

Nielsen, A.E. & Toft, J.M. 1984. Electrolyte crystal growth kinetics. J. Cryst. Growth, vol. 67, p 278-288.

Nüesch, R. & Baumann, W. 1989. Ton- und Sulfatgesteine in Wechselwirkung bei Deformation. Geol. Runds., vol. 78, p 443-457.

Olgaard, D.L., Ko, S.C. & Wong, T.F. 1995. Deformation and pore pressure in dehydrating gypsum under transiently drained conditions. In: C.J. Spiers and T. Takeshita (Editors), The influence of fluids on deformation processes in rocks, Tectonophysics, vol. 245, p 237-248.

Packter, A. 1974. The precipitation of calcium sulphate dihydrate from aqueous solution. J. Cryst. Growth, vol. 21, p 191-194.

Panozzo Heilbrunner, R. 1993. Controlling the spatial distribution of deformation in experimentally deformed and dehydrated gypsum. In: J.D. Boland and J.D. Fitz Gerald (Editors), Defects and processes in the solid state: Geoscience Applications, The McLaren Volume. Elsevier Science Publishers, p 169-194.

Paterson, M.S. 1973. Thermodynamics and its geological applications. Rev. Geoph. Space Phys., vol. 11, p 355-389.

Paterson, M.S. 1995. A theory for granular flow accommodated by material transfer via an intergranular fluid. In: C.J. Spiers and T. Takeshita (Editors), Influence of fluids on deformation processes in rocks. Tectonophysics, vol. 245, p 135-152.

Pharr, G.M. & Ashby, M.F. 1983. On creep enhanced by a liquid phase. Acta Metall., vol. 31, p 129-138.

Posnjak, E. 1938. The system, $CaSO_4$-H_2O. Am. J. Sci., vol. 235-A, p 247-272.

Raj, R. 1982. Creep in polycrystalline aggregates by matter transport through a liquid phase. J. Geoph. Res., vol. 87, p 4731-4739.

Raj, R. & Chyung, C.K. 1981. Solution-precipitation creep in glass ceramics. Acta Metall., vol. 29, p 159-166.

Robin, P.Y.F. 1978. Pressure-solution at grain-to-grain contacts. Geochim. Cosmochim. Acta, vol., 42, p 1383-1389.

Rutter, E.H. 1976. The kinetics of rock deformation by pressure solution. Phil. Trans. Royal Soc. London. A: Math. Phys. Sci., vol. 283, p 203-219.

Rutter, E.H. 1983. Pressure solution in nature, theory and experiment. J. Geol. Soc. London, vol. 140, p 725-740.

Sarig, S. 1994. Fundamentals of aqueous solution growth. In: D.T.J. Hurle (Editor), Handbook of crystal growth, vol.2b, Growth mechanisms and dynamics, p 1217-1269.

Schutjens, P.M.T.M. 1991. Intergranular pressure solution in halite aggregates and quartz sands: an experimental investigation. Geologica Ultraiectina vol. 76, Thesis Utrecht University, pp 233.

Scrutton, A. & Grootscholten, P.A.M. 1981. A study on the dissolution and growth of sodium chloride crystals. Trans. Inst. Chem. Eng., vol. 59, p 238-246.

Shimamoto, T. 1981. Dehydration of simulated gypsum gauge and its effect on the frictional sliding of Tennessee sandstone. EOS, Trans. AGU, vol. 62(17), p 400.

Shimamoto, T. 1986. Strengthening of phyllosilicate and gypsum gouges with increasing temperature: Effect of temperature or moisture elimination? Int. J. Rock Mechanics Min. Sci. Geomech. Abstr., vol. 23(6), p 439-443.

Shimizu, I. 1995. Kinetics of pressure solution creep in quartz: theoretical considerations. In: C.J. Spiers and T. Takeshita (Editors), Influence of fluids on deformation processes in rocks. Tectonophysics, vol. 245, p 121-134.

Shternina, E.B. 1960. Solubility of gypsum in aqueous solutions of salts. Int. Geol. Rev., vol. 2, p 606-616.

Simón, J.L. & Suriano, A. 1986. Diapiric deformations in the Quaternary deposits of the central Ebro Basin, Spain. Geol. Mag., vol. 123(1), p 45-57.

Smith, B.R. and Alexander, A.E. 1970. The effect of additives on the process of crystallization, II. Further studies on calcium sulphate (1). J. Coll. Interf. Sci., vol. 34, p 81-90.

Solé-Sugranes, L. 1978. Gravity and compressive nappes in the central southern Pyrenees (Spain). Am. J. Sci., vol. 278, p 609-637.

Spiers, C.J. & Schutjens, P.M.T.M. 1990. Densification of crystalline aggregates by fluid-phase diffusional creep. In: D.J. Barber and P.D. Meredith (Editors), Deformation Processes in Minerals, Ceramics and Rocks. Unwin Hyman, London, pp. 334-353.

Spiers, C.J. & Brzesowsky, R.H. 1993. Densification behaviour of wet granular salt: theory versus experiment. Seventh Symposium on salt, I : 83-92.

Spiers, C.J., Peach, C.J., Brzesowsky, R.H., Schutjens, P.M.T.M., Liezenberg, J.L. & Zwart, H.J. 1989. Long-term rheological and transport properties of dry and wet salt rocks. Nuclear Science and Technology, EUR 11848 EN. Office for Official Publications of the European Communities, Luxembourg.

Spiers, C.J., Schutjens, P.M.T.M., Brzesowsky, R.H., Peach, C.J., Liezenberg, J.L. & Zwart, H.J. 1990. Densification of crystalline aggregates by fluid-phase diffusional creep. In: R. Knipe and E.H. Rutter (Editors), Deformation mechanisms, rheology and tectonics. J. geol. Soc. Spec. Publ., 54 : 215-227.

Stoop, B.T.J., Larbi, J.A. & Heijnen, W.M.M. 1995. Compaction of FGD-gypsum. Zement Kalk Gips, in press.

Tada, R. & Siever, R. 1986. Experimental knife-edge pressure solution of halite. Geochim. Cosmochim. Acta, vol. 50, p 29-36.

Tadros, M.E. & Mayes, I. 1979. Linear growth rates of calcium sulphate dihydrate crystals in the presence of additives. J. Coll. Interf. Sci., vol. 72-2, p 245-254.

Toriumi, T., Kuwahara, T. & Hara, R. 1938. On the calcium sulfate in seawater II. Solubilities of calcium sulphate hemihydrate in sea water of various concentrations at 65°-150°C. Technol. Rep. Tohuku Imp. Univ., vol. 12, p. 560-570.

Underhill, J.R. 1988. Triassic evaporites and Plio-Quartenary diapirsm in western Greece. J. Geol. Soc. London, vol. 145, p 269-282.

Urai, J.L. 1983. Water assisted dynamic recrystallization and weakening in polycrystalline bischofite. Tectonophysics, vol. 96, p 125-157.

Urai, J.L., Means, W.D. and Lister, G.S. 1986. Dynamic recrystallization of minerals. Geoph. Monograph, vol. 36, p 161-200.

Urai, J.L., Spiers, C.J., Zwart, H.J. & Lister, G.S. 1986. Weakening of rock salt by water during long-term creep. Nature, vol. 324, 554-557.

Van Berkel, J.T., Torrance, J.G. & Schwerdtner, W.M. 1986. Deformed anhydrite nodules: A new type of finite strain gauge in sedimentary rocks. Tectonophysics, vol. 124, p 309-323.

Van der Eerden, J.P. 1994. Crystal growth mechanisms. In: D.T.J. Hurle (Editor), Handbook of Crystal Growth, vol. 1a, Thermodynamics and Kinetics, p 307-475.

Van 't Hoff, J.H., Armstrong, E.F., Hinrichsen, W., Weigert, F. & Just, G. 1903. Gips und Anhydrit. Z. Phys. Chem., vol. 45, p. 257-306

Van Rosmalen, G.M., Daudey, P.J. & Marchee, W.G.J. 1981. An analysis of growth experiments of gypsum crystals in suspension. J. Cryst. Growth, vol. 52, p 801-811.

Visser, H.J.M. & Spiers, C.J. 1992. Compaction experiments on $NaNO_3$ aggregates plus saturated solution: an analogue for partially molten systems. EOS, transactions, AGU, vol. 73, p 528.

Wakai, F. 1994. Step model of solution-precipitation creep. Acta metall. mater., vol. 42, p 1163-1172.

Wall, J.R., Murray, G.E. & Diaz, T.G. 1961. Geologic occurrence of intrusive gypsum and its effect on structural forms in Coahuila marginal folded province of northeastern Mexico. AAPG Bull., vol. 45, p 1504-1522.

Weijnen, M.P.C. 1986. The influence of additives on the crystallization of gypsum. Thesis, Tech. Univ., Delft, 207 pp.

Weyl, P.K. 1959. Pressure solution and force of crystallization - a phenomenological theory. J. Geoph. Res., vol. 64, p 2001-2025.

Williams, S.C. 1986. Experimental pressure solution of gypsum. AAPG Bull., vol. 70(5), p 663.

Williams, S.C. 1988. The shear strength of gypsum single crystals on the three cleavage planes. Tectonophysics, vol. 148, p 163-173.

Wooster, W.A. 1936. On the crystal structure of gypsum, $CaSO_4 \cdot 2H_2O$. Z. Kristall., vol. 94, p 375-396.

Zen, E. 1965. Solubility measurements in the system $CaSO_4$-NaCl-H_2O at 35°, 50°, and 70° C and one atmosphere pressure. J. Petrology, vol. 6, p 124-164.

SAMENVATTING

Gips-gedomineerde evaporiet sequenties spelen een belangrijke rol in de mechanica van "foreland" overschuivings tektoniek. Zij vormen eveneens grootschalige halokinetische structuren en afdichtende formaties die soms geassocieerd zijn met olie- en gasvoorkomens. Het vervormingsgedrag van polykristallijn gips en de onderliggende fysische processen zijn daarom belangrijke onderwerpen in de structurele geologie, tektonofysica en geomechanica. Het vervormings- en verdichtingsgedrag van polykristallijn gips zijn daarnaast van fundamenteel belang voor de taxatie van nieuwe gipsprodukten in toepassingen als dragende elementen in de bouwindustrie. Dit proefschrift doet verslag van een experimenteel, materiaalkundig georienteerd onderzoek met als doel inzicht te verschaffen in het vloei- en verdichtingsgedrag van gips onder zowel natuurlijke als bouwkundige omstandigheden. Speciale aandacht wordt geschonken aan door vloeistoffen geholpen kruip (drukoplossing) en daaraan gerelateerde processen, omdat van deze processen verwacht wordt dat zij belangrijk zijn voor oplosbare stoffen.

In Hoofdstuk 1 is eerder experimenteel onderzoek op gips samengevat. Aspecten van het vervormingsgedrag van gips die nog steeds onvoldoende begrepen worden zijn geïdentificeerd. Tevens zijn de doelstellingen van de huidige studie gedefinieerd.

Hoofdstuk 2 beschrijft hydrostatische compactie kruip experimenten die uitgevoerd zijn op gipsaggregaten (korrelgrootte 15-125 μm, effectieve druk 0,4-3,9 MPa en bij kamertemperatuur). Droge monsters vertonen 10-13% instantane compactie tijdens het aanbrengen van de belasting, waarna er geen kruip meer optreedt. Daarentegen vertonen natte monsters (monsters doordrenkt met verzadigde $CaSO_4$ oplossing) relatief snelle kruip. De compactiesnelheid varieert van aanvankelijk ~10^{-5} s^{-1} tot waardes van ~10^{-9} s^{-1} bij volumeveranderingen van ~12%. De mechanische data die verkregen zijn voor de natte experimenten vertonen een derde tot vierde machts afhankelijkheid van de compactiesnelheid met effectieve druk en een omgekeerd evenredige afhankelijkheid van de compactiesnelheid met korrelgrootte. Als ook onafhankelijke kristalgroeidata voor gips mee in beschouwing worden genomen dan blijkt dat waargenomen trends een goede overeenkomst met theoretische modellen voor korrelgrens-diffusie drukoplossing (in het vervolg GBDPS genoemd). De compactiesnelheid wordt bepaalt door neerslag op de korrel-porie grenzen. Bovendien vertonen de nat-gecompacteerde monsters duidelijk

microstruktureel bewijs voor het optreden van kruip door drukoplossing, zoals korrel-korrel insnijdingen, korrel-korrel contact oplossing en nieuwgroei op de korrel-porie grenzen. Op grond hiervan wordt voorgesteld dat de natte monsters compacteerden door middel van GBDPS kruip waarbij de snelheid bepaald werd door de neerslag reaktie. Er wordt verondersteld dat de afwijking tussen waargenomen en verwachte compactiesnelheden wordt veroorzaakt door onzuiverheden in het natuurlijke startmateriaal (Somerset, Engeland).

In Hoofdstuk 3 wordt het uniaxiale kruipgedrag van nat korrelig gips (uit het Bekken van Parijs) onderzocht in zowel chemisch gesloten als chemisch open systemen. De experimenten werden uitgevoerd bij opgelegde spanningen van 0,5 tot 2,5 MPa, waarbij de korrelgrootte varieerde van 32-282 μm, bij kamertemperatuur en gebruikmakend van porieënvloeistoffen die verzadigd zijn ten opzichte van monsters zonder opgelegde spanning. Controle-experimenten, die uitgevoerd werden op zowel droge als met olie verzadigde monsters, lieten geen kruip zien. Daarentegen vertonen monsters die verzadigd zijn met $CaSO_4$ oplossing een snel kruipgedrag. Bovendien verschaffen de microstructuren die zich in alle monsters ontwikkelden klassiek bewijs voor het optreden van GBDPS. Om een gedetailleerde vergelijking met de theorie te rechtvaardigen wordt aangetoond dat kristalwater, hetgeen aanwezig is in gips, geen invloed heeft op de drijvende kracht en de snelheidsbepalende stappen in het drukoplossingsproces. De resultaten kunnen daarom vergeleken worden met bestaande modellen voor GBDPS. Alhoewel het waargenomen gedrag van de chemisch gesloten experimenten vrijwel gelijk is aan het gedrag van de experimenten die beschreven zijn in Hoofdstuk 2, voldoet het aan geen van de bestaande theoretische modellen voor zowel oplossing-, diffusie-alsmede neerslag-gecontroleerde drukoplossing. Niettemin suggeren onafhankelijke kristalgroei- en oplossingsdata dat neerslag zeer waarschijnlijk de compactiesnelheid controleert. De open-systeem experimenten, waarbij vloeistof door het monster stroomt tijdens de vervorming, leveren aanvullende informatie over neerslag als snelheidsbepalend proces. In deze experimenten kan neerslag niet langer de vervormingssnelheid bepalen, zodat ofwel oplossing, ofwel diffusie snelheidsbepalend zal worden. In dat geval kan een sterke toename van de kruipsnelheid verwacht worden. In de open-systeem experimenten werden inderdaad 10 tot 30 keer snellere vervormingssnelheden gemeten. Hierdoor wordt bevestigd dat de kruipsnelheid door middel van GBDPS in de gesloten-systeem experimenten gecontroleerd wordt door neerslag.

In Hoofdstuk 4 is de groei vàn gips onderzocht gebruikmakend van kristallen en oplossingen gemaakt van natuurlijk gips uit het Bekken van Parijs. Dit is gedaan om een vergelijking te maken met de kruipdata van Hoofstuk 3. De beperkte hoeveelheid resultaten laten zien dat bij kleine drijvende krachten ($\Delta\mu$ < 1 kJ/mole) de neerslag tweede orde kinetiek volgt terwijl bij hogere drijvende krachten de kinetische orde 3 tot 4 is. Deze gegevens komen goed overeen met eerder werk. De data suggereren ook een eerste tot tweede machtsafhankelijkheid van de groeisnelheid met de korrelgrootte bij lage drijvende krachten ($\Delta\mu$ < 1 kJ/mole) en een tweede tot derde machts afhankelijkheid bij hogere drijvende krachten. De experimenteel verkregen groeikinetiek is gebruikt om drukoplossingssnelheden te voorspellen, waarbij neerslag op de korrel-porie grenzen snelheidsbepalend is. De voorspelde kruipsnelheden zijn ~10 keer sneller dan geobserveerde snelheden in de drukoplossingsexperimenten van Hoofdstuk 3. De voorspelde en geobserveerde data laten echter wel een bijna identieke afhankelijkheid van de kruipsnelheid met de opgelegde spanning en korrelgrootte zien. Dit is opnieuw een aanwijzing voor de hypothese dat drukoplossing in gips wordt gecontroleerd door de neerslagsreactie.

Hoofstuk 5 bespreekt de invloed van zoutgehalte in de porieënvloeistof (dat wil zeggen verzadigde gipsoplossingen met NaCl in concentraties van 0,01-6,11M) op het compactie kruipgedrag van korrelig gips (gips uit het Bekken van Parijs). De resultaten vertonen vrijwel identieke mechanische gedragsrelaties en ontwikkeling van microstrukturen in vergelijking met de resultaten van experimenten uitgevoerd met NaCl-vrije porieënvloeistof (Hoofdstuk 3). De kruipsnelheden zijn echter systematisch tot 50 keer sneller in de experimenten met NaCl-houdende porieënvloeistof. Dit versnellende effect van NaCl is geheel consistent met het in de literatuur vermelde versnellende effect zoals dat optreedt bij de groeikinetiek van gips uit NaCl-houdende oplossingen. Dit verschaft extra bewijs dat de compactie van nat gips in chemisch gesloten systemen optreedt door door neerslag-gecontroleerde drukoplossing.

Hoofdstuk 6 vestigt de aandacht op vervormingsprocessen die belangrijk zijn voor het taxeren van de mogelijkheden om nieuwe, dragende bouwelementen te produceren door middel van snelle mechanische verdichting van gips afkomstig van vliegas-ontzwavelings (FGD) processen. Het doet verslag van uniaxiale verdichtingsexperimenten op FGD-gips met een waterinhoud van 0-5%, uitgevoerd bij opgelegde spanningen van 25-530 MPa, bij temperaturen van 20-150°C en belastingssnelheden van 10^4 - 10^7 Pa s^{-1}. Droge monsters verdichten tot porositeiten van 8% bij kamertemperatuur op een tijds-onafhankelijke manier door middel van

kataklase op de korrelschaal, vergezeld door plastische vervorming. De monsters vertonen een reductie van de korrelgrootte. In de natte monsters gaat tijds-onafhankelijke compactie door kataklase en plastische vervorming tevens samen met door vloeistoffen geassisteerde rekristallisatie en drukoplossings-processen. Dit zorgt voor een afname van de korrelgrootereductie, bevordert instantane verdichting en staat onder konstante belasting verdichtingskruip toe. Bij verhoogde temperaturen vertonen droge en natte monsters zowel meer instantane compactie als tijds-afhankelijk gedrag bij konstante belasting. Hierbij treden geen veranderingen op in de verdichtingsmechanismen. Bij temperaturen waar dehydratie begint op te treden (90-110°C) worden in de van oorsprong droge monsters ook vloeistof-geassisteerde mechanismen waargenomen. Bij nog hogere temperaturen vertonen alle monsters gedeeltelijke of gehele dehydratie naar hemihydraat en een slechte verdichting. De dichtste monsters (~1,5% porositeit) werden verkregen door compactie van natte monsters (2,0-2,5gew.% water), bij de hoogste opgelegde spanning (530 MPa), bij temperaturen van 90-100°C, en gebruikmakend van de hoogste belastingssnelheden. Dit materiaal is sterk verhard en geeft aanleiding tot verder onderzoek naar mogelijke dragende toepassingen in de bouwindustrie.

In Hoofdstuk 7 worden algemene conclusies getrokken gebaseerd op bevindingen uit de voorafgaande hoofdstukken. Door het kombineren van drukoplossingsdata en groeikinetiekdata wordt de conclusie getrokken dat drukoplossing in gips aggregaten, onder chemisch gesloten omstandigheden, wordt gecontroleerd door een spiraalgroei neerslag mechanisme bij spanningen lager dan 1 tot 10 MPa, en door door oppervlaktenucleatie beperkte groei bij hogere spanningen. De verkregen data worden gekoppeld aan theorie om zo kruipwetten af te leiden voor deze twee drukoplossings mechanismen, voor zowel poreuze als dichte gips aggregaten rekening houdend met samenstellingseffecten. Deze vergelijkingen worden vervolgens gebruikt om het kruipgedrag van gips gesteente te voorspellen onder zowel natuurlijke omstandigheden als bij toepassingen in de bouw. Tenslotte worden onbeantwoorde vragen geïdentificeerd en suggesties voor verder onderzoek gegeven.

NAWOORD

Hierbij wil ik iedereen bedanken die bijgedragen heeft aan de totstandkoming van dit proefschrift. Mijn dank gaat in de eerste plaats gaat uit naar mijn ouders, voor hun onvoorwaardelijke en volledige steun tijdens mijn studiejaren in Utrecht.

Evenzoveel dank gaat uit naar mijn promotor Chris Spiers, zijn enthousisme voor experimenteel onderzoek en gedrevenheid in het vinden van antwoorden waren voor mij erg motiverend. Vele avonden werden lange "sessions" gehouden om te praten over het onderzoek. Elke keer leverde dat weer nieuwe ideeën op en een nieuwe serie experimenten. Niet altijd werd er over werk gesproken, en op momenten dat dat nodig was toonde Chris zich een echte vriend.

De experimenten die ik heb uitgevoerd had ik nooit kunnen doen zonder de hulp van Colin Peach die mij heeft leren werken met de apparatuur in het HPT. Onontbeerlijk was ook de hulp van de technici: Gert Kastelein, die het compactie vat voor de experimenten van hoofdstuk zes heeft gebouwd, Peter van Krieken die alle "tube set-ups" heeft gemaakt, en Eimert de Graaff die acoustische emissie apparatuur voor mij maakte, hiervoor mijn dank.

Speciale dank gaat uit naar mijn beste vrienden Rian Visser en paranimfen Rob McDonnell en Patrick Speck. Zij hebben delen van het proefschrift doorgelezen en gecorrigeerd en op alle mogelijke manieren geholpen om alles op tijd af te krijgen. Ook Timon Fliervoet heeft een grote bijdrage geleverd door zijn hulp aan te bieden bij het maken van de schematische tekeningen in mijn proefschrift. Ook Magda Martens ben ik veel dank verschuldigd. Zij heeft ervoor gezorgd dat alles altijd op rolletjes liep door de hele papierwinkel bij te houden en mij met raad en daad bij te staan.

Verder zijn er nog een groot aantal mensen die op de een of andere manier hun steentje hebben bijgedragen: ten eerste Coen ten Brink, mijn voorgangers Hans, Peter, Raymond, Bas en Rolf, verre vrienden Alice, Marlina, Mirjam, Ronald en Paul, en mijn huisgenoten Harry, Annemarijn en kiki die er in de laatste twee maanden voor gezorgd hebben dat ik fatsoenlijk te eten kreeg.

CURRICULUM VITAE

01-06-1965   Geboren te Leeuwarden

1977-1985   VWO, Stedelijk Scholen Gemeenschap, Leeuwarden

25-02-1991   Doctoraal examen Geologie, Universiteit Utrecht,
Hoofdvak Structurele Geologie, bijvak Kristallografie

1991-1995   Assitent In Opleiding, vakgroep Geologie,
Universiteit Utrecht